RÉPUBLIQUE FRANÇAISE
Liberté Égalité Fraternité

Université de Toulouse

Doctorat de l'Université de Toulouse

préparé à l'Université Toulouse III - Paul Sabatier

Mécanismes de dissolution de minéraux dans des liquides silicatés d'intérêt industriel

---

Thèse présentée et soutenue, le 10 décembre 2024 par

Fatima YOSHIZAWA

École doctorale
SDU2E - Sciences de l'Univers, de l'Environnement et de l'Espace

Spécialité
Sciences de la Terre et des Planètes Solides

Unité de recherche
IRAP - Institut de Recherche en Astrophysique et Planetologie

Thèse dirigée par
Mike TOPLIS, Ekaterina BUROV et Anne-Céline GAREL-LAURIN

Composition du jury
Mme Nadège OLLIER, Rapporteure, CEA (DRF/IRAMIS/ Laboratoire des Solides Irradiés)
M. Mathieu ROSKOSZ, Rapporteur, MNHN/IMPMC
M. Mathieu ALLIX, Rapporteur, CEMHTI
Mme Stéphanie DUCHENE, Examinatrice, GET/Université Paul Sabatier
M. Philippe PAPET, Examinateur, Polytech / Université Montpellier
Mme Sophie SCHULLER, Examinatrice, CEA Marcoule
M. Mike TOPLIS, Directeur de thèse, Université Toulouse III - Paul Sabatier

Membres invités
Mme Ekaterina Burov, Saint-Gobain Recherche Paris
Mme Anne-Céline Garel-Laurin, Saint-Gobain Recherche Paris

Acknowledgements

Pursuing this PhD has been more than just an academic endeavor. Conducting research in a country different from my own brought its own set of complexities, yet it was the warmth and kindness of the people I encountered that turned this experience into something truly invaluable. Their support, encouragement, and companionship made these three years a remarkable period of growth — both personally and professionally — that I will forever cherish.

I am deeply grateful to my thesis supervisors for their invaluable guidance and support throughout this PhD. Mike, thank you for your pragmatic insights and sharp ideas, which helped refine the scope of this research, even if our exchanges took place mostly via Microsoft Teams rather than in a warmer Toulouse. Anne-Céline and Katia, your unwavering presence, insightful advice, and encouragement shaped this work in countless ways. Your active participation and patience, whether through discussions that opened new paths or through your constant support in moments of doubt, made all the difference. I feel incredibly fortunate to have had such a dedicated and inspiring team by my side.

To my committee members, especially my three reviewers, thank you for your thoughtful suggestions and challenging questions that enriched my understanding and pushed me to think more critically about my work. Special thanks to Stéphanie Duchene for presiding over the committee and for participating in my PhD follow-up meetings in Toulouse, alongside Anastassia Borisova and Franck Pigeonneau.

I am also deeply grateful to Cécile Jousseaume for proposing this PhD subject and connecting me with various industrial actors. A special thanks to Maxime Jacquemin—sharing an office with you was a joy, and your quick, knowledgeable responses to my diffusion matrix questions were a lifesaver !

I cannot express enough gratitude to everyone at SGR, especially within the Minéralogie Appliquée and SVI teams. Coming back to France and finding such supportive and open-minded colleagues made my experience not only enjoyable but also incredibly fruitful.

Huge thanks to Philippe Bossard for his enthusiasm about the digestion tests and for sharing his ideas and experience. Thanks to him, our first experiments with what seemed like fragile platinum foil turned out to be surprisingly successful.

A special thank you to Léa Duboz for her curiosity, engagement, and valuable insights into earth-alkaline oxides in alumina diffusion. It was a pleasure to be her industrial advisor during her internship, and our collaboration allowed me to better communicate and refine my own PhD work.

I am also grateful to Lionel Homo, Régine Faure, and Bertrand Testulat for their work on the EPMA measurements, which formed the core of the experimental data of this PhD. Thank you to Bruno Germain, Andrea Gioia, Victor Haspot, Thierry Cretin, Benedicte Garneau, and Camille Heraud for enabling the measurements with XRD, SIMS, and chemical analyses.

A big thank you to the MEC's refractorists' team for their help with dynamic dissolution tests, sample preparations, introducing me to thermodynamic calculations with FactSage, and welcoming me so warmly to the team after my thesis !

I am grateful for the exchanges and interest shared with the EV department, and a special thanks to Kevin Lippera for his invaluable help in framing the mathematical approach to the dissolution problem—your patience and pedagogy were so appreciated !

To the wonderful SVI team—thank you for welcoming me so warmly. A special thanks to the PhD students I met during these three years ; our coffee and lunch breaks, weekend trips, cakes during the winter blues, picnics, and beers during the summer made the ups and downs of this PhD journey much more memorable.

Arriving in Paris could have been overwhelming, but thanks to the incredible community I found, it was anything but. My Brazilian family in Paris deserves my deepest gratitude for their unwavering support and care : Alan, Adriana, Marcela, Carlos, Marcelo, Gui, Douglas, Catarina and Ilusca (my now former coloc). A very special thanks to Ian, for being always there, trusting my potential, and supporting me during this critical last year.

Thank you to my long-distance oracles—Igor, Milena, Julia, Passos, Malu, Janaina—for listening to my complaints and believing in me, even from afar.

I am eternally indebted to my former mentors at UFSCar and during my research assistantship, who first ignited my passion for science, glass, ceramics, and research. Reuniting with you at various conferences has been a joy that I will always treasure.

Finally, my deepest gratitude goes to my family. Your unwavering belief in me has been my lifeline throughout this journey. I truly could not have accomplished this without your unconditional love and support. Thank you for standing by me every step of the way.

Introduction détaillée en français

La fusion représente plus de 75% de la consommation énergétique totale dans la production du verre [1]. Cette étape critique permet de transformer des matières premières, sous forme de poudre, en un liquide silicaté homogène et exempt de défauts. Le verre fondu peut ensuite être façonné en une large variété de produits tels que des vitres, des contenants ou des fibres. Un aspect essentiel de cette transformation réside dans la dissolution des phases solides, en particulier le quartz issu des grains de sable et les oxydes réfractaires comme l'alumine, au sein du bain de verre. Comprendre ces mécanismes de dissolution est crucial, car une dissolution incomplète de ces matériaux peut entraîner la formation d'inclusions solides, appelées « pierres » ou « infondus » dans l'industrie verrière. La Figure 1 illustre quelques exemples de ces défauts.

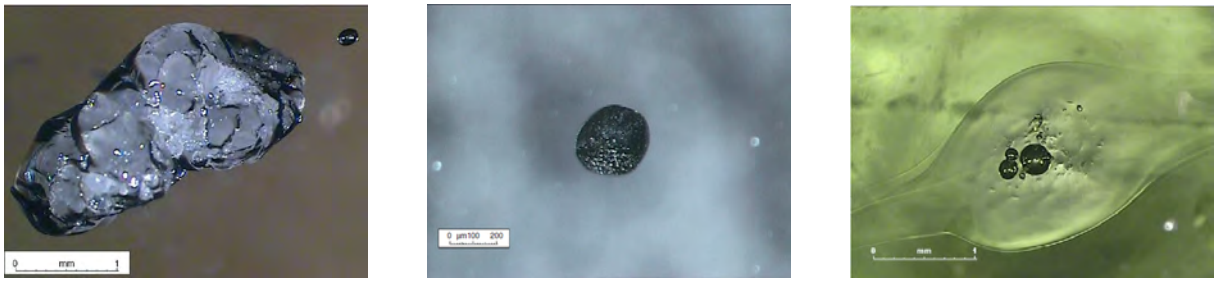

Figure 1 Exemples d'inhomogénéités après l'étape de fusion d'un verre silico-sodo-calcique (observées par microscopie optique) : (gauche) inclusion solide due à une dissolution incomplète de la silice, (milieu) cristal de chromite non dissous, (droite) inhomogénéité dans la phase vitreuse (également appelée « larmes ») de feldspath, avec environ 20% massique d'alumine, enfermant des bulles en son cœur. Depuis [2]

Ces inclusions solides affectent non seulement les propriétés mécaniques et esthétiques du verre, mais elles compromettent également les étapes ultérieures de façonnage, comme le fibrage. Cela entraîne un gaspillage de matières premières, des perturbations dans la production et une diminution du rendement global, augmentant ainsi les coûts de fabrication et le volume de déchets. Une meilleure compréhension des processus de dissolution permetrait de réduire ces pertes et, de manière plus large, améliorer l'efficacité énergétique du procédé, un objectif clé pour l'industrie du verre dans un contexte de pression environnementale accrue.

L'un des principaux défis dans la fabrication du verre réside dans la dissolution des oxydes réfractaires, notamment l'alumine et la silice, qui proviennent à la fois des matières premières et du revêtement des fours. Ces oxydes réfractaires, caractérisés par leurs points de fusion élevés, se dissolvent lentement dans le verre en fusion, augmentant ainsi le risque de défauts. L'alumine, constituant courant des revêtements réfractaires, pose un problème particulier, car sa dissolution peut réduire la durée de vie opérationnelle du four. Dans ce contexte, la résistance à la corrosion

des matériaux réfractaires devient cruciale pour des raisons économiques et environnementales. Les fabricants de réfractaires cherchent à améliorer la résistance à l'érosion et à l'usure de leurs matériaux, tandis que l'érosion de ces matériaux contribue à l'introduction d'inclusions dans le verre fondu, lesquelles doivent se dissoudre rapidement pour éviter des défauts comme l'obstruction des buses ou la contamination des produits finis.

Par ailleurs, la dissolution du quartz, principal composant du sable utilisé dans la production de verre, peut représenter jusqu'à 90% du temps total nécessaire à la conversion des matières premières en liquide silicaté, un paramètre appelé « batch-free time » dans l'industrie verrière [3]. Une gestion efficace de la dissolution est donc essentielle pour maintenir la qualité du verre tout en optimisant l'efficacité de la production. En effet, une dissolution incomplète du quartz peut entraîner des temps de production plus longs, une augmentation des coûts et des défauts dans le produit fini.

La modélisation numérique est devenue un outil puissant pour améliorer notre compréhension du processus de fusion du verre et accroître son efficacité. Les modèles de dynamique des fluides (CFD) ont permis de prédire avec plus de précision les distributions de vitesse et de température au sein du verre fondu, fournissant des informations essentielles sur les mécanismes de transport de masse et les temps de séjour des inclusions solides. Ces résultats peuvent ensuite être traduits en quantités secondaires, telles que les taux de dissolution et les risques d'apparition de défauts, qui sont critiques pour l'optimisation du procédé. Cependant, une limitation clé des modèles existants réside dans le manque de données thermodynamiques et de transport pour les systèmes multicomposants. Contrairement aux modèles binaires simplifiés, qui ne capturent qu'une fraction de la réalité industrielle, les systèmes multicomposants représentent la complexité des verres industriels et nécessitent des approches plus robustes.

Cette thèse vise donc à répondre à une question centrale : *comment mieux comprendre et mesurer la dissolution de l'α-alumine et du quartz dans les systèmes verriers multicomposants, tels que le verre industriel silico-sodo-calcique ?* Alors que les études précédentes se sont concentrées sur des modèles binaires, qui offrent une vision simplifiée des mécanismes de dissolution, cette thèse s'intéresse à un verre industriel, par essence multicomposant. L'objectif est de développer une compréhension complète des interactions entre les constituants dans un système multicomposant afin de permettre ensuite l'essor de modèles plus précis de la dissolution et ainsi améliorer leur capacité à prédire l'apparition de défauts dans le verre.

La structure de cette thèse reflète cette progression de la recherche, passant d'une revue des connaissances actuelles à la mise en place d'une stratégie expérimentale pour mesurer la dissolution de l'alumine et du quartz à l'interface solide-liquide dans un système multicomposant.

Le **chapitre 1** présente un examen détaillé des mécanismes de dissolution de l'alumine et de la silice dans les liquides silicatés dans le contexte de la fusion industrielle du verre, structuré en cinq sections clés. Ce chapitre commence par une présentation du procédé industriel de fusion et du rôle de la modélisation CFD dans la prédiction des comportements de dissolution des inclusions solides. Il explore ensuite les mécanismes de dissolution dans les systèmes binaires, en se concentrant sur les réactions d'interface et le transport de masse par diffusion et convection. Ensuite, il examine les données expérimentales disponibles sur la dissolution de l'alumine et de la silice, en mettant en lumière les lacunes dans les données de solubilité et de diffusivité pour les systèmes multicomposants. Une quatrième section aborde les défis liés à l'application des modèles binaires aux compositions complexes à plusieurs composants, en introduisant une approche matricielle de la diffusivité, plus adaptée à ces systèmes. Enfin, la dernière section identifie les lacunes dans les recherches actuelles et définit le cadre de cette thèse : bien que la dissolution dans un four industriel soit sous advection, la dynamique de dissolution dépend de la

disponibilité de données précises sur la solubilité et la diffusivité, cette dernierère mesurée dans des conditions statiques.

Le **chapitre 2** décrit la stratégie expérimentale mise en place afin de mesurer précisément les profils de diffusion à partir de l'interface solide-verre, en minimisant les effets de convection susceptibles de surestimer les coefficients de diffusion. Il détaille la conception d'un montage expérimental assurant une dissolution statique unidimensionnelle (Figure 2), éliminant les gradients thermiques et la convection. Ce chapitre inclut également la préparation des matériaux, la réalisation des tests de dissolution, et les techniques de caractérisation post-mortem, notamment la microscopie, la spectroscopie Raman et les analyses chimiques par microsonde électronique (EPMA). L'originalité de cette approche repose sur l'utilisation combinée de ces techniques pour capturer avec précision les mécanismes de dissolution à l'échelle microscopique.

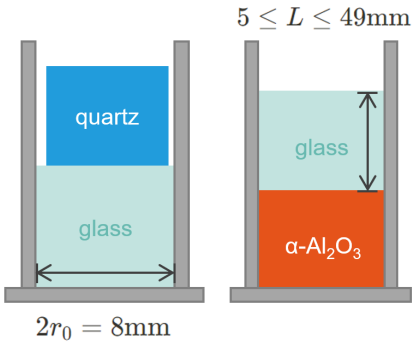

Figure 2 Illustration du montage expérimental afin de réproduire une dissolution statique unidimensionnelle. Les matériaux sont préparés sous la forme des cylindres dont les surfaces en contact ont été préalablement polies.

Le **chapitre 3**, rédigé sous forme d'article publié au *Journal of Non-Crystalline Solids*, se concentre sur la dissolution diffusive de l'α-alumine entre 1300 et 1450 °C. Les profils de composition chimique mesurés par EPMA révèlent un comportement principalement contrôlé par la diffusion, avec des variations significatives de la concentration à l'équilibre en fonction de la température. À des températures supérieures à 1400 °C, l'interface de dissolution entre dans le domaine péralumineux, tandis qu'à des températures plus basses, l'excès de charge de l'alumine dissoute est compensé par des cations alcalins et alcalino-terreux. Ce chapitre montre que la diffusivité de l'alumine peut être approchée par un coefficient pseudo-binaire (EBDC), corrélé à la viscosité du verre à l'interface. Cette approche, bien qu'innovante, souligne également la nécessité de modélisations multi-composants pour une compréhension plus précise des mécanismes de dissolution.

Le **chapitre 4** se focalise sur la dissolution de la silice à 1400 °C, en se concentrant sur les mécanismes de transport de masse et l'évolution microstructurale. Ce chapitre introduit les transformations de phases de la silice et examine leur impact sur les vitesses de dissolution, en intégrant des données expérimentales obtenues à partir de sources variées (quartz et cristobalite). Une attention particulière est accordée aux polymorphes de la silice durant la dissolution, observés grâce à la cartographie Raman, et aux effets de la microstructure sur ces transformations.

Enfin, le chapitre de **conclusion** propose une synthèse des résultats, comparant les mécanismes de dissolution de l'alumine et du quartz, et suggère des pistes pour de futures recherches sur les cinétiques de dissolution dans les systèmes verriers multicomposants. En adoptant une approche multi-composant, cette thèse vise à fournir des prédictions plus précises des taux de dissolution

et à contribuer au développement de modèles industriels améliorés. Les résultats obtenus ne se limitent pas à l'industrie verrière ; ils ouvrent également des perspectives pour d'autres industries utilisant des matériaux réfractaires à haute température, renforçant à la fois la compréhension théorique et les applications pratiques des processus de dissolution dans un contexte industriel plus large.

Introduction

Glass melting is a critical process in the glass manufacturing industry, accounting for over 75% of the total energy consumption [1]. As a multi-phase, high-temperature process, glass melting requires precise control of residence time and flow to ensure the complete conversion of raw materials into defect-free glass. Achieving this transformation efficiently is critical to both the economic viability and environmental sustainability of the industry.

During the melting process, raw materials are transformed into a homogeneous molten glass that can be shaped into a variety of products such as flat glass, containers, and fibers. A critical aspect of this transformation is the dissolution of solid phases, particularly quartz and refractory oxides like alumina, into the melt. The incomplete dissolution of these materials can lead to the formation of solid inclusions, or "stones", in the glass, some examples depicted in Figure 3. These inclusions compromise not only the mechanical properties of the glass but also its aesthetic and processing qualities. In applications such as architectural glass, or glass fibers, these defects can result in significant material waste, production issues, or reduced product performance, thereby increasing production costs and waste.

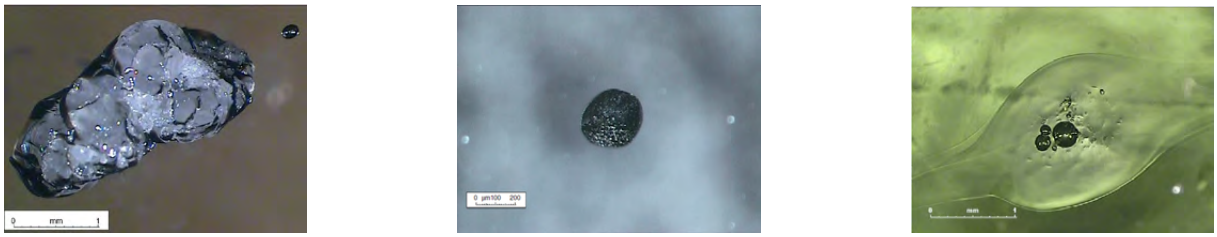

Figure 3 Examples of glass melting inhomogeneities in soda-lime silica glass (observed by optical microscopy) : (left) silica batch solid defect from incomplete dissolution, (middle) undissolved chromite crystal, (right) liquid inhomogeneity (also known as "cord" or "knot") of feldspar, with $\approx$ 20 wt% of Al_2O_3 , enclosing bubbles at its core. From [2]

One of the major challenges in glass manufacturing lies in the dissolution of refractory phases, especially alumina and silica, which can originate from both the raw materials and the furnace lining. These refractory oxides, with their high melting points, dissolve slowly into the molten glass, creating the risk of defects. Alumina, a common component of refractory linings, is particularly problematic as its dissolution can shorten the operational life of the furnace. Similarly, quartz, the primary constituent of the sand used in glass production, plays a crucial role in determining the melting and refining efficiency of the glass. Effective management of the dissolution process is thus essential to maintaining glass quality and optimizing production efficiency.

In industries reliant on high-temperature furnaces with refractory linings, the corrosion resistance of these ceramic-based materials is of significant economic and environmental importance. On

the one hand, manufacturers of refractories seek to improve their resistance to corrosion and wear in contact with slag. On the other hand, the erosion of these materials during industrial processes contributes to inclusions in the melt, which must be dissolved quickly to prevent downstream defects such as nozzle clogging or product contamination.

Numerical modeling has become a powerful tool for enhancing our understanding of the glass melting process and improving its efficiency. Computational Fluid Dynamics (CFD) models have significantly advanced the ability to predict velocity and temperature distributions within the molten glass. These primary outputs can then be translated into secondary quantities, such as minimum residence times and dissolution rates, which are critical for optimizing the process. However, a key limitation of existing models lies in the lack of comprehensive thermodynamic and transport data for multi-component systems. Despite considerable research across various fields, dissolution rates and mass transport coefficients for both silica and alumina remain scattered, indicating that current knowledge of the dissolution process is incomplete.

This research aims to address the following question : *How can we better understand and predict the dissolution mechanisms of α-alumina and quartz in multi-component glass systems, such as industrial soda-lime-silica glass ?* While previous studies have predominantly focused on binary system models, which offer a simplified view of dissolution, they do not capture the complexities of real-world industrial glass melts. In binary systems, the dissolution of a single solid phase into a melt is often governed by straightforward diffusion or interface reaction mechanisms. However, industrial glass compositions contain multiple interacting oxides that influence both the solubility and diffusivity of alumina and silica. The presence of additional components, such as sodium, calcium, and magnesium oxides, creates competing diffusion pathways and affects the chemical potential gradients driving dissolution. A comprehensive understanding of these multi-component interactions is therefore necessary to develop more accurate models of glass dissolution and improve manufacturing outcomes.

The structure of this PhD thesis reflects the research's progression, moving from a review of existing knowledge to the development and application of novel experimental methods. Chapter 1 presents a thorough review of the dissolution mechanisms of alumina and silica in silicate glasses, focusing on how these processes are modeled in the context of industrial glass melting. It also identifies key gaps in the existing literature, particularly the lack of reliable data for multi-component soda-lime silica glass, which forms the foundation for the experimental work presented in subsequent chapters. Chapter 2 outlines the materials and methods used in this study, detailing the design of the experimental setup and the characterization techniques employed. The rationale for focusing on static dissolution, aimed at isolating the diffusion-driven aspects of the process, is also discussed.

Chapter 3, presented as a paper published in the *Journal of Non-Crystalline Solids*, focuses on the diffusive dissolution of alpha-alumina in the 1300 to 1450 °C range. This chapter provides detailed insights into the role of multi-component diffusion in controlling dissolution. Chapter 4 extends the analysis to quartz dissolution at 1400 °C, examining the effects of silica polymorphism and phase transformations on the dissolution rate in soda-lime-silica glass.

The final chapter synthesizes the findings, comparing the dissolution mechanisms of alumina and quartz, and offering perspectives on future research into dissolution kinetics in multi-component glass systems. By adopting a multi-component approach, this research aims to provide more accurate predictions of dissolution rates and contribute to the development of improved models for industrial applications. Ultimately, this work seeks to enhance both the theoretical understanding and practical applications of glass dissolution processes, offering pathways for optimizing glass manufacturing while ensuring product quality and process efficiency.

Table of contents

Extended introduction in French iii

Introduction vii

1 State of the art 1
- 1.1 Introduction to Glass Melting and CFD applications . . . 2
  - 1.1.1 Modeling of the dissolution step . . . 5
- 1.2 Dissolution mechanisms in binary systems . . . 6
  - 1.2.1 Interface reaction contribution . . . 9
  - 1.2.2 Diffusion in the glass contribution . . . 11
  - 1.2.3 Contribution of convection in the glass . . . 19
- 1.3 Available data on alumina and silica dissolution . . . 22
  - 1.3.1 Historical overview of silica and alumina dissolution studies . . . 22
  - 1.3.2 Experimental techniques to measure dissolution . . . 23
  - 1.3.3 Comparative analysis of the dissolution measured properties . . . 24
- 1.4 Complexities in multi-component systems . . . 29
  - 1.4.1 Solubility limits . . . 31
  - 1.4.2 Diffusivity . . . 32
  - 1.4.3 Viscosity and its relationship with diffusivity . . . 37
- 1.5 Summary . . . 41

2 Materials and Methods 43
- 2.1 Strategy of study . . . 44
- 2.2 Design of experimental setup for static dissolution . . . 45
  - 2.2.1 Semi-infinite dissolution hypothesis . . . 45
  - 2.2.2 Free convection assessment due to thermal gradients . . . 48
  - 2.2.3 Free convection assessment due to elements migration into the melt . . . 48
  - 2.2.4 Criteria and experimental setup geometry . . . 50
- 2.3 Starting materials . . . 51
  - 2.3.1 Soda-lime silica glass . . . 52
  - 2.3.2 Alumina . . . 52
  - 2.3.3 Quartz . . . 53
- 2.4 Dissolution tests . . . 54
  - 2.4.1 Samples preparation . . . 54
  - 2.4.2 Heat treatment . . . 54
- 2.5 *Ex-situ* characterization techniques and data analysis . . . 55
  - 2.5.1 Microstructural observation and convection verification . . . 55
  - 2.5.2 Structural evolution by Raman spectroscopy cartographies . . . 56

2.5.3 Chemical composition profiles by EPMA . . . 59
2.5.4 Thermodynamic simulations . . . 60
2.6 Methods summary . . . 63

3 Alumina dissolution 65

4 Quartz dissolution 79
4.1 Introduction and theoretical background . . . 80
4.1.1 Silica polymorphism . . . 80
4.1.2 Thermodynamics calculations . . . 84
4.1.3 Silica diffusive dissolution . . . 93
4.1.4 Theoretical scenarios for quartz dissolution . . . 97
4.2 Silica dissolution methods . . . 100
4.2.1 Experimental setup geometry adaptations . . . 100
4.2.2 Use of silica sources other than quartz as starting material . . . 102
4.2.3 Compilation of silica dissolution tests . . . 105
4.2.4 Quantification of dissolved silica . . . 108
4.3 Microstructure evolution in quartz dissolution . . . 112
4.3.1 Silica polymorphs evolution . . . 117
4.3.2 Dissolved silica evolution . . . 123
4.3.3 Cristobalite dissolution evolution . . . 125
4.3.4 Estimation of cristobalite contribution to dissolution in PSq tests . . . 131
4.4 Mass transport of silica in the glass . . . 134
4.4.1 Thermodynamic equilibrium at the interface . . . 139
4.4.2 Origins of convection onset . . . 141
4.5 Towards a quartz dissolution mechanism . . . 145

Conclusion 147

Conclusion in French 151

Appendices 155

A X-Ray Diffraction (XRD) characterization of starting materials 157

B Considerations on geometric assumptions 161
B.1 Comparison between methods to calculate the initial number of moles . . . 161
B.2 Available interface area for dissolution and lateral gap . . . 162
B.3 Deviations from a rectangular cross section . . . 164

C Optical microscopy and SEM images of silica dissolution samples 167

D Raman map for quartz dissolution after 2 min 173

E Cristobalite structural differences 175

Bibliography 179

Chapter 1

State of the art

This chapter provides a detailed review of the dissolution mechanisms of alumina and silica in silicate glasses in the context of industrial glass melting, structured into five key sections. The chapter begins by introducing the industrial glass melting process and the role of Computational Fluid Dynamics (CFD) in predicting dissolution behavior. It then explores dissolution mechanisms in binary systems, focusing on interface reactions and mass transport through diffusion and convection. The chapter continues by examining available experimental data on alumina and silica dissolution, highlighting gaps in solubility and diffusivity data for multi-component systems. The fourth section addresses the challenges of applying binary system models to complex multi-component compositions. Finally, based on the identified research gaps, the last section delineates the framework of this manuscript.

Chapter's table of contents

1.1 Introduction to Glass Melting and CFD applications . . . 2
1.1.1 Modeling of the dissolution step . . . 5
1.2 Dissolution mechanisms in binary systems . . . 6
1.2.1 Interface reaction contribution . . . 9
1.2.2 Diffusion in the glass contribution . . . 11
1.2.3 Contribution of convection in the glass . . . 19
1.3 Available data on alumina and silica dissolution . . . 22
1.3.1 Historical overview of silica and alumina dissolution studies . . . 22
1.3.2 Experimental techniques to measure dissolution . . . 23
1.3.3 Comparative analysis of the dissolution measured properties . . . 24
1.4 Complexities in multi-component systems . . . 29
1.4.1 Solubility limits . . . 31
1.4.2 Diffusivity . . . 32
1.4.3 Viscosity and its relationship with diffusivity . . . 37
1.5 Summary . . . 41

1.1 Introduction to Glass Melting and CFD applications

The glass melting process is an essential element of industrial glass production, where raw materials are transformed into a homogenous, defect-free glass melt. This melt can subsequently be formed into various geometries, such as flat glass, hollowware, or fibers. Central to this process is the dissolution step, where the reactive dissolution of silica and other components largely determines the quality and efficiency of the melt. Understanding this critical phase is essential for optimizing the glass melting process and reducing solid inclusion defects (also called "stones", some examples depicted in Figure 3).

The glass melting process begins with the meticulous preparation of the batch, which includes the weighing, mixing, and storage of the raw materials. This mixture is then conveyed into the glass furnace. The granular batch is charged through the furnace's lateral side, known as the "doghouse," from where it floats on the melt surface inside the melting tank. It is heated from above by burners and from below by melt convection currents (Figure 1.1). Within this batch blanket, individual chemical reactions occur as the raw materials are exposed to heat [3].

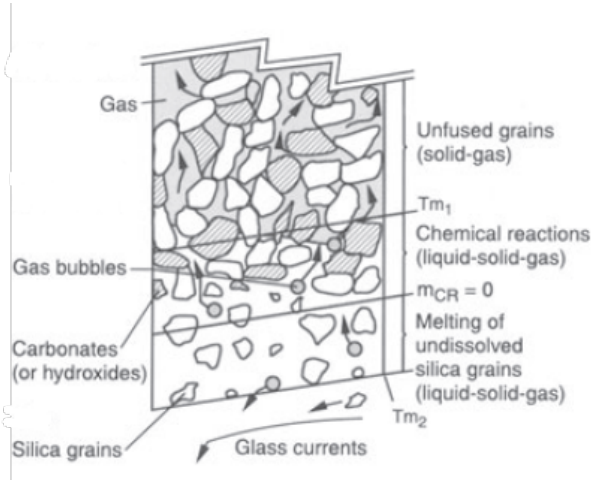

Figure 1.1 Representation of the morphology and sequence of steps at the lower side of the batch blanket during melting. Adapted from [3]

Although commonly referred to as "melting" or "fusion," the process involves the conversion of sand into a liquid through reactive dissolution between silica grains and initial melt phases formed from alkalis and alkaline earth carbonates, which have significantly lower melting points than silicon oxide. Pure silica melts at 1723 °C, a temperature typically not reached in most commercial glass furnaces. However, the interaction with alkali and alkaline earth-rich melts forms eutectic melts with silica, facilitating the dissolution of sand [3]. This results in a foamy, rough melt containing substantial amounts of bubbles and undissolved grains. By the end of a successful primary batch conversion, which usually takes about one hour, only a minor portion of the grains remains undissolved [4].

Residual silica grains complete their digestion into the melt bath during convectional flow during which they come into contact with a melt composition often closer to that of the final glass', therefore, where the chemical forces driving silica dissolution are weaker. According to Beerkens [3], approximately 90% of the time required for complete melting, known as "batch-free time," is determined by the dissolution of silica from sand into the melt. In a more recent review,

Conradt [4] further emphasized that long dwell times are still necessary for the fusion process due to this step.

The kinetics of the dissolution process (or "digestion" step) is highly dependent on temperature, with a hotter melt generally enhancing the solubility limit of the glass bath, the reaction conversion rate, and the mass transfer coefficient. As a result, higher melting temperatures and strong convection currents can reduce the minimum residence time required for complete dissolution. However, this approach can compromise the integrity of the refractory lining, potentially introducing more refractory phases as stone-like defects.

In addition to the challenges of silica dissolution, other refractory phases derived from raw material impurities or furnace lining wear can further delay the digestion process. These phases include corundum (α-Al_2O_3), zircon ($ZrSiO_4$), Al_2SiO_5 polymorphs, spinel ($MgAl_2O_4$), and chromite ($FeCr_2O_4$). Moreover, the increased use of cullet has introduced additional defect sources, such as metallic aluminum from container ware, ceramics, porcelain, and other residues from building demolition sites, which also need to be addressed [2].

In addition to the potential presence of various unwanted solids, silica grain dissolution is accompanied by the formation of bubbles at its interface with the melt, caused by a decrease in gas solubility as basicity decreases. Refining the melt is only viable once bubble generation from silica dissolution is complete [4].

The removal of smaller gas inclusions ("seeds"), bubbles, and dissolved gases is accomplished in the fining process, which relies on buoyancy and the coalescence of small bubbles. Polyvalent ions are introduced to the batch in a specific redox state to release fining gases at high temperatures, promoting bubble growth. These bubbles ascend to the bath surface at a velocity proportional to the square of their diameter. The fining stage requires higher temperatures to initiate fining gas release and decrease viscosity, thereby facilitating bubble ascension. To prevent the dispersion of ascending bubbles, minimal mixing is necessary during this stage [3].

Following fining, the melt undergoes a controlled cooling and homogenization process during the secondary fining or refining stage. During this stage, residual seeds resorb due to the increased solubility of common gases (such as oxygen, CO_2, and SO_2) at lower temperatures.

A significant challenge in the glass melting process is that all these steps, summarized in Table 1.1, and flow conditions must be conducted within a continuous process above the glass transition. In most industrial applications, glass is continuously melted in large, shallow tanks, which vary in size depending on the production scale. These furnaces, with dimensions ranging from $10 \times 6 \times 1$ meters for medium-sized container glass production to $30 \times 10 \times 1.4$ meters for float glass, must accommodate a variety of processes simultaneously, with daily capacities ranging from a few tons to 1000 tons.

Ensuring that each step in the glass melting process is provided with the appropriate conditions within a single tank is a complex task. The design and operation of the furnace must account for

Table 1.1 Glass melting intermediate steps that are conducted at high temperatures, after the preparation of the batch. Adapted from [4]

Intermediate steps	Temperature range	Intrinsic energy demand
Primary batch to melt conversion	600-1200 °C	≈ 2000 MJ/ton
Dissolution ("digestion")	1200-1400 °C	≈ 280 MJ/ton
Fining	1400-1500 °C	≈ 140 MJ (for heating up)
Refining, thermal and chemical homogenization	1350 °C	≈ -220 MJ (heat released)

the spatial separation of steps, which is achieved by managing the convective flows within the tank. Two primary convective vortices, as depicted in Figure 1.2, are created by the strategic distribution of fuel to burners arranged along the longitudinal axis above the glass bath level. Between these vortices, a well-localized hot spot is positioned at the point of maximum energy input, where the temperature is higher than the fining onset value [4, 5].

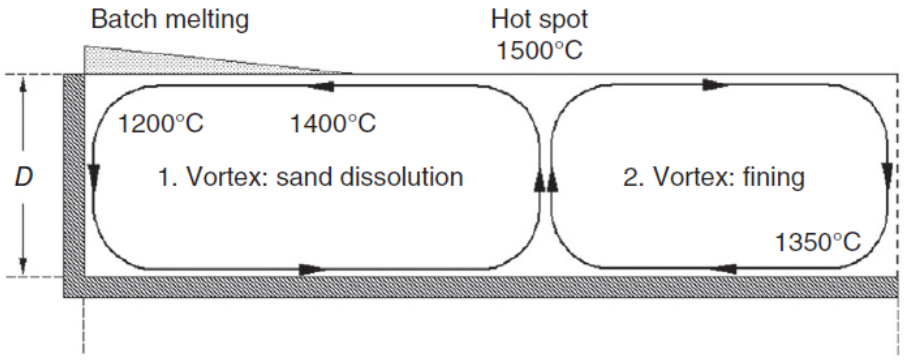

Figure 1.2 Convection vortices in the melting tank of a glass furnace (vertical projection) with side port firing, transit to the refiner indicated by the dotted vertical line. The illustration is not in the real scale : for the float glass furnace, like the one illustrated, the typical dimensions are $30 \times 10 \times 1.4$ (D) m^3. From [4]

During the dissolution step, where convection flows are essential, the first vortex directs the extremely hot melt towards the bottom of the batch blanket, providing heat for the highly endothermic batch conversion stage. Simultaneously, the second vortex transports low-viscosity melt to the surface, helping bubble escape. Meanwhile, the refining step requires a different environment, usually conducted in a thermally separated space from the melter, either by a vertical wall (referred to as the "throat") or by a narrowed segment in float glass furnaces, known as the "waist."

To ensure the production of high-quality glass, the industrial glass melting process must adhere to several critical parameters. A well controlled temperature profile within the melt is essential to enable the various chemical reactions and physical changes required during melting, fining, and refining stages. Sufficient residence time of the glass in the melting tank is crucial for the complete dissolution of raw materials and the removal of bubbles, ensuring homogeneity in the final product. Additionally, maintaining adequate velocity gradients within the melt is necessary to promote effective mixing and heat transfer, while avoiding shortcut flows that could lead to uneven melting and inhomogeneities. In the primary fining zone, minimal mixing is required to prevent the dispersion of ascending bubbles, which could compromise the glass's clarity and quality [3].

These four elements —temperature profile, residence time, velocity gradients, and controlled mixing— are intrinsically linked by the flow characteristics of the melt. Modern advancements in computational tools, particularly Computer Fluid Dynamics (CFD) models, have significantly enhanced the ability to calculate local temperature and flow patterns within the furnace, given a set of well-defined boundary conditions. CFD models provide primary outputs, such as velocity and temperature distributions, which are critical for understanding the complex dynamics within the glass melt [3, 6].

However, to fully leverage the insights provided by CFD, post-processing models are required to translate these primary outputs into physically meaningful secondary quantities. These include

crucial metrics such as sand or silica dissolution rates and minimum dwell time, which directly impact the efficiency and quality of the glass melting process [6]. Accurate physico-chemical data underpin these models, enabling precise predictions and optimizations.

The next section will delve deeper into these post-processing models, highlighting how they integrate experimental data to enhance current understanding of the glass melting process and enable innovations in furnace design and operation.

1.1.1 Modeling of the dissolution step

Understanding the glass melting process is particularly challenging due to the extreme temperatures involved and the limited access to the furnace interior. Direct measurements in such harsh conditions are often not feasible, making it difficult to gain a comprehensive understanding of the internal dynamics of glass tanks. Computational Fluid Dynamics (CFD) models, therefore, provide valuable insights into local temperature and velocity fields within the glass melt.

The adoption of CFD in the glass industry began in the 1980s, initially focusing on optimizing furnace design, reducing energy consumption, and minimizing emissions. Over time, these models have evolved to provide detailed insights into the complex phenomena occurring within glass tanks [6]. Today, the goal is to advance from steady-state simulations to dynamic modelling, which would predict the response of the furnace to changes in the process settings. This shift toward model-predictive control (MPC) aims to optimize the production of defect-free glass by continuously adjusting parameters in response to temporary disturbances or fluctuations on temperature, energy input, or pull rate [3].

A key aspect of predicting the dissolution of refractory phases within the melt is the use of "particle" tracing techniques within CFD models (Figure 1.3). After calculating the flow vectors of the glass melt, an infinitesimal volume of material, or "particle," is traced as it follows the direction of these vectors throughout the tank. The resulting trajectory, which depends on the particle's initial position, determines its residence time in the tank [3]. Paths that involve high temperatures, long residence times, and significant velocity gradients generally provide better conditions for the complete dissolution. To calculate local dissolution rates along these trajectories, post-processing models are required to link the flow and thermal fields generated by CFD to dissolution behavior.

However, the accuracy of these post-processing models is heavily dependent on the availability of precise thermodynamic and transport properties relevant to glass melting. Unfortunately, essential data such as diffusion coefficients and solubility values across various temperatures and compositions are often lacking, limiting the reliability of the predictions. This gap highlights the critical need for comprehensive data collection and a deeper understanding of dissolution behavior to develop more accurate secondary models [3, 6].

In summary, while glass melting modelling has significantly advanced our understanding of the process, particularly in predicting the dissolution of refractory phases, its performance is still limited by the availability of accurate physico-chemical data. The next section will explore the kinetics of dissolution, focusing on the key variables and properties that must be considered to enhance the predictive capabilities of glass melting submodels.

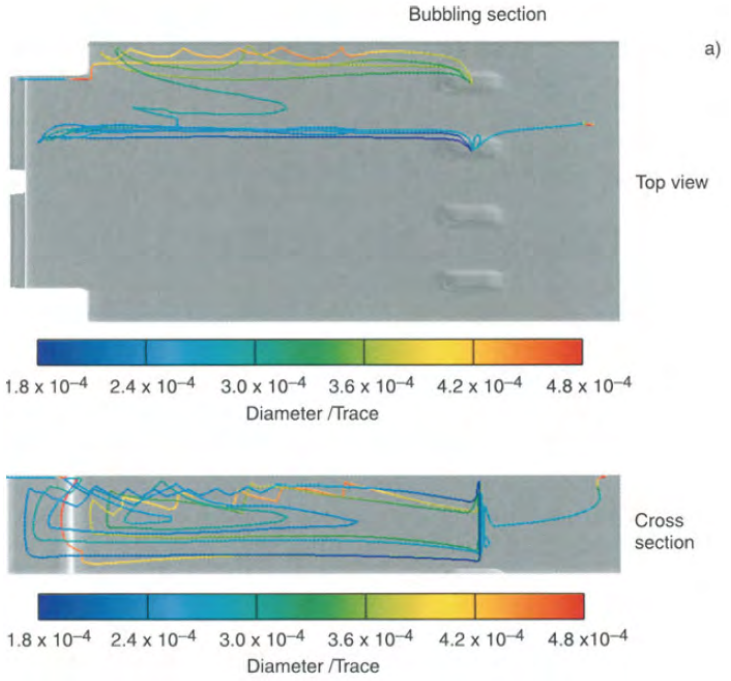

Figure 1.3 Calculated trajectory of a gas seed in a TV-panel glass-melt tank with forced bubbling ; the size of the bubble is indicated by the color scale. From [3]

In summary

Glass melting is a complex, energy-intensive, high-temperature process, that requires sufficient conditions of temperature, residence time, and flow dynamics to ensure complete dissolution of raw materials and the production of defect-free glass. Computational Fluid Dynamics (CFD) has advanced the current understanding of the different melting phenomena, enabling better furnace design and the potential for real-time process optimization through model-predictive control (MPC). However, a critical research gap remains in accurately predicting the dissolution of refractory materials due to limited thermodynamic and transport data. To bridge this gap, further research is needed to :

— Deepen our understanding of the dissolution kinetics of specific oxides.
— Collect reliable physico-chemical data necessary for improving dissolution submodels for glass melting simulations.

Addressing this gap will help to enhance the accuracy of process modelling and contribute to more efficient and reliable glass production.

1.2 Dissolution mechanisms in binary systems

From both industrial and scientific perspectives, the capability to better predict dissolution behavior is of great importance. One of the most frequently applied approaches to understanding the evolution of oxide dissolution over time is the shrinking core model (SCM). This model is based on the chemical engineering treatment of dissolution as a non-catalytic heterogeneous reaction between a solid particle and a fluid phase [7, 8]. The SCM conceptualizes the dissolving particle as a shrinking core surrounded by a layer of reacted material (Figure 1.4). It assumes that

the reaction occurs at the interface between the unreacted core and the surrounding medium, following five subsequent steps :

1. Diffusion of a reactant through the film surrounding the particle to the surface of the solid.
2. Penetration and diffusion of the reactant through the product layer to the interface with the unreacted core.
3. Reaction of the reactant with the solid at this reaction surface.
4. Diffusion of the fluid product through the inert solid layer back to the exterior surface of the solid.
5. Diffusion of the fluid product through the boundary layer into the fluid bulk volume.

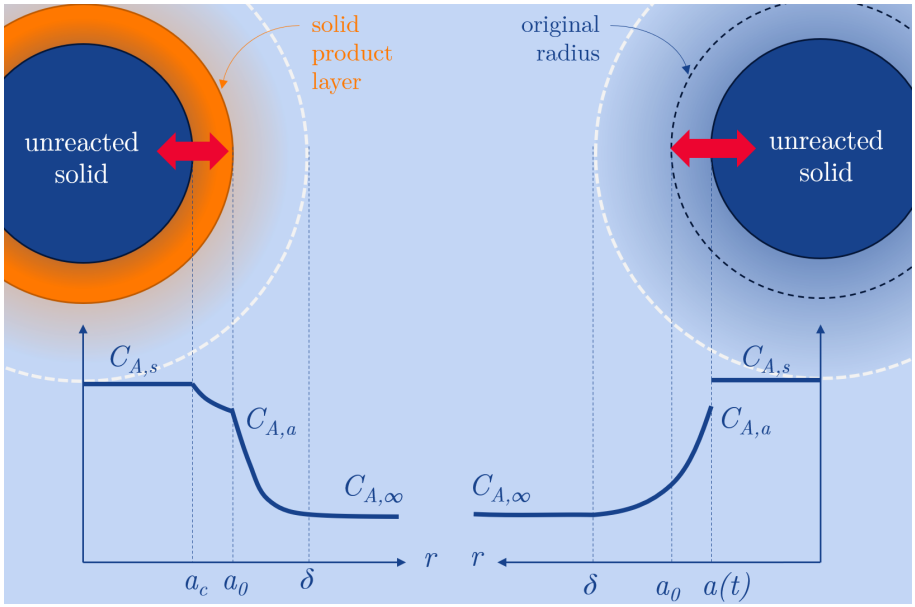

Figure 1.4 Illustration of two cases of the shrinking core model (SCM) : (left) spherical particle of unchanging size with a solid product layer (in orange) ; (right) spherical particle with shrinking radius ($a = f(t)$). The red arrow represents the interface reaction. Adapted from [7]

In certain scenarios, some of these steps may not exist. For instance, if no solid congruent product is formed at the solid reactant surface, steps two and four may not contribute to dissolution kinetics. Additionally, the relative importance of the different steps can vary significantly, with the slowest step often being considered as the rate-controlling mechanism.

Despite its simplicity, the shrinking core model is the most frequently applied model to understand dissolution behavior. However, its assumptions may not precisely match reality, particularly outside gas-solid systems [9]. For example, recent work [8, 10–13] compiling oxide dissolution at high temperatures, including alumina and silica, reveals that observed behavior cannot be fully explained by the SCM rate-controlling mechanism models.

Therefore, a more complete description of dissolution must be considered to better explain the dissolution behavior observed in industrial glass melting furnaces. Considering an isolated sphere of radius a containing a uniform and constant concentration of pure solute $C_{A,s}$, surrounded by an infinite body of liquid of constant temperature and pressure and initial composition $C_{A,\infty}$, maintaining spherical symmetry. The formation of a solid congruent product will not be considered in this model. Both materials are assumed isotropic.

The reaction at the dissolution interface can be interpreted as a reversible reaction involving the migration of atoms from the solid phase to the melt :

$$\mathrm{A_{solid}} \underset{\mathrm{k\leftarrow}}{\overset{\mathrm{k\rightarrow}}{\rightleftharpoons}} \mathrm{A_{glass}}$$

Given that the solid is a pure oxide, a zeroth-order reaction can be assumed for the migration of elements to the melt. The chemical reaction rate can be expressed concerning the element A entering the liquid phase as :

$$\frac{dC_A}{dt} = k_{\rightarrow} - k_{\leftarrow} C_A \tag{1.1}$$

where C_A is the molar concentration of element A per unit volume in the melt . At equilibrium, there is no accumulation, i.e., $\frac{dC_A}{dt} = 0$, and therefore,

$$K_{eq} = \frac{k_{\rightarrow}}{k_{\leftarrow}} = C_A^* \tag{1.2}$$

where K_{eq} is the equilibrium constant, and C_A^* is the thermodynamic equilibrium composition of A in the glass melt. Replacing this relationship in the first equation, the contribution of the chemical reaction to concentration is :

$$\frac{dC_A}{dt} = -k_{\leftarrow}(C_A - C_A^*) \tag{1.3}$$

Given a boundary layer of typical thickness δ where A diffuses around the grain, then the mass balance of the sphere is :

$$\frac{dm}{dt} = \rho_s S \frac{da}{dt} = -\delta M_A S k_{\leftarrow}(C_A - C_A^*) \tag{1.4}$$

where m, S, and ρ_s are the grain's mass, surface, and density, respectively, and M_A is the molar mass of A species. Given that the molar concentration of A per unit volume in the grain is given by $C_{A,s} = \rho_s / M_A$ and an effective kinetic constant $K = -\delta k_{\leftarrow}$, whose dimension is length per unit time, then, the grain size variation is given by :

$$\frac{dV}{dt} = \frac{SK}{C_{A,s}}(C_A - C_A^*) \tag{1.5}$$

Thus, the chemical reaction contribution depends only on the deviation of the chemical composition at the surface of the grain from thermodynamic equilibrium.

Considering a boundary layer around the grain, the diffusion flux of elements A from the interface into the melt must be equal to its release rate from the interface reaction. From Fick's first law of diffusion, the fluxes at the surface of the solid ($r = a$) are :

$$\frac{K}{C_{A,s}}(C_A(r=a) - C_A^*) = \frac{D}{C_{A,s} - C_A(r=a)} \nabla C_A|_{r=a} \cdot \mathbf{n} \tag{1.6}$$

where $C_A(r = a)$ is the composition at the interface, D is the diffusion coefficient in the glass, C_A the concentration field of element A in the fluid, and $\mathbf{n}$ a unit vector normal to the grain interface. For the moment, D is assumed to be a scalar property and constant with respect to both glass composition and space ; this hypothesis will be discussed in a future section (Section 1.4.2).

Beyond this diffusive boundary later, element A can also be transported away from the interface by advection if there is a bulk flow in the glass surrounding the grain. In this case, an advection contribution must be added to the second Fick's law, which describes the evolution of concentration with time :

$$\frac{\partial C_A}{\partial t} + \mathbf{U} \cdot \nabla C_A = D \nabla^2 C_A \tag{1.7}$$

where $\mathbf{U}$ is the Eulerian velocity field in the glass.

The complete behavior of the system can be obtained by solving these three equations, given the initial and boundary conditions of an infinite glass reservoir : $C_A(r, t = 0) = C_A(r \to \infty, t) = C_{A,\infty}$.

Since a general analytical solution for this problem is not available, numerous studies [14–19] have examined different limiting case solutions for the liquid-solid reaction problem, using both analytical and numerical methods. A common simplification is the quasi-steady state assumption, which posits that the movement of the shrinking interface is much slower than the rate at which species diffuse away from it, allowing the concentration profile to stabilize quickly and, therefore, assume that the concentration gradient remains constant over time. Another common simplification is to disregard the radial density flow that emerges when the partial molar volume of the dissolving species A in the glass and the grain differ.

The subsequent sections will examine these works, focusing on how the interface reaction, diffusion of the dissolving component in the surrounding liquid, and convection in the glass affect dissolution behavior. The validity of the quasi-steady state assumption and the implications of neglecting radial density flow will also be assessed. Finally, these limiting cases will be presented and discussed under which conditions they can be considered as good approximations of the complete solution.

1.2.1 Interface reaction contribution

When the chemical reaction rate is significantly slower than mass transport phenomena, Equation 1.5 can be reformulated as :

$$\frac{da}{dt} = K \frac{C_{A,\infty} - C_A^*}{C_{A,s}} \tag{1.8}$$

assuming that the concentration at the melt remains constant at its initial value due to the slow conversion rate. Given that the initial radius of the grain is a_0 and the above conditions, the particle size evolves linearly with time :

$$a(t) = K \frac{C_{A,\infty} - C_A^*}{C_{A,s}} t + a_0 \tag{1.9}$$

In such cases, the chemical composition surrounding the grain remains constant with distance, as the mass transfer of the product occurs much faster than the conversion at the interface. Consequently, the dissolution rate becomes independent of the grain size and is solely a function of the liquid's undersaturation relative to thermodynamic equilibrium.

Reaction-controlled dissolution is less commonly observed in high-temperature silicate melts [20]. However, when mass transport rates increase significantly, the chemical reaction rate's contribution to the dissolution process may become substantial.

Frade and Cable [18], along with Taylor *et al.* [16], introduced a parameter that compares the relative rates of chemical reaction and diffusion, denoted as :

$$k^* = \frac{Ka_0}{D} \tag{1.10}$$

where a_0 represents the initial grain radius. As k^* decreases, diffusion proceeds at a faster rate than the reaction, thereby accentuating the relevance of the interface reaction's contribution. Through numerical solutions for a non-advective dissolution scenario, both sets of authors identified a mixed regime occurring within the range $0.1 < k^* < 10$, with Frade and Cable suggesting a lower limit of 0.01. Figure 1.5 illustrates the evolution of particle radius with respect to dimensionless time ($z = tD/a_0^2$) for various k^* values, alongside a diffusion-controlled case depicted by a dashed line.

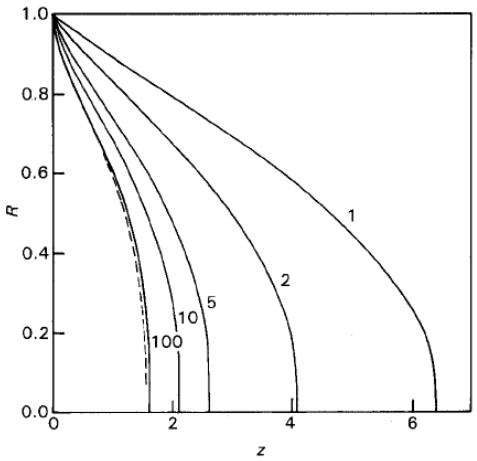

Figure 1.5 Evolution of relative radius of the dissolving particle against the dimensionless time ($z = tD/a_0^2$) for various ratios of chemical reaction rate to diffusivity ($k^* = Ka_0/D = 1, 2, 5, 10, 100$). The quasi-steady state approximation is depicted by the dashed line, and the solubility parameter ϕ used was -0.1. [18]

Within this mixed regime, both authors demonstrated that the quasi-steady state approximation applicable to diffusion-controlled cases remains valid for low solubilities, specifically when :

$$|\phi| = \left| \frac{C_{A,\infty} - C_A^*}{C_{A,s}} \right| \leq 10^{-3} \tag{1.11}$$

as detailed in Table 1.6b and Figure 1.6, where both quasi-steady state (dashed line) and reaction-controlled (dash-dot) cases are depicted for comparison with the mixed regime solutions for different solubilities. While this criteria is often respected in gas-solid reactions, this often does not hold true for liquid-solid systems [16].

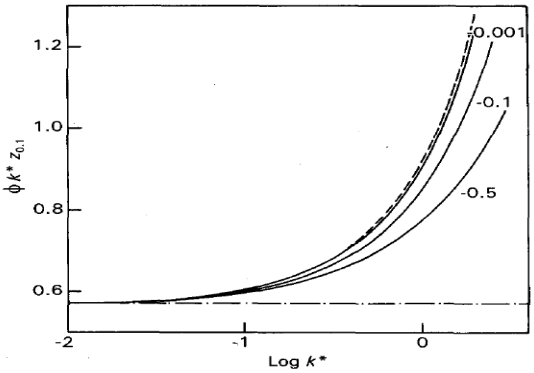

a

k^*	$\|\phi\|z_{0.1}$					
	$\phi = -0.001$		$\phi = -0.1$		$\phi = -0.5$	
	Fd	Qss	Fd	Qss	Fd	Qss
10^{-3}	571.000	570.000	569.000	571.000	570.0000	571.0000
10^{-2}	57.400	57.400	57.200	57.400	57.2000	57.4000
0.1	6.010	6.060	6.020	6.050	5.9800	6.0400
1	0.912	0.922	0.848	0.903	0.7740	0.8400
10	0.395	0.408	0.292	0.367	0.1760	0.2260
10^2	0.341	0.357	0.227	0.309	0.0848	0.1268
10^3	0.336	0.352	0.220	0.303	0.0696	0.1111
10^4	0.336	0.351	0.220	0.302	0.0676	0.1091

b

Figure 1.6 Dimensionless times required to shrink the particle radius to 10% of the original size in respect to different reaction rate to diffusion contribution ratios (k^*). The effect of the solubility parameter is shown by depicting $\phi = -0.001, -0.1, -0.5$ as solid lines on the left. The effect of this parameter on the quality of the quasi-steady state (Qss) approximation is also shown, where the result of the approximation is plotted as the dashed line for comparison with the finite difference solution (Fs) that takes into account the mixed effect. [18]

Furthermore, Frade and Cable [18] investigated the Gibbs-Thomson effect on the equilibrium composition at the interface, noting that as the solid shrinks, its curvature increases. Consequently, the interfacial energy significantly influences the total free energy in smaller particles, leading to an increase in solubility, as indicated by higher absolute ϕ values, compared to a flat interface. This phenomenon suggests the potential for deviation from the quasi-steady state approximation as the particles are close to complete dissolution.

In summary

The effect of reaction rate on dissolution behavior can be categorized based on the parameter $k^* = Ka_0/D$, which compares the relative rates of chemical reaction and diffusion :

- For $k^* < 0.01$, dissolution can be effectively approximated as reaction-controlled. Under this scenario and the initial hypothesis about the nature of reaction, the evolution of particle size is influenced solely by the melt's undersaturation relative to its equilibrium composition.
- For $0.01 < k^* < 10$, both diffusion and reaction rates play significant roles. Although no analytical solution exists for this mixed regime, it can be effectively approximated using the quasi-steady state approach, for systems with low solubility with respect to the solvent.
- For $k^* > 10$, the reaction rate becomes negligible, and dissolution behavior is predominantly governed by mass transport mechanisms, which will be further elaborated in the following sections.

1.2.2 Diffusion in the glass contribution

If the interface reaction is negligible, then the composition at the interface can be assumed as constant and at its thermodynamic equilibrium value, C_A^*. This equilibrium condition allows for

the description of particle size evolution in terms of the diffusive flux at the particle surface, combining Equations 1.5 and 1.6 :

$$\frac{da}{dt} = \frac{D}{C_{A,s} - C_A^*} \nabla C_A|_{r=a} \cdot \mathbf{n} \tag{1.12}$$

where $C_A(r = 0)$ is replaced by the composition at equilibrium, C_A^*.

When diffusion is the exclusive mechanism for mass transfer, Equation 1.7 becomes :

$$\frac{\partial C_A}{\partial t} = D\nabla^2 C_A \tag{1.13}$$

In solving these equations, it is critical to account for the temporal evolution of the interface position, which affects the boundary condition reference for equilibrium composition at $r = a$. Moreover, a mole of solute A often occupies different volumes in the solution and in the solid. Consequently, dissolution typically causes a change in the system's volume, which is accommodated by a radial flow at the interface.

Readey and Cooper [14] and later Cable and Frade [21] proposed a finite difference method to address these complexities. These latter authors circumvented the reference problem by introducing a variable change, $\xi = r/a \in [1, +\infty]$, which immobilises the interface and updates the spatial mesh size at each iteration. The radial density flow is incorporated by modifying Equation 1.13 to include its contribution. In a spherical coordinate system, this results in :

$$\frac{\partial C_A}{\partial t} = D\left[\frac{\partial^2 C_A}{\partial r^2} + \frac{2}{r}\frac{\partial C_A}{\partial r}\right] - \varepsilon\left(\frac{a}{r}\right)^2 \frac{da}{dt}\frac{\partial C_A}{\partial r} \tag{1.14}$$

where $\varepsilon = (1 - C_{A,s}\nu)$, and ν is the partial molar volume of species A in the solution. The complete boundary condition at the interface from Equation 1.12 is then expressed as :

$$\frac{da}{dt} = \frac{D}{C_{A,s} - (1-\varepsilon)C_A^*}\left(\frac{\partial C_A}{\partial r}\right)\Bigg|_{r=a} \tag{1.15}$$

The term $(1-\varepsilon)$ represents the ratio of the volume occupied by a mole of solute in the solution to that in the particle. For $\varepsilon = 1$, there is no volume change in the liquid during dissolution, typical for gas phase inclusions. Conversely, $\varepsilon = 0$ approaches to solid dissolution case, where the system volume remains constant, but the liquid phase volume increases during dissolution. Readey and Cooper [14] also evaluated the dissolution case where $\varepsilon < 0$, i.e., when the volume occupied by the solute A in the solution is greater than in the particle, resulting in an expansion of the system's volume. This radial density flow can distort the concentration profiles developed in the surrounding glass.

The authors considered the following initial and boundary conditions :

- Constant composition at thermodynamic equilibrium at the interface : $C_A(r = a) = C_A^*, t \geq 0$
- Infinite liquid reservoir, implying the far-field composition remains unchanged : $C_A(r \to \infty) = C_{A,\infty}; t \leq 0$ and $C_A(r) = C_{A,\infty}; r > a, t = 0$

Figure 1.7d presents the dimensionless times required to the complete dissolution of a sphere ($z_d = D\tau/a_0^2$, where τ is the total dissolution time). Figures 1.7a and 1.7b illustrate the variation of the relative particle radius ($R = a/a_0$) with respect to the relative dimensionless time ($z/z_d = t/\tau$) for complete dissolution, corresponding to different values of the dimensionless variable $F_a = (C_A^* - C_{A,\infty})/(C_{A,s} - (1-\varepsilon)C_A^*)$. This variable is a solubility parameter, where higher values indicate greater solubility of species A in the melt.

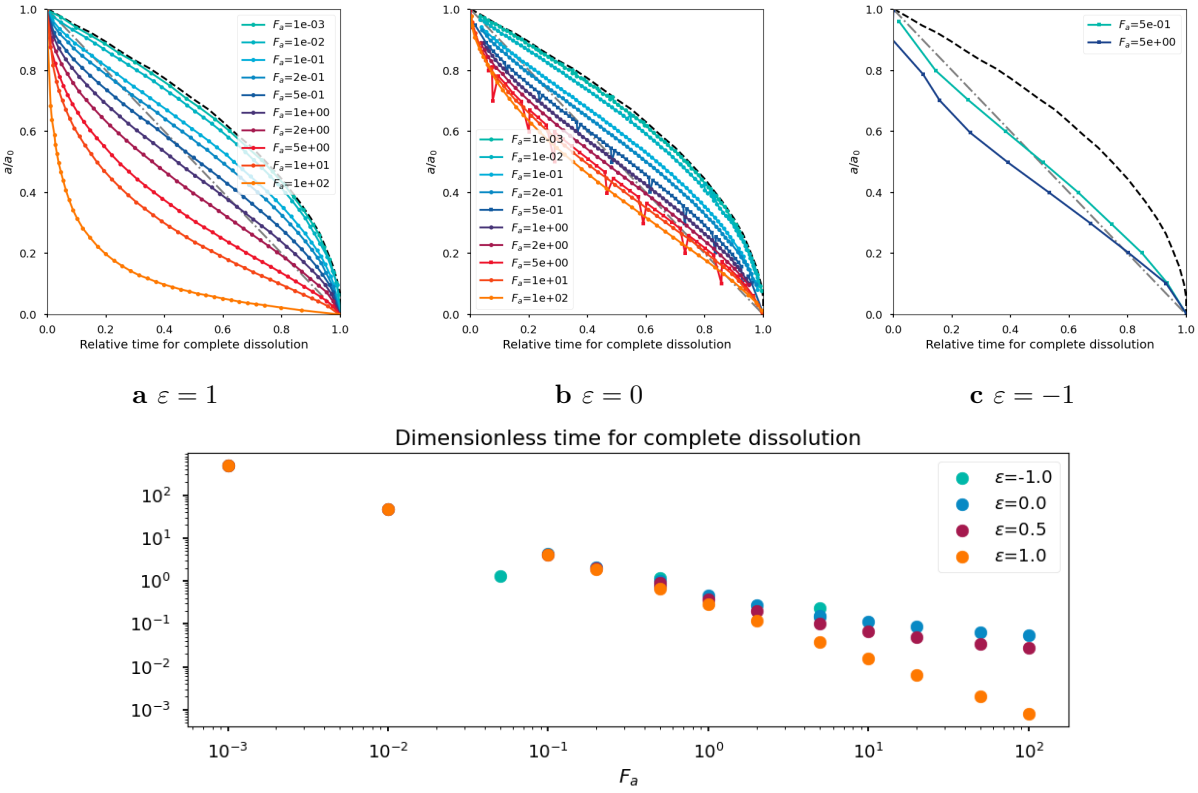

a $\varepsilon = 1$ **b** $\varepsilon = 0$ **c** $\varepsilon = -1$

d $z_d = D\tau/a_0^2$, with τ the complete dissolution time

Figure 1.7 (top) Normalized radius-time curves for dissolving spheres with $F_a = 0.001, 0.01, 0.1, 0.2, 0.5, 1, 2, 5, 10, 100$, where higher values are associated with a higher difference between the solubility of the solute compared to its initial content in the liquid. The black dashed line shows the quasi-steady state approximation. Square markers are from [14] and circular symbols are from [21] (bottom) Plot of dimensionless times for complete dissolution of a sphere with F_a, adapted from [14, 21].

Figure 1.7a highlights the influence of solubility on the dissolution profile shape, which ranges from a decaying curve shape for high values of F_a to parabolic for low solubilities. Figure 1.7d shows that the values of ε do not significantly impact the complete dissolution times for low solubility cases. However, as F_a increases, the importance of ε becomes more pronounced, where lower values imply an increase in the total dissolution time for a fixed value of F_a. These findings suggest that high concentration gradients accelerate initial dissolution rates and influence the accommodation of grain boundary movement by the diffusion of A species away from the interface.

The compositional profile of the liquid near the interface was also calculated by the authors, resulting in Figures 1.8. These figures illustrate the relative dimensionless composition concerning the radial distance relative to the initial grain size ($e = r/a_0$) for various combinations of ε and solubilities F_a.

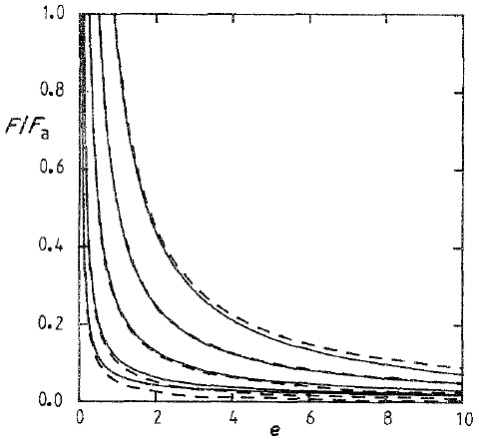

a $\varepsilon = 1$, $F_a = 10^{-4}$ [21]

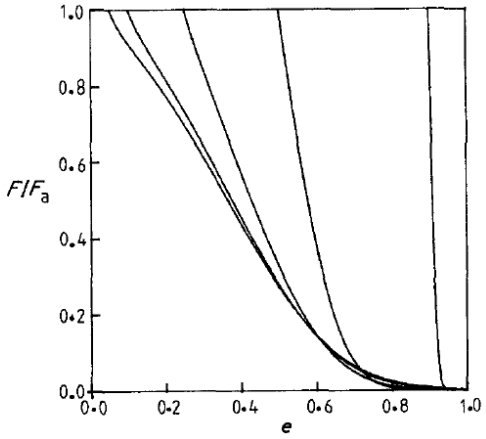

b $\varepsilon = 1$, $F_a = 10$ [21]

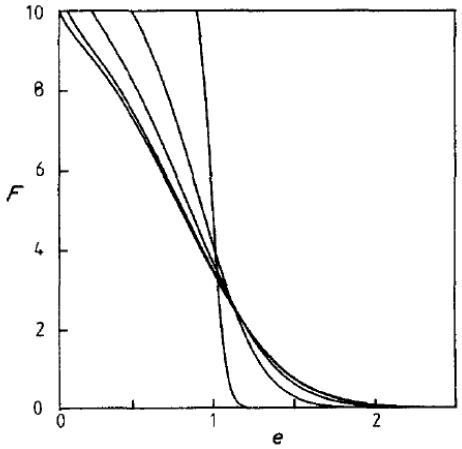

c $\varepsilon = 0$, $F_a = 10$ [21]

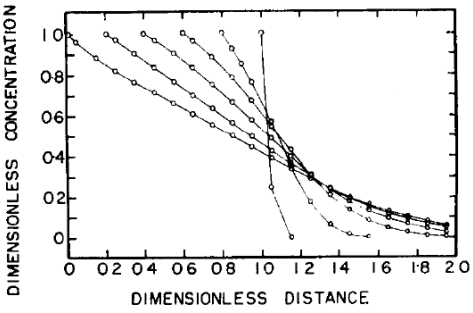

d $\varepsilon = -1$ [14]

Figure 1.8 Calculated dimensionless concentration ($F = (C_A - C_{A,\infty})/(C_{A,s} - C_A^*(1-\varepsilon))$) profiles in respect to $e = r/a_0$ for different stages of dissolution : (from right to left) $a/a_0 = 0.9, 0.5, 0.25, 0.1, 0.01$. Dashed lines in Figure 1.8a depict the quasi-steady state approximation results.

For $\varepsilon = 1$, the effect of particle boundary movement on the diffusion profile is evident. As the

reservoir volume decreases due to a reduction in molar volume when species A migrates to the liquid, forced radial convection occurs. This results in solute accumulation near the interface, particularly towards the end of dissolution (small values of $R = a/a_0$). This effect is significant only for high solubility values, as a larger amount of solute migrates from the grain to the solution, accentuating this radial flow. The solute accumulation accounts for the increasingly slower later stage observed in Figure 1.7a for high F_a values.

For $\varepsilon = 0$, the solution volume increases as dissolution progresses, contributing to the dilation of the boundary layer. For negative values of ε, the outward fluid flow resulting from volume increase tends to further flatten the concentration profiles near the interface, thereby reducing the compositional gradient driving dissolution. The effect of differences in partial molar volume of the solute in the solid and solution becomes particularly pronounced at high solubility levels, as seen for $\varepsilon = 1$. In these cases, the amount of solute incorporated into the solution becomes significant to the radial flow.

While the application of the complete solution is complex, it enables an assessment of the limits of the assumptions and their validity. The following sections detail specific limiting cases that simplify the problem's solution, providing insights into the dissolution dynamics under varying conditions.

Quasi-steady state assumption or invariant field approximation

In the quasi-steady state scenario, it is assumed that the motion of the grain interface, as it shrinks, is rapidly accommodated by diffusion in the surrounding medium. Consequently, the concentration gradient remains constant over time, leading to the condition $\frac{\partial C_A}{\partial t} = 0$. This simplification is instrumental in reducing the complexities associated with the diffusion-controlled dissolution problem.

To solve Equation 1.12, it is necessary to express the concentration gradient $\nabla C_A|_{r=a}$ in terms of known quantities. Assuming spherical symmetry, Equation 1.13 becomes :

$$\frac{d}{dr}\left(r^2 \frac{dC_A}{dr}\right) = 0 \tag{1.16}$$

Given the boundary conditions $C_A(r = a) = C_A^*$ and $C_A(r \to \infty) = C_{A,\infty}$, which reflect an infinite glass reservoir and a constant far-field composition, the solution to this differential equation is :

$$C_A(r) = C_{A,\infty} + \frac{(C_A^* - C_{A,\infty})a}{r} \tag{1.17}$$

At the interface ($r = a$), the concentration gradient can be expressed as :

$$\nabla C_A|_{r=a} = -\frac{(C_A^* - C_{A,\infty})}{a} \tag{1.18}$$

Substituting this expression into Equation 1.12 yields the evolution of the radius :

$$\frac{da}{dt} = \frac{-D(C_A^* - C_{A,\infty})}{a(C_{A,s} - C_A^*)} \tag{1.19}$$

Integrating this equation, while considering the initial condition $a(t = 0) = a_0$, leads to the expression for the quasi-steady state diffusion-controlled dissolution :

$$a(t)^2 = a_0^2 - \frac{2D(C_A^* - C_{A,\infty})}{(C_{A,s} - C_A^*)}t \tag{1.20}$$

where the total time required for complete dissolution, τ_D, is given by :

$$\tau_D = \frac{(C_{A,s} - C_A^*)a_0^2}{2D(C_A^* - C_{A,\infty})} \tag{1.21}$$

As expected from the complete numerical solution, the assumption that the interface shrinking is accommodated by the diffusion profile holds when the amount of solute migrating from the solid to the liquid is small, i.e., at lower solubility levels. Indeed, as illustrated by the dashed lines in Figure 1.7, the quasi-steady state limit case provides a reasonable approximation to the complete diffusive dissolution behavior for $F_a \leq 10^{-3}$. This condition also coincides with the approximation of the reaction-diffusive mixed regime by the quasi-steady state ($|C_{A,\infty} - C_A^*|/C_{A,s} \leq 10^{-3}$). At low solubility, the complete numerical solution for the diffusion-controlled dissolution exhibits reduced sensitivity to the value of ε, and therefore, a low solubility criterion is a sufficient condition to use the quasi-steady state approximation for the diffusion control dissolution.

Flat slab approximation

In the study of dissolution kinetics under conditions of high concentration gradients, it can be assumed that the diffusion layer thickness $(r - a)$ is significantly smaller than the particle size (a). This assumption allows for the simplification of the problem to that of a flat slab dissolution. The scenario considered involves a solid plate of initial length L_0 in contact with a semi-infinite reservoir of liquid, which is initially of uniform composition. The problem is addressed in a one-dimensional Cartesian coordinate system, where the concentration of the solute, C_A, is governed by Fick's second law of diffusion :

$$\frac{\partial C_A}{\partial t} = D\frac{\partial^2 C_A}{\partial x^2} \tag{1.22}$$

The boundary and initial conditions for this problem can be specified as follows :

— The composition at the surface of the solid plate is constant and at equilibrium : $C_A(x = 0, t > 0) = C_A^*$.
— The composition far from the surface remains at its initial value : $C_A(x \leq 0, t = 0) = C_A(x \to +\infty, t \leq 0) = C_{A,\infty}$.

Using the Laplace transformation method, the solution to the diffusion equation under these conditions was developed by Crank [22] as :

$$\frac{C_A - C_{A,\infty}}{C_A^* - C_{A,\infty}} = \text{erfc}\left(\frac{x}{2\sqrt{Dt}}\right) \tag{1.23}$$

where erfc is the complementary error function, defined by :

$$\text{erfc}(\gamma) = 1 - \text{erf}(\gamma) = \frac{2}{\sqrt{\pi}}\int_\gamma^\infty \exp\left(-g^2\right) dg \tag{1.24}$$

This function has the properties : $\text{erfc}(0) = 1$ and $\text{erfc}(\infty) = 0$.

The diffusive flux at the interface, which is equal to the flux of dissolving material from the solid plate (Equation 1.13), is determined by the concentration gradient at the interface :

$$\frac{\partial C_A}{\partial x}\Big|_{x=0} = -\frac{C_A^* - C_{A,\infty}}{\sqrt{\pi}} \frac{1}{2\sqrt{Dt}} \tag{1.25}$$

The evolution of the plate's length L over time is given by :

$$\frac{dL}{dt} = \frac{D}{C_{A,s} - C_A^*} \frac{\partial C}{\partial x}\Big|_{x=0} = -\frac{D}{C_{A,s} - C_A^*} \frac{C_A^* - C_{A,\infty}}{\sqrt{\pi}} \frac{1}{2\sqrt{Dt}} \tag{1.26}$$

Upon integrating this equation, the length of the plate as a function of time is :

$$L(t) = L_0 - \frac{C_A^* - C_{A,\infty}}{C_{A,s} - C_A^*} \sqrt{\frac{4Dt}{\pi}} \tag{1.27}$$

where the time required for complete dissolution is :

$$\tau = \frac{\pi L_0^2}{4D} \left(\frac{C_{A,s} - C_A^*}{C_A^* - C_{A,\infty}} \right)^2 \tag{1.28}$$

Given the assumption that $(r - a) \ll a$ initiating the flat slab approximation, it can be expected that this approximation would deviate from the numerical method for a spherical grain as the dissolution progresses. Indeed, computed profiles by Cable and Frade [21] for moderate and large values of F_a demonstrate a good correspondence with the flat slab analytical solution only for the initial stages of dissolution : $1 > a/a_0 > 0.8$.

However, as dissolution progresses, this approximation tends to overestimate the total dissolution time for moderate values of the parameter F_a and underestimate the dissolution rate towards its end in cases of higher solubility. The accuracy of the flat slab approximation diminishes further as the parameter ε deviates from unity. This is because the solution volume changes with time, leading to a discontinuity in velocity at the interface.

Quasi-stationary or invariant interface approximation

The quasi-stationary or invariant interface approximation assumes that the diffusion profile is not altered by the movement of the interface between particle and slag. Therefore, it means that the diffusion field is the same as if the radius of the particle was fixed as its original size (a_0) [12, 21].

The problem involves solving the second Fick's law using the same approach as for the flat slab case, but in spherical coordinates :

$$\frac{\partial C_A}{\partial t} = D \left[\frac{\partial^2 C_A}{\partial r^2} + \frac{2}{r} \frac{\partial C_A}{\partial r} \right] \tag{1.29}$$

Hence, assuming a constant composition at the interface once equilibrium is reached, and an infinite solution reservoir, the solute concentration at a distance r from the interface can be determined using the same Laplace transformation method as the one used for the flat slab case :

$$\frac{C_A(r) - C_{A,\infty}}{C_A^* - C_{A,\infty}} = \frac{a_0}{r} \operatorname{erfc}\left(\frac{r - a_0}{2\sqrt{Dt}} \right) \tag{1.30}$$

Coupling this equation with the conservation of mass flux at the interface defined by Equation 1.15, the quasi-stationary approximation yields the following differential equation, that must be numerically solved :

$$\frac{da}{dt} = -\frac{C_A^* - C_{A,\infty}}{C_{A,s} - C_A^*}\left(\frac{D}{a} + \sqrt{\frac{D}{\pi t}}\right) \tag{1.31}$$

For shorter periods and steep concentration gradients (where $(r - a) \lll a$), the solution approaches the flat slab approximation. On a radius evolution curve, it displays a sigmoidal shape, as illustrated in Figure 1.9.

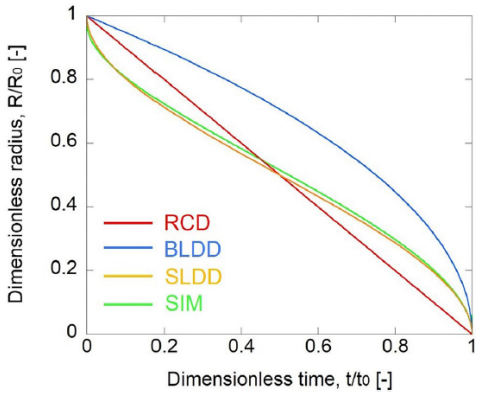

Figure 1.9 Dimensionless radius evolution with time plots for different approximation models : reaction control (RCD), quasi-steady state or invariant field (BLDD) and quasi-stationary or invariant interface (SLDD). An adaptation of the latter is also plotted as SIM. From [8]

Nonetheless, as per Cable and Frade [21], this model tends to increasingly underestimate the total dissolution time as the solubility rises. At present, no analytical limit cases are known to adequately describe the complete dissolution process for high solubility cases.

In summary

The kinetics of diffusive dissolution are significantly influenced by the decreasing size of the dissolving particle. The interaction between the velocity of the interface movement and the response of the diffusive boundary layer can result in the accumulation of solvent near the interface. This phenomenon is contingent upon the initial composition gradient close to the interface and may be exacerbated by the radial density flow, which arises from differences in the partial molar volume of the solute between the solid and liquid phases.

Nonetheless, this effect can be disregarded under certain assumptions, thereby simplifying the problem's resolution. Given C_A^* the thermodynamic equilibrium composition at the interface between a sphere of initial radius a_0 and composition $C_{A,s}$ and a liquid whose bulk composition is $C_{A,\infty}$:

- **For** $F_a = (C_A^* - C_{A,\infty})/(C_{A,s} - (1-\varepsilon)C_A^*) \leq 10^{-3}, \forall \varepsilon$ **:** When solubility values are low, the movement of the boundary can be accommodated by the diffusive boundary layer, with negligible impact of the radial density flow ($\forall \varepsilon$). Consequently, the kinetics can be approximated using the quasi-steady state assumption.
- **For** $F_a = (C_A^* - C_{A,\infty})/(C_{A,s} - (1-\varepsilon)C_A^*) \geq 1$ **:** For higher solubility levels, no analytical solution is known at present to be capable of fully describing the dissolution process. However, as the parameter $\varepsilon \to 1$, the flat slab approximation can effectively describe the initial stages of dissolution ($1 > a/a_0 > 0.8$).

1.2.3 Contribution of convection in the glass

Influence of advection

In the context of the dissolution of solid particles, advection refers to the bulk movement of fluid, which can significantly influence mass transfer beyond diffusion. Advection becomes an important mass transfer mechanism when fluid motion substantially impacts the transport of solute within a system. The Peclet number (Pe) is a dimensionless group that quantifies the ratio between advection and diffusive contributions, thereby characterizing the flow regime around a particle :

$$\mathrm{Pe} = \frac{LU_0}{D} \tag{1.32}$$

where L is the characteristic length of the grain and U_0 is the relative velocity between the particle and the fluid. The absolute local velocity (U) of a single particle relative to the surrounding liquid, due to advection, can be determined using the local velocity gradient extracted from a three-dimensional computational fluid dynamics (CFD) model. This velocity is given by :

$$U = \left[\left(a\frac{dv_x}{dx} \right)^2 + \left(a\frac{dv_y}{dy} \right)^2 + \left(a\frac{dv_z}{dz} \right)^2 \right]^{1/2} \tag{1.33}$$

For high Peclet numbers, advection dominates the bulk flow, although diffusion remains relevant near the flow boundaries, forming a diffusive boundary layer around the grain. As the Peclet number increases, the advective contribution becomes more significant, reducing the thickness of this diffusive boundary layer. Consequently, the fluid flow enhances solute removal from the

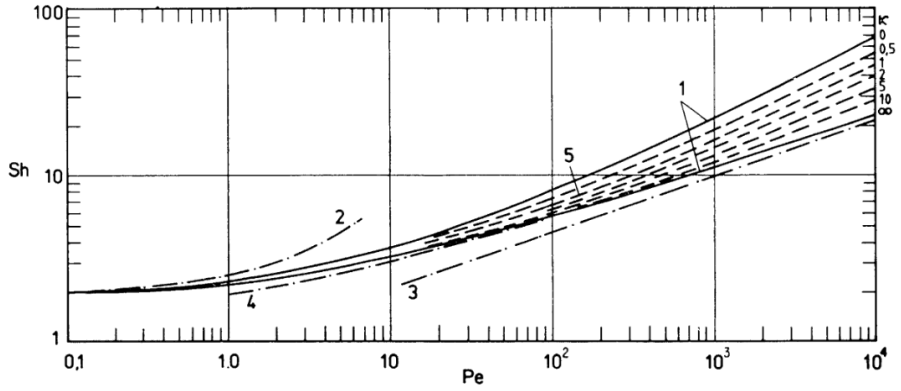

Figure 1.10 External Sherwood number for spheres in Stokes flow. (1) shows the exact numerical solution for rigid spheres, while (5) shows approximate values for the case of fluid spheres, for different viscosity ratios, $\kappa = \eta/\eta_p$, where η_p is the viscosity of the fluid particle. From [23]

vicinity of the particle, thereby increasing the concentration gradient near the interface and, ultimately, the dissolution rate.

The overall mass transfer coefficient (k) is related to the diffusion contribution through the Sherwood number (Sh), defined as :

$$\mathrm{Sh} = \frac{kL}{D} \Rightarrow k = \frac{\mathrm{Sh}}{L} D \tag{1.34}$$

A Sherwood number greater than or equal to the characteristic length (L) indicates an enhanced mass transport rate compared to a purely diffusive regime.

Determining the Sherwood number requires a description of the flow surrounding the particle, which involves both the Peclet and Reynolds numbers. The Reynolds number (Re), defined as the ratio of inertial to viscous forces, indicates whether a flow is laminar or turbulent :

$$\mathrm{Re} = \frac{\rho L U_0}{\eta} = \frac{L U_0}{\nu} \tag{1.35}$$

where η is the fluid viscosity, ν its kinematic viscosity, and ρ the fluid density. The Peclet and Reynolds numbers are related by the Schmidt number (Sc) through the relationship : $\mathrm{Pe} = \mathrm{Re} \cdot \mathrm{Sc} = \mathrm{Re} \cdot \nu/D$.

Numerous empirical and numerically derived relationships between the Sherwood number and the Peclet number exist in the literature, tailored to specific flow conditions. These studies often involve experimental setups where fluid flow conditions are precisely controlled, enabling isolation of advection effects by measuring dissolution rates under varying flow conditions.

For instance, in a steady Stokes flow past a rigid sphere the Sherwood number for different Peclet numbers has been numerically calculated and depicted in Figure 1.10. At small Peclet numbers, the Sherwood number approaches Sh_0, while at large Peclet numbers, the relationship follows $\mathrm{Sh} \propto \mathrm{Pe}^{1/3}$. For a sphere of diameter $2r$ in a stagnant fluid ($\mathrm{Pe} = 0$), the Sherwood number equals 2, implying $k = D/r$. This result suggests that advection can only enhance the mass transport rate relative to a purely diffusive scenario.

Influence of free convection

In addition to advection induced by melt flow currents, natural or free convection can also influence mass transport kinetics. Free convection arises from gradients in density, pressure, and surface energy due to heat or mass transfer [24]. During dissolution, chemical composition gradients may develop, impacting these properties near the dissolving particle.

The mass transport coefficient, as expressed by the Sherwood number, also depends on a free convection parameter known as the Rayleigh number (Ra), defined as :

$$\mathrm{Ra} = \mathrm{Gr}_c\mathrm{Sc} = \frac{gL^3\beta_c(C_s - C_\infty)}{\nu^2}\mathrm{Sc} \Rightarrow \mathrm{Ra} = \frac{gL^3\beta_c\Delta C}{\nu D} \tag{1.36}$$

where g denotes gravitational acceleration, Gr_c represents the compositional Grashof number, and β_c is the compressibility coefficient, defined as $\beta_c = -\frac{1}{\rho_\infty}\left(\frac{\partial\rho}{\partial C}\right)_{C_\infty}$.

For flat plates and horizontal cylinders, within a Rayleigh number range of 1 to 10^{10} under steady-state conditions, the Sherwood number for spheres in natural convection can be expressed as [23] :

$$\mathrm{Sh} = 1.7 + 0.3(1 + 14.86[f(\mathrm{Sc})]\mathrm{Ra})^{1/4} \tag{1.37}$$

where $f(\mathrm{Sc}) = [1 + (0.5/\mathrm{Sc})^{9/16}]^{-16/9}$. Given that the Schmidt number for highly viscous melts such as glass typically exceeds 10^4, $f(\mathrm{Sc}) \approx 1$ [25], simplifying the Sherwood number dependency as :

$$\mathrm{Sh} = 1.7 + 0.3(1 + 14.86\mathrm{Ra})^{1/4} \tag{1.38}$$

Thus, similar to the advection contribution described by the Peclet number, free convection also enhances the mass transfer coefficient.

Assuming free convection coupled with diffusion during the dissolution of a spherical particle in a viscous melt under steady-state conditions, Choudhary [25] numerically calculated the dimensionless time $8Dt(C_a - C_\infty)/(4a_0^2\rho_s)$ against different fractional reductions in diameter for various Rayleigh numbers, considering the particle's initial diameter ($2a_0$) as the characteristic length. The results are presented in Figure 1.11.

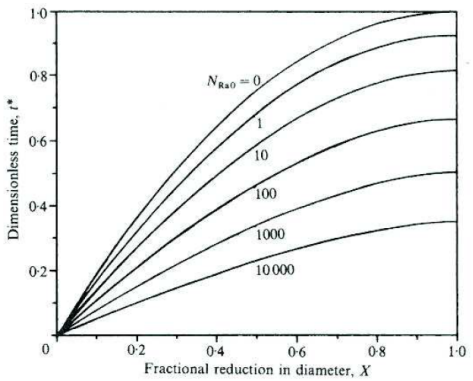

Figure 1.11 Dimensionless time $8Dt(C_a - C_\infty)/(a_0^2\rho_s)$ against different fractional reductions in diameter for various Rayleigh numbers calculated based on the initial diameter of the spherical particle (N_{Ra0} in the figure). From [25]

As mass transport phenomena accelerate, the effect of the interface reaction rate may become more significant, as it remains independent of fluid flow. Consequently, the considerations out-

lined in Section 1.2.1 regarding the k^* coefficient, which relates the reaction rate to the mass transfer rate, may require reevaluation.

In summary

Convection, whether from natural convection or fluid flow advection, enhances the mass transfer coefficient compared to a diffusion-only process. By combining these contributions, along with the radial flow resulting from the particle's volume change, Beerkens *et al.* [26] estimated the effect of various flow conditions on the dissolution of a spherical sand grain in a glass melt at 1400 °C (Figure 1.12). The authors derived the necessary physicochemical data from prior sand dissolution tests, using the mass fraction of sand residue after interrupted melting of raw material batches.

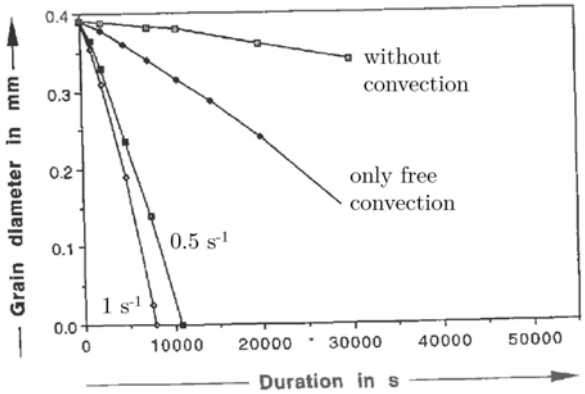

Figure 1.12 Calculated reduction of sand grain diameter during the dissolution in a glass melt for different cases of convection. The fastest rates were calculated considering the case of forced convection with a velocity gradient of 0.5 and 1 s^{-1}. From [26]

It is evident that convection plays a crucial role in the dissolution rate of particles within a real melter, underscoring the importance of developing melt flows to improve the estimation of dissolution rates in glass tanks. However, the overall dissolution rate remains dependent on two key properties : the solubility limit and the diffusion coefficient, the latter of which must be defined under static conditions.

Given the current capability to assess residence time, local temperature, and velocity through CFD models, accurate evaluation using submodels dedicated to predicting dissolution is constrained by the availability of reliable physicochemical data. Consequently, the next section will focus on compiling the current data available for silica and alumina dissolution in silicate melts.

1.3 Available data on alumina and silica dissolution

1.3.1 Historical overview of silica and alumina dissolution studies

The dissolution of alumina and silica in oxide melts has been extensively investigated since the 1960s, driven by interests across various scientific fields. Early studies focused on silica dissolution, primarily in the context of glass science, to improve understanding of the batch-to-melt conversion process. These early experiments, conducted in the 1960s, largely focused

on melts with high alkali content (>50 mol% Na_2O), typically within the Na_2O -SiO_2 binary system [27–31].

More recent research has broadened this focus to include applications such as nuclear waste glass [32] and ironmaking and steelmaking slags [12, 33], which involve multi-component slag compositions. Notably, the majority of silica dissolution studies used amorphous silica. The preference for vitreous silica over crystalline silica was justified by Hlavac and Nademlyska [31], who observed that the diffusivity of silica in sodium disilicate glass (900–1150 °C) was similar for both quartz and amorphous silica. However, they reported that vitreous silica dissolved 17% faster than quartz.

In more recent studies, quartz has been employed as the silica source in volcanological investigations [34–36], particularly in silicate melts simulating natural multi-component systems, such as CaO-Al_2O_3-SiO_2 and CaO-MgO-Al_2O_3-SiO_2 , at temperatures between 1500 and 1600°C. Due to the specific applications of these studies, they were conducted under high-pressure conditions exceeding 0.5 GPa.

In contrast, alumina dissolution studies have been primarily focused on industrial processes, such as refractory corrosion in steelmaking slags, with particular attention to producing clean steel (i.e., free of oxide inclusions) [11, 13, 37–41]. These investigations, conducted mainly in the 1990s, concentrated on ternary systems like CaO-Al_2O_3-SiO_2 and CaO-MgO-Al_2O_3-SiO_2 slags. Yu *et al.* [42] were among the few researchers to examine alumina dissolution in the presence of sodium oxide (3–10 mol%), to evaluate the flux effect on alumina solubility.

1.3.2 Experimental techniques to measure dissolution

Early investigations typically assumed diffusion-controlled dissolution, particularly given the high viscosity of melts [26, 43, 44]. Before the development of advanced techniques like particle radius evolution tracking and electron probe microanalysis (EPMA), support for the mass transport hypothesis came from dynamic corrosion tests, which demonstrated increased material degradation with enhanced melt flow.

Early silica dissolution studies aimed at understanding batch-to-melt conversion often employed the interrupted melting approach [26, 43, 44]. This technique involved measuring the mass of undissolved sand grains after heating batch powders at various temperatures and times, with results obtained through optical observation, X-ray diffraction, and differential thermal analysis. Although these studies provided insights into glass-melting conversion, mass transfer coefficients were subject to numerous assumptions and extrapolations.

In parallel, the rotary finger setup was reported as early as 1964 as an alternative method for measuring dissolution under controlled melt flow [40, 41]. In this setup, a cylindrical refractory sample is immersed in molten glass and rotated at a controlled speed. Some studies utilized this setup without rotation to observe dissolution under free convection. However, the Marangoni effect at the slag-cylinder-atmosphere interface often resulted in non-uniform material loss along the cylinder length. Despite this, the rotary finger setup offered the advantage of controlling melt flow, facilitating the coupling of experimental data with mass transport relationships such as the Levich equation [45, 46] :

$$k = 0.62 D^{2/3} \nu^{-1/6} \omega^{1/2} \Rightarrow \mathrm{Sh} = 0.62 \mathrm{Pe}^{1/2} \mathrm{Sc}^{1/3} \tag{1.39}$$

where k is the mass transfer coefficient, D is the diffusion coefficient, ν is the kinematic viscosity of the melt, and ω is the angular viscosity of the rotating disk. The Levich equation can be rewritten in function of the dimensionless numbers, as discussed in Section 1.2.3.

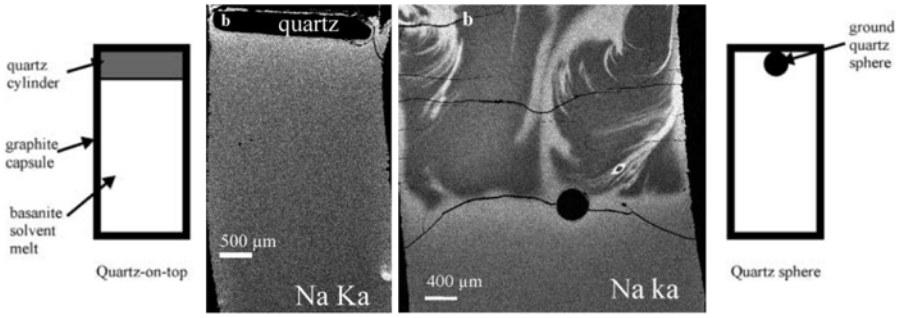

Figure 1.13 Comparison of X-ray maps for sodium obtained from quartz dissolution samples using two different setups : (left) "quartz on top" and (right) using a quartz sphere. Lighter regions show higher concentration. Given quartz is less dense than basanite, the left configuration is gravitationally stable. From [35]

Other experimental setups were later developed to study the dissolution of solid inclusions in slags. For example, researchers measured the evolution of spherical particle radii in the melt before the advent of high-temperature confocal laser scanning microscopy (HT-CLSM). Earlier works involved heating silica spheres on sodium silicate glass, quenching, and microscopically measuring the radius [30,31]. These measurements allowed for constructing a/a_0 plots over time and highlighted the limitations of analytical solutions, such as quasi-steady-state approximations, in fitting experimental dissolution curves. A recent review by Xuan and Mu [8] compiled HT-CLSM results for alumina and silica dissolution, comparing them with conventional shrinking core models. In most cases, analytical approximations failed to describe the observed curves.

Another challenge when using spherical grains is the potential influence of free convection. Some authors [30,38,47] reported grain rotation and buoyancy during tests, as demonstrated by Shaw [35] in his study of quartz dissolution. He compared quartz spheres placed on basanite melt with quartz slabs positioned above or below the basanite. X-ray maps of the spheres revealed signs of free convection, which was less prominent in the more stable quartz-on-top configuration (Figure 1.13)

The slab or capillary setup offers a one-dimensional dissolution case by stacking solid oxide ceramics and glass slabs according to their densities to avoid gravitational instabilities. This method often involves EPMA measurements of the diffusion profile from the interface, enabling the experimental extraction of interface composition [28, 35, 36]. However, this setup restricts dissolution to its initial stages, as complete dissolution requires extended time due to the larger quantity of solid present.

1.3.3 Comparative analysis of the dissolution measured properties

Tables 1.2 and 1.3 present a compilation of these studies, revealing that most describe dissolution as being controlled by mass transport within the melt. Nevertheless, some authors [39, 45, 47] have observed the formation of intermediate solid layers during alumina dissolution in CaO-MgO-Al_2O_3-SiO_2 glasses, particularly spinel layers, when MgO is present. The dissolution process is influenced by the rate of spinel formation, its subsequent dissolution, and solid diffusion through the layer. Sandhage *et al.* [48] further reported that the congruency of this layer to the alumina interface depends on melt flow conditions.

Among silica studies, Shaw [34] was the only researcher to report an induction period during which dissolution was reaction-controlled at the interface. According to him, improved mass transfer rates with increasing temperature can outpace the interface reaction rate and no longer be the rate-limiting step.

Table 1.2 Experimental silica dissolution tests conditions.

Authors	Method	Temperature	Mineral	Glass system	Mechanism
Sammadar et al. (1964) [41]	rotary finger (1200 rpm)	1350 to 1500 °C	amorphous silica	CAS	mass transport in the melt
Schwerdtfeger (1966) [29]	rod (free convection)	1000 to 1400 °C	quartz glass ?	NCS	mass transport in the melt
Kreider and Cooper (1967) [30]	spherical grain	950 °C	quartz	NS	mass transport in the melt
Hlavac and Nademlyska (1969) [31]	spherical grain	900 to 1200 °C	quartz and amorphous silica	NS	mass transport in the melt
Barklage-Hilgefort and Frischat (1980) [28]	slab setup	1200 to 1500 °C	quartz and amorphous silica	NS	mass transport in the melt
Cable and Martlew (1985) [27]	static finger	1000 to 1200 °C	amorphous silica	NS	mass transport in the melt
Liang (1999)	slab setup [36]	1500 °C at 1 GPa	quartz	CAS	mass transport in the melt
Shaw (2006) [34]	slab setup	1600 °C at 1.5 GPa	quartz	CMAS	interface reaction and mass transport
Feichtinger et al. (2014) [12]	CLSM	1450 °C	amorphous silica	CAS	mass transport in the melt
Tian et al. (2019) [33]	CLSM	1470 to 1530 °C	amorphous silica	CMAS	mass transport in the melt

Table 1.3 Experimental alumina dissolution tests conditions.

Author	Method	Temperature	Mineral	Glass system	Mechanism
Cooper and Kingery (1964) [40]	static finger	1510 to 1550 °C	sapphire	CAS	mass transport in the melt
Cooper and Kingery (1964) [40]	rotary finger (1200 rpm)	1345 to 1550 °C	sapphire	CAS	mass transport in the melt
Sammadar et al. (1964) [41]	rotary finger (1200 rpm)	1425 to 1500 °C	sapphire	CAS	mass transport in the melt
Sammadar et al. (1964) [41]	rotary finger (1200 rpm)	1425 to 1500 °C	polycrystalline alumina	CAS	mass transport in the melt
Sandhage and Yurek (1990) [39]	rotary finger (1200 rpm)	1450 to 1550 °C	sapphire	CMAS	mass transport in the melt, but also formation of an intermediate solid product (spinel)
Yu et al. (1997) [42]	rotary finger (200 rpm)	1530 °C	polycrystalline alumina	CAS + Na2O or CaF2	mass transport in the melt
Liu et al. (2007) [38]	CLSM	1470 to 1630 °C	alumina sphere	CAS	mass transport in the melt
Shaw et al. (2018) [49]	slab setup	1600 °C at 1.5 GPa	sapphire	CAS	mass transport in the melt for t >900s
Burhanuddin et al. (2022) [37]	rotary finger (200 rpm)	1450 to 1550 °C	polycrystalline alumina	CMAS	mass transport in the melt
Harmuth and Burhanuddin (2022) [13]	CLSM	1450 to 1550 °C	sapphire	CMAS	mass transport in the melt
Ren et al. (2023) [11]	CLSM	1500 to 1580 °C	alumina grain	CAS	mass transport in the melt

Although some studies report a dissolution rate value, identifying a single rate is not always possible. As discussed earlier, the dissolution rate can vary with time, as illustrated by radius evolution curves. Therefore, studies reporting dissolution rates typically conducted experiments under advection, where dissolution rates are expected to be linear, or under conditions where a parabolic dissolution behavior was observed.

Therefore, available dissolution rate values from a selection of studies have been plotted for both alumina and silica in Figure 1.14. Linear rates are depicted as upward-pointing triangles, while parabolic constants are shown as downward-pointing triangles. The data are plotted with respect to the undersaturation of the starting glass composition relative to the dissolving oxide and

compared with an effective binary diffusion coefficient (EBDC). The definition of this coefficient will be described in more detail in Section 1.4.2. Undersaturation was calculated as the difference between the original content of the dissolving oxide (either alumina or silica) and the interface composition. In cases where the latter was not reported (represented by translucent markers), the thermodynamic equilibrium composition was calculated using methods that will be described in Section 2.5.4. This assumption was made when mass transport was identified as the rate-limiting step for dissolution.

For both silica and alumina, dissolution rates varied by more than an order of magnitude for the same combination of EBDC and undersaturation. This variability is particularly pronounced in alumina works, where dissolution rates measured under different experimental conditions diverge significantly. Studies conducted at lower rotation velocities [37] or in free convection [40] conditions generally reported slower dissolution rates, while glass compositions with low silica content, as in the case of Ren *et al.* [11], showed the fastest dissolution.

One of the main challenges in understanding dissolution rates lies in comparing experimental data and models originally developed for binary systems. Most studies assume a constant diffusivity value across the composition range and calculate an EBDC used to fit experimental data. These values are plotted as a function of temperature and composition in Figure 1.15. While there is a general trend of increasing EBDC with temperature, significant data scattering remains, even when accounting for compositional differences (both initial and equilibrium).

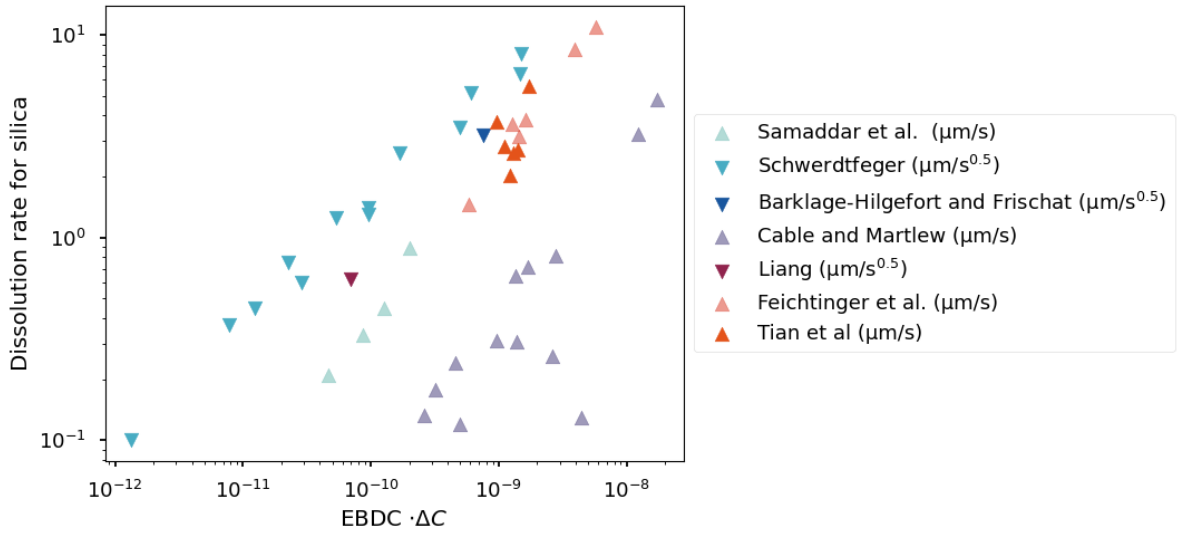

a Data from [12, 27–29, 33, 34, 36, 41]

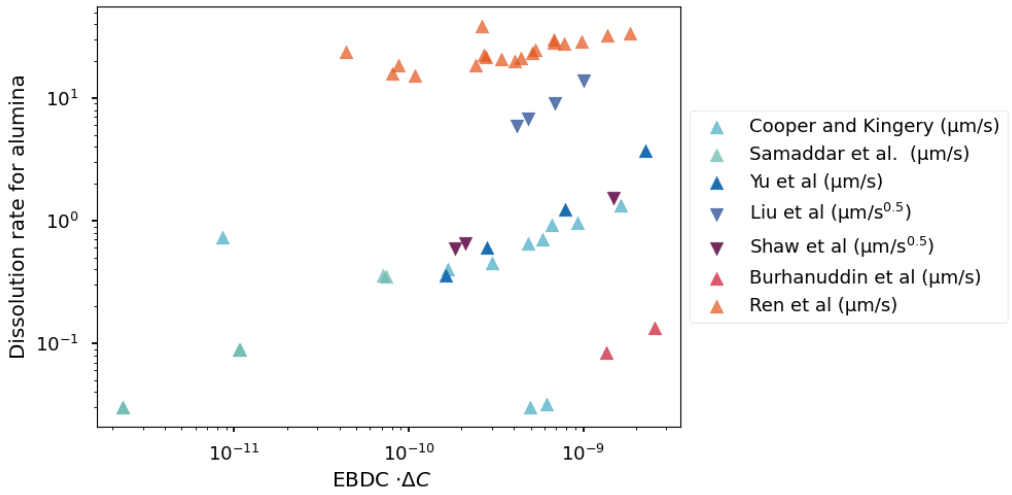

b Data from [11, 37, 38, 40–42, 49]

Figure 1.14 Dissolution rates of silica (1.14b) and alumina (1.14b) as reported in the literature. The data includes both linear and parabolic rate values, compared against the undersaturation, $\Delta C = C_a - C_\infty$ in %wt, and the effective binary diffusion coefficient of the dissolving oxide. Opaque markers represent studies that directly measured interface or equilibrium compositions, while translucent markers indicate studies where these compositions were later calculated through thermodynamic modeling (detailed in Section 2.5.4)

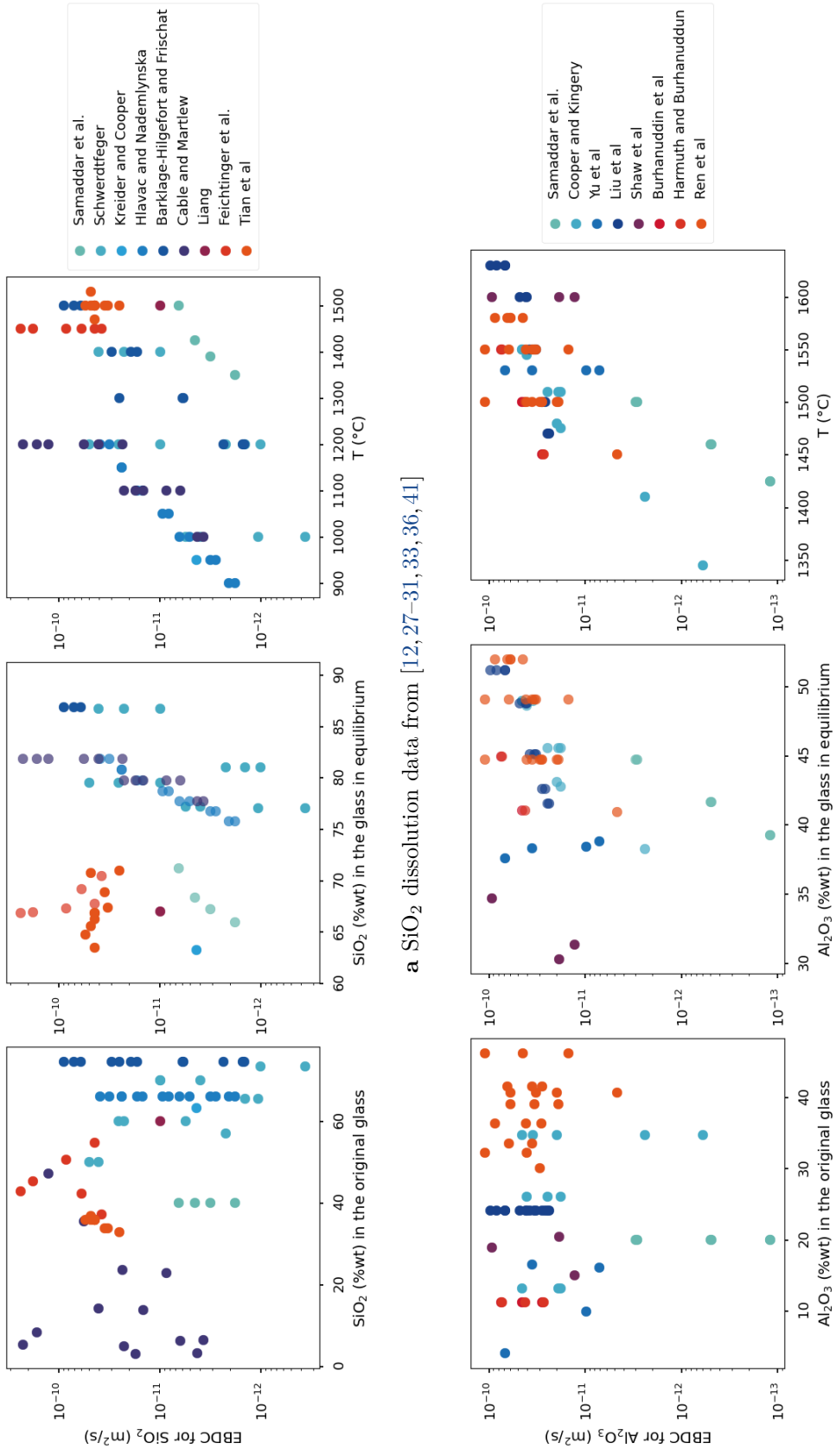

Figure 1.15 Effective binary diffusion coefficient (EBDC) extracted from silica (top) and alumina (bottom) dissolution tests. The values are compared as a function of the initial and interface composition of the glass (in SiO_2 or Al_2O_3), as well as the temperature of the test.

The early works of Cable and Martlew [50] already identified this issue for silica, noting that the calculation of EBDC depends heavily on the fitting model's assumptions. Recently, Harmuth and Burhanuddin [13] have demonstrated that assuming static dissolution in HT-CLSM alumina dissolution tests can lead to an overestimation of its diffusivity by around one order of magnitude. This overestimation occurs when compared to considering the relative movement of the alumina particle falling in the melt due to density differences. Since diffusivity is not directly measured in dissolution tests, the variability observed may stem from discrepancies between experimental setups and the theoretical models applied to the data.

Despite extensive study, dissolution rates and mass transport coefficients for both silica and alumina remain scattered, indicating that understanding of the dissolution process is still incomplete. The experimental methods employed and the models used to fit the data present ongoing challenges and are likely sources of variability. A common practice is to fit experimental dissolution curves for multi-component systems to models developed for binary systems, as outlined in the previous section. The next section will explore the complexities inherent to multi-component systems, such as industrial glass melts, compared to simpler binary systems.

1.4 Complexities in multi-component systems

The models and numerical solutions discussed in Section 1.2.2, which are commonly applied to fit experimental data, were primarily developed based on a two-component system : a pure oxide particle composed solely of species A and an infinite reservoir of the solution, where the solute diffusivity is assumed constant. However, these assumptions are not universally applicable, as demonstrated by some of the experimental data presented in the previous section, which often involved glass compositions containing three or more oxides.

For illustration, two sets of experimental data on silica dissolution—one involving a binary melt [31] and the other a ternary melt [12]—are compared with the comprehensive diffusion-controlled dissolution model detailed in Section 1.2.2. Both studies provided values for the undersaturation parameter (F_a), which facilitated comparison with the curves shown in Figure 1.7. It is important to note, however, that the melt concentration at the particle interface was not directly measured by the authors ; rather, it was assumed to correspond to the thermodynamic equilibrium value. The molar volume difference parameter (ε) value should be consistent for both studies, as both used amorphous silica as the silica source. Figure 1.16 illustrates the radius evolution, compared with curves calculated for an ε value close to zero.

Although the values of the undersaturation parameter (F_a) differ between the two studies, making a direct comparison challenging, it is evident that the dissolution behaviors do not follow the same pattern. According to the dissolution models previously discussed, as (F_a) increases, the curve is expected to transition from a parabolic shape (represented by the quasi-steady-state case in black) to a sigmoidal form. However, for values well above unity, the data for CaO-Al_2O_3-SiO_2 slag [12] appears to fit better with the low-solubility curve. In contrast, the data for the binary $Na_2O \cdot 2\ SiO_2$ [31] exhibit a near-sigmoidal behavior despite their F_a value being lower than that of the ternary system. Although the data has non-negligible scattering, Hlavac and Nademlynska's results align more closely with what is expected for this solubility value, albeit slightly skewed toward a higher solubility curve.

Feichtinger *et al.* [12] recognized that conventional approximation models cannot accurately describe the experimental data, a conclusion echoed by other researchers who employed multi-component systems in high-temperature confocal laser scanning microscopy (HT-CLSM) measurements [8, 51]. Both Feichtinger *et al.* [12] and Xuan and Mu [8] independently proposed

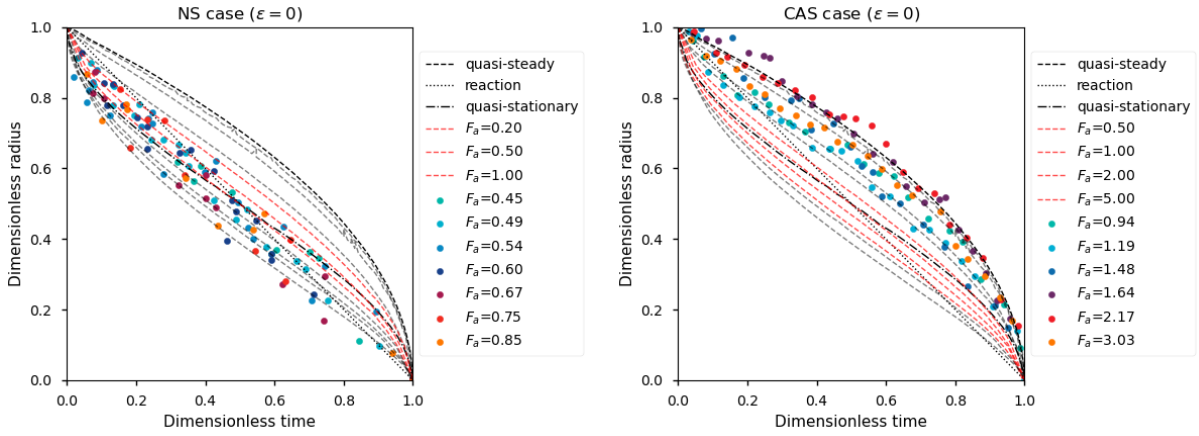

a Binary $Na_2O \cdot 2\ SiO_2$ [31]

b Ternary $CaO\text{-}Al_2O_3\text{-}SiO_2$ [12]

Figure 1.16 Comparison between the numerical model (shown by the curves) proposed by Cable and Frade for binary systems for a diffusive dissolution with experimental data (depicted as coloured circles) for amorphous silica dissolution in a binary (left) and a ternary (right) glass compositions. The reaction controlled, as well as the quasi-steady and quasi-stationary cases are also plotted in black. The curves for values of F_a in the range of the experimental data are represented in red.

modifications to the shrinking core model by introducing a parameter to account for the stretching of the diffusion profile near the interface. This adaptation allows for the fitting of data ranging from sigmoidal (quasi-stationary approximation in Section 1.2.2) to parabolic (quasi-steady state in Section 1.2.2) curves. Their studies reported a correlation between the shape of the dissolution curve and the melt's viscosity, as illustrated by Figure 1.17. Specifically, a more viscous melt at the interface than the bulk is associated with a parabolic dissolution curve, whereas higher viscosity in the bulk (far-field region) is linked to a sigmoidal shape.

Comparing the stretching of diffusion profiles due to viscosity gradients with numerical simulations for binary systems is instructive. According to these simulations, dissolution scenarios where the concentration gradient at the interface is large (i.e., high F_a) produce sigmoidal curves and stretched diffusion profiles (see Figure 1.8). This is attributed to the solute accumulation near the interface, where the shrinking particle is not easily accommodated by the surrounding diffusion profile. Similarly, the modified models suggest that a more viscous bulk melt hinders the accommodation of increasing solute concentrations near the interface.

In conclusion, while binary diffusive dissolution models are inadequate for quantifying radius evolution curves in multi-component slags, their insights into the relationship between solute accumulation, interface concentration gradients, and the capacity of diffusion to accommodate these gradients are consistent with observations in more complex systems. What remains to be addressed is a more accurate description of the concentration gradient at the interface (undersaturation) and the mechanisms by which solute is transported away from the interface in multi-component systems.

This section will explore some of the inherent complexities that arise when transitioning from binary to multi-component systems. Emphasis will be placed on how these changes affect the solubility and, consequently, the undersaturation of the melt, as well as the mass transport of solute away from the interface.

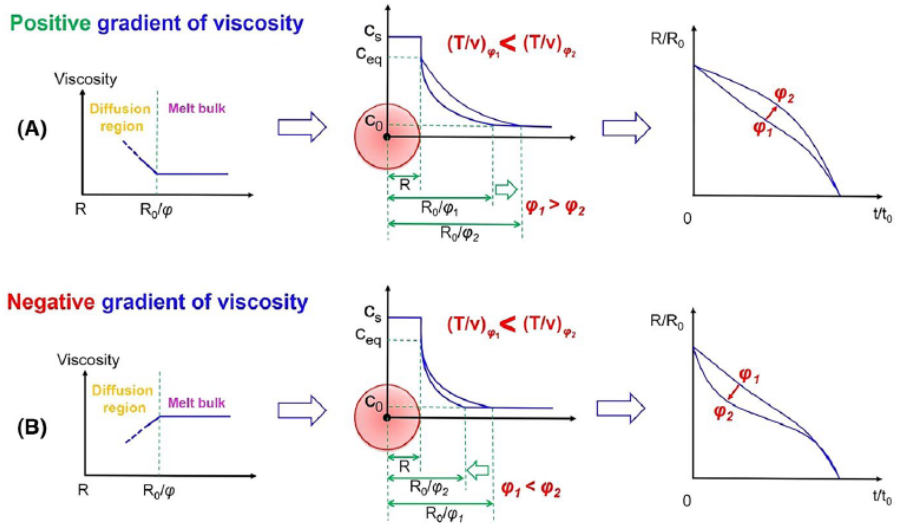

Figure 1.17 Correlation between the diffusion profile stretching parameter ($\phi = R_0/r$, the ratio between the initial particle radius and the diffusion boundary thickness) proposed by Xuan and Mu with the viscosity gradient at the diffusion boundary, and their influence on the shape of the radius evolution curve. From [8]

1.4.1 Solubility limits

Soda-lime-silica glasses typically contain at least two oxides in addition to silica : sodium oxide and calcium oxide. Various industrial and geochemical systems of interest are either ternary or even more complex. According to the Gibbs phase rule [52], increasing the number of components (C) in a system raises the minimum number of independent variables that must be specified to fully define the system, thus increasing the degrees of freedom (ϕ). When considering temperature and pressure as independent variables, alongside the composition of C components, the number of degrees of freedom for a system with P phases in equilibrium is expressed as :

$$\phi = C + 2 - P \tag{1.40}$$

If the goal is to define the solubility parameter based on the difference between the initial composition and its deviation from the thermodynamic equilibrium value under isothermal and isobaric conditions, the degrees of freedom simplify t $\phi = C - 2$, assuming a single solid is in equilibrium with a miscible liquid ($P = 2$). In a binary system ($C = 2 \Rightarrow \phi = 0$), the equilibrium composition at a given temperature and pressure is invariant. However, in more complex systems ($C \geq 3 \Rightarrow \phi \geq 1$), there exists at least one curve, known as the liquidus curve (or entity of dimensionality ϕ), that defines the potential values of solute incorporation into the liquid.

In diffusion-controlled dissolution, the glass's interface composition is assumed to be at thermodynamic equilibrium with the dissolving solid, meaning the composition should align with the liquidus curve. To illustrate, consider a ternary system in which a solid composed solely of component 3 dissolves upon contact with a melt of composition A, shown in Figure 1.18. Initially, it would be expected that the equilibrium composition is determined by point D, the intersection between the liquidus curve and the straight tie-line linking the compositions of the two phases ($A - 3$). In this scenario, the chemical composition in the glass could be characterized by the

concentration of only one component (3), effectively reducing the system to a pseudo-binary one.

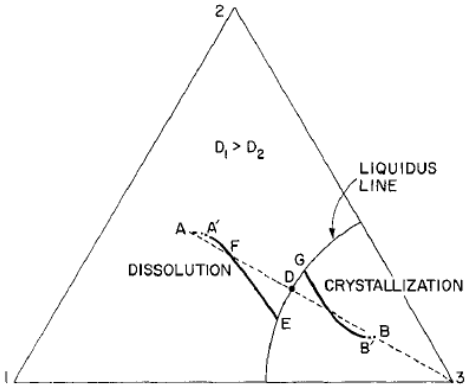

Figure 1.18 Schematic concentration paths for the dissolution of a solid 3 in contact with a glass of composition A. While the straight tie-line intersection with the liquidus curve corresponds to the point D, if the mobilities of the components are not equal, the concentration path is not necessarily linear. For example, if component 1 is the fastest, the intersection would be closer to E. From [53]

However, in multi-component systems, the various species exhibit different mobilities, and the concentration profiles in the melt do not necessarily follow the straight tie-line. A relative enrichment of the more mobile species often occurs at the interface during dissolution [53]. Although this example focuses on a ternary system, the same principle applies to more complex compositions.

As indicated by the translucent markers in Figure 1.14, only a limited number of experimental dissolution studies report interface compositions, and an even smaller subset provides experimentally measured compositions. Among those that do, works by Liang [36], Shaw [34, 49], and Sandhage [54], who reported electron probe microanalysis (EPMA) measurements of the interface composition in multi-component melts, observed deviations from the straight tie-line.

Thus, in multi-component glasses where the dissolution path does not conform to the straight tie-line, determining the interface composition becomes complex and is influenced by the mobilities of other components. Furthermore, the chemical distribution of dissolved species cannot be described solely by the solute composition, as assumed in a pseudo-binary model. This highlights the additional complexities in defining an undersaturation parameter for multi-component systems.

1.4.2 Diffusivity

The models presented in Section 1.2 rely on a diffusion coefficient, a property that relates mass flux to a concentration gradient. Understanding this concept in greater detail is essential for accurately describing the dissolution mechanisms in glass systems, especially when dealing with complex, multi-component compositions.

Diffusivity and its dependencies Diffusivity, or the diffusion coefficient, describes the rate at which atomic species are transported via thermally activated random motion [55]. More

rigorously, diffusivity links the mass flux of a component to its chemical potential gradient. When the chemical potential is replaced by concentration, an implicit assumption is made that the diffusivity depends on variables such as temperature, pressure, and composition. These variables define the thermodynamic relationships between chemical potential and concentration, making diffusivity context-dependent [56].

In simple systems, diffusion coefficients can be measured under different conditions. In the absence of a concentration gradient, self-diffusivity describes the random motion of species, often measured using isotopic gradients or molecular dynamics simulations. When the diffusing species is present in trace amounts (less than 1% by weight), its diffusivity is referred to as trace element diffusivity [57]. Diffusion data compilations [55, 58, 59] showed that trace element diffusivity is influenced by the species' electric field strength, defined as the ratio of its valence to ionic radius. Higher electric field strength increases the interaction with the surrounding matrix, reducing diffusivity. For example, Zhang and Gan [60] demonstrated that diffusivity in rhyolitic melts follows a specific order based on field strength :

$$\begin{aligned} &\mathrm{H_2} > \mathrm{He} > \mathrm{Li} \approx \mathrm{Na} > \mathrm{Cu} > \mathrm{K} > \mathrm{Ne} > \mathrm{Ar} \approx \mathrm{CO_2} \\ &\approx \mathrm{Cl} \approx \mathrm{F} > \mathrm{Ba} > \mathrm{Ca} > \mathrm{Mg} > \mathrm{B} \approx \mathrm{REE} > \mathrm{Zr} \approx \mathrm{Ti} \approx \mathrm{Si} \approx \mathrm{P} \end{aligned} \quad (1)$$

Diffusivity in binary systems In binary systems, diffusion occurs between two components, and diffusivity is referred to as interdiffusivity or mutual diffusivity. Fick's first law is commonly used to describe the flux of one component in relation to its concentration gradient. However, in industrial applications, binary systems are seldom sufficient to capture the complexity of glass melts that contain multiple species interacting with one another.

Moving to multi-component systems While binary systems can be effectively described using interdiffusion, multi-component systems require a more rigorous treatment. Fick's law, developed for binary diffusion, becomes insufficient when interactions between more than two species must be accounted for. In these cases, a scalar diffusion coefficient cannot fully describe the system [60]. Instead, the diffusion of a given species must be considered as part of a coupled system, where the transport of each species is influenced by the concentration gradients of all others in the melt.

In multi-component diffusion, the flux of a given component is modeled as a linear combination of the concentration gradients of independent species in the system. According to Onsager [61], this results in a multi-component form of Fick's law, where the diffusion coefficient is replaced by a diffusion matrix. For an isotropic system, the first Fick's law becomes :

$$\mathbf{J}_i = -\sum_{j=1}^{n-1} D_{i,j} \nabla C_j \quad (1.41)$$

where $D_{i,j}$ are elements of the $(n-1)\times(n-1)$ diffusion matrix $[\mathbf{D}]$, and C_j represents the molar fraction of component j. In the absence of bulk flow, and that diffusivity does not depends on concentration, the second Fick's law is reformulated as :

(1) REE stands for rare earth elements.

$$\frac{\partial C_i}{\partial t} = \sum_{j=1}^{n-1} D_{i,j} \nabla^2 C_j \tag{1.42}$$

For a ternary system in a one-dimensional context, this can be expressed as :

$$\begin{aligned} \frac{\partial C_1}{\partial t} &= D_{1,1} \frac{\partial^2 C_1}{\partial x^2} + D_{1,2} \frac{\partial^2 C_2}{\partial x^2} \\ \frac{\partial C_2}{\partial t} &= D_{2,1} \frac{\partial^2 C_1}{\partial x^2} + D_{2,2} \frac{\partial^2 C_2}{\partial x^2} \end{aligned}$$

In matrix form :

$$\frac{\partial}{\partial t} \begin{bmatrix} C_1 \\ C_2 \end{bmatrix} = \begin{bmatrix} D_{1,1} & D_{1,2} \\ D_{2,1} & D_{2,2} \end{bmatrix} \frac{\partial^2}{\partial x^2} \begin{bmatrix} C_1 \\ C_2 \end{bmatrix} \tag{1.43}$$

The diffusion matrix in this system describes the interaction between species and their collective migration through the melt.

Eigenvectors and eigenvalues of the diffusion matrix To simplify multi-component diffusion, the diffusion matrix can be diagonalized, decomposing it into eigenvectors and eigenvalues :

$$[\mathbf{D}] = [\mathbf{B}][\mathbf{\Lambda}][\mathbf{B}]^{-1} \tag{1.44}$$

where $[\mathbf{B}]$ consists of the eigenvectors of the diffusion matrix, and $[\mathbf{\Lambda}]$ is a diagonal matrix with eigenvalues of $[\mathbf{D}]$. Linearizing the composition in terms of these eigenvectors allows the diffusion equations to be uncoupled :

$$\frac{\partial}{\partial t} \begin{bmatrix} U_1 \\ U_2 \end{bmatrix} = \begin{bmatrix} \lambda_1 & 0 \\ 0 & \lambda_2 \end{bmatrix} \frac{\partial^2}{\partial x^2} \begin{bmatrix} U_1 \\ U_2 \end{bmatrix} \tag{1.45}$$

The approach of multi-component diffusion, as opposed to binary diffusion, allows for the interaction and coupling between different chemical components. One notable phenomenon arising from this coupling is uphill diffusion, where a component can diffuse against its own concentration gradient. This occurs when the off-diagonal terms of the diffusion matrix are comparable to the diagonal ones, indicating significant coupling between components [56].

The diffusion matrix's eigenvectors can be interpreted as exchange reactions, describing how components interact to migrate through the phase. The corresponding eigenvalues are associated with the rates of these interactions. For a fixed length L, this results in independent time scales associated with each eigenvalue ($\tau_i^0 = L^2/\lambda_i$).

For $t \gg \tau_1^0$, where τ_1^0 is the characteristic time for the fastest eigenvector, the gradient of the species associated with it diminishes, leading to a quasi-steady state diffusion. In dissolution problems within ternary systems, this implies that these species arrive most rapidly at the interface, potentially influencing the concentration at the interface. Given that the solubility composition is defined by a curve rather than being invariant, this rapid arrival can shift the interface composition from the expected tie-line linking the far-field composition and the solid oxide primary field.

Effective Binary Diffusion Coefficient (EBDC) In practice, multi-component diffusion is sometimes approximated using Effective Binary Diffusion Coefficients (EBDCs). In this approach, the component of interest is treated as the independent variable, while all other components are considered dependent variables. The flux for the component i is expressed as :

$$J_i = -\text{EBDC}_i \frac{\partial C_i}{\partial x} \tag{1.46}$$

Due to the possible coupling between elements, the dynamics of the component of interest can be influenced by more than one eigenvalue. If a quasi-steady state diffusion is achieved for one of them, the apparent diffusivity will vary over time. This situation is illustrated by Liang's Figure 1.19 [56], showing how the dynamics of multi-component systems can interfere on the calculation of EBDC.

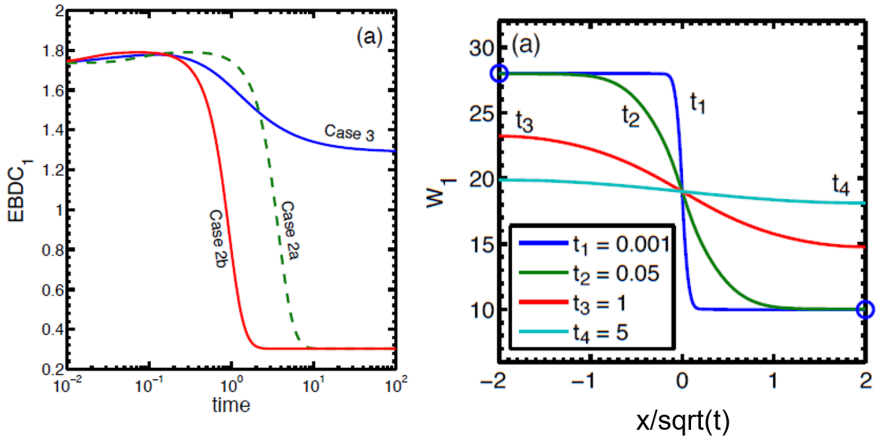

Figure 1.19 Evolution of the effective binary diffusion coefficient (EBDC) with time (left) EBDC for the composition w_1 in respect of time. (right) Plot of the diffusion profile of w_1 in a confined medium for the Case 3 scenario. It is possible to see that the value of EBDC at $t = 0.05$ is different from $t = 5$, which can be reflected on the reduction of the concentration gradients. From [56]

Implications for this study The dissolution of corundum and quartz in soda-lime silica glass represents a multi-component system, necessitating the consideration of the aforementioned factors for accurate data interpretation. Previous research has measured diffusion matrices for silicate glasses in Na_2O-CaO-SiO_2 (NCS), CaO-Al_2O_3-SiO_2 (CAS), Na_2O-CaO-Al_2O_3-SiO_2 (NCAS), and CaO-MgO-Al_2O_3-SiO_2 (CMAS) systems at temperatures ranging from 1100 to 1500 °C [36, 62–64], revealing the existence of element coupling during diffusion. For instance, Liang [36, 65] applied the diffusion matrix for the CAS system to model quartz dissolution in glass, successfully predicting dissolution rates and interface compositions. Table 1.4 summarizes some of the reported diffusion matrices for these systems.

Challenges in measuring diffusion matrices While diffusion matrices offer valuable insights, their measurement is complex and time-consuming. To determine all possible exchange directions between components, diffusion couples must be prepared for each orthogonal direction around a central composition [67]. Additionally, the assumption of constant diffusivity across compositions, as required by Fick's second law, necessitates that matrices be measured within narrow compositional ranges (e.g., ± 5% mol). The effect of alumina content on diffusion has

Table 1.4 Eigenvalues and eigenvectors for diffusion matrices reported in the literature for silicate glasses.

Composition (wt%)	Eigenvectors	Eigenvalues ($\times 10^{-12} m^2.s^{-1}$)	T (°C)	Source
NCS 16-12-72	$Na_2O \leftrightarrow 0.85CaO + 0.15SiO_2$ $0.27Na_2O + 0.73CaO \leftrightarrow SiO_2$	105 4.4	1200	[62]
BNS 18-14-68	$Na_2O \leftrightarrow 0.9SiO_2 + 0.1B_2O_3$ $SiO_2 \leftrightarrow 0.75B_2O_3 + 0.25Na_2O$	10.1 0.51	1100	[66]
KAS D-3 9-16-75	$K_2O \leftrightarrow 0.14Al_2O_3 + 0.86SiO_2$ $0.75Al_2O_3 + 0.25K_2O \leftrightarrow SiO_2$	0.07 1×10^{-3}	1400	[67]
KAS 17a 16-9-75	$K_2O \leftrightarrow 0.01Al_2O_3 + 0.99SiO_2$ $0.98Al_2O_3 + 0.02K_2O \leftrightarrow SiO_2$	10.8 0.04	1400	[67]
KAS 23 8-17-74	$K_2O \leftrightarrow 0.02Al_2O_3 + 0.98SiO_2$ $0.8Al_2O_3 + 0.2K_2O \leftrightarrow SiO_2$	14.4 0.08	1600	[67]
NAS 19-9-72	$Na_2O \leftrightarrow SiO_2$ $SiO_2 \leftrightarrow Al_2O_3$	0.74 0.04	1200	not published data (SVI laboratory)
NKASH	$Na_2O \leftrightarrow SiO_2$ $K_2O \leftrightarrow SiO_2$ $Al_2O_3 + 0.21Na_2O + 0.28H_2O \leftrightarrow 1.57SiO_2$ $H_2O \leftrightarrow SiO_2$	550 540 3.4 280	1600	[68]
CAS 16 30-20-50	$CaO \leftrightarrow 0.58Al_2O_3 + 0.42SiO_2$ $Al_2O_3 \leftrightarrow 0.15CaO + 0.85SiO_2$	99 23	1500	[65]
CAS A 25-13-62	$CaO \leftrightarrow 0.41Al_2O_3 + 0.59SiO_2$ $0.81Al_2O_3 + 0.19CaO \leftrightarrow SiO_2$	34 8.3	1500	[65]
CAS B 28-15-57	$CaO \leftrightarrow 0.54Al_2O_3 + 0.46SiO_2$ $0.93Al_2O_3 + 0.07CaO \leftrightarrow SiO_2$	47 23	1500	[65]
CAS D 23-15-62	$CaO \leftrightarrow 0.52Al_2O_3 + 0.48SiO_2$ $0.62Al_2O_3 + 0.38CaO \leftrightarrow SiO_2$	36 11	1500	[65]
MAS 22-18-60	$MgO \leftrightarrow 0.54Al_2O_3 + 0.46SiO_2$ $0.68Al_2O_3 + 0.32MgO \leftrightarrow SiO_2$	70 20	1550	[69]
CMAS 9-7-20-64	$CaO \leftrightarrow 0.36MgO + 0.32Al_2O_3 + 0.32SiO_2$ $MgO \leftrightarrow 0.07CaO + 0.53Al_2O_3 + 0.4SiO_2$ $0.13CaO + 0.26MgO + 0.61Al_2O_3 \leftrightarrow SiO_2$	59 26 3.2	1500	[69]
NCAS 13-11-11-65	$Na_2O + 0.02Al_2O_3 \leftrightarrow 0.92CaO + 0.09SiO_2$ $CaO + 0.02Na_2O \leftrightarrow 0.47Al_2O_3 + 0.52SiO_2$ $CaO + 0.17SiO_2 \leftrightarrow 0.99Al_2O_3 + 0.15Na_2O$	29.5 0.58 0.3	1200	[70]
NCASZ 13-11-11-63-3	$0.97Na_2O + 0.1SiO_2 \leftrightarrow CaO + (Al_2O_3 + ZrO_2)$ $CaO \leftrightarrow 0.15Al_2O_3 + 0.75SiO_2 + (Na_2O + ZrO_2)$ $0.59CaO + 0.68SiO_2 \leftrightarrow Al_2O_3 + (Na_2O + ZrO_2)$ $ZrO_2 + 0.13CaO \leftrightarrow 0.78Al_2O_3 + (Na_2O + ZrO_2)$	38.2 0.83 0.12 0.06	1200	[71]
NCAS 17-13-5-65	$Na_2O \leftrightarrow 0.93CaO + 0.01Al_2O_3 + 0.06SiO_2$ $0.02Na_2O + CaO \leftrightarrow 0.12Al_2O_3 + 0.91SiO_2$ $0.9CaO + 0.13SiO_2 \leftrightarrow 0.03Na_2O + Al_2O_3$	110.7 2.39 0.52	1200	[64]
NCAS 17-13-5-65	$Na_2O + 0.01Al_2O_3 \leftrightarrow 0.98CaO + 0.03SiO_2$ $CaO \leftrightarrow 0.19Al_2O_3 + 0.81SiO_2$ $CaO \leftrightarrow 0.04Na_2O + 0.76Al_2O_3 + 0.2SiO_2$	395.34 6.01 2.90	1350	[64]
NCAS 9-8-23-60	$Na_2O \leftrightarrow 0.86CaO + 0.04Al_2O_3 + 0.11SiO_2$ $CaO \leftrightarrow 0.2Na_2O + 0.36Al_2O_3 + 0.43SiO_2$ $0.02Na_2O + SiO_2 \leftrightarrow 0.7Al_2O_3 + 0.33CaO$	226.38 9.81 0.55	1500	[64]

been observed in the NCAS systems studied by Claireaux *et al.* [63, 70] and Jacquemin [64], where alumina variations between 3%, 7%, and 15% mol altered the slowest diffusion pathways.

Although diffusion matrices are indispensable for understanding multi-component systems, their complexity prompts investigation into alternative transport properties, such as viscosity. The next section will explore the potential of viscosity as a proxy for diffusivity, especially in relation to atomic transport properties in glass melts.

In summary

- Diffusion in multi-component systems is described by a more rigorous approach that replaces a scalar diffusion coefficient with a diffusion matrix.
- Therefore, the diffusion matrix approach seems more adapted to describe the dissolution of these elements in a silicate melt, given that it accounts for the coupling between the species.
- Eigenvectors of the diffusion matrix relate how different species interact and move through the melt, while eigenvalues can be understood as their exchange rates.
- The cautious use of Effective Binary Diffusion Coefficients (EBDCs) can approximate multi-component diffusion but may vary over time due to coupling effects.

1.4.3 Viscosity and its relationship with diffusivity

Rigorously measured diffusion coefficients provide valuable insights into atomic transport within glass melts, but their determination in multi-component systems is often complex due to the labor-intensive and time-consuming process of measuring diffusion matrices. As a complementary approach, viscosity—while unable to capture individual species coupling effects—can offer indirect insights into the overall behavior of the melt.

Transport properties like diffusion, viscosity, and electrical conductivity are all linked to atomic mobility, though they reflect different aspects of this behavior. Viscosity measures the melt's resistance to deformation and is tied to the timescale of structural relaxation, especially in silicate melts. Electrical conductivity, in contrast, is dominated by fast-moving alkali ions such as Na and K, which reflect localized processes and may not capture the broader structural dynamics of network-formers [55].

Ni *et al.* [55] distinguished between intrinsic and extrinsic diffusivities based on species' transport characteristics. Fast-diffusing species, such as alkali ions, are primarily governed by their own ionic properties and show limited sensitivity to melt conditions. In contrast, network-forming species, such as alumina and silica, are classified as extrinsic diffusivity species. These species exhibit lower diffusivities and higher activation energies, as their transport is strongly dependent on the collective dynamics of the melt structure and is influenced by external factors such as temperature and composition.

The coupling between viscosity and diffusivity can be expected for these extrinsic diffusivity species, and thus for network formers like alumina and silica. The theoretical correspondence between viscosity and diffusivity has long been proposed for network formers, as their atomic mobility is influenced by the rearrangement of the melt's polymerized structure and thus the collective structural relaxation, a process well described by viscosity.

The theoretical relationship between viscosity and diffusivity for network-forming species can be described by the Eyring equation :

$$D_E = \frac{kT}{\eta d} \tag{1.47}$$

where k is the Boltzmann constant, T the absolute temperature, η the melt viscosity, and d the jump distance, typically the diameter of the O^{2-} ion [63, 72]. This equation predicts an inverse relationship between viscosity and diffusivity, suggesting that viscosity could serve as a proxy for diffusivity, particularly for network formers like alumina and silica in multi-component systems.

Given this theoretical basis, Section 1.3's data was analyzed to investigate this potential correlation. Viscosity was calculated using the GlassPy predict Python module, based on the GlassNet model for silicate and aluminosilicate melts [73]. Both bulk and interface viscosities were calculated based on the chemical composition and temperature of each test. The comparison between EBDC and viscosity is plotted in Figure 1.20.

The data showed a weak correlation between Effective Binary Diffusion Coefficient (EBDC) values and viscosity normalized by the absolute temperature (η/T) . However, the slope of this trend was less steep than predicted by the Eyring equation, likely due to the wide range of viscosities examined and uncertainties in determining interface compositions. This suggests that viscosity, while important for describing bulk properties, does not fully account for the atomic-scale interactions governing diffusion in multi-component systems.

Further attempts to correlate bulk viscosity with dissolution rates (Figure 1.21), following the approach suggested by Gou *et al.* [10] and Ren *et al.* [11], which links dissolution rates to the undersaturation-to-viscosity ratio, did not show significant improvements compared to Figure 1.14a. An alternative transport property does not yet explain the segmentation between alumina dissolution rates found using different experimental setups.

In recent adaptations of the shrinking core model, viscosity gradients replaced the undersaturation term i. These models, proposed by Feichtinger *et al.* and Xuan and Mu [8, 12], have shown that viscosity can approximate the dissolution curve shape for network-forming components like silica and alumina (Figure 1.17). In such cases, viscosity provides a closer approximation of bulk transport kinetics in multi-component systems rather than EBDC and solute undersaturation.

In conclusion, while the theoretical foundation supports a strong connection between viscosity and diffusivity, particularly for network-forming species, this is less evident in the currently available experimental data for dissolution of silica and alumina, compiled in Section 1.3. It is likely that the values of EBDC were significantly influenced by the discrepancies between the experimental conditions and the fitting models used to interpret the data from dissolution experiments. These factors may obscure the expected relationship between viscosity and diffusivity, leading to the observed variability.

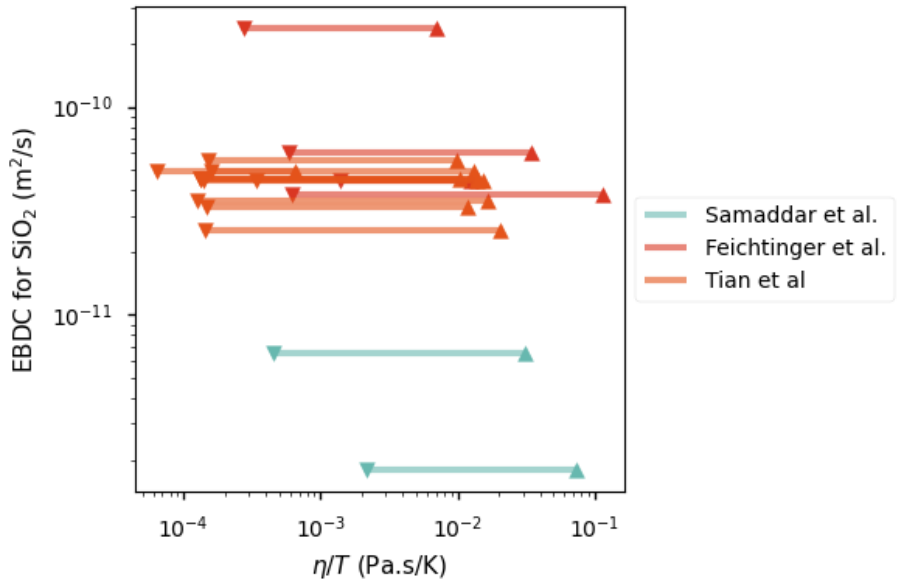

a SiO_2 dissolution data from [12, 33, 41]

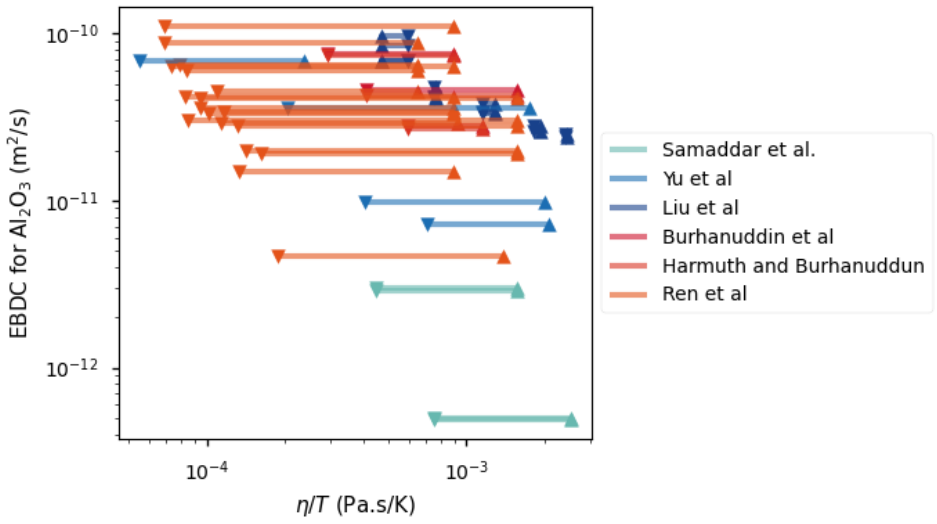

b Al_2O_3 dissolution data from [11, 13, 37, 38, 41, 42]

Figure 1.20 Effective binary diffusion coefficient (EBDC) vs the viscosity to temperature ratio for silica (top) and alumina (bottom) dissolution data in multi-component compositions from the literature. Viscosity was calculated based on the chemical composition of the original melt (marker pointed down), the interface glass (triangle pointing up), and the temperature of dissolution. The interface composition was assumed to be in thermodynamic equilibrium, and it was calculated as detailed earlier in Section 1.3.

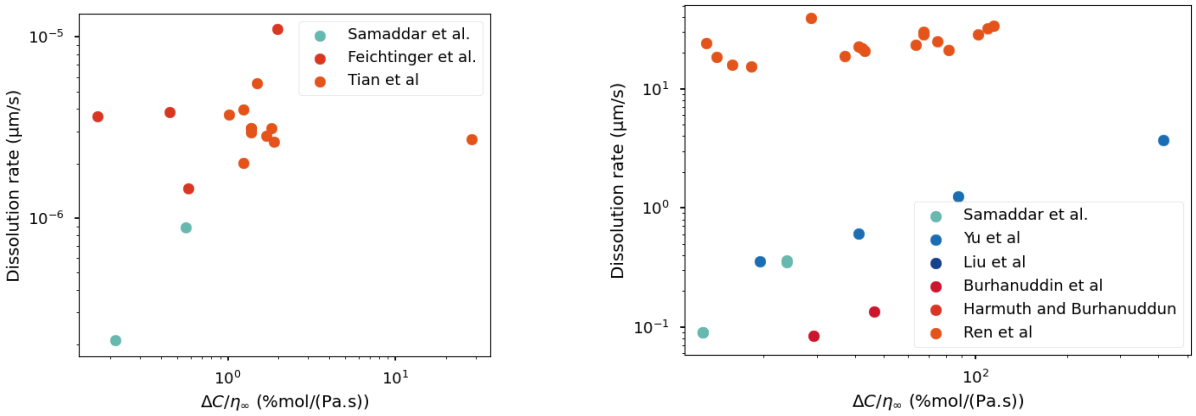

a SiO_2 dissolution data from [12, 33, 41]

b Al_2O_3 dissolution data from [11, 13, 37, 38, 41, 42]

Figure 1.21 Linear dissolution rate in function of the undersaturation normalized by the viscosity of the original composition of the fluid for the available literature data of silica (left) and alumina (right) dissolution in multi-component melts. The undersaturation was calculated as the difference between the solute composition (SiO_2 or Al_2O_3) in the original glass and at the interface. The interface composition was assumed to be in thermodynamic equilibrium, and it was calculated as detailed earlier in Section 1.3.

1.5 Summary

This chapter reviews the current understanding of alumina and silica dissolution mechanisms in silicate melts, both from theoretical models and experimentally collected data. Such an understanding is critical for converting the results of Computational Fluid Dynamics (CFD) simulations, which are widely used to model the industrial glass melting process, into practical predictions such as the minimum residence time of a particle necessary to avoid solid inclusion defects.

It is crucial to translate CFD outputs—such as temperature and velocity fields within the glass melting step—into a quantitative model that accurately predicts material consumption due to dissolution to ensure efficient industrial glass-melting processes. Such a model for industrial glass is still lacking. However it will help determine the minimum residence time of particles in the glass-making furnace, reducing the risk of solid inclusion defects and optimizing production efficiency.

Section 1.2 demonstrated that dissolution in binary systems has been well-characterized by numerical solutions, with mixed contributions from interface reactions, diffusion in the melt, and radial flow due to molar volume changes. Analytical approximations such as the quasi-steady state and flat slab models have been proven useful for mapping the validity range of these solutions. In Section 1.2.3, the effects of advection and free convection within the melt were highlighted as significant factors that enhance the mass transport of solutes away from the interface, accelerating dissolution.

However, even considering intense fluid flow, dissolution models still depend on the undersaturation of the melt (the difference between the melt's original composition and the thermodynamic equilibrium at the solid-melt interface) and diffusion coefficients. Section 1.3 gathered available experimental data on alumina and silica dissolution in silicate melts, revealing that most studies report dissolution dominated by mass transport. Despite the volume of research, significant variability in diffusivity values for both oxides has been observed, likely due to differences in experimental conditions and assumptions used to model the dissolution process. Notably, few studies have directly measured interface compositions, and only a handful [34, 36, 49, 54] have provided experimentally determined values for undersaturation.

Another possible source of discrepancy is the oversimplification of treating multi-component systems as pseudo-binary, which overlooks the complex coupling between multiple species—particularly in the case of silica and alumina motion. As discussed in Section 1.4, a more rigorous treatment of undersaturation and diffusivity in multi-component systems is necessary, though it remains challenging. While some proxies for multi-component diffusion have been suggested, they often come at the expense of fully understanding the underlying physical mechanisms.

Building on the identified gaps, this study seeks to provide a deeper understanding of the dissolution mechanisms of two common oxides—alumina and silica—within the context of industrial soda-lime-silica glass melting. Drawing on insights from previous research in other compositional systems, this study adopts an experimental strategy designed to accurately measure diffusion profiles from the solid-melt interface and to eliminate convection effects that could lead to overestimated mass transport coefficients. This strategy will be detailed in the next chapter.

Chapter 2

Materials and Methods

This chapter outlines the experimental methods used to investigate the dissolution of alumina and quartz in soda-lime silica glass. It details the design of a vertical slab stack setup to ensure one-dimensional static dissolution, avoiding convection and thermal gradients. The chapter describes the preparation of starting materials, the execution of dissolution tests, and the subsequent *ex-situ* characterization techniques, including microstructural , Raman spectroscopy, and compositional observations, electron probe microanalysis (EPMA). These methods aim to provide a comprehensive understanding of the dissolution mechanisms and the factors influencing the process.

Chapter's table of contents

2.1 Strategy of study . . . 44
2.2 Design of experimental setup for static dissolution . . . 45
2.2.1 Semi-infinite dissolution hypothesis . . . 45
2.2.2 Free convection assessment due to thermal gradients . . . 48
2.2.3 Free convection assessment due to elements migration into the melt . . . 48
2.2.4 Criteria and experimental setup geometry . . . 50
2.3 Starting materials . . . 51
2.3.1 Soda-lime silica glass . . . 52
2.3.2 Alumina . . . 52
2.3.3 Quartz . . . 53
2.4 Dissolution tests . . . 54
2.4.1 Samples preparation . . . 54
2.4.2 Heat treatment . . . 54
2.5 *Ex-situ* characterization techniques and data analysis . . . 55
2.5.1 Microstructural observation and convection verification . . . 55
2.5.2 Structural evolution by Raman spectroscopy cartographies . . . 56
2.5.3 Chemical composition profiles by EPMA . . . 59
2.5.4 Thermodynamic simulations . . . 60
2.6 Methods summary . . . 63

2.1 Strategy of study

The strategy of this study revolves around the dissolution of alumina and silica in contact with an industrial soda-lime silica glass. As detailed in Section 1.3, earlier research has employed melt-quenching studies and grain dissolution tests [26, 43, 44], methods that only provide an empirical equation without shedding light on the mechanisms driving the process itself. The aim of this study is to go toward that understanding ; quoted methods can not be used.

Dissolution, as outlined in Chapter 1.2, is a sequence of physical processes (Figure 1.4) : interface reaction and mass transport via diffusion and convection [7, 74–76], and can be described by solving simultaneously Equations 1.3, 1.6 and 1.7, recapped below :

$$\frac{dC_A}{dt} = -k_{\leftarrow}(C_A - C_A^*)$$
$$\frac{K}{C_{A,s}}(C_A(r=a) - C_A^*) = \frac{D}{C_{A,s} - C_A(r=a)}\nabla C_A|_{r=a} \cdot \mathbf{n}$$
$$\frac{\partial C_A}{\partial t} + \mathbf{U} \cdot \nabla C_A = D\nabla^2 C_A$$

where t is time, K is an effective kinetic constant based on the nature of the interface reaction (defined in Section 1.2), C_A the concentration field of the dissolving component A in the glass, C_A^* is the thermodynamic equilibrium composition, $C_A(r=a)$ is its composition at the interface, D is the diffusion coefficient of A in the glass, $\mathbf{n}$ a unit vector normal to the interface, and $\mathbf{U}$ is the Eulerian velocity field in the glass.

While industrial glass melting often involves forced convection, the phenomena observed in the static case are always present, albeit constrained to a smaller boundary layer. This work addresses the static case to isolate the dissolution reaction at the interface and the mass transport of the product by diffusion. It presumes in Equation 1.7 :

$$\mathbf{U} \cdot \nabla C_A = 0 \tag{2.1}$$

This approach allows us to collect experimental data for comparison with physical phenomena and to better understand the phenomena at the grain scale. Notably, a non-scalar approach to both composition undersaturation and diffusivity is likely required to adequately describe the dissolution in soda-lime silica glass, as detailed in Section 1.4.

Therefore, an experimental setup and method were designed to avoid convection and isolate the effects in a static case dissolution, considering the multi-component nature of this system. The following sections of this chapter will detail the methodology employed :

1. **Design of experimental setup for static dissolution** : This section will describe the experimental setup geometry designed to reproduce the assumptions of a one-dimensional static dissolution case in an infinite reservoir.
2. **Starting materials** : Description of the starting materials (soda-lime silica glass, alumina, and quartz), including chemical composition and structural characterization.
3. **Dissolution tests** : Detailed protocol for samples preparation and dissolution tests.
4. ***Ex-situ* characterization techniques and data analysis** : This section will describe the techniques used for characterizing the samples, including electron probe microanalysis (EPMA) for chemical composition, Raman spectroscopy for structural evolution, and microscopy for microstructural observations.

2.2 Design of experimental setup for static dissolution

Previous works highlight the influence of experimental setup and geometry on dissolution measurements [35,37,77], in particular the potential generation of undesired effects like free convection, thermal gradients, and crucible contamination.

Building on prior research [35, 36, 46, 49, 78], experiments in the geoscience literature typically use a high-pressure (1 GPa) vertical slab stack assembly to measure one-dimensional dissolution between solute and solvent. The materials are arranged as cylindrical slabs stacked vertically (Figure 2.1), providing a direct interface perpendicular to the dissolution direction. To mitigate gravitational instabilities, materials are organized by density, with the less dense material placed above the denser one.

Potential contamination from consumable alumina or silica crucibles is avoided by opting for a platinum container.

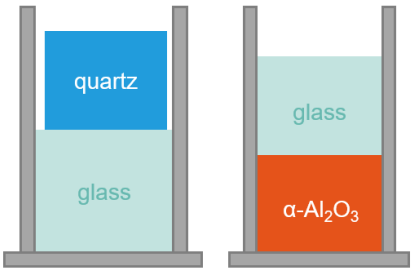

Figure 2.1 Vertical slab stack schematic geometry. The materials are stacked vertically according to their density and enveloped by a platinum container.

The configuration and timing of the dissolution tests are chosen based on several key considerations :

1. Ensure the validity of the assumption of an infinite solvent reservoir, implying that the far-field composition remains the same as the initial one throughout the experiment ;
2. Avoid free convection due to thermal gradients ;
3. Avoid the phenomenon of double-diffusive convection, which can occur when density inversions are generated by diffusion.

The upcoming sections delve into the specifics of each of these key considerations and how they affect the choice of setup geometry and experimental duration for the successful measurement of dissolution tests.

2.2.1 Semi-infinite dissolution hypothesis

To conform to the semi-infinite medium hypothesis, the glass composition at the extremity should match the original composition at the end of the dissolution tests. If this is not that case, we face a situation where the medium begins to saturate, which no longer reflects the scenario of a small particle surrounded by a large volume of glass melt.

To calculate the minimum height of the glass slab, determination of the theoretical glass composition at its extremity considering a finite reservoir of length L is needed. Next, the conditions under which the composition at the far-field in the confined case starts deviating from the original composition are determined.

Applying Fick's second law (Equation 1.22) for a confined reservoir of length L, the boundary condition at $x = L$ is that there is no flux of matter, $\nabla C_{x=L} = 0, \forall t$. In this case, an analytical solution is unavailable and it needs to be numerically solved. Using a Fourier series solution, the concentration of element i at distance x at time t can be determined by :

$$C_i(x,t) = (C_{i,x=0} - C_{i,t=0}) \left(1 - \sum_{\alpha_k=\pi/2}^{\infty} \frac{2}{\alpha_k} \sin\left(\frac{\alpha_k x}{L}\right) \exp\left(-\frac{D_i t \alpha_k^2}{L^2}\right) \right) + C_{i,t=0} \tag{2.2}$$

Here, the eigenvalue $\alpha_k = (k + 1/2)\pi$. For the current calculations, $k = 200$ ensured good convergence and was used for the following results.

Assuming that dissolution is controlled by diffusion, the glass at the interface is already in thermodynamic equilibrium : $C_{x=0} = C_{\text{eq}}$. The glass composition in equilibrium with pure silica and alumina at 1400 and 1450 °C was calculated using thermodynamic calculations based on the minimization of the system's free energy. FactSage (version 8.0) Equilib module was used for this purpose. Details concerning the thermodynamic calculations for alumina and quartz dissolution are provided in Chapters 3 and 4, respectively.

The diffusivities D_i were taken from the diffusion matrices of Jacquemin [64] for a melt containing 15%mol Al_2O_3 for estimating alumina dissolution and a 3%mol Al_2O_3 containing glass for estimating quartz dissolution. As the matrices were obtained at different temperatures, the eigenvalues were adjusted to 1400 °C using activation energies from a 7%mol Al_2O_3 containing glass diffusion matrix [63]. It is assumed that the exchange reactions are similar in this temperature range.

The previous equation for each oxide profile was calculated for each linearized composition along the eigenvectors basis defined by the matrices (Equation 1.45). Then, the inverse operation was performed to recover the profiles in terms of regular oxides.

Despite the chemical gradient imposed by the dissolution being in terms of alumina and silica, other components will also diffuse due to the cooperative movement in the glass network. Therefore, all oxide theoretical profiles had to be calculated. It is known that alkalis and earth-alkali are more mobile than alumina and silica, and more likely to reach the glass extremity first.

Applying the same methodology for different lengths and time durations at 1400 and 1450 °C allows to determine the minimum length of the glass slab. The difference between the compositions at several slab heights (L) and the original glass ($\Delta C_{x=L} = C_{x=L,\text{confined}} - C_{t=0}$) were plotted for different lengths and durations in Figure 2.2. The threshold for deviation from the semi-infinite hypothesis was $\pm$ 0.5%mol, close to the chemical resolution of EPMA measurements (further details in Section 2.5.3).

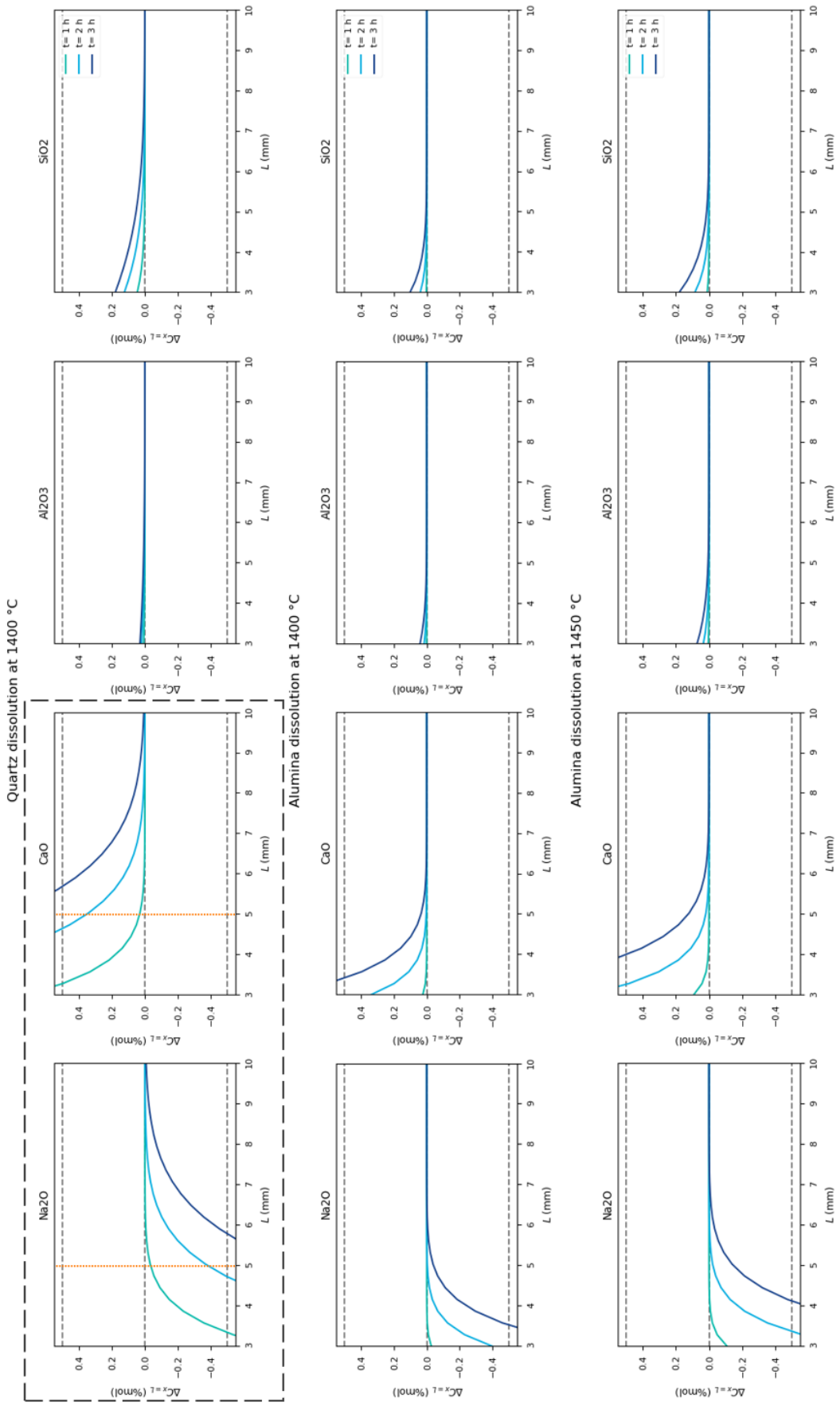

Figure 2.2 Calculated difference of the glass composition at its extremity for the confined case against the original composition with the total length of the reservoir for three different durations of heat treatment at 1400 and 1450 °C. The dashed gray lines at ±0.5%mol refers to the chemical resolution of EPMA.

As expected, sodium and calcium oxide saturate the glass first. Additionally, quartz dissolution saturates the glass faster than alumina, even at 1450 °C. By limiting the dissolution tests to 2 hours, the chosen minimum height for the glass samples should be higher than 5 mm.

2.2.2 Free convection assessment due to thermal gradients

The furnace's lateral heating elements will heat the assembly, potentially creating non-uniform temperature distributions within the molten glass. This can result in significant thermal gradients along the radial axis, which are a primary source of Marangoni-Bénard instabilities. These instabilities occur due to surface tension gradients induced by temperature differences on the molten glass surface. Regions with higher temperatures typically have lower surface tension, causing fluid to flow from hotter to cooler areas and creating convective currents [24].

The Marangoni number (Ma), a dimensionless number, quantifies the relative importance of surface tension forces to viscous forces. It is defined as :

$$\mathrm{Ma} = \frac{|\gamma_T|\Delta T L}{\nu\alpha} \tag{2.3}$$

Here, γ_T is the variation coefficient of surface tension with temperature, ΔT is the temperature gradient, L is the typical length, ν is the kinematic viscosity of the glass, and α is the thermal diffusivity of the glass.

In a typical case with no-slip lateral walls and a flat, non-deformable free surface, the onset of this instability occurs at $\mathrm{Ma}_c \approx 80$ [79, 80]. Hence, the critical height can be defined by :

$$L_c = \frac{80 \cdot \eta\alpha}{|\gamma_T|\Delta T} \tag{2.4}$$

The property values used to estimate the critical height for a soda-lime silica molten glass at 1400 °C were :

- $\eta = 14.12$ Pa.s, measured by Saint-Gobain Research Paris at 1398 °C ;
- $\alpha = 3.5 \times 10^{-7} \mathrm{m}^2/s$, measured for a soda-lime silica glass at 1380 °C [81] ;
- $\gamma_T = -8 \times 10^{-6}$ J/(m^2°C), measured for a 19.5%mol Na_2O binary silicate glass between 900 to 1400 °C [82]

For the extreme $\Delta T = 1400$ °C, the maximum length is 49 mm, which is significantly larger than the 5 mm maximum previously considered for the glass cylindrical slabs.

Though rough, this estimate takes into account potential thermal gradients in the molten glass slab, indicating that thermal gradients may not significantly contribute to convection in the proposed experimental setup. Evidently, adding an alumina or quartz tablet to the system could introduce further instabilities. This is because the inclusion of these oxides alters the properties of the melt near the interface, such as thermal diffusivity, surface tension, and density. These issues will be further addressed in the following subsection.

2.2.3 Free convection assessment due to elements migration into the melt

As alumina or dissolved silica begins to migrate from the solid-liquid interface into the molten glass, changes occur in the chemical composition and subsequently in density. If dissolution is diffusion-controlled, the composition and hence densities will not be homogeneous along the distance from the interface.

The incorporation of solute in the glass also affects the composition of other components in the solvent due to the coupled nature of diffusion. Moreover, the exchange rates of these species are unequal, resulting in varied gradients affecting the fluid's density. This is akin to the double-diffusive convection observed in seawater [83]. The interaction between these gradients may create complex convective patterns with regions of differing density, driven by the fastest diffusion of one component over the other.

An effective Rayleigh number, inspired by Equation 1.36, can compare the buoyancy forces due to density gradients created by the diffusion profile in the melt with the viscous flow, where viscosity will also vary with the composition. Using the same interface composition and matrices used for the semi-infinite assessment, the theoretical diffusion profiles ($N = 500$ points) were calculated assuming an infinite melt reservoir. Then, both viscosity (η) and density (ρ) at 1400 °C for each composition in the profile were predicted using the GlassPy's module predict with the GlassNet model, adapted for silicate and aluminosilicate glasses [73]. The variation of the kinematic viscosity ($\nu = \eta/\rho$) along the distance normalized by the square root of time for the dissolution cases of quartz and alumina are shown in Figure 2.3.

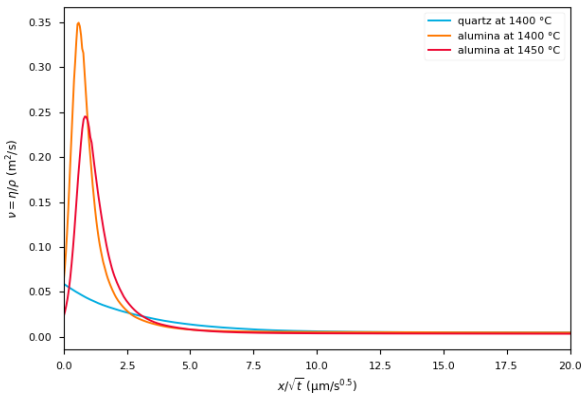

Figure 2.3 Calculated kinematic viscosity evolution from theoretical composition profiles assuming a diffusive-dissolution for quartz and alumina in contact with the soda-lime silica glass. The maximum calculated close to alumina interface can be a source of instabilities given the discontinuity on density.

Due to the coupled nature of diffusion, the kinematic viscosity for alumina dissolution does not follow a progressive behaviour throughout the melt, potentially inducing discontinuities and initiating instabilities in the dissolution front.

Liang [65, 84] studied initially gravitationally stable diffusion couples and proposed an effective Rayleigh number to predict the onset of these fingering instabilities in a multicomponent fluid with an axisymmetric geometry, such as the vertical slab stack setup. For each exchange direction, a relationship of this type can be defined :

$$\mathrm{Ra}_i = \frac{g d^3}{\lambda_i} \beta_i \Delta U_i \tag{2.5}$$

where g is the acceleration due to gravity, d is the characteristic length, λ_i is the eigenvalue of the ith exchange reaction, ΔU_i is the difference between the linearized compositions along the ith eigenvector for the two extremities defined by d, and β_i is the variation of the ratio ρ/η with respect to U_i. For a diffusive dissolution scenario, the characteristic length can be approximated by the characteristic diffusion length $2\sqrt{\lambda_i t}$, where t is time.

Thus, Equation 2.5 becomes :

$$\mathrm{Ra}_i = 8gt^{3/2}\lambda_i^{1/2}\beta_i\Delta U_i \tag{2.6}$$

Considering all exchange reactions, it is possible to obtain the effective Rayleigh number for the convection induced by coupled diffusion, described by a 3×3 diffusion matrix :

$$\mathrm{Ra}_e = 8gt^{3/2}\begin{bmatrix}\beta_1\\ \beta_2\\ \beta_3\end{bmatrix}^T\begin{bmatrix}\lambda_1^{1/2} & 0 & 0\\ 0 & \lambda_2^{1/2} & 0\\ 0 & 0 & \lambda_3^{1/2}\end{bmatrix}\begin{bmatrix}\Delta U_1\\ \Delta U_2\\ \Delta U_3\end{bmatrix} \tag{2.7}$$

The critical effective Rayleigh number for the onset of convection in a cylindrical container increases as the system's aspect ratio decreases, i.e., the cylinder radius, r_0, divided by the diffusion length $d \sim 2\sqrt{\lambda_1 t}$ [84]. The assymptotic value for short times or $r_0/d \to \infty$ is $(27/4)\pi^4$. Therefore, while the time duration influences both effective and critical values, decreasing the radius of the setup only affects the critical value. The resolution for $\mathrm{Ra}_c = f(r_0/d)$ was extracted from Figure 2 of Liang's work [84].

By performing calculations using the previously theoretical diffusion profiles for quartz and alumina dissolution at 1400 and 1450 °C until 3 hours, the curves for Ra_e and Ra_c are obtained and displayed in Figure 2.4, with radii varying between 4 to 6 mm.

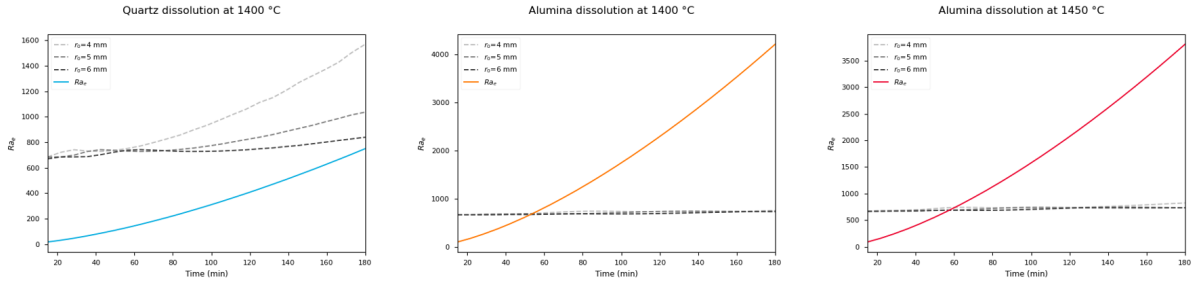

Figure 2.4 Effective Rayleigh for quartz (left) and alumina dissolution in soda-lime silica glass at 1400 (middle) and 1450 °C (right). Dashed gray curves represent the critical value for the onset of natural convection for different values of cylinder radii (r_0).

While quartz dissolution is not expected to surpass any of the critical values for durations less than 3 hours, alumina dissolution is more prone to instabilities for t longer than 1 hour at both temperatures. This could be expected from the kinematic viscosity behaviour from Figure 2.3. Moreover, it is worth noting that the critical values (dashed gray curves in Figure 2.4) are almost the same for the chosen diameters, and have little influence on the onset of instabilities during alumina dissolution. Limiting the time duration of the dissolution tests is more crucial than the geometry to avoid free convection due to density gradients for the above cases.

By extrapolating quartz dissolution at 1400 °C for extended periods, the effective Rayleigh number is estimated to cross the critical value at around 200 minutes for an initial radius of 6 mm and at around 325 minutes for an initial radius of 5 mm. Therefore, slabs with a diameter ($2r_0$) of 8 mm were selected to extend the time-span of stability.

2.2.4 Criteria and experimental setup geometry

To ensure the validity of the semi-infinite dissolution case in a static environment, several criteria were established and summarized by the Figure 2.5.

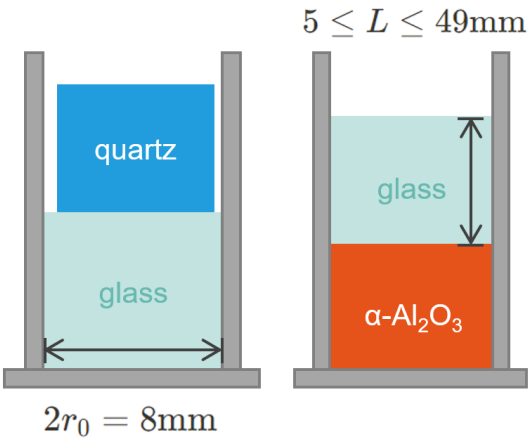

Figure 2.5 Geometry criteria for the cylinder piston experimental setup based on the criteria to avoid saturation and natural convection.

— The minimum height for the glass slab was set at 5 mm for quartz dissolution tests lasting up to 2 hours. For alumina dissolution at 1400 and 1450 °C, this assumption holds true for tests longer than 3 hours ;
— To mitigate the effects of convection caused by potential thermal gradients, the maximum height for the glass slab was limited to 49 mm ;
— The diameter of the slabs was fixed at 8 mm to prevent convection due to density gradients. However, the primary criterion to avoid these disruptions was to limit the duration of alumina dissolution tests to less than 1 hour.

In addition, it was planned to utilize polished surface slabs to mitigate air entrapment caused by surface roughness.

Although these measures were taken to anticipate possible disruptions to the initial hypothesis, the list of potential sources of perturbations is not exhaustive. For instance, the effect of the solute on Marangoni-Bénard convection [85] was not considered. Therefore, the potential presence of convection was examined for all the samples using Scanning Electron Microscopy and Energy Dispersive X-ray Spectroscopy (SEM-EDS), as well as Raman spectroscopy cartographies. Further details about these methods can be found in Section 2.5.

2.3 Starting materials

In the vertical slab stack setup, the solid and melt phases are loaded as slabs with polished surfaces, approximating one-dimensional dissolution. For this study, industrial soda-lime silica glass is used as the solvent, representing the molten glass bath in an industrial furnace. This glass is used to study the dissolution of two solid phases, alumina and quartz, the most common refractory phases present in typical glass melting furnaces, either as contaminants, corrosion products, or raw materials. This study investigates how the dissolution of each of these important solid phases occurs, offering the possibility to compare their behavior and provide constraints for quantitative modeling.

This section will detail the preparation and properties of the starting materials.

2.3.1 Soda-lime silica glass

The glass source used is an industrial float glass sheet produced in the first quarter of 2021. Approximately 1 kg of this starting material was crushed and remelted in a platinum crucible within an oxygen-gas flame furnace at a temperature of 1450 °C for a duration of 6 hours. This process was undertaken to ensure the homogeneity of the glass and to shape it into blocks with dimensions of 100 × 100 × 30 mm. These samples were then annealed at a temperature of 560 °C for one hour, followed by gradual cooling to avoid stresses induced by quenching.

The composition of the resultant glass was determined using 24 electroprobe microanalysis (EPMA) measurements, with the average and standard deviation presented in Table 2.1. Further details of the EPMA protocol are provided in Section 2.5.3.

Na_2O	K_2O	CaO	MgO	Al_2O_3	SiO_2
13.4 ± 0.1	0.02 ± 0.01 *	10.7 ± 0.1	2.9 ± 0.1	0.35 ± 0.02 *	71.9 ± 0.2

Table 2.1 Chemical composition of the initial soda-lime silica glass in molar fraction, based on 24 EPMA points measured along the thickness of the glass block. (*) symbol indicates values that are under the EPMA chemical resolution.

2.3.2 Alumina

The source of alumina used was a 75 × 50 × 4 mm sintered 99.4 ± 0.5% wt alumina plate provide by Umicore. Its composition was determined from 22 EPMA measurements across the plate, using a sapphire reference (additional details can be found in Section 2.5.3), as presented in Table 2.2.

Na_2O	K_2O	CaO	MgO	Al_2O_3	SiO_2
0.09 ± 0.2 *	0.01 ± 0.01 *	0.07 ± 0.08 *	0.6 ± 0.9	98.6 ± 1.1	0.4 ± 0.3 *

Table 2.2 Chemical composition of the initial alumina in molar fraction, based on 22 EPMA points measured along the thickness of the plate. (*) symbol indicates values that are under the EPMA chemical resolution.

The primary phase is α-Al_2O_3 , characterised by Raman spectroscopy and X-Ray Diffraction (Figure A.1), and compared with literature spectra for corundum [86] as well as with a sapphire sample (Figure 2.6). Further details on the spectroscopy measurements are provided in Section 2.5.2.

An initial test was conducted using a synthetic monocrystal of sapphire rather than the polycrystalline alumina in the dissolution tests with glass at 1400 °C. This test is detailed in Section 3.1 of the paper in Chapter 3 and was designed to check if there is an influence of crystallinity on dissolution behavior. No discernible differences were observed in the diffusion chemical profiles in the glass close to the dissolution interface, leading to the conclusion that subsequent tests could be exclusively conducted on the sintered alumina slab.

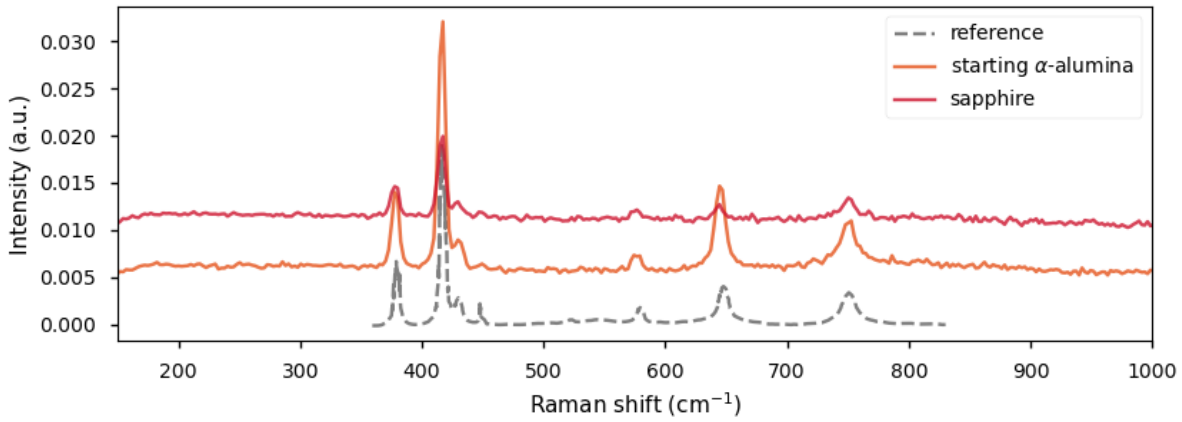

Figure 2.6 Raman spectra for the slab in sintered alumina (in orange), recovered piece of sapphire (in red) and the reference spectra for α-Al_2O_3 (in dashed gray line) from [86]. The spectra intensities were shifted to better visualization.

2.3.3 Quartz

The silica source employed are prefabricated Roditi slabs with a diameter of 8 mm a height of 4 mm, and a surface roughness less than $Ra < 1$ nm. The z-axis of the hexagonal α-quartz crystal structure aligns with the cylinder axis, parallel to the height and perpendicular to the slab surfaces. Raman spectroscopy and X-Ray Diffraction (Figure A.2) confirmed the primary component to be quartz, as shown by comparison with spectra reported in the literature [87] for α-quartz in Figure 2.7.

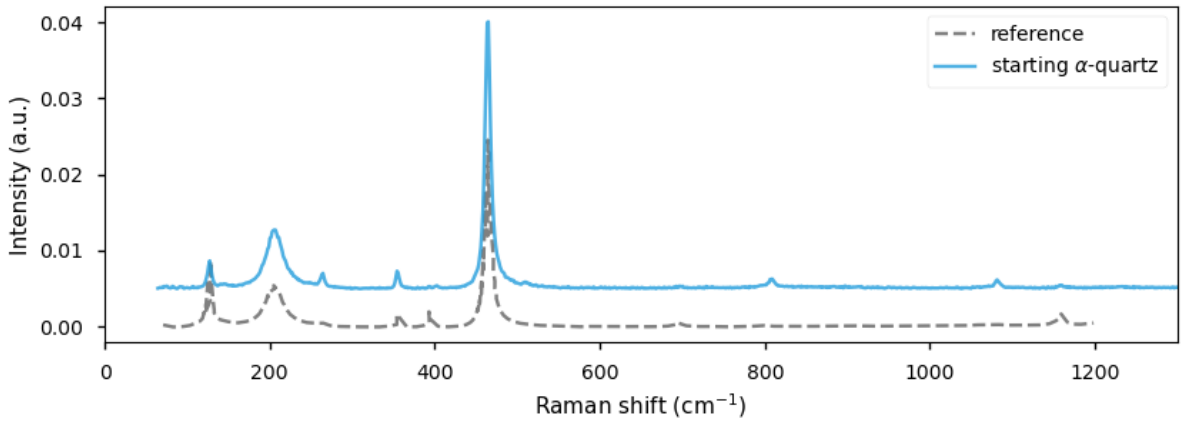

Figure 2.7 Raman spectra for the quartz slab used (in light blue) and the reference spectra for α-SiO_2 (in dashed gray line) from [87]. The spectra intensities were shifted to better visualisation.

The composition of the starting material was checked by conducting 100 points of EPMA along the cylinder height, using an amorphous silica sample as a reference. The results in Table 2.3 confirm that other elements present are at the level of impurity, less than 0.03% mol, which falls below the EPMA chemical resolution.

Table 2.3 Chemical composition of the quartz slab (in %mol) by Electron Probe Microanalysis and semi-quantitative X-Ray Fluorescence analysis. The values with (*) are below the chemical resolution of EPMA.

	EPMA	**XRF**
SiO_2	100.8 ± 0.2	97.4
Al_2O_3	0.00 ± 0.01 *	0.3
Na_2O	0.007 ± 0.008*	1.2
K_2O	0.003 ± 0.004*	0.
CaO	0.007 ± 0.008*	0.7
MgO	0.01 ± 0.02*	0.13

Additional silica sources, introduced to assess different silica polymorphs, were also employed in this study. Further details regarding these additional sources will be discussed in Chapter 4.2.2.

2.4 Dissolution tests

2.4.1 Samples preparation

While quartz slabs were already at the appropriate dimension, alumina plates and glass blocks required preparation to achieve the desired geometry for the cylindrical slabs.

Cylinders with a diameter of 8 mm were obtained from the glass blocks and alumina plates through core drilling. Owing to the differing hardness of alumina and glass, specific diamond drill bits were employed. Considering the 30 mm thickness of the glass blocks, the cylinders acquired from core drilling were subsequently cut into shorter disks using a precision cutting machine. The faces of both alumina and glass slabs were ground to ensure parallel surfaces and uniform height. All cutting operations were performed with water as a cooling agent and lubricant.

An optical quality surface was achieved by polishing one surface of each disk sequentially using 6 µm and 1 µm diamond paste. Following polishing, the initial height of the disks was measured using a digital caliper and then underwent thorough cleaning to remove residual diamond paste and debris. This was accomplished by ultrasonic cleaning in acetone for a duration of 15 minutes and drying.

The prepared disks were stacked according to the materials density ratio and enclosed within a platinum-gold foil, as illustrated by Figure 2.8 *a* and *b*. Platinum foil served as an inert crucible and a bottom plug, preventing potential leakages of the molten glass into the furnace during the heat treatments. The initial mass of the setup was measured before the heat treatments using a precision balance.

2.4.2 Heat treatment

The heat treatment process was conducted using a Nabertherm high-temperature furnace equipped with thermocouple measurements to monitor and control the temperature. An electric furnace capable of reaching temperatures up to 1600°C was used. The temperature inside the furnace was monitored using a type S thermocouple (Pt-PtRh10%) placed in close proximity to the samples to ensure accurate temperature readings. The furnace was preheated to the target

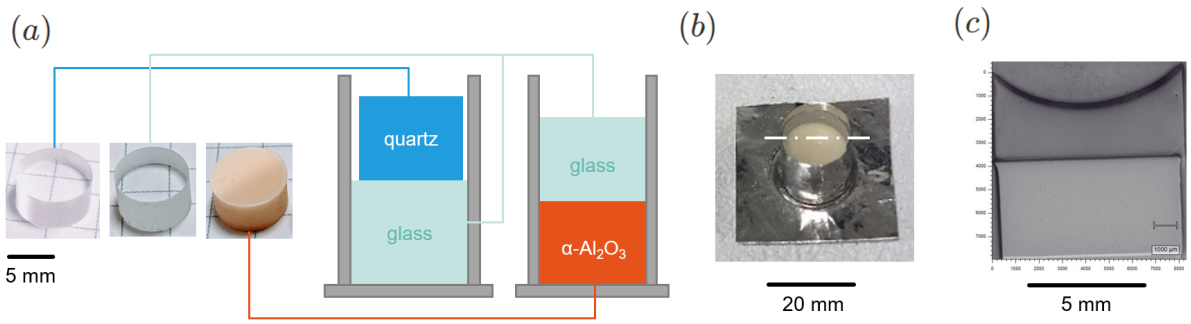

Figure 2.8 (a) Illustration of the experimental setup and photos of the cylindrical slabs used. (b) Photo of the actual setup prior to an alumina dissolution test ; the dot-dash line represents the perpendicular cut to recover the section to be characterized. (c) Micrograph of a polished cross section of an alumina sample after dissolution test.

temperature, and the samples were introduced into the hot zone. Stabilization ($\pm$ 3°C) was achieved within about 1 minute. Isothermal treatments ranging from 10 minutes to 24 hours were carried out for the temperature range between 1300 to 1450°C for alumina dissolution and at 1400°C for quartz tests. The detailed conditions of the heat treatments for each case are compiled in Chapters 3 and 4, respectively. Experimental duration was measured as the time following that at which the thermocouple indicated the desired temperature (the time required to reach nominal temperature was typically 1 minute).

Quenching was performed in air by extracting the sample from the furnace, corresponding to an approximate rate of 630°C per second, for temperatures above the glass transition. Once cooled, the final mass of the assembly was measured to check for eventual significant mass loss ($>$ 0.5%wt), and then the samples were carefully removed from the platinum-gold foil. The samples were then embedded in epoxy under vacuum conditions to avoid air entrapment, especially close to the interface. Sections perpendicular to the interface were obtained by precision cutting of these embedded samples and then polished using both 6 and 1 µm diamond paste for microscopic analysis and further characterization. Figure 2.8 summarizes the described steps for samples preparation before (a and b) and after (c) heat treatment.

2.5 *Ex-situ* characterization techniques and data analysis

2.5.1 Microstructural observation and convection verification

The microscopy observations were conducted to assess the microstructural integrity and chemical contrast of the polished cross sections. The initial step involved a qualitative evaluation using both an optical microscope and a binocular. The binocular allowed for capturing a comprehensive image of the entire sample, which facilitated the estimation of slab lengths after dissolution. This was achieved using magnification objectives of 0.75×, 1×, and 2×, although it is noted that this method offers limited spatial resolution.

Further inspection was carried out using an optical microscope configured to bright-field mode in reflection. Magnifications ranged from 5× to 50×, allowing examination of the surface for potential interface irregularities, bubbles, or intermediate phases. These features are critical as they could potentially influence the measurements of EPMA chemical profiles. If present,

observed microstructural features were documented.

To complement the optical microscopy and enhance the analysis in terms of spatial and chemical resolution, the polished sections were also subjected to observation under a Quanta FEG Scanning Electron Microscope (SEM) equipped with Energy Dispersive X-ray Spectroscopy (EDS/EDX). Sample preparation for SEM involved mounting the sections on aluminum stubs using double-sided carbon tape. Connectivity between the tape's base and the section's top surface was ensured by a brush of silver ink. A sputter coater was then employed to apply a 10-15 nm carbon layer, which served to mitigate charging effects during SEM observations.

The SEM was operated with an acceleration voltage set at 15 kV and a working distance maintained around 10 mm, utilizing the High Vacuum mode (between 9.10^{-5} to 5.10^{-7} mbar). The Backscattered Electron (BSE) detector was employed to obtain images that provided chemical contrast, which was particularly useful for checking for convection within the samples. Additionally, Secondary Electron (SE) imaging was performed in the same regions to discern whether variations in gray hues were attributable to chemical differences or to topographical features such as shadows and bubbles.

A systematic approach was adopted for imaging, beginning with a low-magnification focused image that served as a baseline reference. Magnification was incrementally increased to closely examine features of interest, such as secondary phases, with subsequent refocusing and astigmatism correction. Optimal contrast and brightness settings were adjusted to ensure clarity.

Chemical composition and element distribution within the samples were analyzed through EDS/EDX. This included generating elemental maps to visualize the spatial distribution of elements, particularly to confirm or refute the presence of natural convection following dissolution. Point EDS/EDX spectra were also acquired for secondary phases to provide insights into their chemical constitution.

The positions of heterogeneities were meticulously recorded to identify regions that conformed to the hypothesis of a perpendicular dissolution front. This was particularly important to avoid areas proximal to the sample corners, where the hypothesis was less likely to be valid.

2.5.2 Structural evolution by Raman spectroscopy cartographies

Raman spectroscopy is a powerful analytical technique based on the inelastic scattering of monochromatic light, known as Raman scattering. When light interacts with a molecule, most photons are elastically scattered (Rayleigh scattering), but a small fraction undergoes inelastic scattering, resulting in a shift in energy corresponding to the vibrational modes of the molecule. This shift provides a molecular fingerprint that can be used for material identification and characterization [88]. The Raman effect is particularly sensitive to changes in molecular vibrations, making it an excellent tool for studying chemical bonds, phase transitions, and molecular interactions [89].

The non-destructive nature, high chemical specificity, and ability to analyze samples in various states without extensive sample preparation make Raman spectroscopy a versatile technique. It proves particularly effective for studying structural modifications in both amorphous and crystalline phases, making it an apt characterization technique for studying dissolution between glass and crystals, such as alumina and quartz. In the case of oxide glasses, Raman spectroscopy can recognize the vibrational modes of the Si-O network, which are sensitive to the type and concentration of present cations. This sensitivity allows for the identification of structural changes like network depolymerization or the formation of new silicate species. For crystalline phases, Raman

Mode	**Alumina dissolution**	**Silica dissolution**
Ponctual	405 nm laser 1 second	532 nm laser 3-4 seconds
Cartography (using Renishaw's MapHR mode)	405 nm laser 1 second for each point LiveTrack on 1 to 10 µm step size for near the interface regions	532 nm laser 3-4 seconds for each point LiveTrack on 0.5 to 10 µm step size for near the interface regions 25 µm step size for larger cartographies

Table 2.4 Experimental parameters for Raman spectra acquisitions in ponctual and cartography modes, according to the dissolution test.

spectroscopy can detect shifts in peak positions and changes in peak intensities, indicative of alterations in the crystal structure or the emergence of new crystalline phases [90, 91].

In this study, a Ranishaw Invia Qontor Raman spectrometer equipped with 532 nm (green) and 405 nm (blue) lasers was used to investigate the structural alterations in soda-lime silica glasses due to the incorporation of silica and alumina after the dissolution tests. The blue laser was employed to evaluate alumina dissolution samples due to spectra saturation using the 532 nm laser source. The spectrometer was configured with an 1800 tr/mm grating and a 1024 pixels charge-coupled detector (CCD) to capture the Raman spectra with spectral resolution 1.2 cm^{-1} for the acquisition with 532 nm laser and 2.4 cm^{-1} with 405 nm laser.

Raman mapping or cartography, employed to obtain spatially resolved chemical information across the glass samples, involves scanning the sample in a grid pattern to collect spectra from multiple points. The output is a spectral hypercube, i.e. a 3D dataset with two spatial dimensions and one spectral dimension. The spectrometer used in this study is coupled with a Leica DM 2500 microscope and a motorized stage in (x, y, z) dimensions with a spatial resolution of 0.1 µm, which allows focus of the laser on the sample surface through the 100× objective. During spatially resolved cartography measurements, Renishaw's LiveTrack system [(1)] was used to correct for focus fluctuations due to topographic variations in the sample. A compilation of the parameters used for silica and alumina dissolution samples which give a probed volume around 1 $µm^3$ is provided in Table 2.4.

Preprocessing of Raman spectra

Despite the array of advantages associated with the technique, there are limitations to consider. These include fluorescence interference, which can obscure Raman signals, and the relatively weak intensity of Raman scattering, which may necessitate extended acquisition times or enhanced techniques. Preprocessing of spectra is often necessary to reduce noise, remove background signals, and normalize spectra, thereby facilitating comparison between different datasets [92].

The initial step necessitates the removal of cosmic rays, which are spurious, intense peaks caused by high-energy particles. This is achieved using Ranishaw Wire 5.3 software, which identifies

[(1)] LiveTrack system adjust the z height of the motorized stage to keep the laser spot diameter constant. For further information, the reader is referred to Renishaw website : https://www.renishaw.com/en/livetrack--38126

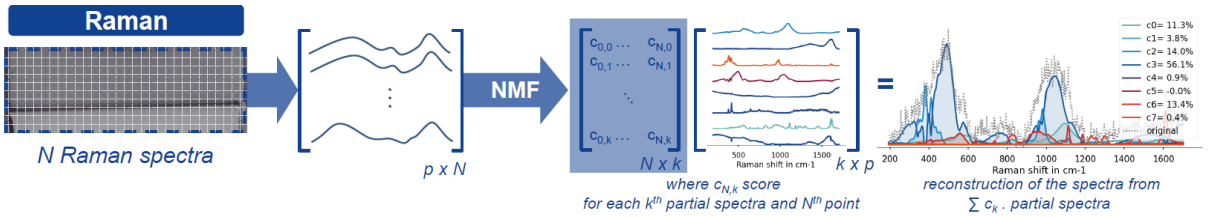

Figure 2.9 Raman map processing and NMF analysis : (from left to right) starting from a Raman map containing N spectra with p values for Raman shifts, the PCA reduced spectra are decomposed on k non-negative components, each one associated with a set of weights c_k that contains N elements for each point of the Raman map. The spectra can then be reconstructed from the linear combination of the p partial spectra.

these outliers based on a nearest neighbor algorithm and the characteristic width of the peaks. Following the removal of cosmic rays, the subsequently described steps are performed using an internally developed Python code, dedicated to spectra treatment [(2)].

Subsequently, baseline correction is carried out using a polynomial fitting to eliminate background fluorescence or baseline drift, which can obscure the true Raman peaks. Normalization of the spectra intensity by its complete surface area is also crucial to account for variations in signal intensity due to differences in laser power or sample thickness. Single-point spectra are treated until this step.

Particularly when dealing with large datasets, such as Raman cartographies that can contain up to 10,000 spectra, reducing the dimensionality of the data is crucial. Principal Component Analysis (PCA) is used in these cases to identify the main sources of variance in the spectra. PCA assists in noise reduction and ensures that the essential features of the Raman spectra are preserved [93]. Typically, the number of components in PCA is set to be greater than 10 to avoid distorting or losing important Raman peaks and bands.

Non-Negative Matrix Factorization (NMF) treatment for Raman maps

Raman spectra of glasses, where the Raman spectra are broad and overlapping due to its amorphous nature, are difficult to resolve using traditional methods. Non-Negative Matrix Factorization (NMF) can decompose complex spectral data into into a set of non-negative components without requiring prior knowledge of the sample's structure [94,95]. Alongside these partial Raman spectra (PRS), NMF provides a set of weights for each spatial point in the Raman map, indicating the contribution of each component at each location. The sum of all PRS' weights for each point is equal to one. The used strategy is illustrated in Figure 2.9. NMF treatment was applied on the PCA treated Raman maps, using the same in-house Python code used for spectra preprocessing.

The weights of the components obtained from NMF can be used for quantitative analysis, allowing for better comparison with other analytical techniques like Electron Probe Micro-Analyzer (EPMA) chemical composition profiles [95].

Plotting the weights of the components in heat maps can help identify the distribution of different components simultaneously. This feature is particularly useful for detecting convection

[(2)] The scripts used in this work were adapted from the set of Python codes available at https://github.com/svi-lab/deconvolution-raman

perturbations in quartz dissolution samples, where the chemical contrast between the original glass and a silica-enriched glass is not high enough to be detected by techniques like Energy Dispersive X-ray Spectroscopy (EDS) mapping. Raman spectroscopy, with its capability to detect vibrational mode fingerprints, proves to be a superior method in such cases. Further details about the specific uses of NMF in quartz dissolution will be described in Section 4.2.4.

2.5.3 Chemical composition profiles by EPMA

Electron Probe Microanalysis (EPMA) is a powerful microanalytical technique that utilizes a focused electron beam to stimulate the emission of characteristic X-rays from a sample, allowing for precise elemental analysis at the micrometer scale. Developed in the 1950s by Raimond Castaing, EPMA has since become an important tool in materials science and engineering for its ability to provide both qualitative and quantitative compositional data with high spatial resolution. The technique employs wavelength-dispersive spectrometers (WDS) to measure the emitted X-rays, enabling the detection of elements from beryllium (Be) to uranium (U) with sensitivities as high as 1-100 parts per million (ppm) and accuracies of 1-2% for elements present at concentrations above 10 weight percent [96].

WDS provides an order of magnitude better spectral resolution (approximately 2-10 eV) compared to EDS (approximately 120-130 eV), allowing for the precise separation of overlapping peaks and more accurate identification of elements. This higher resolution is crucial for detecting trace elements and resolving closely spaced X-ray lines, which EDS often struggle with due to its broader peaks and potential peak overlaps. Additionally, EPMA's WDS achieves lower detection limits, compared to the EDS, making EPMA more suitable for quantitative analysis [96,97].

In this study, chemical profiles were acquired using a Cameca SXFive electron probe (EPMA). The samples, which had already undergone SEM-EDS/EDX observations (Section 2.5.1), were already carbon-coated to prevent charging. They were mounted in a sample holder designed for six samples, ensuring that all surfaces were aligned in the same plane. The analysis was carried out using a 15 kV accelerating voltage, 10 nA beam current, and 10 s counting times for both peaks and background for all the elements, except for Si, which required 20 seconds. Peak and intensity standardizations were achieved by referencing against soda-lime silica glass of identical composition for elements Si, Na, Ca, Mg, Al, and K, as well as against sapphire for Al, and against amorphous silica for Si. The reference materials were measured and calibrated on the same day as each measurement. The use of sapphire and amorphous silica was necessary to better measure the quartz and alumina tablets, as well as the silica or alumina-enriched glass close to the dissolution interface.

Initially, three line scans with a 9 µm step size were executed perpendicular to the interface, maintaining a separation of 60 µm between profiles. They were positioned in a convection-free central region of the sample and regions free of cracks. Additionally, another profile, characterized by a step size of 50 µm, is acquired, covering the last point of the smaller step until the entire length of the glass to monitor potential far-field compositional shifts.

A probe area of 40 × 2 µm was chosen to prevent sodium migration, while ensuring points were spaced by at least 9 µm to mitigate the same concern. Detailed measurements of distances and potential misalignments between the initial measured point's footprint center in the glass and the alumina-glass interface were conducted using SEM in secondary electron mode (details about experimental parameters on Section 2.5.1). This enabled the correction of the distance from the interface and, thus, of the compositional profiles. It is noteworthy that only experimentl points

falling within the weight range of 98 to 102% were retained for inclusion in the analysis. Data processing employed the X-Phi routine to ensure robustness [98].

Preprocessing of EPMA profiles

The collected EPMA profiles undergo preprocessing to facilitate a more comprehensive interpretation of the dissolution phenomena. Initially, data normalization occurs via the total sum to account for variations in the total measured intensities.

As underscored in Chapter 1, the composition at the interface ($x = 0$) is pivotal in describing the dissolution kinetics. Nonetheless, a significant challenge lies in the fact that the first point measured in the glass, or the last one measured in the solid phase, often includes contributions from both the solid and the glass due to the microprobe volume. This overlap can lead to inaccuracies in the composition measured at the interface.

Despite careful sample preparation, there is potential for interface disruption during quenching, which can create a small gap between the two phases. This disruption can further complicate the accurate measurement of the interface composition. Additionally, the measurement point closest to the interface often falls outside the acceptable weight percentage range of 98 to 102%, rendering it unreliable for precise analysis.

To address these challenges, the interface composition is approximated through linear extrapolation of the first two exploitable measurement points in the glass for each line scan. This extrapolated value will be denoted as C_{ext}.

2.5.4 Thermodynamic simulations

Although dissolution rates are controlled by kinetics, their driving force is the chemical potential gradient between the solid and the solvent. Hence, thermodynamic calculations serve as a powerful tool to better understand the direction of dissolution. To this end, thermodynamic simulations based on the minimization of the system's free energy were conducted using FactSage (version 8.0), a comprehensive database and software suite collaboratively developed by ThermFact/CRTC (Montreal) and GTT-Technologies (Aachen) [99].

In this study, the FToxid database, which contains compounds and solutions for oxide databases, was utilized. Two primary modules, "Equilib" and "Phase Diagram", were employed. Given an input of elements or compounds and a set of final conditions (temperature and pressure), the "Equilib" module calculates the concentrations of chemical species at a chemical equilibrium state using Gibbs energy minimization. Prior to the calculation, the user must select the potential pure solids, solid solutions, and liquid among the possible outputs. The latter phase, labeled as *"slag"* by FactSage, is the phase existing in a liquid state at the temperature and pressure of interest and is the phase that will be quenched as the glass phase.

The "Phase Diagram" module was also utilized to draft pseudo-binary and pseudo-ternary phase diagrams. While these diagrams could not provide the actual thermodynamics for a system with more than four components, they can indicate trends for larger domains of composition than "Equilib"'s results. Therefore, FactSage-calculated phase diagrams for the studied system must be interpreted with the assumptions that allowed for simplifying the system to a ternary or binary diagram, such as the assumption of a constant ratio between the alkalis or the alkaline earth elements.

The original composition of the glass was simulated as a mixture of the oxides that compose it, in the same molar fraction as its chemical composition measured by EPMA (Table 2.1), whose sum equals 1 mol. Then, this 1 mol of mixture was inserted as the input in the Equilib module, where only the *"slag"* (liquid) solution was authorized as the phase in equilibrium at the temperature of interest (either 1300, 1350, 1400, or 1450 °C). This operation is necessary to transform the mixture of isolated oxides into a liquid phase, thereby considering their interactions. This compound is labeled as *"stream"* by FactSage and was used to simulate the original glass. This step is particularly crucial when the initial state of the glass must be considered, i.e., enthalpy and Gibbs free energy variation calculations.

The dissolution process was simulated using the "Equilib" module by inputting a variable molar fraction (A parameter in FactSage) of the solid to be dissolved and the complementary molar fraction ($1 - A$) of the original glass *"stream"* at 1 atm and the temperature of interest. The goal of this calculation was to estimate the solid-to-melt ratio needed for full dissolution, the *liquidus* composition along the tie-line between the glass and the solid compositions, as well as the thermodynamic activities of secondary phases that may precipitate during dissolution.

The "para-equilibrium" option in the "Equilib" module was not selected, and therefore, all elements were assumed to move with the same mobility, and the global equilibrium (the chemical potential for all elements balanced between two phases) was reached. Consequently, performing the dissolution as detailed provides only the results for a compositional path throughout the straight tie-line linking the glass and the pure solid compositions (light green tie-line in Figure 2.10). This implies that it provides one possible solution, but not the whole range of possible dissolution outcomes.

As discussed in Section 1.4, the solubility of a solute in a multi-component fluid is not invariant, even for a fixed temperature and pressure. In the dissolution cases studied in this work, if the system is simplified to only four components (alkalis, alkaline earth, silica, and alumina), the number of degrees of freedom (ϕ) for two phases ($P = 2$) coexisting can be predicted by the Gibbs phase rule (Equation 1.40) : $\phi = C - P \Rightarrow \phi \geq 4 - 2 \Rightarrow \phi \geq 2$. This implies that the *liquidus* (i.e., the glass composition in equilibrium with the dissolving solid) is indeed a surface (at minimum) instead of a single solution.

This presents a challenge when comparing the measured interface composition and the thermodynamics, given that there is not a single solution but a surface of them to describe if the glass is in chemical equilibrium or not. To verify this, the strategy used was to assume that the variation between a point close to this *liquidus* "surface" and the tie-line linking this point to the pure solid composition would be a better approximation given the proximity to the actual equilibrium composition (orange circle vs blue star in Figure 2.10). Therefore, to check how far the measured composition of the glass near the interface was from equilibrium, 1 mol of glass with a composition equivalent to the nearest experimental glass composition at the interface for each measured EPMA profile and 1 mol of the solid was examined at 1 atm and the temperature of the test. The equilibrium composition of the glass was determined by the chemical composition of the *"slag"* phase, from the intersection between the enriched glass composition tie-line with the *liquidus* surface (orange tie-line in Figure 2.10).

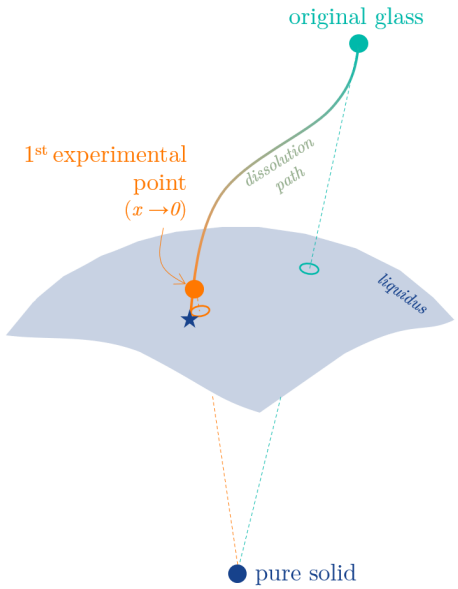

Figure 2.10 Schematic illustration of a hypothetical *liquidus* surface, which separates the liquid and pure solid compositions, with tie-lines represented as dashed lines. The dissolution path (curved gradient line) may not coincide with the green tie-line connecting the original glass and pure solid, indicating that the actual interface composition can differ significantly from the expected intersection on the *liquidus*. By considering a tie-line closer to the interface composition (orange line), the deviation from the actual value (blue star) is minimized

2.6 Methods summary

This chapter provided a comprehensive overview of the materials, experimental methods, and characterization techniques employed in this research. The vertical slab stack setup was utilized to study both alumina and quartz dissolution in soda-lime silica glass. However, the experimental protocol varied slightly between the two materials due to their specific properties, as illustrated by Figure 2.11.

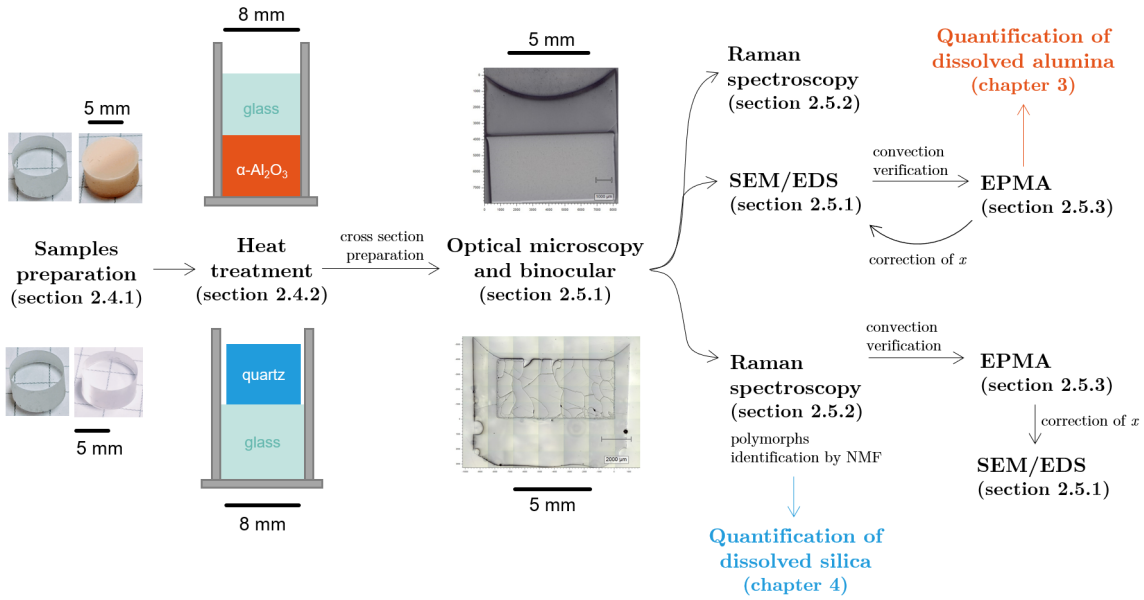

Figure 2.11 Schematic representation of the experimental protocol for investigating the dissolution of alumina and quartz in soda-lime silica glass.

Heat treatment conditions, including temperatures and time durations, differed for the two solutes, are further detailed in Chapters 3 and 4. Additionally, the setup for quartz required minor adaptations to accommodate its expansion during heating, points discussed in Section 4.2.

Although the same characterization techniques were applied to both alumina and quartz, the methods for quantifying the dissolved alumina and silica varied. For alumina dissolution, Electron Probe Micro-Analyzer (EPMA) profiles were employed to quantify the incorporated alumina, and the convection-free samples facilitated the acquisition of rigorous data for a better description of the diffusion contribution.

In contrast, the dissolution of quartz relied heavily on Raman spectroscopy due to the lower chemical contrast between quartz and the original glass and to better understand the effects of silica polymorphism. Therefore, the data analysis methods for dissolved material performed in both cases were not identical and are detailed in the following dedicated chapters.

Chapter 3

Alumina dissolution

Journal of Non-Crystalline Solids 650 (2025) 123351

Contents lists available at ScienceDirect

Journal of Non-Crystalline Solids

journal homepage: www.elsevier.com/locate/jnoncrysol

Diffusive dissolution of α-alumina in industrial soda-lime silica glass

Fatima T. Yoshizawa [a,b,c,*], Anne-Céline Garel-Laurin [a], Ekaterina Burov [a,b], Michael J. Toplis [c]

[a] Saint-Gobain Recherche, 41 quai Lucien Lefranc, BP 135, Aubervilliers Cedex, 93303, France
[b] Surface du Verre et Interfaces, UMR 125 CNRS/Saint-Gobain Recherche, 41 quai Lucien Lefranc, BP 135, Aubervilliers Cedex, 93303, France
[c] Institut de Recherche en Astrophysique et Planétologie (Université de Toulouse 3, Paul Sabatier, CNRS), 14 Avenue Edouard Belin, Toulouse, 31400, France

ARTICLE INFO

Keywords:
Multicomponent diffusion
Soda-lime silica glass
Alumina
Dissolution

ABSTRACT

This study advances the understanding of alumina dissolution mechanisms in industrial soda-lime-silica glass. Electron Probe Micro-Analysis (EPMA) revealed diffusion-controlled behavior between 1300 and 1450 °C, with interface melt compositions varying significantly with temperature. These variations align with thermodynamic predictions. At temperatures ≥ 1400 °C, the interface enters the peraluminous field, while at lower temperatures, it lies in the domain of excess charge-balancing cations. Compositional profiles, including uphill diffusion at ≥ 1400 °C, necessitate a multicomponent diffusion matrix approach. Two primary exchange mechanisms are identified: the first involves alumina and charge-balancing cations (mainly Mg+Ca), and the second involves silica and charge-balanced alumina. However, alumina diffusivity can be approximated using an effective binary diffusion coefficient (EBDC), which correlates with the viscosity of the interface melt, even when a viscosity maximum is present. These results emphasize the importance of multicomponent approaches to understanding mineral dissolution and diffusion, particularly in peraluminous systems.

1. Introduction

Glass melting furnaces are engineered to yield uniform glass, yet defects may occur, detrimentally impacting the glass's mechanical, processing, and aesthetic properties. These defects are often linked to the incomplete dissolution of refractory phases, such as aluminum and chromium oxide, that either occur as impurities in raw materials or from interaction with the furnace lining.

In addition, from the standpoint of refractory furnace linings, understanding the kinetics of alumina dissolution in the presence of molten silicate helps understand the factors controlling furnace lifetime. Several studies have explored alumina corrosion [1–4], offering empirical laws for quantifying dissolution rate as a function of melt composition, convection, and temperature gradients. However, these data cannot be used directly to predict the lifetimes of solid inclusions in the industrial glass-making process.

On the other hand, numerical modeling, particularly Computational Fluid Dynamics (CFD), emerges as a promising tool for understanding glass melting furnaces. CFD facilitates the depiction of thermal and flow fields within the melt. Nevertheless, these models, too, require precise physicochemical data in order to simulate mineral dissolution [5,6].

In this context, the study presented here aims to furnish data of directly relevant to alumina dissolution in an industrial soda-lime-silica glass melt. The dissolution process can be interpreted as a heterogeneous reaction between a solid phase (alumina) and the melt. The driving force for dissolution lies in the chemical potential difference between the two phases. Alumina assimilation into the glass occurs via an interface reaction followed by mass transport mechanisms that transfer reaction products away from the mineral surface.

Dissolution kinetics are thus potentially sensitive to the rate of this interface reaction. If this step is the slowest, the solid–liquid interface does not reach thermodynamic equilibrium within the timescale of observation and may, in this case, control the overall dissolution kinetics. On the other hand, if the interface reaction is rapid, the solid–liquid interface may approach thermodynamic equilibrium. In this case, reaction products are transported away from the solid–liquid interface via diffusion in the liquid. If one assumes static conditions (i.e., without advection) and constant diffusion coefficients, composition profiles should conform to Fick's second law [3,7–9].

$$\frac{\partial C}{\partial t} = D\frac{\partial^2 C}{\partial x^2} \tag{1}$$

where D is the diffusion coefficient (or diffusivity) in m^2/s, C is the chemical composition, t is time and x the distance.

In order to model dissolution, it is essential to understand the variables involved and collect relevant data for the system of interest. Since the chemical potential difference between the solid and liquid phases is the ultimate driving force for dissolution, variables that influence

* Corresponding author.
E-mail address: FatimaTiemi.Yoshizawa@saint-gobain.com (F.T. Yoshizawa).

https://doi.org/10.1016/j.jnoncrysol.2024.123351
Received 23 September 2024; Received in revised form 27 November 2024; Accepted 27 November 2024
Available online 9 December 2024
0022-3093/© 2024 Elsevier B.V. All rights are reserved, including those for text and data mining, AI training, and similar technologies.

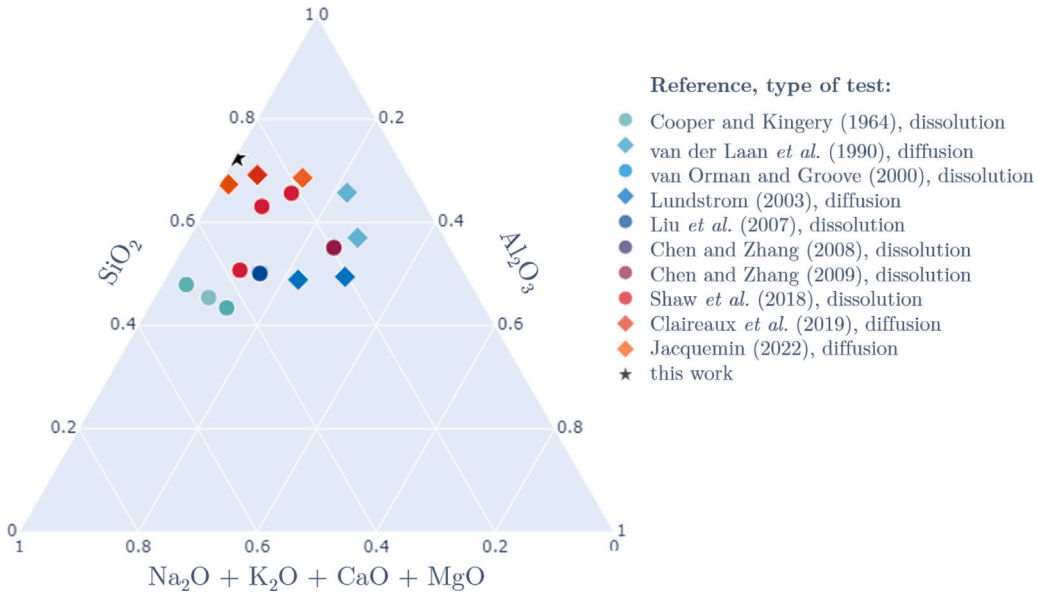

Fig. 1. Compilation in %mol of initial glass compositions used for different literature studies devoted to alumina diffusivity. The bottom left apex corresponds to the sum of Na_2O, K_2O, CaO and MgO. Apart from the composition of this work (black star), diffusion studies are displayed as diamonds and dissolution studies by circles; not all dissolution studies were performed with aluminum oxide.

this property will impact dissolution kinetics. These include temperature, chemical composition (melt and mineral), and pressure [10]. Beyond the thermodynamic perspective, it is crucial to consider the time scale of interest as thermodynamic equilibrium may or may not be approached. Finally, relative movements between solid and liquid may generate mass transport by convection, influencing dissolution kinetics.

Alumina dissolution in the temperature range of 1450 to 1650 °C has been the subject of several studies on corrosion of refractory materials [1,2,4,11,12], even though the melt of interest is principally CaO-Al_2O_3-SiO_2 (CAS) slags, motivated by problems related to steelmaking furnaces. Earth Science (e.g. volcanology) applications have also motivated interest in the dissolution of alumina and aluminate minerals in contact with aluminosilicate melts in the temperature range 1200 to 1600 °C [7,13–18], albeit under higher pressures (around 0.5 GPa) than those encountered in glass-making furnaces. Finally, recent diffusion matrix studies [19–21] have focused on diffusion between melt compositions closer to industrial soda-lime silica glass in the temperature range 1200–1500 °C, but do not study mineral dissolution. Fig. 1 summarizes compositions studied in the literature, where it may be appreciated that the majority have low alkali and low silica contents compared to industrial soda lime glass.

Furthermore, the experimental approaches adopted among these studies vary. As illustrated by Shaw [22] for the case of quartz dissolution in a silicate melt, the geometry of the experimental setup influences the measured dissolution rate. This effect can be assigned to the onset of convective flow and relative movement between the solid and liquid phases. For instance, in dissolution tests using spherical grains, such flow was observed, invalidating the assumption of a static state [4,11].

Other studies opted for dissolution of alumina cylinders under forced melt flow (advection), which approaches the solicitations found in industrial furnaces [1,2,12]. However, in these cases, the diffusivity data for alumina are often a side-product and not always reported.

Conversely, diffusivity data from diffusion couple tests [13,19–21,23] are better constrained. However, they are limited to a range of compositions since no solid phase is added to the melt, limiting the extent of chemical enrichment. The compositions of the materials that compose the diffusion couple endmembers are shown as diamond markers in Fig. 1.

In summary, despite the number of studies treating the question of alumina corrosion and dissolution in the glass science and geochemistry communities, the diffusion coefficients of elements in the melt that (in static conditions) ultimately control dissolution rate, are not necessarily measured and/or reported. In light of these shortcomings, this study aims to understand better the mechanisms controlling alumina dissolution in industrial soda-lime-silica glass between 1300 and 1450 °C.

2. Methods

In this study, the dissolution of cylindrical slabs is measured, inspired by previous work e.g. [8,15,18,22] as summarized in Fig. 2. This experimental setup represents semi-infinite 1D dissolution. For short times and without density inversions, this geometry maintains a consistent far-field composition and mitigates convective effects.

Several factors were considered to ensure that experimental conditions conform to the desired semi-infinite dissolution scenario. Firstly, the setup geometry and heat treatment durations were chosen to maintain the glass's semi-infinite condition and avoid free convection, thus maintaining static conditions during the dissolution tests.

Satisfying the semi-infinite condition of the solute requires that the far-field composition does not vary from its initial value. For this reason, the minimum height of the molten reservoir was calculated for various heat treatment durations using the diffusion matrix of [21] for a glass containing 15% mol Al_2O_3. This method was used to estimate the time limit at which the composition at the extremity of the sample deviated by more than ± 0.5% mol from the original composition, considering all oxides, not only alumina. For example, at 1450 °C, the concentrations of Na_2O and CaO no longer matched the original composition after 4 h for a glass reservoir 4 mm high.

Additionally, the setup was designed to prevent convection, which could arise from density differences due to thermal gradients and double-diffusive convection. The furnace's heating elements were positioned laterally to avoid Rayleigh-Benard instability. Calculations as a function of setup diameter indicate that convection should only occur for a diameter larger than a meter.

Despite these precautions, the non-monotonous behavior of chemical profiles when coupled diffusion operates raises additional challenges. As described by Liang [24], free convection may be driven

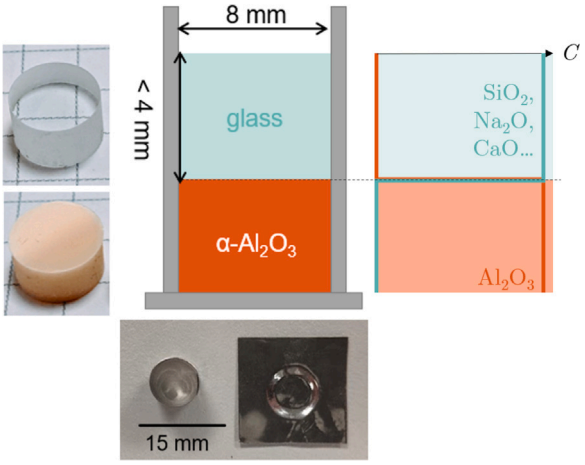

Fig. 2. The sintered alumina slab (bottom left) exclusively contains Al_2O_3, with negligible concentrations of the other oxides. The glass slab (top left), positioned above to avoid gravitational instabilities, is the source of the remaining oxides that can be available during dissolution. The ensemble is then enveloped in a platinum-gold foil (bottom) with a bottom cap to avoid eventual leakages.

Table 1
Composition in %mol of starting materials measured by EPMA.

% mol	Soda-lime silica glass	Sintered alumina
Na_2O+K_2O	13.4 ± 0.1	0.1 ± 0.1
CaO + MgO	13.6 ± 0.1	0.1 ± 0.1
Al_2O_3	0.35 ± 0.02	98.5 ± 0.5
SiO_2	71.9 ± 0.2	0.4 ± 0.3

by the coupling of elements' diffusion, which is influenced by heat treatment duration and diameter. However, since the instability threshold is primarily sensitive to the former, double-diffusive perturbations were avoided by limiting the duration of dissolution tests rather than modifying the assembly design.

To prepare the starting materials, circular disks 8 mm in diameter were obtained by core drilling. One surface of each disk was ground and polished using 6 and 1 μm diamond paste to achieve a height of approximately 4 mm. These disks were then stacked and enclosed within a platinum-gold foil, serving as an inert crucible. The glass disk was placed on top of the alumina disk to ensure gravitational stability during experimentation.

The glass composition used was a soda-lime silica glass sheet from Saint-Gobain Glass. The source of alumina was a sintered Al_2O_3 plate from Umicore (99.4 ± 0.5% wt). The compositions derived from EPMA measurements of both starting materials are presented in Table 1.

The setup was subsequently introduced into an electric furnace preheated to the desired temperature: 1300, 1350, 1400, or 1450 °C. Temperature was monitored by a dedicated thermocouple, and thermal stabilization (±3 °C) was achieved within about 1 min. Isothermal treatments ranging from 10 min to 24 h were carried out for each temperature (see Appendix). The experimental duration was measured as the time following the time the thermocouple indicated the desired temperature (the time required to reach the nominal temperature was typically 1 min).

Quenching was performed in air by extracting the sample from the furnace, corresponding to an approximate rate of 630 °C per second for temperatures above the glass transition. These quenched samples were then embedded in epoxy under vacuum conditions to avoid air entrapment, especially close to the interface. Sections perpendicular to the interface were extracted from these embedded samples and polished using 6 and 1 μm diamond paste for microscopic analysis and further characterization.

Table 2
Compilation of experimental conditions for each temperature, indicating the presence of convection (✓) or not (✗) for each measured EPMA profile. Only samples without convection were considered for the analysis. (m) corresponds to dissolution tests using monocrystalline slab as the corundum source.

	1300 °C	1350 °C	1400 °C	1450 °C
10 min				✗✗✗✗
15 min			✗✗✗ ✗✗✗✗	✗✗✗✓
20 min				✗✗✗✗
25 min				✗✗✗✗
30 min	✗✗✗		✗✗✗✗✗✗✗✗✗ (m) ✗✗✗✓	✗✗✗✓
45 min		✗✗✗		
60 min	✗✗✗	✗✗✗	✗✗✗	
90 min	✗✗✗			
120 min	✗✗✗	✗✗✗	✗✗✗✓	
150 min	✗✗✗			
180 min			✓✓✓✓	
210 min	✗✗✗			
360 min			✓✓	
1440 min			✓✓✓✓ (m) ✓✓✓✓	

The potential presence of convection was assessed following quenching and preparation of the samples. Scanning electron microscopy (SEM) in back-scattered mode and energy dispersive X-ray spectroscopy (EDS) mapping were performed using a Quanta FEG coupled with EDS. Heat treatments displaying potential convection effects were excluded from subsequent analysis (that assumes static dissolution).

Compositional profiles for each sample were measured in at least three different regions to exclude potential convection perturbations on the dissolution front, as summarized in Table 2. The chemical profiles were acquired using a Cameca SXFive electron probe (EPMA) at Saint-Gobain Research Paris. Initially, three traverses with a 9 μm step size were executed perpendicular to the interface, maintaining a separation of 60 μm between profiles. These traverses were strategically positioned in the central region of the sample or regions free of cracks. Additionally, another traverse, characterized by a step size of 50 μm, extended across the interface, covering the entire length of the glass to monitor far-field compositional shifts.

Analyses were carried out using a 15 kV accelerating voltage, 10 nA beam current, and 10 s counting times for both peaks and background for all the elements, except for Si (20 instead of 10 s). Peak and intensity standardizations were made by referencing against soda-lime silica glass of identical composition for elements Si, Na, Ca, Mg, and K, and against sapphire for Al. The accuracy of the composition measurements (in wt%) is estimated at ±0.4 wt% for Na_2O, ±0.3 wt% for CaO, MgO and Al_2O_3, and ±0.7 wt% for SiO_2. Data processing employed the X-Phi routine [25] to ensure robustness.

An electron-beam area of 40 × 2 μm was chosen to prevent sodium migration while ensuring points were spaced by at least 9 μm to mitigate the same concern. Detailed measurements were conducted using SEM in secondary electron mode to correct compositional profile shifts towards the interface. This involved assessing distances and potential misalignments from the initial measurement point's center on the glass to the alumina-glass interface, enhancing accuracy. The tilt between the line scan and the interface was measured and accounted for during the analysis, with the tilt angle found to be less than 5°.

Only measurements falling within the weight range of 98 to 102% were retained for inclusion in the analysis.

3. Results

The dissolution experiments that show no signs of convection (see Table 2) have diffusion profiles that are parallel to the mineral-liquid interface with no turbulence or perturbation, as confirmed by EDS

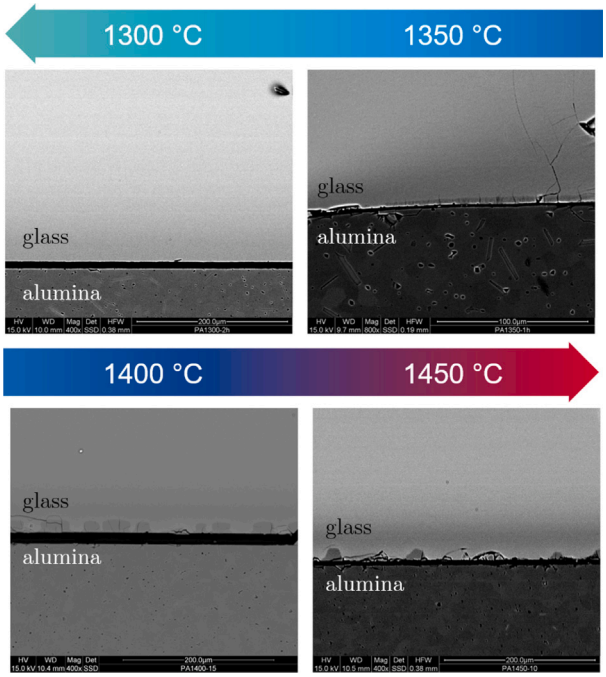

Fig. 3. SEM images in back-scattered electrons (BSE) mode of the interface between alumina (bottom) and glass (top) slabs after dissolution tests at different temperatures. The intermediate phase is slightly darker than the glass at the interface, as a continuous layer for 1350 °C and as semi-circles for higher temperatures. The magnification of the 1350 °C image is twice the other temperatures for better visualization of the intermediate layer.

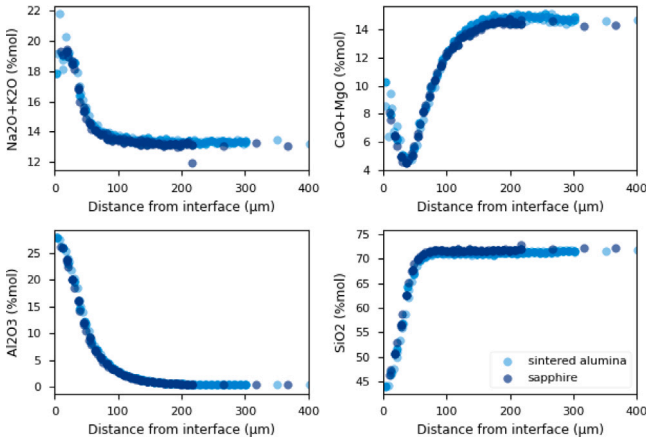

Fig. 4. Chemical profiles (%mol) in the glass after a dissolution test with sapphire and sintered alumina for 30 min at 1400 °C. Although the measurements covered the entire sample length, the data plotted are limited to the first 400 μm for better visibility.

maps, corresponding to one-dimensional dissolution under static conditions. Despite occasional cracking due to quenching, the alumina-glass interface remained sharp, held together by epoxy mounting.

At a temperature of 1350 °C, we observe a continuous layer of crystalline material at the glass-alumina interface, indicating incongruent dissolution. However, an intermediate phase is present in the 1400 to 1450 °C temperature range but does not form a continuous layer at the interface. No intermediate phase was observed for dissolution experiments performed at 1300 °C. Fig. 3 illustrates the microstructure of the interface after dissolution in different temperatures.

Focused-beam EDS analysis allows us to estimate that these intermediate phases exhibit chemical compositions resembling nepheline ($Na_2Al_2Si_2O_8$), with higher silica content in the 1350 °C samples. Interestingly, while the Raman spectra of the intermediate phase at 1400 and 1450 °C match the signature of carnegieite (consistent with the chemical composition $Na_2Al_2Si_2O_8$), the corresponding phase at lower temperature remains unidentified. Data points for which the EPMA beam overlapped both phases were excluded from consideration in the chemical profiles of the glass.

3.1. Comparison between alumina sources

The potential influence of the alumina source on the dissolution behavior was investigated by conducting four measurements using a non-oriented monocrystalline slab as the alumina source. These measurements were performed under identical conditions, each lasting 30 min at 1400 °C (refer to PAm-1400-30 samples in Appendix).

A comparative analysis was conducted with conventional sintered alumina subjected to the same heat treatment (refer to PA1400-30-5 to PA1400-30-9 in Appendix), as depicted in Fig. 4. It is of note that both alumina sources contained corundum (α-alumina) as the alumina polymorph.

This comparison aimed to assess the potential impact of the microstructural characteristics of polycrystalline alumina, specifically porosity, and grain boundaries, in contrast to a monolithic alumina source. However, no discernible differences were observed in the chemical profiles between the two materials. Consequently, subsequent tests were exclusively conducted on the sintered alumina slab.

It is important to note that the monocrystalline slab was not oriented, which precluded any further conclusions regarding the effect of crystallographic orientation on corundum dissolution. Nevertheless, the results clearly indicate that the dissolution behavior of alpha-alumina does not vary between monocrystalline and polycrystalline sources used in this work.

3.2. Glass chemical profiles

A comparative analysis of glass compositional profiles, illustrated in Fig. 5 with the distance from the interface normalized to the square root of heat treatment duration, reveals consistent patterns across all temperatures. The time-normalized profiles significantly overlap for each temperature, indicating uniform behavior.

Notably, the semi-infinite hypothesis is confirmed for all studied conditions of time and temperature, with the far-field composition falling within the experimental error range of the initial glass composition, represented by the dashed line.

Furthermore, the compositional profiles for each oxide show a similar form at all temperatures/times, displaying a stretching effect towards longer diffusion distances as the temperature increases. This behavior is consistent with a diffusive mechanism controlling the dissolution process.

In the compositional profile of alkaline-earth oxides, a distinct minimum near the mineral interface gives way to a smooth transition towards the bulk composition with increasing distance. In contrast, alkali oxides exhibit a pronounced maximum near the interface, followed by a gradual return to the bulk composition. These contrasting trends become less pronounced at lower temperatures, where both alkali and alkaline-earth oxides show reduced inflection points near the interface, likely due to shorter diffusion distances at 1300 and 1350 °C and the need for finer spatial resolution. Despite these variations, the overall shape of the compositional profiles remains consistent across all temperatures examined in this study.

3.3. Interface composition and thermodynamic equilibrium

In the vicinity of the mineral interface, variations in glass composition are observed as a function of heat treatment temperature. Higher temperatures exhibit reduced alkalis and silica content, with higher alkaline earth and alumina content. The observed differences in interface

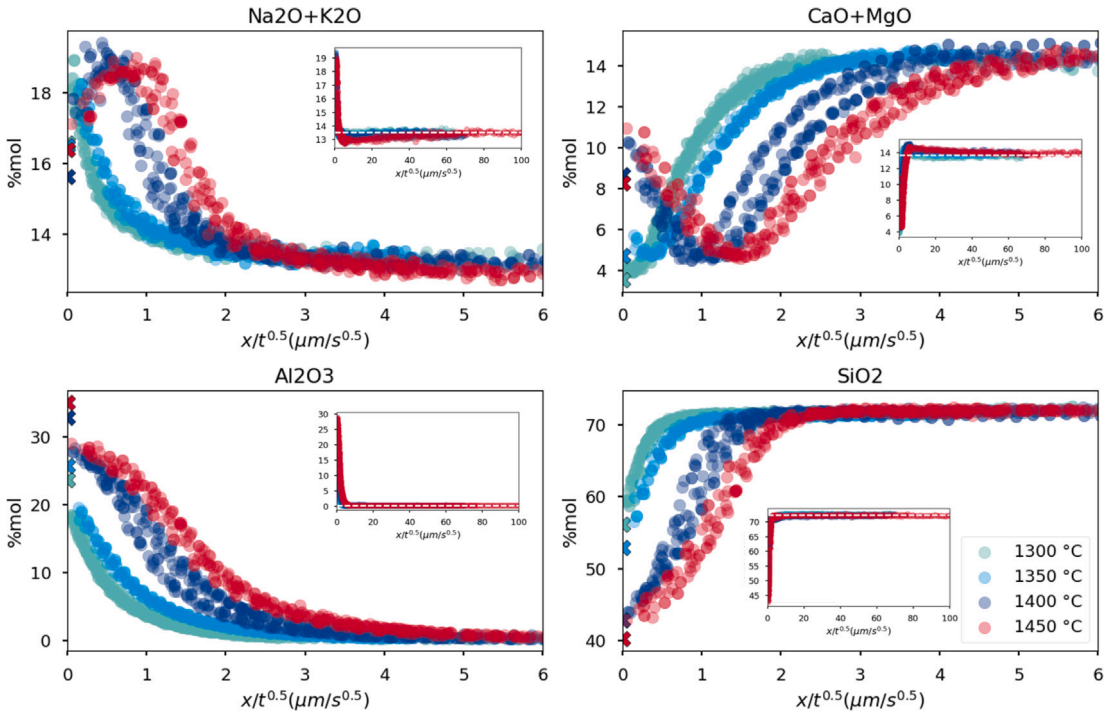

Fig. 5. Chemical profiles in %mol as a function of the distance from the interface normalized by the square root of the heat treatment duration for all temperatures. The data displayed are limited to a normalized distance of 6 $\mu m/s^{0.5}$ for better visibility of inflections in the compositional profile. An inset illustrates the behavior until 100 $\mu m/s^{0.5}$ to compare with the original glass composition (white dashed line). The crosses at $x/t^{0.5} = 0$ represent the equilibrium composition predicted by thermodynamic calculations for each temperature.

composition between higher and lower temperature experiments could potentially stem from a combination of: (i) difficulty in estimating the actual interface composition due to the limited spatial resolution of EPMA, particularly for slower diffusion kinetics and shorter heat treatments at lower temperatures (1300 and 1350 °C) (i.e., with short diffusion profiles), or (ii) incomplete approach to interface equilibrium at lower temperature/time, or (iii) a real effect linked to variations in the equilibrium composition as a function of temperature.

The first of these possibilities highlights the difficulty of accurately measuring the composition at the alumina-liquid interface ($x = 0$), as the first point measured in the glass is typically shifted from the actual interface due to spatial resolution limitations. This shift is compounded by the fact that compositions near the interface often exceed 100 ± 2% wt because the microprobe's measurement volume has contributions from both glass and alumina. The distance of the first valid EPMA point to the interface is estimated using SEM in secondary electron mode. Still, even this may be compromised by potential interface disruption during quenching, despite careful sample preparation. To take account of these issues, the interface composition is approximated through the linear extrapolation of the first two exploitable measurement points in the glass for each traverse, denoted as C_{ext} in Fig. 6 (values listed in Appendix). Despite the uncertainties associated with these corrections, the scattering of values of C_{ext} between experiments at different temperatures cannot be exclusively explained by problems with estimating accurate interface compositions.

Concerning the possibility that interface equilibrium was not attained, we note that the differences observed are not a function of time but only temperature, arguing against this explanation.

Finally, to assess equilibrium effects, we performed thermodynamic calculations based on minimizing the system's free energy [26] to predict the chemical composition of glass melt in equilibrium with alumina at different temperatures. These simulations were conducted using FactSage (version 8.0), a comprehensive database and software suite developed collaboratively by Thermfact/CRCT (Montreal) and GTT-Technologies (Aachen).

The database employed in this study is FToxid, which contains compounds and solutions for oxide databases. We calculated the equilibrium phases and their chemical compositions using the Equilib module, considering pure solids, solid solutions for carnegieite and nepheline, and liquid. The latter phase, referred to as "slag" by FactSage, exists in a liquid state at the temperature and pressure of interest and will be quenched as the glassy phase.

Thermodynamic equilibrium at the dissolution interface was simulated by adding 1 mol of glass equal to the nearest experimental glass composition at the interface for each measured profile and 1 mol of α-alumina at 1 atm and the treatment temperature. The equilibrium composition of the glass can then be determined by the chemical composition of the "slag" phase. The same approach also allows for predicting secondary phase precipitation, mole fractions, and thermodynamic activities.

The average value of the thermodynamic prediction for the glass composition, when in equilibrium with alumina at each temperature, is represented by cross symbols in Fig. 5 at $x = 0$. Both experimental data and thermodynamic predictions indicate a significant increase in alumina solubility between 1350 and 1400 °C.

The C_{ext} values from each EPMA measurement were compared with their corresponding thermodynamic predictions (C_{eq-FS}) for the interface glass composition at equilibrium with alumina in Fig. 6, as a function of heat treatment duration and temperature. While there are offsets in the absolute values for each oxide, we draw attention to the fact that offsets are independent of temperature and more or less independent of time. In other words, the observed variations in interface composition are perfectly consistent with a dominant thermodynamic effect. Of note is that equilibrium melts vary significantly over the temperature range studied here (differences of 15 wt% of Al_2O_3 and SiO_2 over 150 °C) and that the equilibrium melt crosses the metaluminous join near 1400 °C, occurring in the peraluminous field at higher temperature.

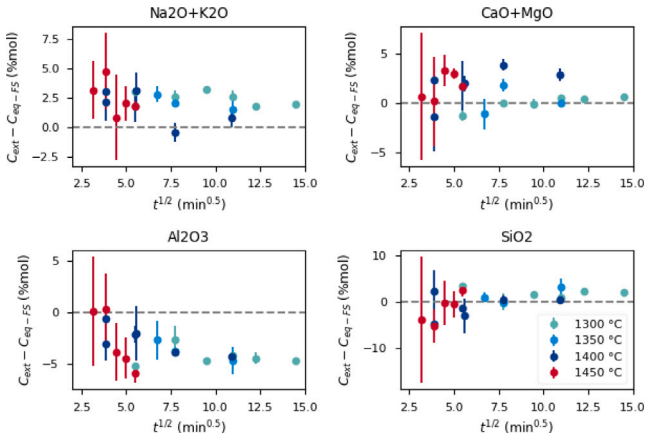

Fig. 6. Chemical composition difference in %mol between extrapolated experimental data at x = 0 and thermodynamic predictions for different heat treatment durations.

3.4. Exchange diffusion directions and compositional space

The chemical profiles depicted in Fig. 4 are plotted in a pseudo-ternary representation in Fig. 7. This figure illustrates that compositional profiles at a given temperature lie perfectly on top of one another, regardless of the duration of heat treatment.

However, as noted above, the significant increase in Al-solubility as a function of temperature leads to interface melt compositions that cross the metaluminous join (illustrated by the blue dashed line in Fig. 7).

In all cases, a pronounced deviation from a linear tie-line between the initial melt and Al_2O_3 (dash-dot line in Fig. 7) is observed in all profiles, with observed profiles following a curved path, that may be described by at least two discernible orientations for the tested temperatures.

While the superposition of normalized profiles aligns with a diffusion-controlled dissolution process, the inflections in the profiles of Fig. 5 suggest coupled diffusion among the elements. In such a scenario, the diffusion of a given component of the melt is sensitive to the concentration gradient of that element and the concentration gradients of the other melt elements. Mathematically, this can be considered by replacing a single diffusivity coefficient with a diffusion matrix in Fick's second law [27].

$$\frac{\partial}{\partial t}\begin{bmatrix} C_1 \\ C_2 \\ C_3 \\ C_4 \end{bmatrix} = \begin{bmatrix} D_{1,1} & D_{1,2} & D_{1,3} & D_{1,4} \\ D_{2,1} & D_{2,2} & D_{2,3} & D_{2,4} \\ D_{3,1} & D_{3,2} & D_{3,3} & D_{3,4} \\ D_{4,1} & D_{4,2} & D_{4,3} & D_{4,4} \end{bmatrix} \frac{\partial^2}{\partial x^2}\begin{bmatrix} C_1 \\ C_2 \\ C_3 \\ C_4 \end{bmatrix} \tag{2}$$

Given the constraint that the sum of all oxides must be 100%, only $N-1$ independent oxides exist. By adopting one oxide as dependent, eigenvalues and eigenvectors associated with the $(N-1)\times(N-1)$ matrix can be extracted. Decoupling Fick's law involves projecting compositions along the eigenvalues:

$$\frac{\partial U_i}{\partial t} = \lambda_i \frac{\partial^2 U_i}{\partial x^2} \tag{3}$$

Here, U_i represents the projection of compositional profiles for different species in alignment with eigenvector i, while λ_i denotes the corresponding eigenvalue.

We assume that the initial compositions of both alumina and glass are uniform, with each phase being compositionally homogeneous across the entire sample at $t = 0$. In a semi-infinite model, the far-field composition remains constant (denoted by subscript $t = 0$) throughout the duration of the dissolution process.

When diffusion controls dissolution, thermodynamic equilibrium dictates the interface composition at $x = 0$, which remains constant for all $t > 0$. This equilibrium condition provides a second boundary condition, enabling the derivation of an analytical solution for Eq. (3) under these conditions:

$$U_i(x,t) = (U_{i,x=0} - U_{i,t=0})\mathrm{erfc}\left(\frac{x}{2\sqrt{\lambda_i t}}\right) + U_{i,t=0} \tag{4}$$

where erfc is the complementary error function. $U_{i,x=0}$ and $U_{i,t=0}$ were calculated by linearizing the experimental composition extrapolated to the interface (C_{ext} detailed in the previous section) and the median of the far-field composition[1] for each measurement, respectively.

Applying an approach similar to Claireaux et al. [28], a diffusion matrix for each temperature is obtained through least-square minimization of the difference between theoretical and experimental dissolution profiles. For this purpose, the open-source Python module *multidiff*[2] was adapted to account for the specific boundary conditions of dissolution experiments, which differ from diffusion couple tests. These adaptations included adopting Eq. (4) as the theoretical curve to describe the semi-infinite dissolution scenario under static conditions and ensuring the optimization algorithm accurately determined eigenvalues and eigenvectors. For simplicity, the six components were reduced to a four-component system, considering similar behavior for alkali oxides on the one hand and alkaline earth oxides on the other (in addition to silica and alumina). Silica was chosen as the dependent component of the matrix (Nth oxide).

This results in three independent components, generating three possible eigenvectors and eigenvalues for each temperature (as shown in Table 3). An initial guess, using the diffusion matrix calculated for a 15% mol Al_2O_3 NCAS glass at 1500 °C by Jacquemin [21], was employed to initiate the calculation of eigenvectors. For this initialization, the eigenvalues for each temperature were estimated assuming an Arrhenian-type behavior and using an activation energy of 134 kJ/mol found for the first exchange reaction [19].

As expected, the calculations for the two lower temperatures revealed three distinct eigenvectors for the simplified four-oxide system. However, above 1400 °C, the second and third exchange reactions are indistinguishable within error. This degeneracy between the last two eigenvectors in our dissolution experiments is unsurprising, as not all possible exchange reactions between elements were observed. During alumina dissolution, the solid phase initially served as the sole source of alumina, while the molten glass supplied all other elements. Additionally, there is a preferential exchange direction since the alumina solid does not accommodate solid solubility. A more comprehensive definition of the diffusion matrix would require exploration of additional orthogonal exchange directions to avoid parallel eigenvectors [29].

Within the 1300 to 1450 °C range, two types of exchange reactions are detected at all four temperatures: (i) an exchange mainly between alumina and alkaline earth oxides, and (ii) the exchange between silica and all other elements, consistent with exchange with charge-balanced alumina.

In order to explore commonalities between eigenvectors at different temperatures, an additional analysis was conducted, assuming common eigenvectors for all temperatures, akin to Claireaux et al.'s [19] approach in an NCAS glass system between 1200–1360 °C. This approach simultaneously treats data for all temperatures and provides more data for the matrix optimization method described above. Table 4 presents the resulting eigenvalues and eigenvectors using this strategy. This matrix will be discussed in the following sections.

The same two groups of exchange reactions are found using this approach, and their respective eigenvalues are close to those calculated

[1] The median was calculated using ξ last points of the EPMA profile, where ξ is the maximum integer between 5 and 0.1 times the total number of points of the profile.

[2] Available at https://pythonhosted.org/multidiff/.

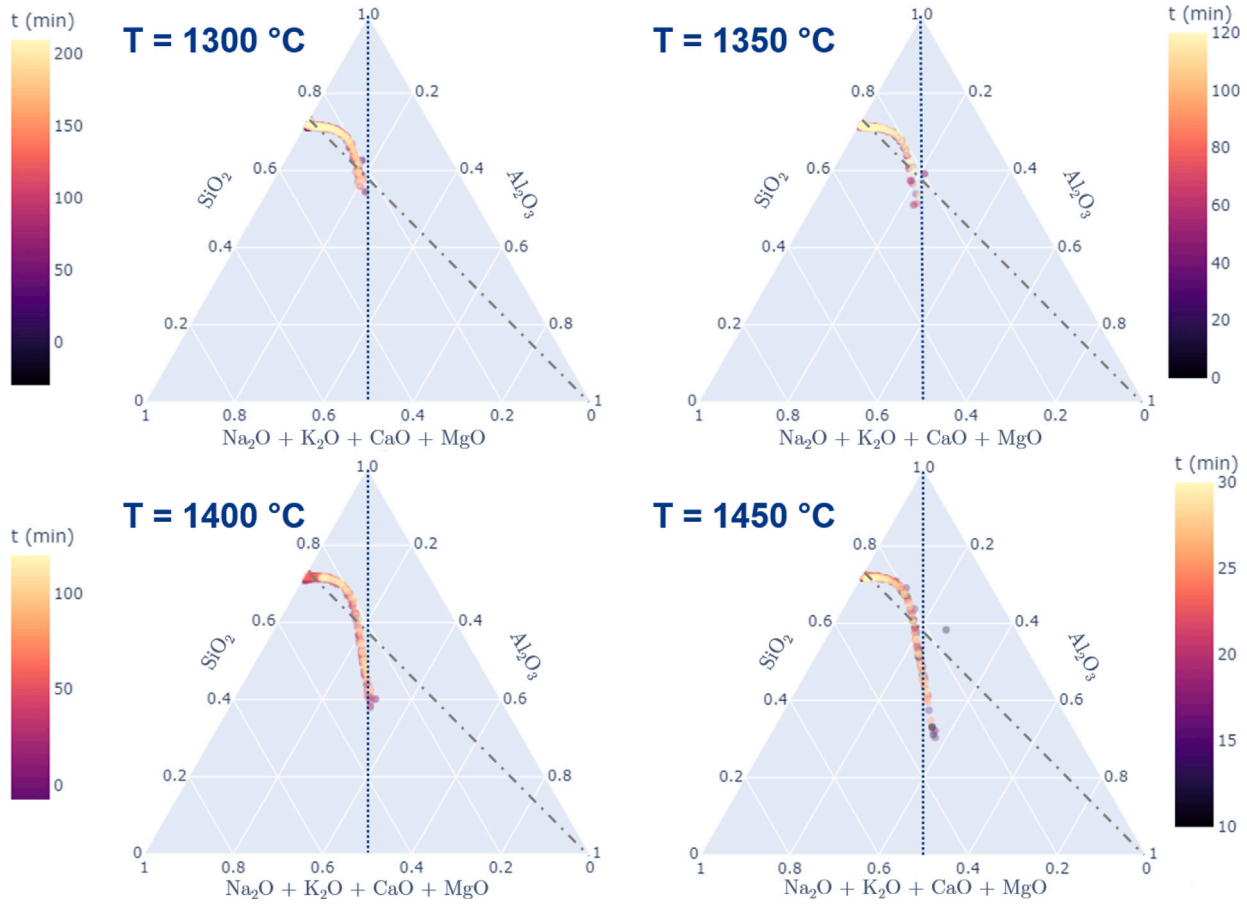

Fig. 7. Chemical profiles are plotted in the compositional space for each temperature (in %mol). The bottom left apex corresponds to the sum of Na_2O, K_2O, CaO and MgO. The gray dash-dot line represents the tie-line between the original glass composition and pure alumina, while the blue dashed line displays the meta-aluminous join.

Table 3
Eigenvalues (in 10^{-13} m^2/s) and eigenvectors calculated independently for each temperature. For 1400 and 1450 °C, the third and second eigenvectors are identical. Relative errors on the values are less than 5% [19].

	1300 °C			1350 °C			1400 °C		1450 °C	
λ_i	131.9	3.9	0.4	438.8	6.8	0.8	9.6	2.0	18.2	3.7
Na_2O+K_2O	0.06	−0.12	0.28	−0.05	−0.15	0.20	−0.11	0.22	−0.06	0.31
CaO+MgO	0.52	1	0.22	0.67	1	0.38	1	0.38	1	0.26
Al_2O_3	0.42	−0.87	0.50	0.38	−0.95	0.41	−0.81	0.40	−0.83	0.43
SiO_2	−1	−0.01	−1	−1	0.10	−1	−0.08	−1	−0.11	−1

Table 4
Eigenvalues (in 10^{-13} m^2/s) calculated for a shared basis of eigenvectors among all evaluated temperatures. As observed for matrices calculated independently at 1400 and 1450 °C, the third and second eigenvectors are identical when all data are treated together. Relative errors on the values are less than 5% [19].

Na_2O+K_2O	−0.11	0.34
CaO+MgO	1	0.24
Al_2O_3	−0.96	0.42
SiO_2	0.07	−1
	λ_1	λ_2
1300 °C	3.2	0.5
1350 °C	5.9	1.0
1400 °C	9.7	1.6
1450 °C	18.3	3.3

independently, displayed in Table 3. The degeneracy between the two last eigenvectors is also found using a shared eigenvector basis. For the whole temperature range, the ratio between eigenvalues is almost constant, with the fastest for the entire temperature range eigenvalue being about six times faster than the slowest.

This approach assumes that the exchange reactions that describe diffusion are constant across the studied temperature range. Given the excellent agreement between theoretical profiles calculated using this common eigenvector basis for all temperatures (Fig. 8), we deem this hypothesis valid. Therefore, the Discussion section will primarily focus on the matrices in Table 4.

4. Discussion

4.1. Eigenvectors as exchange reactions

The eigenvectors derived from the diffusion matrix offer an understanding of the exchange reactions governing the diffusive dissolution of alumina. As highlighted in the preceding section, two distinctive groups of exchange reactions can be distinguished from Table 4.

The primary eigenvector describes an exchange between alkaline earth oxides and alumina, with minimal dependence on silica and alkalis. This strong coupling between Al_2O_3 and CaO is consistent with previous observations in CAS, NCAS, NCAS-Zr, and CMAS systems [19–21,30]. The associated eigenvalue, approximately six times faster than

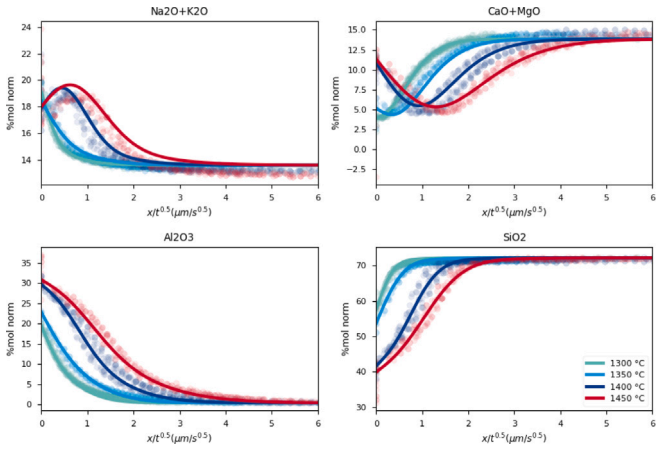

Fig. 8. Superposition of chemical profiles (in %mol) from experimental EPMA data (translucent dots) and the theoretical profiles (solid lines) calculated from the diffusion matrix in Table 4. For the latter, the interface composition was calculated as the median value for each temperature.

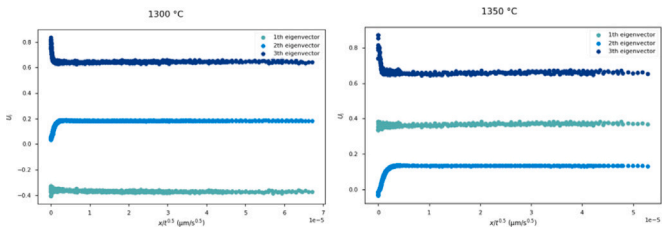

Fig. 9. Contribution of each eigenvector throughout the chemical profiles for 1300 (left) and 1350 °C (right) tests. These values (U_i) are calculated by linearizing the composition along each eigenvector.

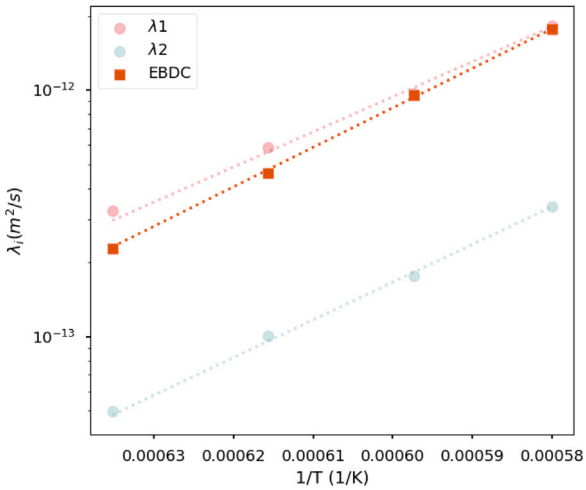

Fig. 10. Variation of eigenvalues and the effective binary coefficient of diffusion (EBDC) for alumina in function of reciprocal temperature. Both eigenvalues and EBDC were calculated using the common eigenvector basis for all temperatures (Table 4 matrices).

the second, effectively characterizes the far-from-interface region with subtle compositional gradients. Jacquemin [21] interprets this reaction as an exchange between calcium and glass network formers, with increasing contributions from alumina compared to silica as the glass composition approaches the peraluminous field. Our study reveals a departure from prior work as the calculated eigenvector exhibits almost no dependence on silica, even as the temperature increases, resulting in an excess of alumina near the interface, surpassing the Al/Ca ratio of the meta-aluminous join (Fig. 7).

The second eigenvector broadly describes the exchange of charge-balanced Al with Si which is visible in the interface region. This exchange reaction is identified as the slowest solely for alumina-rich compositions, exceeding 15% mol in the initial glass [21] or alumina dissolution [18]. Shaw et al. [18] propose that the sluggish exchange rate of this reaction arises from a lack of charge compensators in the peraluminous domain, consistent with our observations. However, Jacquemin [21] notes asymmetries in diffusion couple profiles approaching the meta-aluminous join, suggesting a potential shift in exchange mechanisms from peralkaline to peraluminous scenarios.

Given the valence difference between aluminum and silicon cations in the glass network, the association of alkali or alkaline earth oxides with alumina in all exchange reactions is consistent with expectations.

Surprisingly, the fastest eigenvector – identified only at temperatures of 1300 and 1350 °C in an independent set of eigenvectors (Table 3) – closely aligns with the exchange reaction occurring between silica and alumina. This alignment is unexpected, especially considering the significant differences in the calculated eigenvalues. To better understand the physical implications of this exchange reaction, its contribution (U_1) in the diffusion profile was calculated using Eq. (3) and displayed in Fig. 9. Among the two eigenvectors that are also part of the common basis, the second exchange reaction predominantly characterizes the far-field region, while the slowest (third) eigenvector effectively describes the dissolving interface region, where higher alumina gradients are present. However, the fastest eigenvector, restricted to temperatures of 1300 and 1350 °C, appears to contribute across the whole profile. Notably, this rapid exchange reaction between silica and alumina occurs at temperatures with more limited alumina solubility, where the interface compositions do not cross the meta-aluminous join. However, the current data do not permit further interpretation of this eigenvector.

In the literature, faster exchange reactions between alkalis and alkaline earth oxides have been derived from diffusion couple experiments designed for complete determination of the diffusion matrix, with associated eigenvalues typically 20 to 40 times higher than CaO exchange with network formers' [19–21,31]. The absence of this eigenvector derived from our data is linked to the fact that (in contrast to the diffusion couple method with multiple diffusion couples around a single composition) our dissolution tests explore a limited range of compositional space and cannot be used to find all exchange reactions, as detailed in the preceding section. The same is also true for the mechanism involving the exchange of Al and Si with low-valence cations observed in previous studies [8,19,21,32], but that cannot be observed here because of the forced anti-correlation between silica and alumina that results from alumina dissolution.

4.2. Eigenvalues dependence with temperature

Given the excellent agreement observed between experimental data and theoretical profiles in Fig. 8, and assuming a consistent eigenvector basis across the entire temperature spectrum (Table 4), a comparative analysis of the temperature-dependent behavior of associated eigenvalues becomes feasible. Fig. 10 illustrates the exponential dependence of these eigenvalues as a function of reciprocal temperature, aligning with an Arrhenian-type behavior. This alignment may be used to calculate the activation energy for each exchange reaction, offering valuable insights into the underlying energetics.

In addition to the eigenvalues, the effective binary diffusion coefficient (EBDC) for alumina was calculated at each temperature using theoretical profiles. This calculation assumes a binary diffusion scenario, treating alumina's exchange with all other oxides as a single

Table 5
Activation energy calculated assuming an Arrhenian-type behavior of eigenvalues from the common eigenvector basis, and effective binary diffusion coefficient (EBDC) for alumina with temperature, as well as their coefficients of determination (R^2).

	Activation energy (kJ/mol)	R^2
λ_1	251	0.999
λ_2	316	0.992
EBDC	306	0.997

component. The EBDC for alumina was determined by fitting the alumina profile itself with a binary diffusion version of Eq. (4):

$$C_i(x,t) = (C_{i,x=0} - C_{i,t=0})\mathrm{erfc}\left(\frac{x}{2\sqrt{\mathrm{EBDC}t}}\right) + C_{i,t=0} \quad (5)$$

where C is the alumina composition instead of the linearized contribution, and EBDC replaces the eigenvalue in Eq. (4).

This approach applies to alumina in light of profiles that approach an error function (Fig. 8, bottom left), allowing for comparison with a broader range of literature values, as pseudo-binary coefficients of diffusion are more frequently reported than diffusion matrices.

Similar to the eigenvalues, the EBDC for alumina is depicted as a function of $1/T$ in Fig. 10, showing a remarkable approach to Arrhenian-type behavior. Values of the EBDC for Al are close to those of the eigenvalue of the exchange reaction between alkaline earth oxides and alumina at all temperatures.

For a comprehensive summary, Table 5 presents activation energy values for both eigenvalues and the alumina-associated EBDC, demonstrating excellent agreement with Arrhenian behavior. Notably, these activation energies closely resemble those reported for the slowest eigenvalues of an NCAS diffusion matrix containing 7% mol Al_2O_3, calculated for the temperature range 1200 to 1360 °C [19]. In the same study, Claireaux et al. [19] found similar activation energy from viscosity measurements of the same glass system.

4.3. Literature diffusion coefficients comparison and viscosity relationship

To compare our alumina diffusivity data with those of the literature requires taking into account the effects of chemical composition, temperature, and measurement methods. Complexities arise from different methodologies used by different studies. For example, most aluminum diffusivities in the literature are reported as effective binary diffusion coefficients (EBDC) in different melts, treating alumina as one component and combining all other components [33]. The comparison with studies that derive diffusion matrices requires theoretical profiles for alumina and subsequent EBDC calculation, which is feasible only for monotonic profiles.

In order to address the diverse chemical composition and/or temperature, viscosity is potentially a relevant parameter to link these properties and allow a comparison with the literature data. In detail, viscosities predicted by the quasi-chemical model used by FactSage seem to be overestimated when compared to experimental data [21,28], but may nevertheless be used as a comparative tool in relative terms, even if not as an absolute measure.

In addition, dissolution data present additional challenges due to varying compositions and viscosities along the sample's chemical profiles. To tackle this, minimum, maximum, and interface viscosities were calculated when both interface and matrix data were available. For cases where only interface and original compositions were provided, viscosity was limited to this compositional range.

Notably, Shaw et al., Claireaux et al. and Jacquemin [18,19,21] are among the few studies presenting data as diffusion matrices, with only Shaw et al. [18] employing dissolution tests, akin to our work. Considering coupled diffusion, the viscosity behavior may not be monotonous, with the possibility that the interface composition is not necessarily at a viscosity extremum. This phenomenon is particularly the case for experiments showing uphill diffusion.

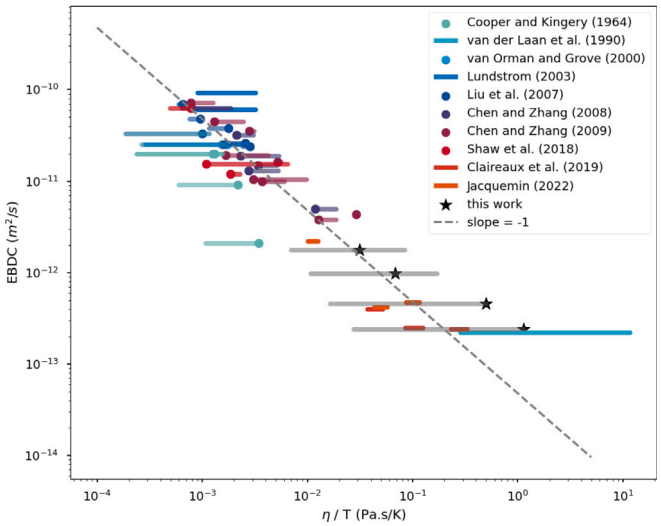

Fig. 11. Compilation of effective binary coefficient of diffusion for alumina as a function of viscosity and temperature ratio. The EBDC covers a range of viscosities, from the lower to higher viscosity compositions along the profile. The position of the symbol indicates the viscosity of the interface for data from dissolution tests. The data without markers are from diffusion couple tests. The dashed line is a linear regression imposing the −1 slope, assuming Eyring's diffusivity. Further details can be found in the text.

The compilation of alumina diffusivities expressed as an EBDC value as a function of viscosity range over temperature is illustrated in Fig. 11 (c.f. Fig. 1 for the compositions of the melts considered).

Assuming that diffusivity has a dependence on viscosity according to the Eyring equation, a plot of $\ln D$ as a function of $\ln \eta/T$ should theoretically have a slope of −1:

$$D = \frac{k_B T}{\eta \lambda} \quad (6)$$

where k_B is the Boltzmann constant, T is the absolute temperature in kelvin, η is viscosity, and λ is the "jump-distance" during each diffusive step.

This potential −1 slope between EBDC and viscosity-temperature ratio in the log–log scale is plotted as the dashed gray line in Fig. 11. This comparison shows that there is a good first-order agreement with theoretical expectations. In detail, the viscosity that best fits this correlation is the viscosity at the mineral-liquid interface (rather than the maximum value encountered along the diffusion profile). Furthermore, the intercept value of this fitting provides a $\lambda = 2.9$ angströms, which agrees with the O^{2-} ion diameter commonly found as the diffusive step in anhydrous polymerized melts [19,34,35].

Even so, only 62% of the variance can be explained by the dependence on the ratio of the interface viscosity to absolute temperature. This fit seems inadequate as we approach higher values of viscosity to temperature ($\eta/T > 10^{-1}$ Pa s/K), including this work's dissolution data for lower temperatures.

The interface and maximum viscosity values are the same for the 1300 and 1350 °C data since no noticeable maximum or minimum is visible in the chemical profiles (Fig. 5). As pointed out as a challenge for the interface composition definition, the EPMA spatial resolution restricts a better definition of an eventual inflection region in the behavior close to the interface, as seen for 1400 and 1450 °C.

However, for $\eta/T < 10^{-1}$ Pa s/K, the alumina EBDC seems to be coupled with the viscosity near the interface, as expected by Eyring diffusivity for network forming elements. This trend for alumina was consistently seen in data from different sources, coming from both scalar diffusivities and matrix data, indicating that the EBDC approximation is satisfactory in describing alumina diffusivity.

Table 6
4 × 4 diffusion matrices calculated from the eigenvalues and eigenvectors using a shared basis for all temperatures. The diagonal terms, i.e., the coefficients that link the diffusivity of one element to its own chemical composition gradient, are highlighted in light gray.

	T = 1300 °C			
	Na_2O+K_2O	CaO+MgO	Al_2O_3	SiO_2
Na_2O+K_2O	2.2	−2.22	1.07	−1.06
CaO+MgO	32.7	4.85	−34.2	−3.33
Al_2O_3	−30.3	−3.85	33.4	0.708
SiO_2	−4.62	1.23	−0.284	3.68
	T = 1350 °C			
	Na_2O+K_2O	CaO+MgO	Al_2O_3	SiO_2
Na_2O+K_2O	0.693	−2.29	3.72	−2.12
CaO+MgO	50.9	10.7	−55.6	−5.92
Al_2O_3	−56.1	−4.57	59.8	0.83
SiO_2	4.46	−3.78	−7.89	7.22
	T = 1400 °C			
	Na_2O+K_2O	CaO+MgO	Al_2O_3	SiO_2
Na_2O+K_2O	−18.9	4.89	17.6	−3.66
CaO+MgO	69.3	25.6	−84.8	−10.1
Al_2O_3	−120	3.27	116	1.34
SiO_2	70	−33.8	−48.6	12.4
	T = 1450 °C			
	Na_2O+K_2O	CaO+MgO	Al_2O_3	SiO_2
Na_2O+K_2O	−33.5	8.62	31.8	−6.99
CaO+MgO	126	47.6	−155	−18.7
Al_2O_3	−220	5.65	212	2.14
SiO_2	127	−61.9	−88.9	23.6

The description of alumina diffusivity by an effective binary coefficient was possible due to its continuous behavior along the diffusion profiles, i.e., no uphill diffusion. Mathematically, the necessary and sufficient conditions to observe uphill diffusion are a significant participation of off-diagonal terms compared to diagonal ones, and when the sign of the diffusive flux of the given element of interest is reversed due to the strong coupling of this element with the concentration gradients of the other diffusing components [27]. If we express the eigenvalues and eigenvectors as 4 × 4 diffusion matrices, it is possible to compare the contributions of each element on each component diffusivity. Table 6 displays the Table 4 results as matrices. For all temperatures, the diagonal term for alumina is always greater than the off-diagonal terms, which means that its diffusivity principally depends on its own chemical gradient. Meanwhile, alkaline and earth-alkaline oxides display the opposite trend: the off-diagonal terms are comparable to the diagonal terms, suggesting that their mobilities are highly influenced by the other components' chemical composition gradients and, thus, displaying uphill diffusion features.

Therefore, the diffusivities of components less subjected to strong coupling (i.e., the case for alumina) can be approximated by an EBDC. However, to better understand what happens in the whole studied system, the behavior of all the elements must be considered, including elements with strong coupling between them. Thanks to the diffusion matrix approach, features like the onset of convection, even in an initially gravitational stable setup, as well as the interface composition falling outside of the tie-line, can be better explained.

5. Conclusions

In conclusion, this study contributes to clarifying the mechanisms that govern the dissolution of alumina in soda-lime-silica glass compositions. Chemical profiles derived from electron probe micro-analysis (EPMA) in the glass exhibited diffusion-controlled behavior across all studied temperatures, from 1300 to 1450 °C.

However, a single diffusion coefficient cannot explain the inflections observed in the profiles of alkalis and alkaline-earth oxides. Instead, a multicomponent diffusion approach is required, replacing scalar diffusivity with a diffusion matrix. This approach revealed two primary exchange reactions that persist throughout the examined temperature range. The first eigenvector corresponds to an exchange between alumina and alkaline earth oxides (visible in the far-field region). At the same time, the second describes an exchange between the network formers (visible near the dissolving interface).

Given the absence of uphill diffusion for alumina profiles, this oxide's diffusivity can be approximated by an effective binary coefficient (EBDC). Considering this value as a function of the viscosities of melt across the dissolution profile shows a good correlation between the interface viscosity and the diffusivity. Interestingly, our data indicate that the interface viscosity does not necessarily correspond to the maximum viscosity in the glass, especially for samples for which the interface melt composition crosses the meta-aluminous join. Moreover, the maximum viscosity does not seem to hinder alumina diffusion, suggesting that melt mobility at the mineral-liquid interface (correlated to viscosity) is a rate-limiting step.

While these results agree with previously reported data for alumina diffusivity, they also underline the need to consider the coupling among the elements composing the glass structure to fully understand dissolution phenomena. Further investigations are necessary to describe better the specific mechanisms behind the mobility of the glass entities in the peraluminous domain, as displayed by the near-interface region of our dissolution test samples.

CRediT authorship contribution statement

Fatima T. Yoshizawa: Writing – original draft, Visualization, Methodology, Investigation, Formal analysis, Data curation. **Anne-Céline Garel-Laurin:** Writing – review & editing, Validation, Supervision, Resources. **Ekaterina Burov:** Writing – review & editing, Validation, Supervision, Project administration, Conceptualization. **Michael J. Toplis:** Writing – review & editing, Validation, Supervision, Project administration, Funding acquisition, Conceptualization.

Declaration of competing interest

The authors declare the following financial interests/personal relationships which may be considered as potential competing interests: Fatima Tiemi Yoshizawa reports financial support and equipment, drugs, or supplies were provided by Saint-Gobain Recherche. If there are other authors, they declare that they have no known competing financial interests or personal relationships that could have appeared to influence the work reported in this paper.

Acknowledgments

The authors would like to thank Lionel Homo, Bertrand Testulat, and Régine Faure for their valuable assistance with EPMA measurements, and Mikayel Arzakantsyan for providing the sapphire sample. This research was supported by the CNRS and Saint-Gobain Recherche, with additional financial support from ANRT through the CIFRE fellowship (2021/0002).

Appendix. Detailed compilation of all the experiments

See Table A.7.

Data availability

Data is available in the manuscript.

Table A.7
Compilation of experimental conditions for each sample. The first digits in the samples' name are the nominal temperature in °C, followed by the nominal time duration in minutes and then by the replica number. PAm corresponds to dissolution tests using sapphire as the alumina source. Only samples without convection were considered for the analysis.

Sample name	Alumina source	Convection	Time duration (min)	Measured temperature (°C)	Interface composition (mol)					
					Na2O	K2O	Al2O3	CaO	MgO	SiO2
PA1300-30-1	Sintered alumina	No	30	1298,1 ± 1,0	19,2%	0,1%	17,9%	2,7%	0,1%	60,0%
PA1300-30-2	Sintered alumina	No	30	1298,1 ± 1,0	17,9%	0,1%	17,3%	2,0%	0,1%	62,5%
PA1300-30-3	Sintered alumina	No	30	1298,1 ± 1,0	17,9%	0,1%	17,3%	2,0%	0,1%	62,5%
PA1300-60-1	Sintered alumina	No	60	1296,8 ± 0,6	18,3%	0,0%	19,3%	3,4%	0,2%	58,8%
PA1300-60-2	Sintered alumina	No	60	1296,8 ± 0,6	19,8%	0,0%	22,2%	3,5%	0,1%	54,4%
PA1300-60-3	Sintered alumina	No	60	1296,8 ± 0,6	19,8%	0,0%	22,2%	3,5%	0,1%	54,4%
PA1300-90-1	Sintered alumina	No	90	1300 ± 0	20,0%	0,0%	19,1%	3,5%	0,3%	57,0%
PA1300-90-2	Sintered alumina	No	90	1300 ± 0	19,7%	0,0%	18,7%	2,9%	0,1%	58,7%
PA1300-90-3	Sintered alumina	No	90	1300 ± 0	19,7%	0,0%	18,7%	2,9%	0,1%	58,7%
PA1300-120-1	Sintered alumina	No	120	1298,4 ± 0,6	19,0%	0,0%	19,2%	3,7%	0,4%	57,8%
PA1300-120-2	Sintered alumina	No	120	1298,4 ± 0,6	19,9%	0,0%	20,2%	3,8%	0,2%	55,9%
PA1300-120-3	Sintered alumina	No	120	1298,4 ± 0,6	19,9%	0,0%	20,2%	3,8%	0,2%	55,9%
PA1300-150-1	Sintered alumina	No	150	1300 ± 0	18,9%	0,0%	18,8%	3,7%	0,3%	58,3%
PA1300-150-2	Sintered alumina	No	150	1300 ± 0	18,4%	0,0%	19,9%	3,6%	0,3%	57,6%
PA1300-150-3	Sintered alumina	No	150	1300 ± 0	18,4%	0,0%	19,9%	3,6%	0,3%	57,6%
PA1300-210-1	Sintered alumina	No	210	1300 ± 0	19,2%	0,0%	19,8%	4,1%	0,3%	56,5%
PA1300-210-2	Sintered alumina	No	210	1300 ± 0	18,6%	0,0%	19,4%	3,9%	0,3%	57,8%
PA1300-210-3	Sintered alumina	No	210	1300 ± 0	18,6%	0,0%	19,4%	3,9%	0,3%	57,8%
PA1350-45-1	Sintered alumina	No	45	1349,0 ± 0,5	18,6%	0,0%	21,8%	5,4%	0,3%	53,8%
PA1350-45-2	Sintered alumina	No	45	1349,0 ± 0,5	17,2%	0,1%	21,1%	2,3%	0,3%	59,1%
PA1350-45-3	Sintered alumina	No	45	1349,0 ± 0,5	17,2%	0,1%	21,1%	2,3%	0,3%	59,1%
PA1350-60-1	Sintered alumina	No	60	1349,5 ± 0,6	19,5%	0,0%	23,2%	5,4%	0,4%	51,4%
PA1350-60-2	Sintered alumina	No	60	1349,5 ± 0,6	19,8%	0,0%	22,7%	5,8%	0,6%	51,0%
PA1350-60-3	Sintered alumina	No	60	1349,5 ± 0,6	19,8%	0,0%	22,7%	5,8%	0,6%	51,0%
PA1350-120-1	Sintered alumina	No	120	1348,8 ± 0,4	18,1%	0,0%	20,9%	4,7%	0,4%	55,9%
PA1350-120-2	Sintered alumina	No	120	1348,8 ± 0,4	18,4%	0,0%	22,9%	4,8%	0,4%	53,5%
PA1350-120-3	Sintered alumina	No	120	1348,8 ± 0,4	18,4%	0,0%	22,9%	4,8%	0,4%	53,5%
PA1400-15-1	Sintered alumina	No	15	1401,7 ± 2,7	17,8%	0,1%	30,3%	10,2%	0,8%	40,8%
PA1400-15-2	Sintered alumina	No	15	1401,7 ± 2,7	21,4%	0,1%	31,9%	6,4%	0,1%	40,2%
PA1400-15-3	Sintered alumina	No	15	1401,7 ± 2,7	20,5%	0,2%	28,6%	2,2%	−0,7%	49,2%
PA1400-15-4	Sintered alumina	No	15	1401,7 ± 2,7	20,5%	0,2%	28,6%	2,2%	−0,7%	49,2%
PA1400-15-5	Sintered alumina	No	15	1402,2 ± 3,1	19,2%	0,0%	31,6%	10,2%	0,7%	38,2%
PA1400-15-6	Sintered alumina	No	15	1402,2 ± 3,1	19,3%	0,1%	31,7%	8,6%	0,3%	40,1%
PA1400-15-7	Sintered alumina	No	15	1401,7 ± 2,7	18,9%	0,0%	32,6%	8,9%	0,1%	39,6%
PA1400-15-8	Sintered alumina	No	15	1401,7 ± 2,7	18,8%	0,0%	28,6%	5,8%	−0,7%	47,4%
PA1400-30-1	Sintered alumina	No	30	1400 ± 0	17,9%	0,0%	30,4%	10,6%	0,9%	40,2%
PA1400-30-2	Sintered alumina	No	30	1400 ± 0	21,9%	0,1%	32,7%	5,3%	−0,2%	40,2%
PA1400-30-3	Sintered alumina	No	30	1400 ± 0	20,2%	0,0%	33,1%	9,3%	0,4%	36,9%
PA1400-30-4	Sintered alumina	No	30	1400 ± 0	20,2%	0,0%	33,1%	9,3%	0,4%	36,9%
PA1400-30-5	Sintered alumina	No	31	1396,3 ± 0,8	21,5%	0,0%	33,2%	9,3%	0,4%	35,6%
PA1400-30-6	Sintered alumina	No	31	1396,3 ± 0,8	22,7%	0,1%	33,5%	7,9%	0,1%	35,7%
PA1400-30-7	Sintered alumina	No	31	1396,3 ± 0,8	17,8%	0,1%	28,9%	10,0%	0,9%	42,5%
PA1400-30-8	Sintered alumina	No	31	1396,3 ± 0,8	17,8%	0,1%	28,9%	10,0%	0,9%	42,5%
PA1400-30-9	Sintered alumina	No	31	1396,3 ± 0,8	22,4%	0,1%	33,8%	7,6%	0,5%	35,7%
PAm1400-30-1	Sapphire	No	31	1396,3 ± 0,8	19,7%	0,1%	29,5%	9,0%	0,7%	40,9%
PAm1400-30-2	Sapphire	No	31	1396,3 ± 0,8	19,8%	0,1%	31,1%	8,8%	0,8%	39,5%
PAm1400-30-3	Sapphire	No	31	1396,3 ± 0,8	22,0%	0,0%	31,7%	7,7%	0,6%	37,9%
PAm1400-30-4	Sapphire	Yes	31	1396,3 ± 0,8	22,0%	0,0%	31,7%	7,7%	0,6%	37,9%
PA1400-60-1	Sintered alumina	No	60	1399,4 ± 0,8	17,1%	0,0%	29,3%	10,1%	0,8%	42,7%
PA1400-60-2	Sintered alumina	No	60	1399,4 ± 0,8	18,8%	0,0%	30,1%	9,6%	0,6%	40,8%
PA1400-60-3	Sintered alumina	No	60	1399,4 ± 0,8	16,2%	0,0%	29,6%	11,1%	0,8%	42,3%
PA1400-60-4	Sintered alumina	No	60	1399,4 ± 0,8	16,2%	0,0%	29,6%	11,1%	0,8%	42,3%
PA1400-120-1	Sintered alumina	No	119	1398,9 ± 0,6	16,9%	0,0%	29,0%	10,4%	0,9%	42,8%
PA1400-120-2	Sintered alumina	No	119	1398,9 ± 0,6	17,1%	0,0%	29,4%	10,3%	0,7%	42,5%
PA1400-120-3	Sintered alumina	No	119	1398,9 ± 0,6	17,9%	0,0%	29,4%	9,5%	0,7%	42,4%
PA1400-120-4	Sintered alumina	Yes	119	1398,9 ± 0,6	17,9%	0,0%	29,4%	9,5%	0,7%	42,4%
PA1400-180-1	Sintered alumina	Yes	179	1399,3 ± 0,7	16,8%	0,0%	26,5%	9,7%	1,1%	45,8%
PA1400-180-2	Sintered alumina	Yes	179	1399,3 ± 0,7	16,9%	0,0%	26,9%	9,6%	1,0%	45,6%
PA1400-180-3	Sintered alumina	Yes	179	1399,3 ± 0,7	18,3%	0,0%	29,4%	9,7%	0,7%	41,8%
PA1400-180-4	Sintered alumina	Yes	179	1399,3 ± 0,7	16,9%	0,0%	26,5%	9,9%	1,1%	45,6%
PA1400-360-3	Sintered alumina	Yes	359	1399,4 ± 0,7	16,9%	0,0%	26,5%	9,9%	1,1%	45,6%
PA1400-360-4	Sintered alumina	Yes	359	1399,4 ± 0,7	12,7%	0,0%	26,6%	12,9%	1,8%	46,0%
PA1400-1440-1	Sintered alumina	Yes	1440	1399,8 ± 0,7	10,4%	0,0%	24,9%	13,1%	3,3%	48,3%
PA1400-1440-2	Sintered alumina	Yes	1440	1399,8 ± 0,7	10,5%	0,0%	25,2%	12,9%	3,2%	48,2%
PA1400-1440-3	Sintered alumina	Yes	1440	1399,8 ± 0,7	10,7%	0,0%	24,5%	13,1%	3,0%	48,6%
PA1400-1440-4	Sintered alumina	Yes	1440	1399,8 ± 0,7	10,7%	0,0%	24,5%	13,1%	3,0%	48,6%
PAm1400-1440-1	Sapphire	Yes	1440	1399,8 ± 0,7	9,8%	0,0%	25,7%	13,3%	3,3%	47,8%
PAm1400-1440-2	Sapphire	Yes	1440	1399,8 ± 0,7	10,2%	0,0%	25,2%	13,3%	3,2%	48,2%
PAm1400-1440-3	Sapphire	Yes	1440	1399,8 ± 0,7	9,9%	0,0%	23,5%	12,6%	3,0%	51,0%
PAm1400-1440-4	Sapphire	Yes	1440	1399,8 ± 0,7	9,9%	0,0%	23,5%	12,6%	3,0%	51,0%
PA1450-10-1	Sintered alumina	No	10	1449,5 ± 2,0	21,8%	0,1%	36,6%	9,4%	1,1%	31,1%
PA1450-10-2	Sintered alumina	No	10	1449,5 ± 2,0	19,2%	0,1%	25,9%	−2,0%	−1,5%	58,3%

(*continued on next page*)

Table A.7 (*continued*).

PA1450-10-3	Sintered alumina	No	10	1449,5 ± 2,0	20,2%	0,0%	35,3%	10,7%	0,6%	33,2%
PA1450-10-4	Sintered alumina	No	10	1449,5 ± 2,0	20,2%	0,0%	35,3%	10,7%	0,6%	33,2%
PA1450-15-1	Sintered alumina	No	15	1448,3 ± 1,3	21,3%	0,0%	36,6%	9,5%	0,4%	32,1%
PA1450-15-2	Sintered alumina	No	15	1448,3 ± 1,3	23,8%	0,1%	37,0%	3,7%	−0,7%	36,1%
PA1450-15-3	Sintered alumina	No	15	1448,3 ± 1,3	17,8%	0,0%	32,5%	11,4%	0,8%	37,5%
PA1450-15-4	Sintered alumina	Yes	15	1448,3 ± 1,3	17,8%	0,0%	32,5%	11,4%	0,8%	37,5%
PA1450-20-1	Sintered alumina	No	20	1449,1 ± 1,6	21,3%	0,0%	36,2%	9,8%	0,6%	32,1%
PA1450-20-2	Sintered alumina	No	20	1449,1 ± 1,6	16,6%	0,0%	30,5%	10,9%	0,8%	41,1%
PA1450-20-3	Sintered alumina	No	20	1449,1 ± 1,6	16,9%	0,0%	30,1%	10,7%	0,8%	41,5%
PA1450-20-4	Sintered alumina	No	20	1449,1 ± 1,6	16,9%	0,0%	30,1%	10,7%	0,8%	41,5%
PA1450-25-1	Sintered alumina	No	25	1448,2 ± 1,1	19,2%	0,0%	34,2%	10,8%	0,9%	34,8%
PA1450-25-2	Sintered alumina	No	25	1448,2 ± 1,1	17,4%	0,0%	31,1%	10,9%	0,9%	39,7%
PA1450-25-3	Sintered alumina	No	25	1448,2 ± 1,1	16,7%	0,0%	30,3%	11,5%	1,1%	40,4%
PA1450-25-4	Sintered alumina	No	25	1448,2 ± 1,1	16,7%	0,0%	30,3%	11,5%	1,1%	40,4%
PA1450-30-1	Sintered alumina	No	30	1449,0 ± 1,0	17,5%	0,0%	29,8%	9,6%	0,9%	42,2%
PA1450-30-2	Sintered alumina	No	30	1449,0 ± 1,0	17,0%	0,0%	29,4%	10,1%	1,0%	42,5%
PA1450-30-3	Sintered alumina	No	30	1449,0 ± 1,0	18,2%	0,0%	30,3%	9,4%	1,1%	41,0%
PA1450-30-4	Sintered alumina	Yes	30	1449,0 ± 1,0	18,2%	0,0%	30,3%	9,4%	1,1%	41,0%

References

[1] A.R. Cooper, W.D. Kingery, Dissolution in ceramic systems: I, molecular diffusion, natural convection, and forced convection studies of sapphire dissolution in calcium aluminum silicate, J. Am. Ceram. Soc. 47 (1) (1964).

[2] K.H. Sandhage, G.J. Yurek, Indirect dissolution of sapphire into silicate melts, J. Am. Ceram. Soc. 71 (6) (1988).

[3] Y. Zhang, Geochemical Kinetics, Princeton University Press, Princeton, N.J, 2008.

[4] J. Liu, F. Verhaeghe, M. Guo, B. Blanpain, P. Wollants, In situ observation of the dissolution of spherical alumina particles in CaO–Al2O3–SiO2 melts, J. Am. Ceram. Soc. 90 (12) (2007).

[5] M.K. Choudhary, R. Venuturumilli, M.R. Hyre, Mathematical modeling of flow and heat transfer phenomena in glass melting, delivery, and forming processes, Int. J. Appl. Glass Sci. 1 (2) (2010).

[6] R. Beerkens, Modeling of the melting process in industrial glass furnaces, in: Mathematical Simulation in Glass Technology, Springer, 2002, pp. 17–73.

[7] Y. Zhang, D. Walker, C.E. Lesher, Diffusive crystal dissolution, Contrib. Miner. Pet. 102 (1989) 492–513.

[8] Y. Liang, Diffusive dissolution in ternary systems: analysis with applications to quartz and quartzite dissolution in molten silicates, Geochim. Cosmochim. Acta 63 (23–24) (1999) 3983–3995.

[9] Y. Liang, Kinetics of crystal-melt reaction in partially molten silicates: 1. grain scale processes, Geochem. Geophys. Geosyst. 4 (5) (2003).

[10] M.J. Moran, H.N. Shapiro, D.D. Boettner, M.B. Bailey, Fundamentals of Engineering Thermodynamics, John Wiley & Sons, 2010.

[11] S. Zhang, H.R. Rezaie, H. Sarpoolaky, W.E. Lee, Alumina dissolution into silicate slag, J. Am. Ceram. Soc. 83 (4) (2000).

[12] X. Yu, R. Pomfret, K. Coley, Dissolution of alumina in mold fluxes, Metall. Mater. Trans. B 28 (1997) 275–279.

[13] J.A. van Orman, T.L. Grove, Origin of lunar high-titanium ultramafic glasses: Constraints from phase relations and dissolution kinetics of clinopyroxene-ilmenite cumulates, Meteorit. Planet. Sci. 35 (4) (2000) 783–794.

[14] Z. Morgan, Y. Liang, P. Hess, An experimental study of anorthosite dissolution in lunar picritic magmas: Implications for crustal assimilation processes, Geochim. Cosmochim. Acta (2006).

[15] Y. Chen, Y. Zhang, Olivine dissolution in basaltic melt, Geochim. Cosmochim. Acta (2008).

[16] Y. Chen, Y. Zhang, Clinopyroxene dissolution in basaltic melt, Geochim. Cosmochim. Acta (2009).

[17] Y. Zhang, H. Ni, Y. Chen, Diffusion data in silicate melts, Rev. Mineral. Geochem. 72 (1) (2010) 311–408.

[18] C.S.J. Shaw, K.B. Klausen, H. Mao, Kinetics of dissolution of sapphire in melts in the CaO–Al2O3–SiO2 system, Geochim. Cosmochim. Acta (2018).

[19] C. Claireaux, Influence of temperature on multicomponent diffusion in calcium and sodium aluminosilicate melts, J. Non-Cryst. Solids (2019).

[20] M. Ficheux, Influence of zirconium on cation mobilities in Na2O-CaO-Al2O3-SiO2 melts: A multicomponent diffusion and XANES study, Geochim. Cosmochim. Acta (2020).

[21] M. Jacquemin, Mobilité Couplée à Haute Température et Modifications Structurales dans les Verres Na2O-CaO-Al2O3-SiO2 (Ph.D. thesis), Université d'Orléans, 2022, Available at https://theses.hal.science/tel-04097368.

[22] C.S. Shaw, The effect of experiment geometry on the mechanism and rate of dissolution of quartz in basanite at 0.5 GPa and 1350 C, Contrib. Miner. Pet. 139 (5) (2000) 509–525.

[23] C. Lundstrom, An experimental investigation of the diffusive infiltration of alkalis into partially molten peridotite: Implications for mantle melting processes, Geochem. Geophys. Geosyst. 4 (9) (2003).

[24] Y. Liang, Axisymmetric double-diffusive convection in a cylindrical container: Linear stability analysis with applications to molten CaO–Al 2 O 3-SiO 2, Geophys. Monogr. Ser. 94 (1995) 115–124.

[25] C. Merlet, An accurate computer correction program for quantitative electron probe microanalysis, Microchim. Acta 114 (1994) 363–376.

[26] C.W. Bale, P. Chartrand, S. Degterov, G. Eriksson, K. Hack, R.B. Mahfoud, J. Melançon, A. Pelton, S. Petersen, Factsage thermochemical software and databases, CALPHAD 26 (2) (2002) 189–228.

[27] Y. Liang, Multicomponent diffusion in molten silicates: Theory, experiments, and geological applications, Rev. Mineral. Geochem. 72 (1) (2010) 409–446.

[28] C. Claireaux, M.-H. Chopinet, E. Burov, E. Gouillart, M. Roskosz, M.J. Toplis, Atomic mobility in calcium and sodium aluminosilicate melts at 1200 C, Geochim. Cosmochim. Acta 192 (2016) 235–247.

[29] S. Chakraborty, D.B. Dingwell, D.C. Rubie, Multicomponent diffusion in ternary silicate melts in the system K2O-A12O3-SiO2: II. Mechanisms, systematics, and geological applications, Geochim. Cosmochim. Acta 59 (2) (1995) 265–277.

[30] Y. Liang, F. Richter, A. Davis, E. Brucewatson, Diffusion in silicate melts: I. self diffusion in CaO-AI203-SiO2 at 1500 °C and 1 GPa, Geochim. Cosmochim. Acta (1996).

[31] A.F. Trial, F.J. Spera, Measuring the multiõmponentelusion matrix: Expriment design and data analysis for silicate melts, Geochim. Cosmochim. Acta (1994).

[32] F.M. Richter, Y. Liang, W.G. Minarik, Multicomponent diffusion and convection in molten MgO–Al2O3–SiO2, Geochim. Cosmochim. Acta 62 (11) (1998) 1985–1991.

[33] Y. Zhang, T. Gan, Diffusion in melts and magmas, Rev. Mineral. Geochem. 87 (1) (2022) 283–337.

[34] D.R. Baker, Estimation of diffusion coefficients during interdiffusion of geologic melts: Application of transition state theory, Chem. Geol. 98 (1–2) (1992) 11–21.

[35] H. Ni, H. Hui, G. Steinle-Neumann, Transport properties of silicate melts, Rev. Geophys. 53 (2015) 715–744, http://dx.doi.org/10.1002/2015rg000485.

Chapter 4

Quartz dissolution

This chapter provides a comprehensive analysis of quartz dissolution in soda-lime silica glass at 1400°C, focusing on mass transport and microstructural evolution. Beginning with a theoretical overview of silica polymorphism and thermodynamics, the chapter explores the potential role of phase transformations on dissolution rates and on how to experimentally measure it. The chapter concludes with a proposed dissolution mechanism, integrating the influence of solubility, diffusivity, and microstructural changes observed during the experiments.

Chapter's table of contents

4.1 Introduction and theoretical background . . . 80
4.1.1 Silica polymorphism . . . 80
4.1.2 Thermodynamics calculations . . . 84
4.1.3 Silica diffusive dissolution . . . 93
4.1.4 Theoretical scenarios for quartz dissolution . . . 97
4.2 Silica dissolution methods . . . 100
4.2.1 Experimental setup geometry adaptations . . . 100
4.2.2 Use of silica sources other than quartz as starting material . . . 102
4.2.3 Compilation of silica dissolution tests . . . 105
4.2.4 Quantification of dissolved silica . . . 108
4.3 Microstructure evolution in quartz dissolution . . . 112
4.3.1 Silica polymorphs evolution . . . 117
4.3.2 Dissolved silica evolution . . . 123
4.3.3 Cristobalite dissolution evolution . . . 125
4.3.4 Estimation of cristobalite contribution to dissolution in PSq tests . . . 131
4.4 Mass transport of silica in the glass . . . 134
4.4.1 Thermodynamic equilibrium at the interface . . . 139
4.4.2 Origins of convection onset . . . 141
4.5 Towards a quartz dissolution mechanism . . . 145

4.1 Introduction and theoretical background

The primary raw material for industrial-scale soda-lime-silica glass melting is sand, which consists predominantly of crystalline silica in the form of quartz, being the most refractory compound intentionally added to the batch. As detailed in Section 1.1, the dissolution of sand grains within the glass bath can account for up to 90% of the total time required for complete melting [3]. This process must be concluded before the onset of the refining step in the glass tank. Due to the extended dwell times required, optimizing silica dissolution kinetics has been the subject of significant research interest since the 1960s [27–31].

The literature reviewed in Section 1.3 indicates that silica dissolution is predominantly controlled by mass transport mechanisms. Hlavac and Nademlynska's [31] seminal work revealed no significant differences in the diffusivities of quartz and amorphous silica, leading many subsequent studies to use amorphous silica as the primary source [12, 27, 29, 33, 41]. However, the same authors also reported variations in total dissolution time between crystalline and amorphous silica, a difference often overlooked in studies focused on sand grain dissolution in glass baths. This discrepancy emphasizes the need to account for the specific properties of quartz during the dissolution process.

This chapter aims to provide an in-depth analysis of quartz dissolution when in contact with industrial soda-lime-silica glass at 1400°C. The experimental setup used in this study was specifically designed to eliminate free convection effects, encouraging precise measurements of two key parameters necessary for modeling dissolution : solubility and diffusivity.

The chapter begins with a theoretical background on silica polymorphism under low-pressure conditions, offering insights into the challenges associated with using quartz as a silica source for dissolution tests. Following this, theoretical calculations based on thermodynamic simulations and diffusion matrices will be presented, providing a foundation for interpreting the experimental results.

4.1.1 Silica polymorphism

The α-quartz, which is the most stable and abundant form of silica on Earth, forms the main constituent of sand used for glass melting. Despite having the same chemical composition, silica can exist in multiple crystalline forms, known as polymorphs, which vary in their crystalline structures and physical properties. These polymorphs are thermodynamically stable in different temperature and pressure ranges (Figure 4.1). The low-pressure silica polymorphs include quartz, tridymite, and cristobalite, each of which has high-temperature (β) and low-temperature (α) forms [100].

All the low-pressure forms of silica are characterized by a network of oxygen tetrahedra surrounding a silicon atom. These tetrahedra share corners, hence each oxygen atom is shared between two silicon atoms. The corner-sharing tetrahedral networks increase the possibilities of silica structures due to the higher degree of freedom compared to edge or face-shared structures [102].

Several studies have proposed a topological description of the mid-range order of silicate structures based on network neighbors connectivity, and rings formed by tetrahedra [102–104]. These rings can be described not only in terms of the number of tetrahedra but also by their distribution of angles, roundness, and flatness ("roughness"). This additional characterization of ring shape helps to better describe the connectivity of the network and will aid in elucidating the properties and behaviors of the different polymorphs (Figure 4.2).

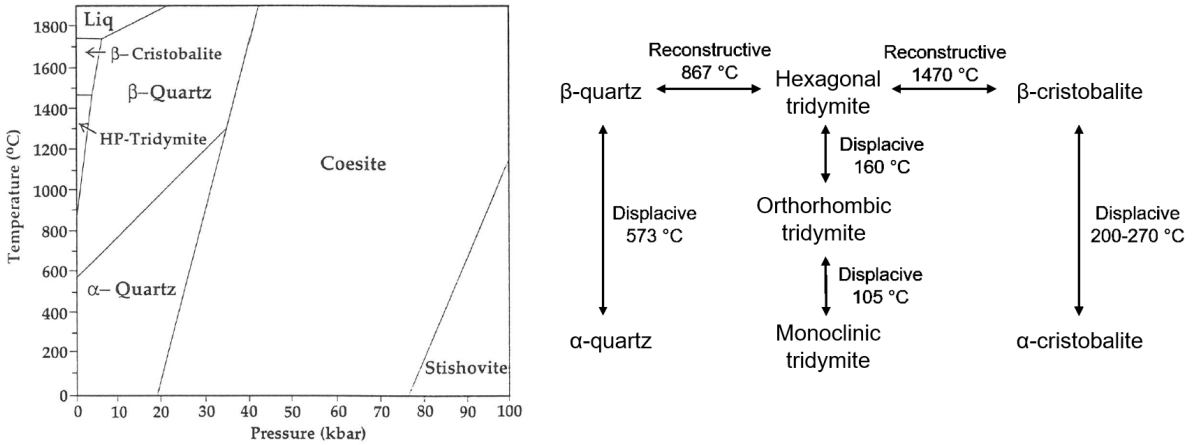

Figure 4.1 (left) Phase diagram for the silica system [100]. (right) Low-pressure silica phase transformations (adapted from [101])

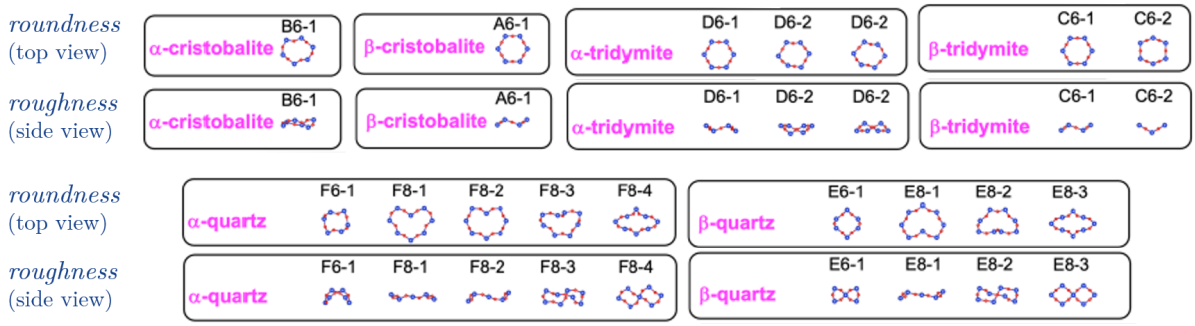

Figure 4.2 Isomorphic primitive rings in crystalline SiO_2 , from [104]. *"Roundness"* relates to the top view of the primary ring, while *"roughness"* corresponds to the out of plane distribution. The so-called β-tridymite refers to the hexagonal tridymite, while the α-tridymite is likely OP trydimite.

The notion that larger rings are associated with less densely packed structures cannot fully explain the differences in properties among the polymorphs. Indeed, high temperature and low pressure polymorphs display a more symmetric structure, that is, a narrower distribution of ring sizes that are rounder and flatter, but still have a lower density compared to their low-temperature counterparts. This phenomenon can be explained by the ability of longer chains to fold in about themselves more easily than a short one. This results in a higher number of network neighbors surrounding a SiO_4 tetrahedron, and a more connected network [102, 103].

Table 4.1 Properties of low-pressure silica polymorphs and amorphous silica

Phase	Crystal system	Molar volume in cm^3/mol	Density in g/cm^3	Reference
α-quartz	Trigonal	22.684	2.649	[105]
β-quartz	Hexagonal	23.688	2.536	[105]
PO-10 tridymite	Pseudo-orthorhombic	26.400	2.276	[106]
MX-1 tridymite	Monoclinic	26.584	2.260	[107]
MC tridymite	Monoclinic	26.614	2.257	[105]
OP tridymite	Orthorhombic	26.870	2.236	[105]
OC tridymite	Orthorhombic	27.323	2.199	[105]
LHP trydimite	Hexagonal	27.465	2.188	[105]
HP tridymite	Hexagonal	27.499	2.185	[105]
α-cristobalite	Tetragonal	25.737	2.334	[105]
β-cristobalite	Cubic	27.285	2.202	[105]
amorphous silica		26.942	2.230	[108]

Table 4.1 highlights the substantial difference between cristobalite and tridymite structures compared to quartz behavior. The more flexible and open structures of high-temperature polymorphs can accommodate a wider range of cations and have larger molar volumes. The increase in molar volume (and thus, decrease in density) can reach up to 20% between quartz and cristobalite.

This change needs to be considered as operations occur outside the quartz stability range temperatures during glass melting processes. In this context, it becomes essential to detail the kinetics of these transformations.

Phase transformation kinetics between low-pressure silica polymorphs

As well as the transformations between them, quartz, tridymite, and cristobalite also undergo transformations between their low and high-temperature forms (Figure 4.2b). Silica transformations can then be classified into two types : displacive and reconstructive. The displacive transformations involve the distortion of the high-temperature (β) forms to create the low-temperature (α) versions. Because these transformations do not require extensive atomic rearrangement, they can occur almost instantaneously on heating and cooling [100, 109].

On the other hand, the reconstructive transformations between quartz, tridymite, and cristobalite involve the breaking and reforming of chemical bonds, which lead to a reorganization of the crystal structure. These transformations are generally slower and irreversible. Marians and Hobbs [102] proposed a concept of configurational barrier besides the energetic one, based on their observations of quartz structural modifications due to ionizing radiation. This barrier can be described by a configurational distance that represents the exact number of interchanged bond pairs required to transition between two distinct states of the material.

Their topological study revealed that a conversion of quartz to cristobalite necessitates the breaking and reforming of roughly one-third of all bonds. This massive, simultaneous breaking of

bonds renders the event more akin to melting than a solid-state transformation. Chaklader and Roberts' [110] experimental data supports this observation, indicating that this transformation involves an amorphous intermediate transition phase. Kuellmer and Poe [111] suggested that the transition likely occurs through the formation of either quartz with a large number of dislocations or highly distorted cristobalite. In both scenarios, the solid transformation appears to be intermediated by a highly disordered state.

Impurities that act as mineralizers can play a significant role in this phase transformation. The addition of fluxes, such as alkali and alkaline earth oxides, can create liquid phases with lower melting points than pure silica [112, 113]. These phases facilitate the solution-reprecipitation mechanism that can assist the nucleation and growth of cristobalite.

Cristobalite and tridymite, which are cristobalite polytypes, possess more open structures than quartz. These structures allow for interstices large enough to accommodate atoms, such as sodium, potassium, or calcium [113–115]. These atoms may help stabilize the tridymite structure. Some authors suggest that it only forms in the presence of impurities, usually following the formation of cristobalite [116, 117]. Experimental findings by Holmquist [118] indicate that quartz, in the presence of an alkali oxide, converted directly to tridymite only in a very narrow temperature range : between 877 ± 6 °C and 898 ± 5 °C, depending on the alkali.

Stevens et al. [109] proposed that the cristobalite first formed in the presence of alkali is relatively disordered and contains a number of tridymite stacking faults. This structure then converts to true tridymite depending on both alkali concentration and temperature [109, 113].

Based on this knowledge, we can assume that during industrial glass melting, quartz is outside its temperature stability domain and in contact with a molten glass containing both alkali and earth alkali oxides. These combined conditions tend to favor the formation of high-temperature polymorphs and, consequently, more voluminous solids. Given the high likelihood of an expansion of about 20%, tracking the geometry of quartz grains is not a suitable proxy for studying its dissolution in conditions commonly found during glass melting.

In summary

- In the temperature range of the glass-melting process, quartz is not the stable form of silica. Between 867°C and 1470°C, tridymite is stable, and at even higher temperatures, cristobalite becomes the stable form.
- Tridymite and cristobalite have much more open structures and larger molar volumes than quartz, with tridymite having a 16% larger molar volume than quartz at high temperatures [105].
- The reconstructive transformation of quartz into high-temperature phases is generally slow. However, cristobalite tends to appear first instead of forming tridymite, even at lower temperatures. Tridymite may only form later when mineralizers, such as alkalis, are present.
- The reconstructive transformation of quartz into high-temperature forms can be sped up by alkalis, which promote the dissolution and reprecipitation of silica from a liquid phase.
- In the presence of alkalis and alkaline earth oxides, quartz is likely to transform into the larger-volume polymorphs tridymite and cristobalite during dissolution in soda-lime silica glass.

4.1.2 Thermodynamics calculations

Although the primary interest of this study lies in the kinetic mechanisms involved in dissolution, acknowledging the thermodynamics of the process is crucial for understanding the equilibrium state towards which the system is progressing. Quartz dissolution presents a challenge due to the multiplicity of silica polymorphs in the 1400 °C temperature range and the lack of consensus regarding tridymite being a pure silica polymorph [100, 109]. In this respect, the FactSage FactOxid database considers tridymite as a pure silica polymorph with high and low-temperature forms, without distinguishing between monoclinic, hexagonal, or orthorhombic structures. More recent literature proposes new databases that do not recognize tridymite as a pure silica polymorph [116, 117]; however, no equivalent thermodynamic data are available for assessing tridymite as a binary compound. The FactOxid database assumes all low-pressure silica polymorphs to be pure solids, thus no solid solution is considered.

To simulate the tie line between the original glass composition in contact with quartz at 1400 °C and 1 atm, increasing molar fractions of silica were incorporated in the original glass composition, as detailed in Section 2.5.4. When allowing for all pure solids and glass (referred to as *"slag"* in the FactSage framework) to form, the only products were high-temperature tridymite and a glass phase. The molar fraction of each phase with increasing silica incorporation is illustrated in Figure 4.3 for both the single glass phase and the phase separation cases.

Figure 4.3 indicates that no transition other than the dissolution of tridymite is predicted along this tie line at 1400 °C. Complete dissolution is predicted for solid silica molar fractions exceeding 39%. If phase separation is considered, a second glass phase coexists with the main phase only when tridymite is also present, with the exception of the narrow range of 35 to 39% silica molar fraction, where both glass phases exist without any solid phase.

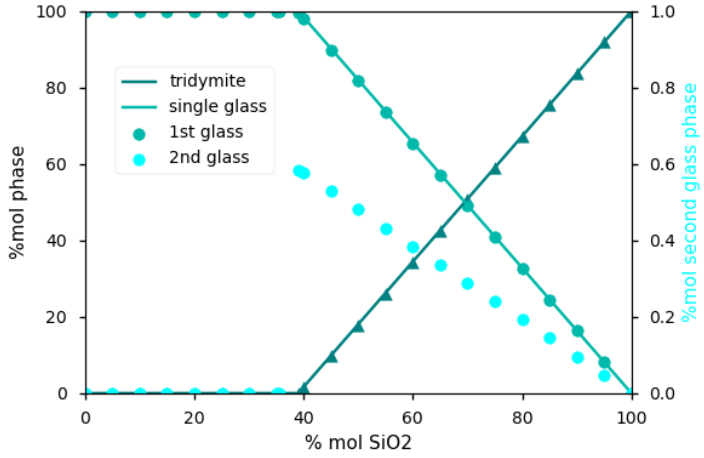

Figure 4.3 Evolution of the molar fraction of each phase as solid silica is increasingly incorporated into the original glass composition. Solid lines depict the scenario for a miscible glass phase (single *"slag"*). At the same time, markers represent the results for phase-separated glass (circles for "*slag*" phase and triangles for tridymite). Due to the small amount of the secondary glass phase, its molar fraction is shown on the cyan secondary axis on the right for clearer visualization.

The evolution of the chemical composition of the glass is depicted in Figure 4.4. This includes cases for both a single glass phase (solid line) and two glass phases (represented by circles).

The secondary glass phase (cyan circles) exhibits a higher alumina content and lower alkaline earth oxide content, with no significant impact on silica solubility. However, as the main glass phases are nearly equivalent whether considering the immiscibility gap of the glass or not, and the second phase accounts for no more than 0.6% mol of the glass phase, the minor glass phase impact may be negligible.

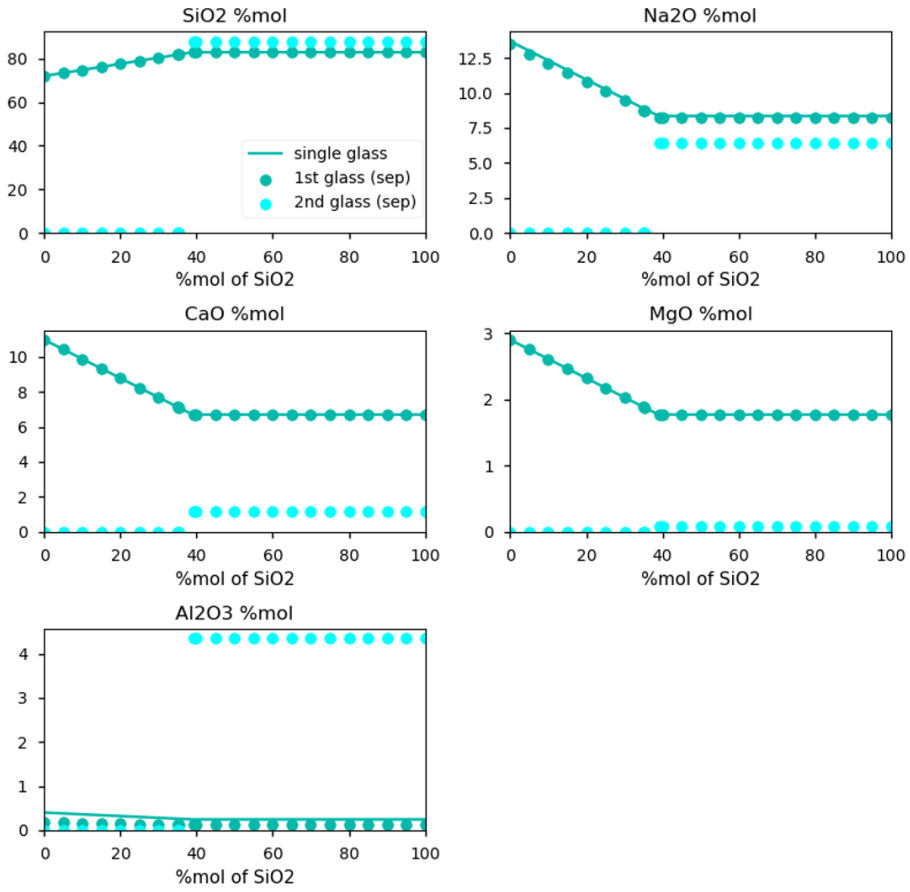

Figure 4.4 Evolution of the glass composition (mol%) in equilibrium as solid silica is incorporated into the glass. The left extremity ($x = 0$) represents the original glass composition. Solid lines indicate a single glass phase, while markers denote immiscible glass. Cyan circles show the composition of the second glass phase.

As expected for simple mixing (along a straight tie line), the glass composition remains constant when both solid and liquid coexist, corresponding to the intersection between the *liquidus* surface and this tie line (green tie-line in Figure 2.10). As discussed in Section 2.5.4, this composition is one of the possible *liquidus* compositions but not the only one. By simplifying the original glass + quartz system to a pseudo-ternary one (alkali, alkaline earth, and silica), it is possible to approximate the *liquidus* curve visually instead of identifying a single point. To construct the pseudo-ternary phase diagram in Figure 4.5, aluminum and potassium oxides contents in the original glass (0.35% and 0.02% mol, respectively) were neglected, and it was assumed that the ratio between alkaline earth oxides would remain consistent with the original glass (CaO/(CaO+MgO) $\approx$ 0.78). Isotherms at 1200, 1300, 1400, and 1500 °C were added for reference.

Considering the possible trajectories between the original composition of the glass and the primary field of high-temperature tridymite (green dashed lines in the right diagram of Figure 4.5),

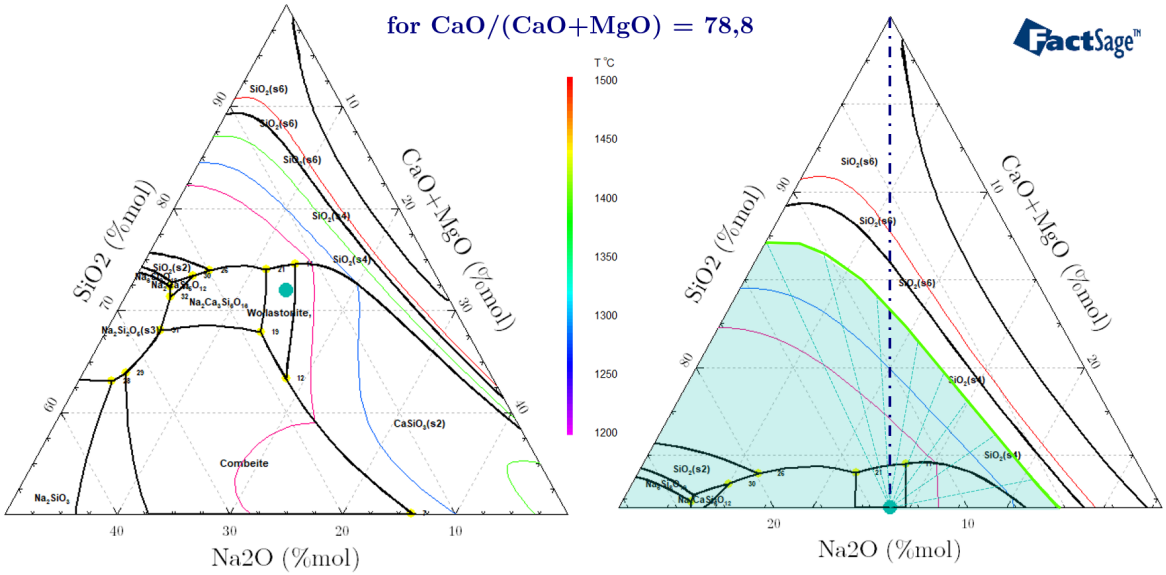

Figure 4.5 Pseudo-ternary diagrams for the SiO_2-Na_2O-(CaO+MgO) system at 1 atm, constructed by using FactSage and assuming a constant ratio of alkaline earth metals as in the original glass and neglecting potassium and aluminum oxides, and without glass phase separation. The SiO_2 axis does not start at 0%, and the other axes are limited to 50 %mol for better visibility. Isothermal curves at 1200, 1300, 1400 (green), and 1500 °C are shown. The green circle marks the original glass composition. The region highlighted in the zoomed-in diagram on the right indicates where the liquid is the only stable phase at 1400 °C. The dark blue dot-dashed line represents the straight tie-line between the two extreme compositions, defining the cut for constructing the pseudo-binary diagram in Figure 4.6. The other dotted green lines represent alternative possible tie lines between the original glass and the liquidus. The subscript (s4) denotes high tridymite, and (s6) denotes β-cristobalite.

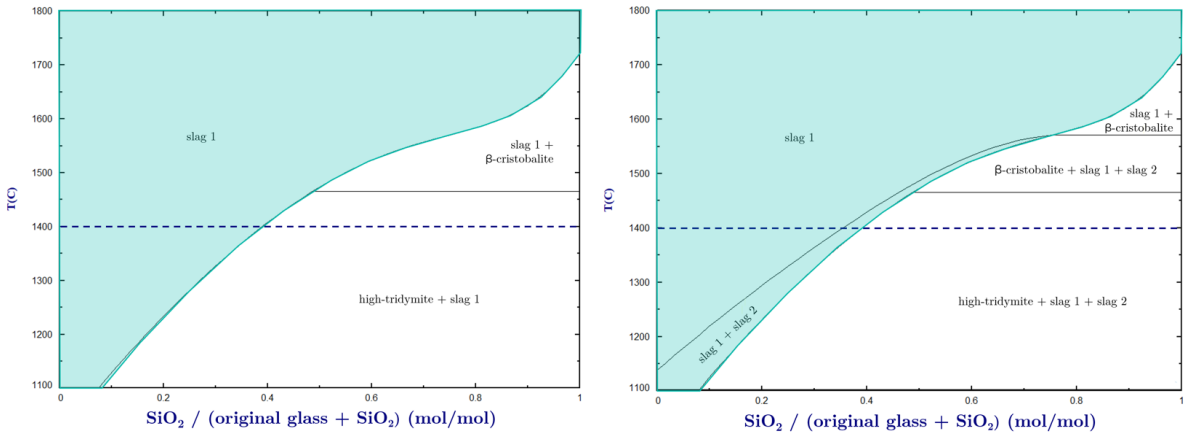

Figure 4.6 Pseudo-binary diagram at 1 atm between the original glass composition ($x = 0$) and silica. The left diagram represents the perpendicular cut indicated by the dark blue dot-dashed line in Figure 4.5, under the same assumptions. The right diagram includes the consideration of glass phase separation.

it is evident that no other intermediate phase is predicted at 1400 °C. Below this temperature, the precipitation of $CaSiO_3$ and combeite ($Na_2O \cdot 2\,CaO \cdot 3\,SiO_2$) is possible if the glass is enriched in alkaline earth oxides. Conversely, if the glass is enriched in sodium, the precipitation of other phases is not predicted even at temperatures as low as 1200 °C.

A pseudo-binary diagram is derived from the straight tie line cut shown as a dark blue dash-dot line in Figure 4.5 and displayed in Figure 4.6. The left extremity represents the original glass composition, with the glass stability field highlighted. It is evident that along this tie line, no phase other than silica polymorphs and glass is predicted above 1100 °C. The transition from tridymite to cristobalite is predicted at 1465 °C, with no dependence of the stable polymorph on glass infiltration. As expected, as the temperature decreases, the silica solubility of the glass phase reduces, resulting in a higher fraction of the solid phase. For the single glass phase, the molar fractions and chemical compositions depicted in Figures 4.3 and 4.4 can be extracted from the representation of the 1400 °C dashed line in Figure 4.6.

From these elements, only the dissolution of a silica polymorph is expected above 1300 °C, even when considering tie lines other than that starting from the original glass. Although these thermodynamic simulations predict only tridymite as the silica solid structure up to 1465 °C, the discussion in Section 4.1.1 indicates that other silica polymorphs may occur as metastable phases. Therefore, an evaluation of the final polymorph in the dissolution enthalpy was also performed to determine if there is a thermodynamic argument for expecting a difference in the dissolution driving force among the different low-pressure silica polymorphs.

Silica polymorphs effect on dissolution enthalpy

Figure 4.3 displays only the stable phases for each silica molar fraction incorporated into the glass. However, it is worth considering possible metastable phases, in light of the observations of previous works that highlight the challenges of forming tridymite from quartz [100, 118]. Since all silica polymorphs are considered pure solids by FactSage, their thermodynamic activities must equal 1 to be stable. Observing the evolution of their thermodynamic activity with glass incorporation (Figure 4.7), it is evident that the activity of cristobalite remains very close to 1.

This implies that, in the absence of tridymite saturation, cristobalite formation is plausible.

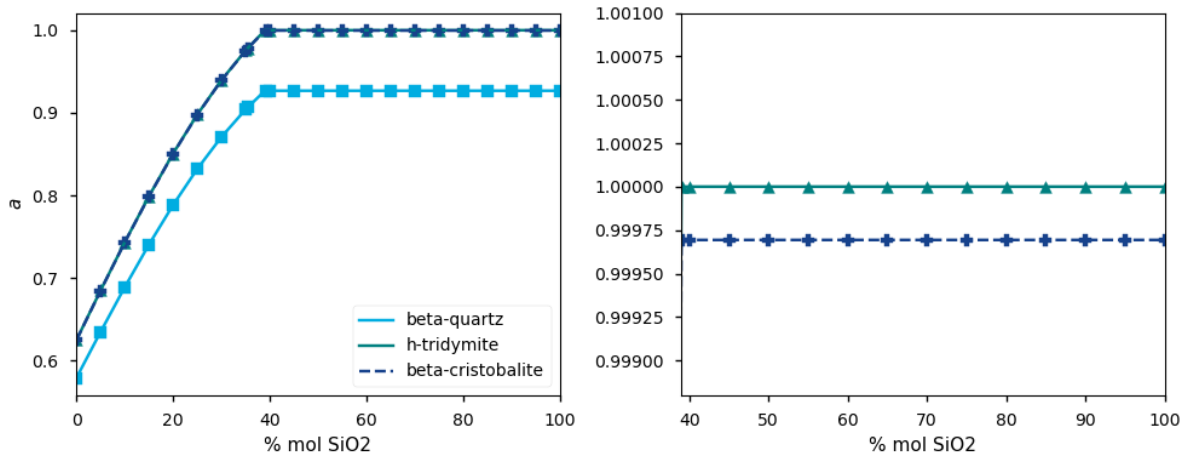

Figure 4.7 Thermodynamic activity of high-temperature silica polymorphs as silica incorporation increases. Scatter markers represent phase separation case, while solid lines depict the single glass phase assumption. The right graph provides a close-up to highlight the nearly overlapping activities of tridymite and cristobalite.

To better compare the impact of silica polymorph on the dissolution driving force, the Gibbs free energy difference of dissolution (ΔG) was calculated, considering the formation of the three high-temperature polymorphs. Two effects were analyzed : the effect of the initial polymorph on dissolution and the effect of the polymorph formed during dissolution. The compilation of the cases calculated is presented in Table 4.2.

Table 4.2 Nomenclature for the thermodynamic calculations on the effect of starting and forced silica polymorph on dissolution enthalpy

as the starting phase at the end	**β-quartz**	**h-tridymite**	**β-cristobalite**
β-quartz	qua-qua	tri-qua	cri-qua
h-tridymite	qua-tri	tri-tri	cri-tri
β-cristobalite	qua-cri	tri-cri	cri-cri
no forced phase	standard-qua	standard-tri	standard-cri

As detailed in Section 2.5.4, FactSage's Equilib module allows for selecting the possible reaction products (including pure solids, solutions, and slag). In the standard or "no forced phase" case, no limitations were imposed on the products, and thus the calculation reveals the most stable scenario given the employed database. Conversely, when imposing a specific polymorph, only the polymorph of interest and the slag were selected as possible products.

To evaluate the effect of polymorph on dissolution correctly, it is essential to isolate this step accurately. Figure 4.8 illustrates the dissolution test cycle actually employed, highlighting in orange the step to assess the polymorph effect. Consequently, the enthalpy of heating both glass and the polymorph to 1400 °C (ΔH_{heat}) was not considered to avoid swamping the effect of interest with the highly endothermic step of heating the system from room temperature to the dissolution temperature.

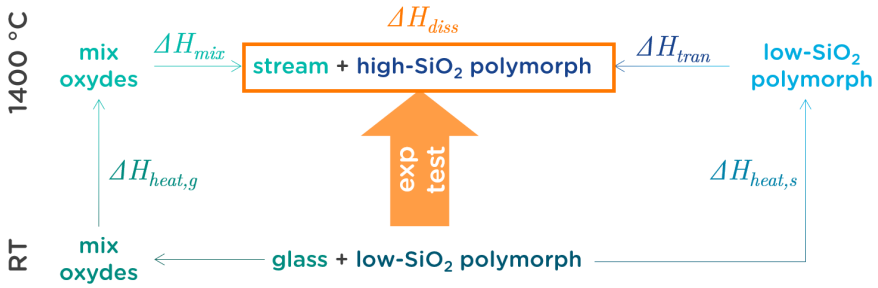

Figure 4.8 Illustration of the different steps in the dissolution process from room temperature (RT) to 1400 °C. The orange rectangle highlights the specific process being compared among the silica polymorphs, excluding the enthalpy of heating, mixing, and displacive phase transitions between polymorphs.

For this purpose, the reactants were considered with the initial condition already at 1400 °C. Consequently, only the high-temperature forms of quartz, tridymite, and cristobalite were used. As detailed in Section 2.5.4, the original glass was reported as a *"slag stream"*, where the elements were already combined in a single phase, avoiding the effect of enthalpy of association among them in the calculations (ΔH_{mix}).

The same protocol of incorporating increasing fractions of the silica polymorph with the glass was followed using the Equilib module. However, instead of analyzing the entire range from 0 to 100%, the focus was on the dissolution transition itself, i.e., the moment when the silica polymorph activity approaches 1, but its molar fraction is still 0. At this onset of dissolution, both enthalpy (ΔH_{diss}) and Gibbs free energy (ΔG_{diss}) variations, silica polymorph molar fraction, and silica content in the glass were calculated. For enthalpy and Gibbs free energy variation, Figure 4.9 illustrates the variation between the initial state (solid + glass at 1400 °C not in contact) and the dissolution onset property. Since the sum of both phases is equal to 1, the values are already normalized for 1 mol.

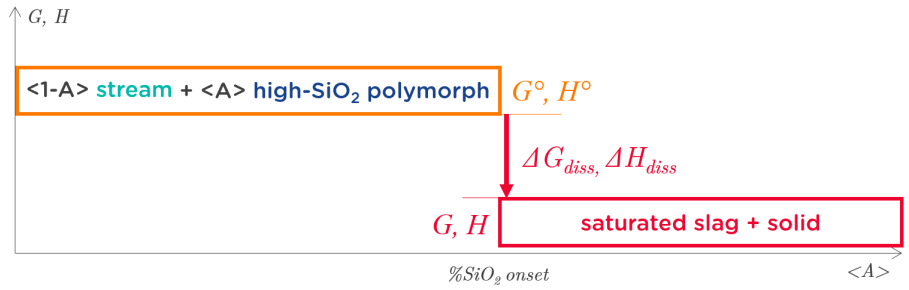

Figure 4.9 Illustration of the ΔG considered to evaluate the potential differences between the dissolution driving forces of different polymorphs.

Table 4.3 presents the standard case results starting with different polymorphs. All cases revealed a precipitation of tridymite for silica incorporations above 39% mol. The *liquidus* composition exhibited an 82.9% mol SiO_2 content for all cases. No other phases were reported, although the thermodynamic activity for high-cristobalite was 0.9997 for all the standard cases. The dissolution was always endothermic ($\Delta H_{\text{diss}} > 0$) and spontaneous ($\Delta G_{\text{diss}} < 0$).

Table 4.3 Results of the standard cases starting with different silica polymorphs. The values are normalized for 1 mol.

Properties	**standard-qua**	**standard-tri**	**standard-cri**
ΔG_{diss} (J)	-1240	-830	-832
$G°$ (kJ)	-1050.8	-1051.1	-1051.1
$\Delta H_{\textbf{diss}}$ (J)	8668	7710	7667
$H°$ (kJ)	-765.5	-764.5	-764.5
SiO_2 content in glass (% mol)	82.9	82.9	82.9
Solid SiO_2 (% mol)	39	39	39

The Gibbs free energy differences indicate that starting with quartz is slightly more favorable, even though it is also slightly more endothermic. This is likely related to the higher difference in the quartz crystalline structure compared to the open glass network, which is closer to the less dense cristobalite and tridymite structures. It is also notable that tridymite and cristobalite exhibited almost identical values, corroborating with the cristobalite activity being very close to stability.

When forcing the stabilization of each polymorph (Figure 4.10), it becomes clear that retaining quartz as the silica polymorph is less favorable than the others. Even when quartz is the original silica source and is maintained during dissolution, its Gibbs free energy variation is still less spontaneous than transforming into other polymorphs during dissolution. Once again, tridymite and cristobalite exhibited almost identical behavior. Imposing the formation of tridymite corresponds to the standard case ("no forced"), given that it is the stable polymorph.

While, from the thermodynamics point of view, the starting polymorph did not impact the solid silica solubility in the glass, retaining quartz as the silica solid resulted in an increase in the silica content in the *liquidus* glass and consequently delayed the quartz primary field for silica incorporations above 81% mol. The glass composition in equilibrium with each type of silica polymorph is provided in Table 4.4.

Table 4.4 Composition of glass in equilibrium with forced-stabilized silica polymorphs at 1400 °C, determined by the intersection of the tie-line between the original glass composition and the polymorph apex with the *liquidus* curve.

(%mol)	**β-quartz**	**high-tridymite**	**β-cristobalite**
Na_2O	2.6	8.4	8.4
CaO	2.0	6.7	6.7
MgO	0.5	1.8	1.8
Al_2O_3	0.1	0.2	0.2
SiO_2	94.8	82.9	82.9

Starting with quartz offers a slight advantage over other, more stable polymorphs. However, maintaining quartz at 1400 °C is unfavorable and tends to transform into other polymorphs. When comparing the initial and final polymorph effects on both Gibbs free energy and enthalpy variation (Figure 4.11), the final polymorph can explain better the variations on these properties than the initial silica phase. In other words, the decrease in Gibbs free energy from starting with quartz is counterbalanced by the non-spontaneous process of maintaining it as the silica polymorph.

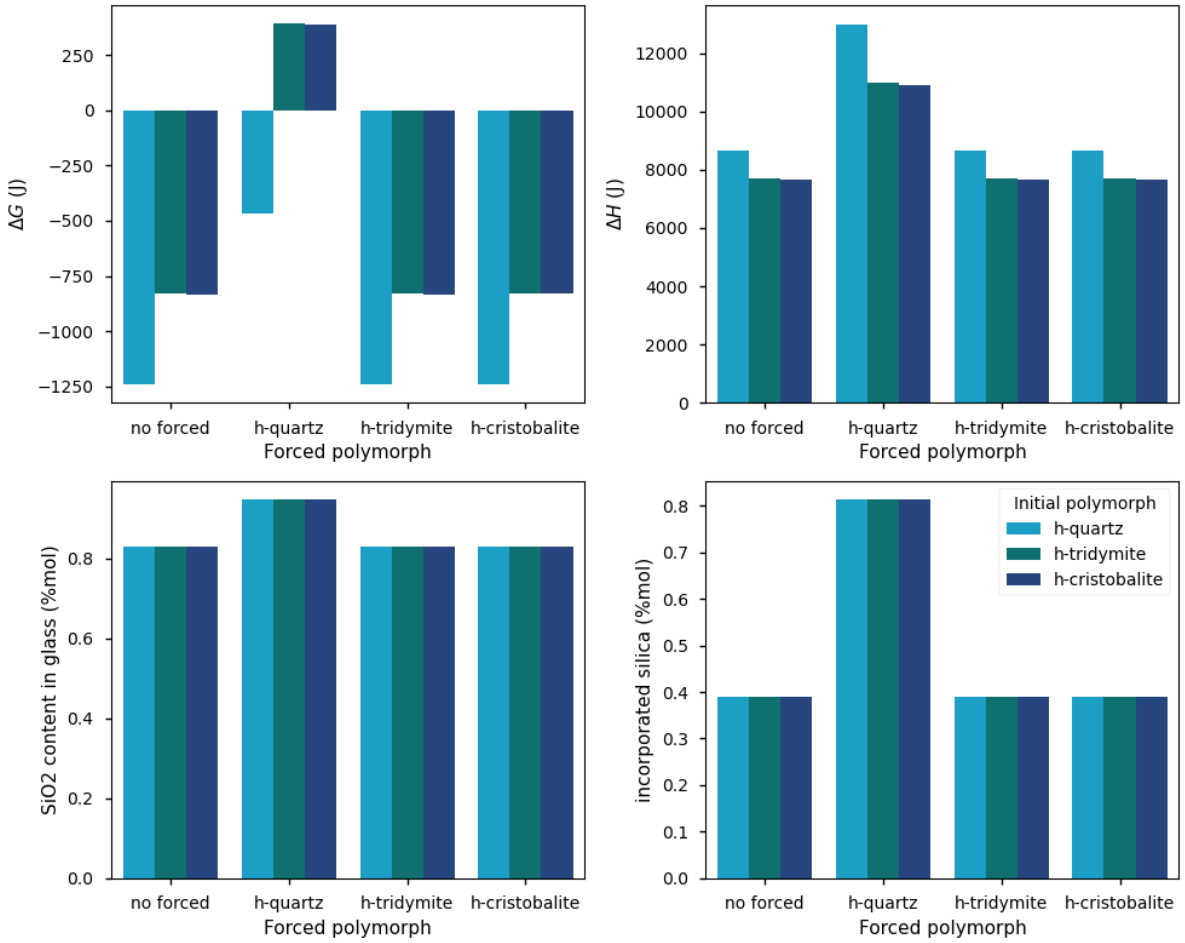

Figure 4.10 Results taking into account the forced polymorph and the initial polymorph. The standard case is shown as the "no forced" label.

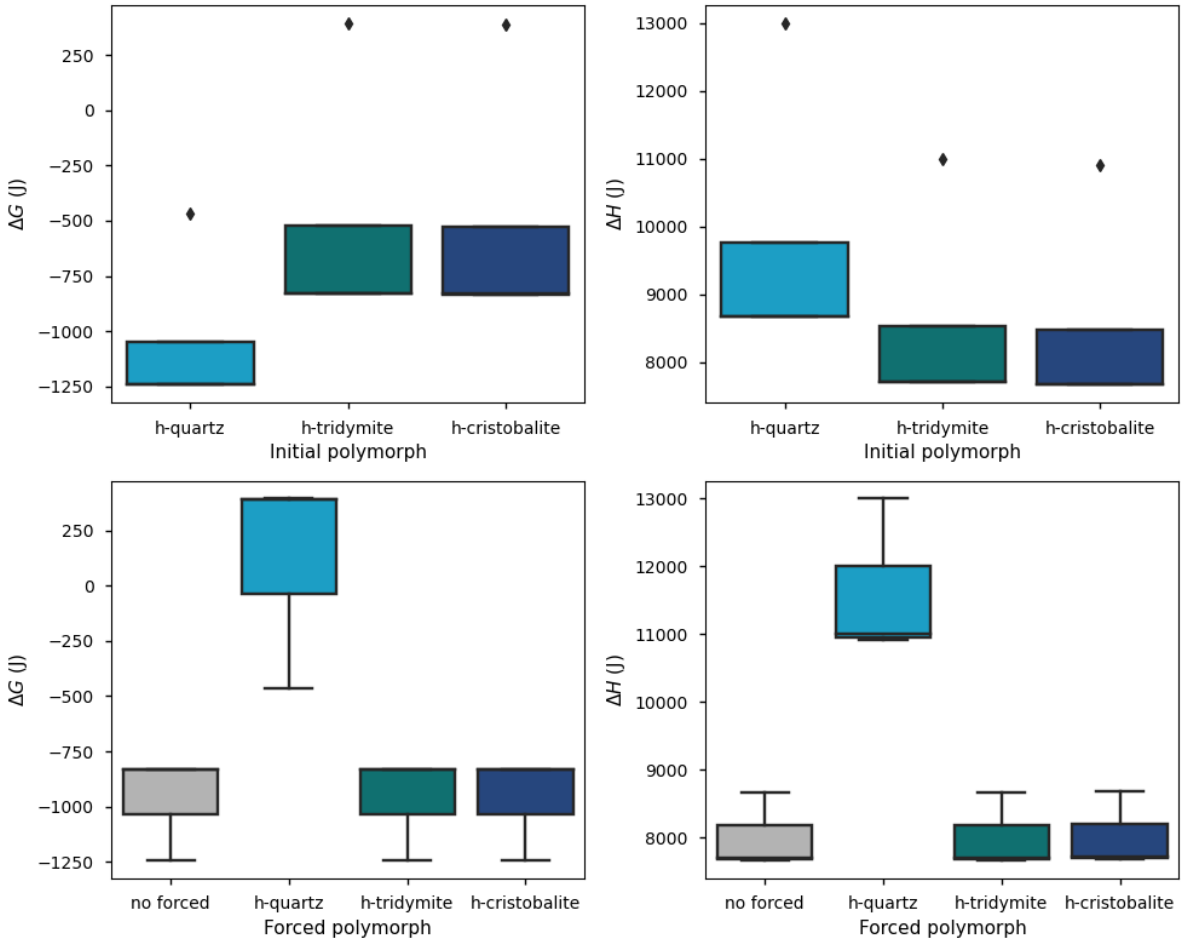

Figure 4.11 Effect of both initial and forced silica polymorph on Gibbs free energy and enthalpy variations. Whiskers were defined at 1.5 × interquartile range (between the 25th and 75th percentiles to define the outliers (diamond markers).

In summary

- Thermodynamic calculations were performed to check for any secondary phases during silica dissolution in soda-lime-silica glass. Tridymite is predicted as the stable polymorph at 1400°C, with all silica phases considered pure solids.
- No solid phases other than tridymite (or cristobalite) are expected above 1300°C. Higher silica incorporation can occur if the interface glass composition is enriched in alkalis.
- Cristobalite's thermodynamic activity was calculated to be near unity, supporting its likely precipitation, which aligns with previous observations of early cristobalite formation.
- The effect of silica polymorphs on the Gibbs free energy and enthalpy of dissolution was evaluated. The decrease in Gibbs free energy when starting with quartz is offset by the difficulty of maintaining it as a stable phase. For a 1400 °C dissolution, cristobalite and tridymite showed nearly identical values for Gibbs free energy, enthalpy, *liquidus* composition, and solid silica fraction, whether as the starting or final phase.

4.1.3 Silica diffusive dissolution

Assuming that the composition at the dissolution interface reaches thermodynamic equilibrium, the dissolution process is primarily governed by mass transport, as reported by most of the works compiled in Section 1.3. In the absence of convection, which is not expected under the static conditions of this study, dissolution is controlled by diffusion.

As outlined in Section 1.4.2, the diffusion behavior in multi-component systems, such as soda-lime-silica glass, requires a multi-component diffusion approach. In such systems, the concentration gradient of each element is influenced by the compositional variations of other elements, as expressed through an adapted form of Fick's second law :

$$\frac{\partial C_i}{\partial t} = \sum_{j=1}^{n-1} D_{i,j} \nabla^2 C_j \tag{4.1}$$

where $D_{i,j}$ are elements of the $(n-1)\times(n-1)$ diffusion matrix $[\mathbf{D}]$, and C_j represents the molar fraction of component j.

The theoretical concentration profiles can be calculated by solving Fick's second law for multi-component systems, using appropriate boundary and initial conditions for the dissolution process. To simplify these calculations, the linearized compositions (as described in Equation 1.45) are applied along the eigenvectors of the diffusion matrix, instead of using concentrations expressed in terms of individual oxides.

$$\frac{\partial U}{\partial t} = [\mathbf{\Lambda}] \nabla^2 U \tag{4.2}$$

where U is the linearized composition along the diffusion matrix eigenvectors, and $[\mathbf{\Lambda}]$ is a diagonal matrix with the eigenvalues.

For these calculations, the interface composition is assumed to remain constant ($U(x=0) = U^*, \forall t$) and is defined by the *liquidus* composition, determined in the previous section for the standard cases. Two distinct scenarios are considered for the boundary conditions at the other extremity of the glass reservoir :

1. **Semi-infinite glass reservoir** : In this case, the far-field composition is assumed to remain constant and identical to the original glass composition : $U_\infty = U(t = 0)$ This scenario corresponds to the analytical solution of the flat slab (Equation 1.23), given by :

$$U_i(x,t) = (U_i^* - U_{i,\infty})\text{erfc}\left(\frac{x}{2\sqrt{\lambda_i t}}\right) + U_{i,\infty} \tag{4.3}$$

   where U_i is the linearized composition along the ith eigenvector, erfc is the complementary error function, x is the distance from the interface, and λ_i the associated eigenvalue.
2. **Finite glass reservoir** : For a finite reservoir of length L, no mass flux is assumed at the reservoir extremity : $\nabla U_{x=L} = 0, \forall t$. Known as confined dissolution, this scenario can be approximated using the Fourier series solution from Equation 2.2 for the linearized compositions U_i, replacing D by the ith eigenvalue, λ_i.

Both cases were used in Section 2.2 to determine the minimum required length of the glass and the maximum duration for the dissolution experiments.

For the present calculations, two diffusion matrices were used, representing glass compositions similar to soda-lime-silica glass :

— **NCS matrix** (16%wt Na_2O, 12%wt CaO, and 72%wt SiO_2) by Trial and Spera [62], measured at 1200 °C ;
— **NCAS matrix** (16.8%wt Na_2O, 13.7%wt CaO, 5.0%wt Al_2O_3, and 64.5%wt SiO_2) by Jacquemin [64], also measured at 1200 °C.

The eigenvalues and eigenvectors derived from these matrices are displayed in Table 4.5. Since the original matrices were obtained at 1200°C, they may underestimate the diffusion profiles for the quartz dissolution experiments conducted at 1400°C. To address this, the eigenvalues were adjusted using activation energies reported by Claireaux *et al.* [63] for similar exchange reactions : 134 kJ/mol for the fastest eigenvalue and 200 kJ/mol for the slowest one. The corrected eigenvalues at 1400°C, denoted as $\lambda_{i,1400}$, are also provided in Table 4.5.

Table 4.5 Eigenvalues ($\lambda_{i,1200}$) and eigenvectors (v_i) for NCS and NCAS diffusion matrices, used for the calculation of the theoretical diffusion profiles. The corrected eigenvalues for 1400 °C are shown as $\lambda_{i,1400}$

	NCAS [64]			**NCS [62]**	
$\lambda_{i,1200}$ ($\times 10^{-12}$ m^2/s)	110.7	2.39	0.52	105	4.4
$\lambda_{i,1400}$ ($\times 10^{-12}$ m^2/s)	409.4	16.83	3.66	388.3	31.0
	v_1	v_2	v_3	v_1	v_2
Na_2O	1.0	0.02	0.03	1.0	0.27
CaO	-0.93	1.	-0.9	-0.85	0.73
Al_2O_3	-0.01	-0.12	1.0		
SiO_2	-0.06	-0.9	-0.13	-0.15	-1.0

For the initial interface composition, the *liquidus* values calculated for a single liquid phase in equilibrium with tridymite (see Table 4.4) were normalized for the NCS or NCAS system and then linearized using the corresponding eigenvector basis.

The glass reservoir length was fixed at 5 mm in the experimental setup, and three time intervals—2, 4, and 24 hours—were analyzed. The results for both semi-infinite and confined dissolution cases, using the two diffusion matrices, are presented in Figure 4.12.

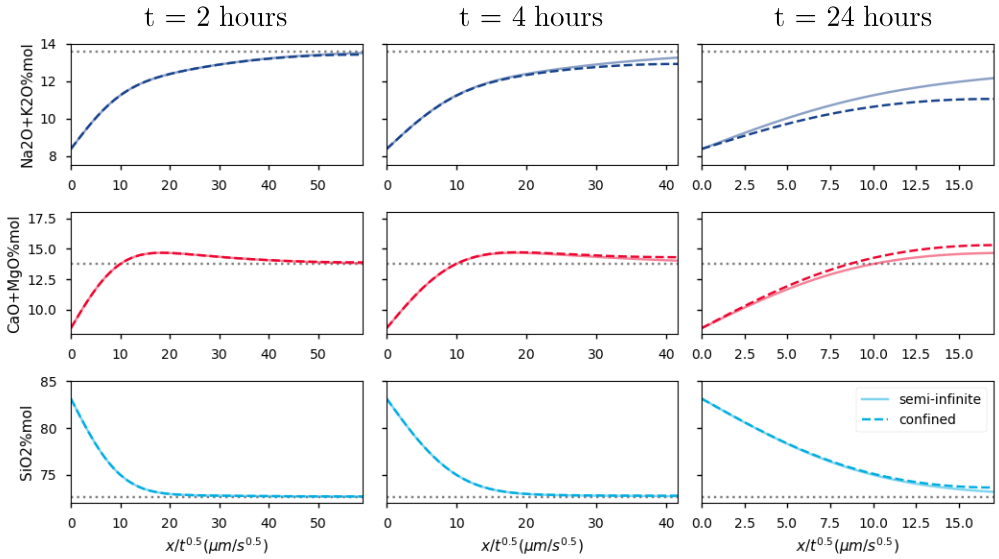

a NCS matrix

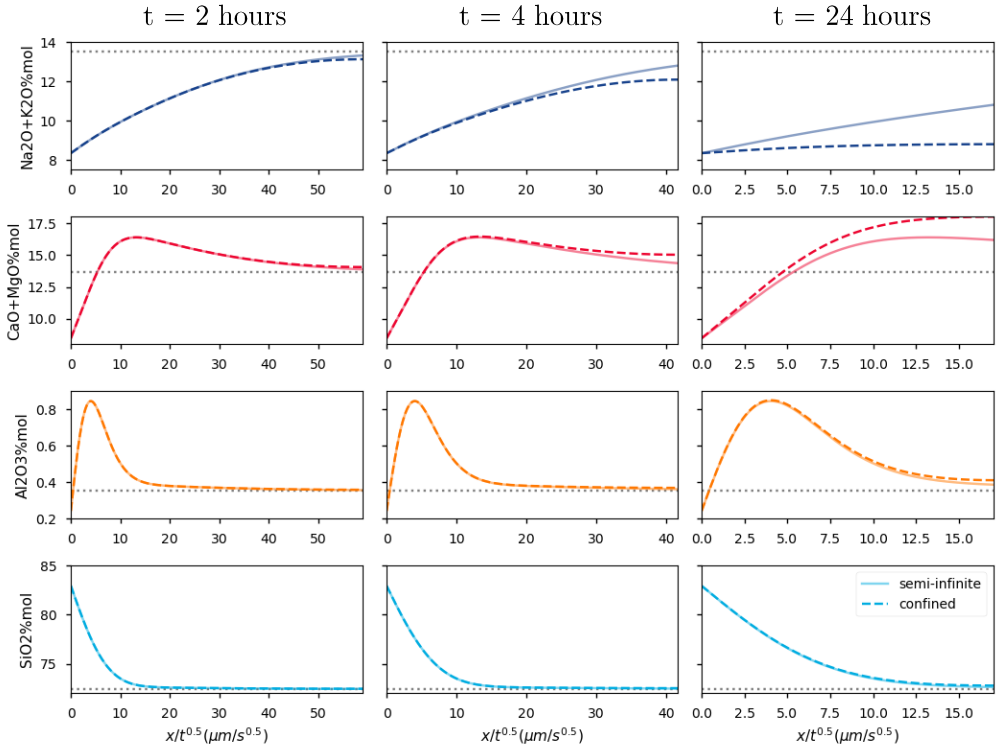

b NCAS matrix

Figure 4.12 Calculated diffusion profiles in the glass after silica dissolution at 1400 °C, using the NCS (top) and NCAS (bottom) diffusion matrices. Both the semi-infinite and the confined cases were plotted for a fixed length L of 5 mm. The confined case deviates from the semi-infinite assumption after 4 hours for both diffusion matrices. The original composition of the glass is represented by the gray dashed lines.

As predicted in Section 2.2.1, the alkali and alkaline-earth oxides reach the reservoir extremity first when using both diffusion matrices. This rapid diffusion explains why quartz dissolution tests were limited to 2 hours (Figure 2.2); beyond this time, the semi-infinite assumption is no longer valid. The characteristic timescale for the first eigenvalue, corrected for 1400°C, suggests that the exchange between alkali and alkaline-earth cations reaches a steady state after approximately 17.5 hours over a 5 mm length.

Both diffusion matrices indicate that the second eigenvector represents the coupling between calcium and silica, as evidenced by a peak in the alkaline-earth diffusion profiles. However, despite this coupling, the silica diffusion profile remains smooth, without any significant inflections. The pseudo-binary diffusion coefficients (EBDCs) for silica are calculated to be 3.4×10^{-11} m^2/s for the NCS matrix and 1.8×10^{-11} m^2/s for the NCAS matrix, based on the silica profiles for $t = 2$ h (valid semi-infinite condition), which were consistent with values reported in the literature for silica dissolution at 1400°C (Figure 1.15a). Notably, no significant differences emerge between the results obtained from the two matrices.

Given the depletion of alkali and alkaline-earth network modifiers, a highly viscous layer is expected to form near the quartz interface. Using the GlassPy module "predict" with the GlassNet model, the viscosity profile was estimated, as shown in Figure 4.13. This profile indicates a progressive decrease in viscosity with no inversions, consistent with previous calculations performed to assess the possibility of free convection due to density inversions. Based on these results (shown in Figure 2.4), no convection onsets are anticipated before 325 minutes for a 10 mm diameter slab, and no perturbations are expected in an 8 mm diameter geometry.

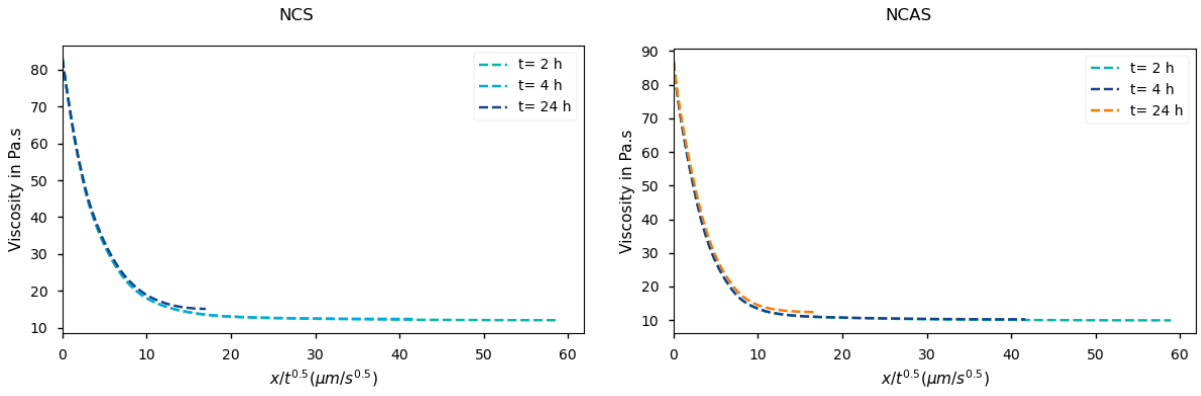

Figure 4.13 Calculated viscosity profile in the glass after silica dissolution, based on the diffusion profiles of Figure 4.12, using the NCS (left) and NCAS (right) diffusion matrices.

Furthermore, the viscosity profile closely mirrors the silica diffusion profile, supporting the dominant control of silica content on viscous flow in this composition range. However, when the EBDC value is substituted into the Eyring diffusivity equation (Equation 1.47) and an O^{2-} ion diameter of 2.8 Å is assumed as the jump distance, the associated viscosity values (2.4 and 4.6 Pa · s for NCS and NCAS matrices, respectively) underestimate the estimated diffusivity of silica.

When similar calculations were performed assuming quartz stability instead of tridymite, the results were comparable, with no inflections in the silica diffusion profile and EBDC values in

the range of 10^{-11} m^2/s. However, the viscosity near the interface exhibited very high values ($> 10^4$ $Pa \cdot s$) due to the elevated silica content. This steep viscosity gradient did not improve the correspondence with the Eyring diffusivity, which continued to underestimate the EBDC derived from the diffusion matrices.

Although these findings highlight differences in the stability of quartz at 1400°C, the focus will remain on the tridymite case due to the challenges associated with stabilizing quartz under these conditions. Since the equilibrium composition for glass in contact with β-cristobalite is identical to that of high-temperature tridymite, the diffusion profiles presented here can also be extended to the case of cristobalite.

In summary

- Using previously reported Na_2O-CaO-SiO_2 (NCS) [62] and Na_2O-CaO-Al_2O_3-SiO_2 (NCAS) [64] diffusion matrices, silica dissolution profiles were predicted based on a diffusion-controlled mechanism, assuming the *liquidus* composition at the interface with tridymite.
- For a confined dissolution scenario with a 5 mm reservoir, the semi-infinite assumption becomes invalid after 2 hours due to rapid alkali and alkaline earth exchanges.
- Both matrices showed similar results, with a coupled exchange between calcium oxide and silica. Despite this, the silica diffusion profile remained smooth, with effective binary diffusion coefficients (EBDCs) of 3.4×10^{-11} m^2/s for the NCS matrix and 1.8×10^{-11} m^2/s for the NCAS matrix.
- The calculated viscosity profile follows a similar trend to silica, though the Eyring diffusivity likely underestimates the values derived from the diffusion matrices.

4.1.4 Theoretical scenarios for quartz dissolution

The theoretical background presented in previous sections indicates that quartz dissolution in soda-lime silica glass at 1400 °C is significantly influenced by its potential phase transformation into more voluminous silica polymorphs, particularly tridymite and cristobalite. Besides quartz being outside its temperature stability range under these conditions, the presence of alkalis, alkaline earth elements, and a liquid phase also appear to accelerate this transformation, further affecting its dissolution behavior.

Because tridymite and cristobalite have larger molar volumes than quartz, tracking geometric changes in quartz particles during dissolution can be misleading. The expansion associated with phase transformation may distort the dissolution rate, making geometric measurements unreliable. Previous studies [28,30,31] on quartz dissolution in binary glass systems ($SiO_2 - Na_2O$) at temperatures ranging from 900 to 1500 °C indicate that these conditions favor the formation of other silica polymorphs than quartz [(1)]. Hlavac and Nademlynska [31] reported that "dissolution is more rapid in the first stage than predicted by the diffusion equation," which they attributed to the presence of a reactive layer at the solid surface, likely caused by cracks or surface defects. Later, Barklage-Hilgefort and Frischat [28] confirmed this observation through scanning electron microscopy (SEM) images (Figure 4.14), suggesting that "SiO_2 glass [amorphous silica]

[(1)] Liang's [36] and Shaw's [34] works, although using a very similar setup as that adopted in this work, studied quartz dissolution under high pressure (1 to 1.5 GPa), where tridymite nor cristobalite are stable (Figure 4.1).

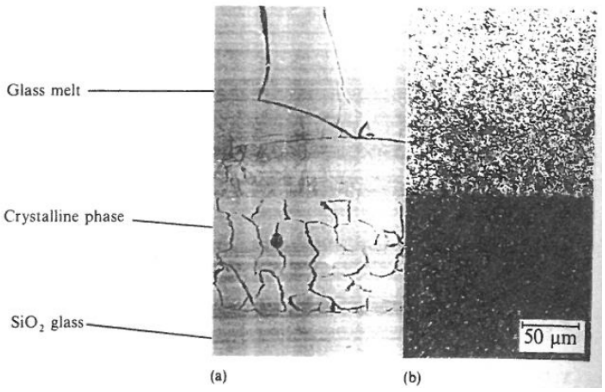

Figure 4.14 (left) Scanning electron microscopy (SEM) of the interface between amorphous silica and the $Na_2O \cdot 3\,SiO_2$ glass melt and (right) a qualitative distribution of Na_2O, with brighter areas showing more sodium oxide. From [28]

is converted to tridymite or cristobalite, and the same happens with quartz. Dissolution of the new phase then takes place."

These studies observed the phase transformation in both quartz and amorphous silica. However, this transformation is often overlooked in later research involving amorphous silica dissolution [12,27,29,33,41]. Despite the observed transformation, there appears to be no significant impact on the diffusivity of silica, regardless of the starting polymorph. None of the studies comparing quartz and amorphous silica dissolution in sodium silicate melts reported significant differences in the interdiffusion coefficient of silica between the two sources. This observation suggests that the phase transformation may not influence diffusivity, a point explored further below.

Thermodynamic calculations in Section 4.1.2 revealed that the equilibrium composition of the glass at the dissolution interface is not influenced by the initial silica polymorph. However, the Gibbs free energy of dissolution is slightly more negative when quartz is the starting polymorph (Table 4.3). Despite this, if dissolution is governed by mass transport phenomena, the acceleration of the interface reaction would have a minor influence, as it is not expected to be the rate-limiting step.

Nevertheless, if quartz remains a metastable phase during dissolution, the *liquidus* composition is altered, leading to increased silica solubility in the glass and greater undersaturation (Table 4.4). Assuming that the diffusivity of silica can be approximated by the EBDC obtained from Trial and Spera's [62] diffusion matrix (3.4×10^{-11} m^2/s), and that these diffusivities are independent of the silica polymorph, different dissolution scenarios can be estimated based on variations in the molar volume of the solid phase and the *liquidus* composition.

The necessary properties for these calculations are displayed in Table 4.6. Using molar volume data compiled by Toplis [119], the conversion from molar fraction to molar fraction per unit volume was conducted. The ratios of partial volume in solid to melt (ε) for β-quartz, HP-tridymite, β-cristobalite, and amorphous silica were calculated from Table 4.1. The reader is referred to Section 1.2.2 for a detailed explanation on the physical meaning of F_a and ε.

In the standard cases, it is assumed that the equilibrium composition corresponds to the glass in contact with tridymite, implying the absence of metastable silica polymorphs. However, no significant differences in the equilibrium composition at the interface are expected for cristobalite, as both tridymite and cristobalite share the same equilibrium composition with the glass (Table 4.4). The differences between these cases lie in the solid phase being dissolved. Since the

Table 4.6 Variables calculated from equilibrium compositions in Table 4.4. The concentration in moles per unit volume for the soda-lime silica glass (f_∞) and the glass at the interface (f_a) were converted using the molar volumes in [119]. ε values were obtained from Table 4.1

	standard-qua	**standard-tri**	**standard-cri**	**standard-amo**	**qua-qua**	**amo-qua**
f_∞ (mol/m^3)			25872			
f_a (mol/m^3)	30087	30087	30087	30087	34966	34966
ε	-0.14	0.02	0.01	0.001	-0.14	0.001
F_a	0.52	0.60	0.59	0.59	3.63	4.12

molar volumes of tridymite and cristobalite are similar to vitreous silica (Table 4.1), ε remains close to zero. As a result, no significant volume change is expected as silica migrates from these polymorphs into the glass. However, silica released from quartz occupies a larger volume in solution than in the solid phase, potentially increasing radial flow near the interface and flattening the concentration gradients (as discussed in Section 1.2.2 and illustrated in Figure 1.8).

The "qua-qua" scenario considers quartz remaining as the metastable solid phase in contact with the glass. Another scenario is also examined, where the interface composition remains as if quartz is metastable, but the silica source is amorphous. Compared with the standard cases, assuming that the interface composition is determined by metastable quartz significantly increases the undersaturation parameter (F_a).

Furthermore, given that the experimental setup closely approximates the flat slab model (Section 1.2.2), the dissolution length during the early stages can be calculated. This model was chosen since the quasi-steady-state approximation (Section 1.2.2) is invalid in this case, as the undersaturation exceeds the approximation's validity limit ($F_a \leq 10^{-3}$). The results of these calculations, shown in Figure 4.15, illustrate the dissolution behavior until 20% dissolution, which falls within the flat slab approximation's validity range.

The results indicate that the glass composition at the interface is the primary factor influencing dissolution rates, with a marked acceleration observed when quartz is present as a metastable phase in contact with silica-rich glass. Even faster dissolution would be expected if amorphous silica were in contact with this high-silica glass, as there would be less solute accumulation near the interface.

Conversely, if thermodynamic equilibrium is assumed at the interface, the dissolution proceeds more slowly. This thermodynamic equilibrium assumption corresponds to the standard case discussed earlier, where the glass composition is in equilibrium with tridymite, and no metastable silica polymorph is present. Under these conditions, quartz dissolves more slowly than other silica sources due to its smaller molar volume relative to the partial molar volume of silica in the glass. Hlavac and Nademlynska [31] reported that vitreous silica dissolves in 83% of the time required for quartz.

All scenarios discussed here assume that the solid phase remains unchanged during dissolution. In these cases, tracking changes in the geometric properties of the dissolving solid (e.g., length) is meaningful, as the solid phase undergoes size reduction solely due to dissolution.

However, as discussed in earlier sections, quartz will likely undergo phase transformation into tridymite or cristobalite during dissolution. Therefore, in addition to the dissolution dynamics, the volume expansion associated with the phase transformation must also be considered.

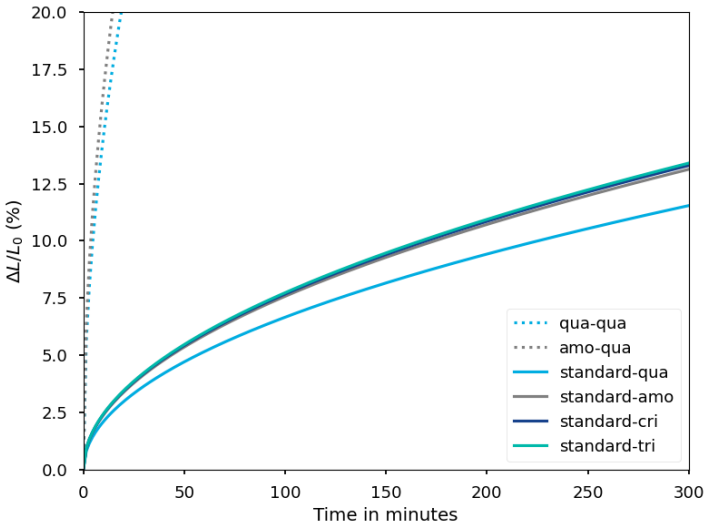

Figure 4.15 Relative dissolved length considering the flat slab approximation. Solid lines show the standard case, where the glass composition at the interface is in equilibrium with tridymite. The dotted lines, however, show the case if quartz is assumed to be metastable and the glass composition is in equilibrium with it. Standard cases for amorphous silica (gray), cristobalite (dark blue), and tridymite (green) almost superpose themselves.

Despite this added complexity, understanding quartz dissolution remains critical, as quartz is the primary form of silica found in sand grains, the main raw material used in industrial glass production. The following section will address the adaptations made to the experimental setup and quantifying methodology, described in Chapter 2, to account for the specific challenges posed by quartz dissolution.

4.2 Silica dissolution methods

4.2.1 Experimental setup geometry adaptations

Given the potential volume expansion due to the transformation of quartz into high-temperature polymorphs, it is anticipated that the original sample (tablet) will expand by approximately 20% during the dissolution test. However, because the tablet is wrapped and constrained by the platinum foil, such expansion can induce deformation in the assembly if quartz expansion is not taken into account. This phenomenon was observed during tests conducted for 30 minutes and 1 hour at 1400 °C (Figure 4.16), using both glass and quartz tablets of the same diameter. In these instances, the expansion was significant enough to open the assembly.

Consequently, quartz dissolution tests were conducted using a 10 mm diameter glass, instead of the initially proposed 8 mm geometry, to allow space for quartz expansion during dissolution. Although the increase in diameter could potentially favor double-diffusive convection (Section 2.2.3), such disruption would only be expected for tests longer than 325 minutes when using a 10 mm diameter glass, as indicated in Figure 2.4.

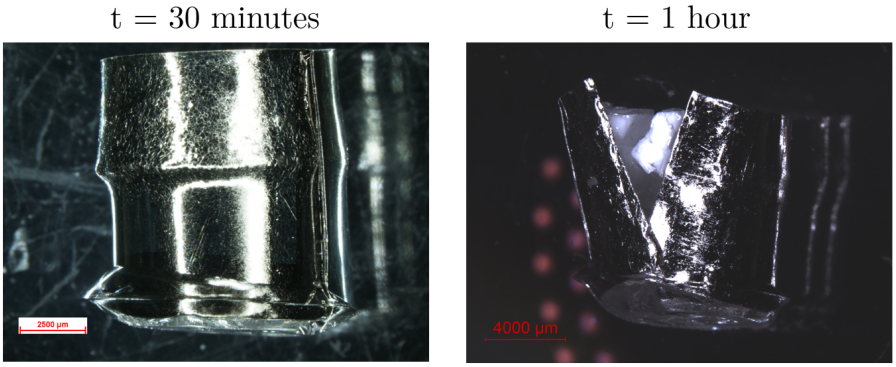

Figure 4.16 Photos of samples after dissolution tests at 1400 °C for 30 minutes (left) and 1 hour (right) using the same initial diameter for both glass and quartz tablets (8 mm). Due to the volume expansion of quartz at high temperatures, it deforms the platinum gold foil.

Another impact of the potential phase transformation from quartz to more voluminous polymorphs is the inversion of density between the silica source and the glass. As explained in Section 2.2, denser material is placed at the bottom to avoid buoyancy due to gravitational instabilities. However, while quartz is denser than soda-lime silica glass, both tridymite and cristobalite are less dense than the original glass, as depicted in Figure 4.17.

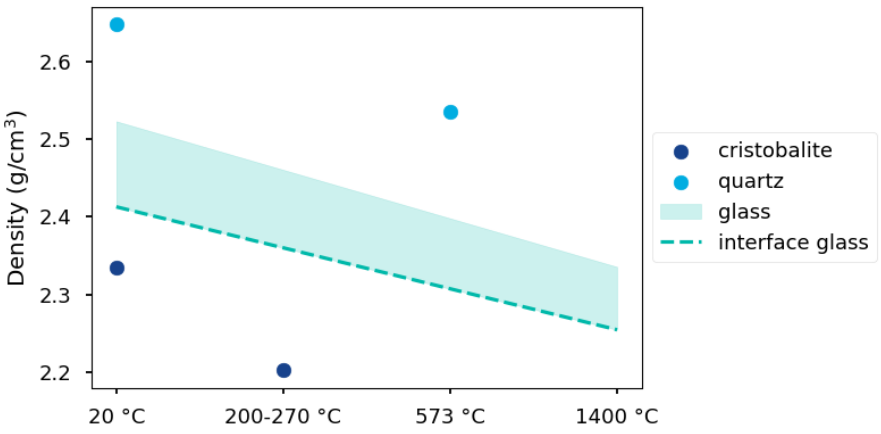

Figure 4.17 Density variation for different temperatures for quartz and cristobalite, considering their low- and high-temperature forms. The density range for glass is shown as the shaded area, with the interface value as the inferior limit. Densities for the original glass and interface composition were calculated based on GlassPy's "predict" module for density.

Given this possibility, a comparison was made between the relative positions of quartz and glass in the setup under the same dissolution test conditions : 1400 °C for 15 minutes. Figure 4.18 illustrates the tested configurations. In all cases, the surfaces comprising the interface were polished, as in the original setup.

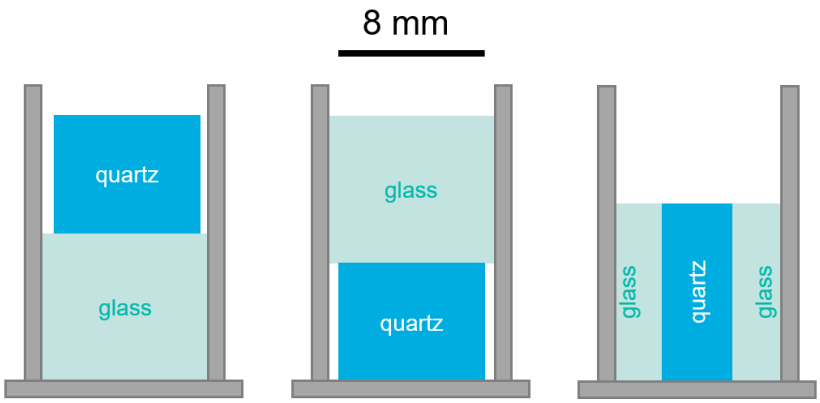

Figure 4.18 Setup configurations used to compare the effect of density inversion during quartz dissolution at 1400 °C for 15 minutes. (from left to right) : "silica on top" or PSq-1400-15, "silica on bottom" or PSqd-1400-15, and "vertical sandwich" or PSqs-1400-15.

The third configuration involved placing the quartz and glass interface vertically to suppress potential gravitational effects due to density inversions. For this setup, the original quartz tablet was ground around the perimeter to produce a rectangular shape while maintaining the same crystalline orientation and polished surface quality in contact with the glass. The glass was cut into a higher cylinder and then halved to produce two half tablets. Their perpendicular surfaces were polished, as these would become the dissolution interface in the vertical setup. The two halves of glass were then placed in contact with the quartz tablet and enclosed by platinum-gold foil, acting as a crucible.

It is noteworthy that the mole fraction of quartz in this setup is higher than in the other experiments : 51%, compared to the 39% maximum silica content for full dissolution according to Figure 4.3. Therefore, complete dissolution is not expected in this case, given the high quantity of silica that cannot be entirely incorporated by the glass due to its limited solubility. However, given the very short time of dissolution, it was assumed that this difference is not relevant, as even in assemblies where full dissolution is possible (mole fraction of quartz $\approx$ 36% for the "silica on top" setup, see Table 4.8), such a scenario is not observed for 15 minutes.

The results of the comparison between the three setups will be detailed and discussed in Section 4.4.2. However, it is important to note that none of the setups entirely avoided perturbations in the dissolution front. Therefore, the geometry with silica on top, using a 10 mm diameter glass and an 8 mm diameter quartz, was retained as the standard geometry for silica dissolution tests. Unless explicitly stated otherwise, this geometry will be assumed for the dissolution test samples discussed in the following.

4.2.2 Use of silica sources other than quartz as starting material

To address the effects of the transformation from quartz to other silica polymorphs, previously transformed cristobalite tablets were also employed as starting materials in the dissolution tests, in addition to quartz monocrystalline tablets. Cristobalite was sourced from a fused-cast silica refractory brick, whose chemical composition was measured using both Electron Probe Micro-Analysis (EPMA) and X-Ray Fluorescence (XRF), as detailed in Table 4.7.

Table 4.7 Chemical composition of the fused-cast refractory brick (in %mol) by Electron Probe Microanalysis and semi-quantitative X-Ray Fluorescence analysis. The values with (*) are below the chemical resolution of EPMA.

	EPMA	**XRF**
SiO_2	100.1 ± 0.5	99.5
Al_2O_3	0.006 ± 0.008*	0.11
Na_2O	0.004 ± 0.006*	0.01
K_2O	0.003 ± 0.004*	0.006
CaO	0.005 ± 0.009*	0.1
MgO	0.01 ± 0.02*	0.01

The fused-cast silica refractory brick was sectioned into 5 mm slices using a diamond circular saw designed for refractories. The tablets were then core drilled into 10 mm diameter tablets to match the glass diameter, given the low density of both amorphous silica and cristobalite.

The microstructure of the amorphous silica refractory is depicted in Figure 4.19, illustrating large fused-cast silica grains within a finer matrix, which also comprises amorphous silica.

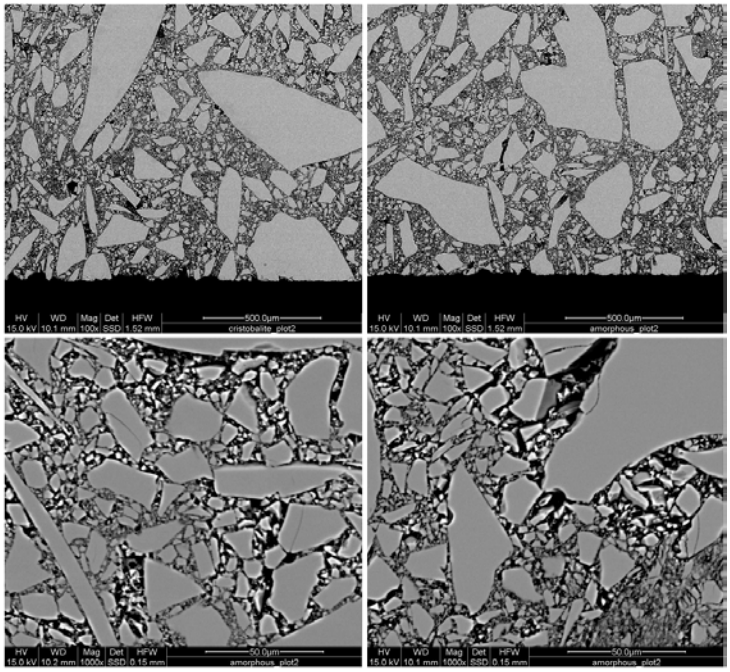

Figure 4.19 Scanning Electron Microscope (SEM) using Backscattered Electron (BSE) mode images of the initial microstructure of fused-cast silica refractory tablet. The top images are at a lower magnification, and the bottom images zoom into the refractory's matrix fine microstructure.

While the heterogeneous distribution of grain sizes can influence dissolution behavior, the particle packing likely facilitated the formation of a cristobalite tablet stiff enough for handling without collapsing.

The amorphous silica tablets underwent heat treatment at 1504 °C for at least 95 hours using the same electric furnace employed for the dissolution tests. This temperature was selected

because it exceeds the 1470 °C threshold required for the transformation to cristobalite from pure silica [101, 120]. The tablets were placed on platinum-gold foil to avoid contamination from direct contact with the furnace refractories. The specific heat treatments for each cristobalite sample prepared are compiled in Table 4.8, which includes all silica dissolution tests.

The resulting tablet surface, intended for contact with the glass interface during dissolution tests, was polished post-heat treatment. The microstructure obtained after 95 hours at 1504 °C, illustrated in Figure 4.20, shows a homogeneous distribution of grain sizes, smaller than those in the original amorphous silica refractory. Both Raman spectroscopy mapping (Figure 4.21) and X-Ray Diffraction (XRD, in Figure A.3) confirmed the formation of cristobalite throughout the tablet, validating the formation of this polymorph for studying its effect on silica dissolution.

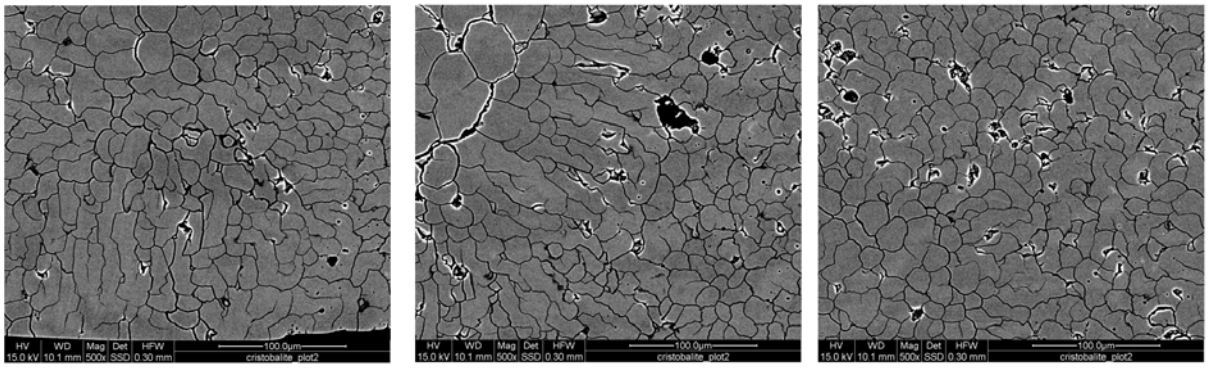

Figure 4.20 Scanning Electron Microscope (SEM) using Backscattered Electron (BSE) mode images of the initial microstructure of the manufactured cristobalite tablet, after heat treatment at 1504 °C for 95 hours.

A preliminary attempt to obtain cristobalite from the quartz tablet under similar conditions resulted in the original piece collapsing post-heat treatment (Figure 4.22 left), despite XRD indicating cristobalite formation (Figure A.4). This may be attributed to the anisotropic behavior of the monocrystalline quartz tablet subjected to intense heating and subsequent extreme volume expansion due to phase transformation. Another test using amorphous silica cylinders as cristobalite precursors was also conducted (Figure 4.22 right). Although this did not collapse entirely like the quartz, the resulting cristobalite tablet was very fragile after cooling and unsuitable for interface polishing prior to dissolution tests.



Figure 4.22 Trials of using the monocrystalline quartz (left) and amorphous silica cylinders (right) as precursors for cristobalite formation by heat treating them at 1500 °C for 4 days and 17 hours.

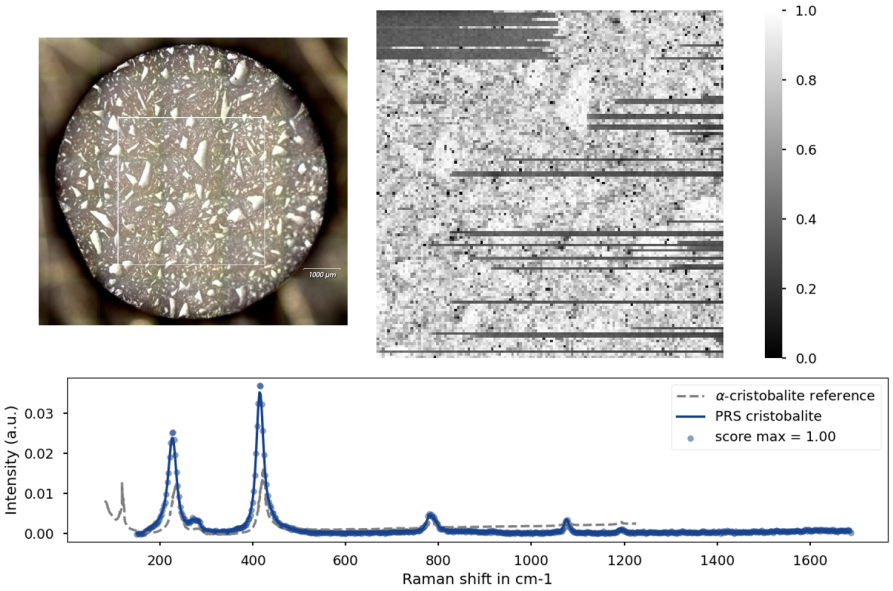

Figure 4.21 Raman mapping of the manufactured cristobalite tablet's top surface, after heat treating the fused-cast silica brick at 1504 °C. The measurement region is enclosed by the white rectangle, and the cristobalite heatmap is displayed by the black and white square in the right corner. A reference spectra for α-cristobalite from [121] is displayed as a gray dashed line for comparison with the main spectra obtained from the Raman mapping.

4.2.3 Compilation of silica dissolution tests

To better comprehend quartz dissolution in glass, an additional silica source was employed, necessitating a reduction in the scope of the silica dissolution tests to a single temperature of 1400 °C. The compilation of all dissolution tests is presented in Table 4.8. To distinguish the different silica sources used for the dissolution tests, the sample names were designated as follows : those using quartz start with PSq, and those using cristobalite start with PSc.

According to the criteria calculated and detailed in Section 2.2.1, the semi-infinite dissolution assumption is no longer valid for quartz dissolution tests lasting longer than two hours for a 5 mm height glass slab at 1400 °C (Figure 2.2). Consequently, dissolution tests ranging from 15 minutes to 2 hours were preferred.

Additionally, three further time intervals were included : 2 minutes, 4 hours, and 24 hours. The very short dissolution test was conducted to examine the formation of high-temperature polymorphs from quartz, even during the furnace temperature stabilization phase, which lasts between 1 to 2 minutes. At the other extreme, a 24-hour test was conducted to observe the evolution of silica polymorphism from both silica sources in contact with the molten glass. Finally, the 4-hour test provides an intermediate duration between 2 hours and 24 hours, while still within the threshold of convection onset for a 10 mm diameter glass slab (Figure 2.4). Notably, after 4 hours, the glass is no longer expected to be an infinite reservoir and may begin to be saturated by the silica dissolution.

As detailed in the previous section, the comparison of different geometries conducted with quartz in varying configurations for 15 minutes at 1400 °C are also included in Table 4.8. The configurations where silica is positioned at the bottom and in a vertical sandwich are indicated with the

suffixes -d and -s, respectively, following the PSq nomenclature. As previously mentioned in Section 4.2.1, PSq-1400-15 denotes the silica-on-top setup, which was maintained as the standard configuration for silica dissolution tests.

Table 4.8 Summary of experimental parameters for silica dissolution tests. The third letter denotes the silica source (quartz or cristobalite tablets), and the final digits represent the nominal test duration in minutes. Tests comparing setup geometry after 15 minutes are also included. Due to the initial quartz tablet's unique geometry in the vertical sandwich setup, the diameters of both glass and quartz are not specified in this table.

Sample name	T (°C)	t (min)	Silica source	Cristobalite preparation	Setup geometry	Silica diameter (mm)	Silica thickness (mm)	Glass diameter (mm)	Glass thickness (mm)	Solid silica %mol
PSq-1400-00	1400	2	Quartz		silica on top	8.0 ± 0.2	5.08 ± 0.02	8	3.13 ± 0.04	
PSqs-1400-15	1400 ± 2	15	Quartz		vertical sandwich		3.993 ± 0.003			51%
PSqd-1400-15	1399 ± 2	15	Quartz		silica on bottom	8.0 ± 0.2	3.988 ± 0.001	8	5.08 ± 0.01	47%
PSq-1400-15	1400 ± 2	15	Quartz		silica on top	8.0 ± 0.2	3.988 ± 0.001	10	5.01 ± 0.03	36%
PSc-1400-15	1401 ± 3	15	Cristobalite	1504.4 ± 0.9 for 287 h	silica on top	7.38 ± 0.01	3.079 ± 0.006	10	4.466 ± 0.008	33%
PSq1400-50	1401 ± 1	50	Quartz		silica on top	8.0 ± 0.2	3.988 ± 0.001	10	6.459 ± 0.006	30%
PSc-1400-50	1401 ± 1	50	Cristobalite	1504.4 ± 0.9 for 95 h	silica on top	9.52 ± 0.04	2.562 ± 0.004	10	5.24 ± 0.02	28%
PSq1400-85	1399.5 ± 0.8	85	Quartz		silica on top	8.0 ± 0.2	3.988 ± 0.002	10	5.29 ± 0.02	34%
PSc-1400-85	1399.5 ± 0.8	85	Cristobalite	1504.4 ± 0.9 for 95 h	silica on top	9.5 ± 0.1	2.94 ± 0.09	10	5.17 ± 0.01	30%
PSq-1400-120	1399.0 ± 0.6	120	Quartz		silica on top	8.0 ± 0.2	3.988 ± 0.001	10	4.984 ± 0.008	36%
PSc-1400-120	1399.0 ± 0.6	120	Cristobalite	1503.5 ± 0.8 for 291 h	silica on top	7.38 ± 0.01	3.018 ± 0.001	10	5.169 ± 0.003	22%
PSq1400-240	1399.0 ± 0.8	241	Quartz		silica on top	8.0 ± 0.2	3.995 ± 0.003	10	5.292 ± 0.004	34%
PSc-1400-240	1399.0 ± 0.8	241	Cristobalite	1504.4 ± 0.9 for 95 h	silica on top	9.4 ± 0.1	2.49 ± 0.01	10	6.31 ± 0.04	24%
PSq-1400-1440	1399.0 ± 0.7	1442	Quartz		silica on top	8.0 ± 0.2	3.993 ± 0.002	10	6.396 ± 0.005	30%
PSc-1400-1440	1399.0 ± 0.7	1442	Cristobalite	1503.5 ± 0.8 for 291 h	silica on top	7.38 ± 0.01	3.19 ± 0.02	10	4.874 ± 0.005	24%

4.2.4 Quantification of dissolved silica

As detailed in Section 4.1.1, the process of quartz transformation into high-temperature polymorphs induces a significant volume expansion, which can mask the anticipated shrinkage due to quartz dissolution. As such, measuring the dissolved silica using geometric properties, namely length, area, or volume, is hindered by these two opposing phenomena. Therefore, the proposed method for quantification involves measuring the number of moles of dissolved silica.

One approach involves calculating the silica content incorporated into the glass after dissolution by measuring the difference between the initial silica content in the glass and the amount present after the dissolution test. This method was employed successfully in alumina dissolution tests (Chapter 3), where the chemical profiles were measured using Electron Probe Micro-Analysis (EPMA).

However, the current protocol for measuring profiles with EPMA assumes that the dissolution front is perpendicular to the interface and homogeneous, i.e., the process is one-dimensional. While this assumption held true for alumina dissolution, it was seldom observed in quartz dissolution samples, as shown by EPMA and Scanning Electron Microscopy with Energy Dispersive Spectroscopy (SEM/EDS) observations, as it will be described in Section 4.4. The origins of these phenomena will be further discussed in Section 4.4.2.

In addition, a method that quantifies the dissolved amounts of various silica polymorphs would be useful for comparing the kinetics of both dissolution and phase transformation, given their potential coexistence. EPMA and SEM/EDS, which rely on chemical contrast, are inadequate for distinguishing between polymorphs because these phases share the same chemical composition.

In light of this, Raman spectroscopy mapping, which is sensitive to the material structure, has proven to be a valuable method for distinguishing these differences. By applying the Non-negative Matrix Factorization (NMF) strategy on spectral maps of post-dissolution samples, it was possible to obtain the partial Raman spectra (PRS) (see Section 2.5.2 for details). Thanks to the defined Raman response of crystalline phases, different PRS could be associated with a given silica polymorph. Besides the crystalline phases, original glass, silica-enriched glass, epoxy resin surrounding the assembly and inside the pores, were also often identified as NMF's components. Less frequently, experimental artifacts, such as carbon layer residues from a prior EPMA measurement or roughness signal, were also identified.

For each spatial point and each PRS, there is a corresponding weight, whose sum is equal to one. To calculate the contribution of each silica polymorph component, the partial spectra of non-crystalline phases, epoxy resin, and surface experimental artifacts were neglected, and the relevant PRS weights were normalized. The weights are then filtered using Otsu's method to exclude the background contribution. The points where the threshold is not attained are assigned a value of zero. The remaining points retain their PRS weights, which are normalized again to ensure their sum equals unity. By multiplying the pixel area in the Raman map with the calculated weight for each polymorph in each pixel, and then integrating over the whole cartography, it is possible to calculate an area for the polymorph, normalized by its partial Raman spectra's weight. This procedure is depicted in Figure 4.23. Some of Raman mappings were performed only in half of the grain, and theirs surface was multiplied by two in these cases.

To convert these areas into the number of silica moles, a correction based on molar volume was proposed, using the molar volume values from Table 4.1 for each identified polymorph. Therefore, the estimated area for each polymorph needs to be converted into an equivalent volume. Given the initial geometry of the slab and assuming that axial symmetry is maintained

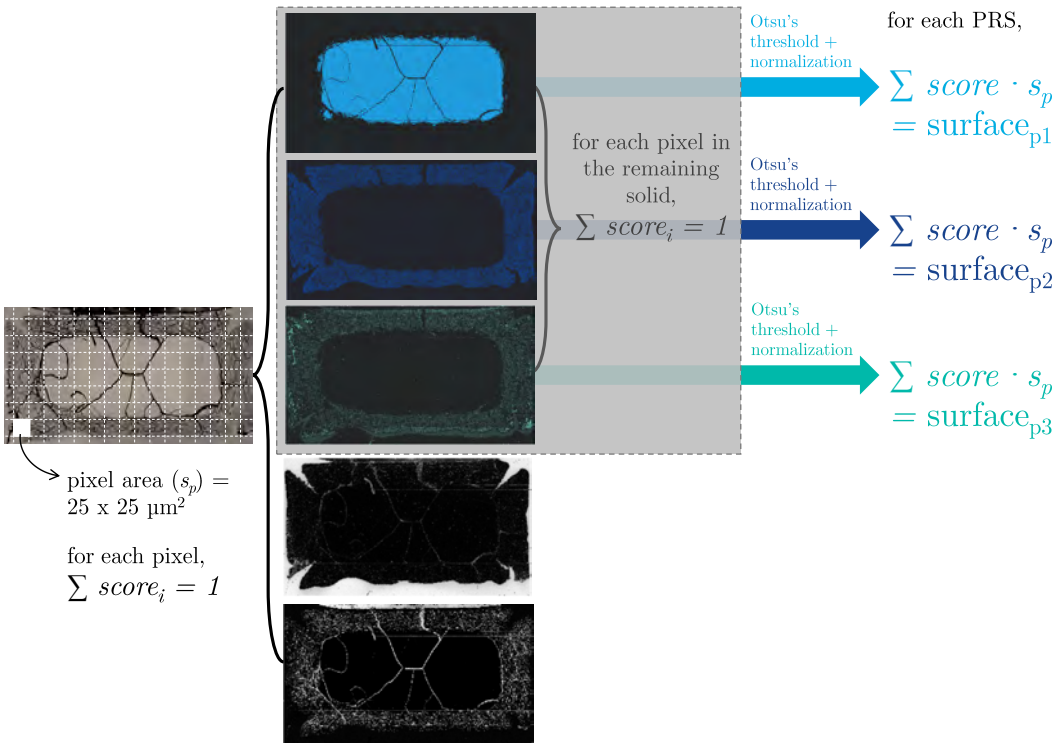

Figure 4.23 Schematic illustration of the method used to identify the surfaces of various silica polymorphs from Raman mapping of post-dissolution samples. Each polymorph's contribution is quantified through the Non-negative Matrix Factorization (NMF) score of the corresponding Partial Raman Spectrum (PRS) for each pixel ($score_i$). The total surface area associated with each silica phase is then determined by multiplying the sum of the respective NMF score by the pixel area (s_p).

after dissolution, it is reasonable to approach the geometry of the consumed solid as a cylinder. For this geometry, the cross section surface corresponds to $2rh$, where r is the radius of the cylinder and h, its thickness. Considering that a cylinder is a stack of disks of area πr^2 along the axis defined by h, the equivalent volume of a cylinder of cross section area of $2rh$ can be expressed as :

$$V_{\text{eq}} = \pi r^2 h \Rightarrow V_{\text{eq}} = \pi r(rh) \Rightarrow V_{\text{eq}} = \pi r \frac{\text{surface}_{\perp}}{2} \tag{4.4}$$

where $\text{surface}_{\perp}$ is the cross section surface and r will be assumed as the characteristic length.

The surface area of each polymorph, obtained through Raman mapping and NMF analysis, was then converted into an equivalent volume by multiplying it by $\pi r/2$, where r is the radius of the remaining solid after dissolution, measured from five different segments using the ImageJ software on post-dissolution samples' micrographs. This equivalent cylinder volume for each polymorph was divided by the molar volume (V_m) of its corresponding low-temperature form to determine the number of silica moles : $\hat{N} = V_{\text{eq}}/V_m$.

The number of dissolved silica moles was determined by subtracting the moles remaining in the solid phase from the initial amount in the sample. The initial quantity of silica moles was calculated using the sample's initial mass (m_0) and the molar mass of SiO_2 (60.08 g/mol) : $\hat{N}_0 = m_0/\text{MM}_{SiO_2}$. Using initial mass to estimate the number of moles was preferred for the original slabs, particularly because sintered cristobalite samples had residual porosity. In these cases, using and correcting volume with cristobalite's molar volume would overestimate the number of moles. Although it was not viable to measure the mass of the remaining solid after dissolution, the cartographies of the cross-sections provided an assessment of porosity. A comparison between estimations using both mass and geometric dimensions for the initial tablets, detailed in Section B.1 in Appendix B, revealed that both methods yielded comparable results for quartz slabs. However, for cristobalite slabs, the molar volume estimation consistently produced higher values than mass-based calculations, likely due to an approximate 8% porosity.

Normalizing the number of dissolved silica moles and the remaining moles by the available interface surface was essential for two reasons : first, the slab diameter changes during dissolution, and second, the initial diameters of quartz and cristobalite slabs were different (as shown in Table 4.8). Without this normalization, comparing the dissolution amounts of quartz and cristobalite would be problematic, as their differing diameters would lead to inconsistent dissolution measurements across the available surface.

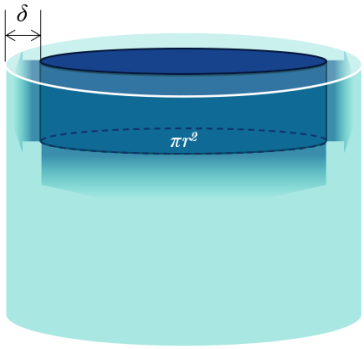

Figure 4.24 Schematic illustration of the possible available interfaces between the solid and the glass

As illustrated in Figure 4.24, the dissolution interface comprises both the bottom face of the slab (πr^2) and its lateral surface ($2\pi rh$). To accommodate the expansion, the glass slab's diameter was larger than that of the quartz slab (Figure 4.16). However, the lateral gap between crystalline silica and the melt was not designed to mitigate confined dissolution. During extended dissolution tests, these gaps may become saturated with silica, thus ceasing to function as active interfaces. Section B.2 in Appendix B discusses instances where these lateral gaps reach a steady-state diffusion for silica, leading to deactivation. Notably, in the PSq-1440 test, the dissolution interface was limited to the slab's bottom face.

Silica dissolution and the presence of different polymorphs were quantified as a function of the number of dissolved silica moles, normalized by the available interface area. Since the interface can be calculated using both the initial and final dimensions of the slab, it is represented as a range between these values. Figure 4.25 summarizes and illustrates this quantification approach.

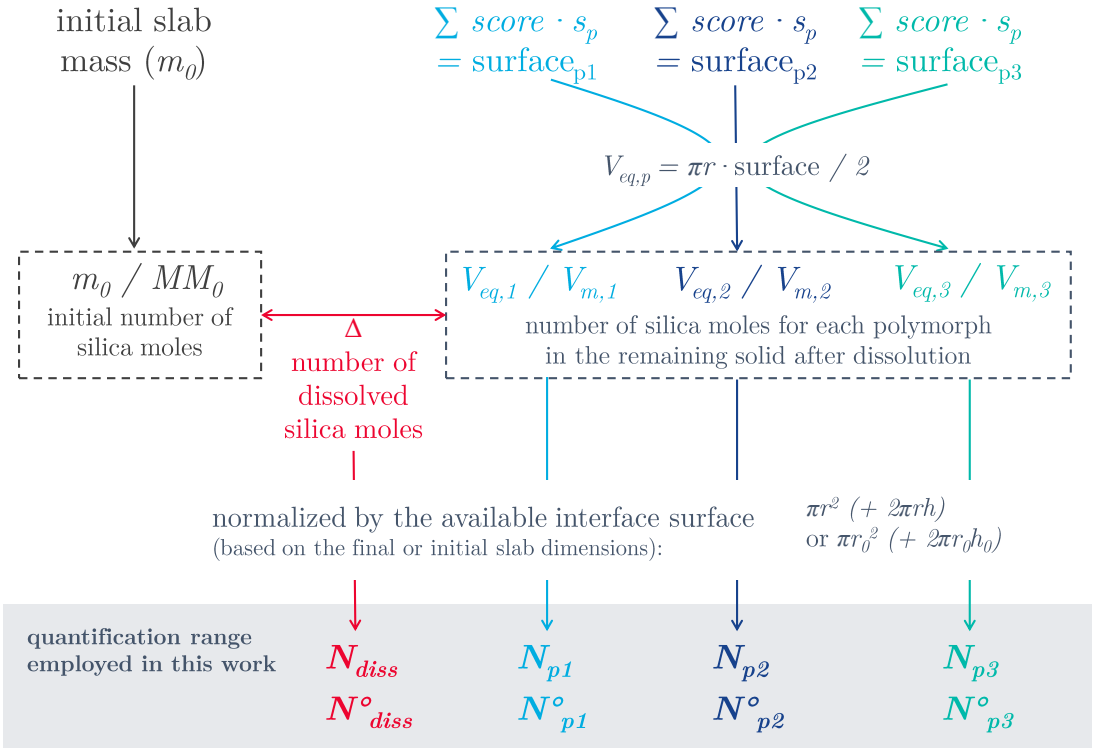

Figure 4.25 Illustration of the procedure for quantifying dissolved silica moles using Raman mapping scores of post-dissolution samples, as shown in Figure 4.23. The number of silica moles dissolved is calculated by assessing the difference (Δ) between the remaining silica phases and the number of moles in the initial tablet. This value is then normalized to the available interface surface, accounting for variations in the dimensions of the silica tablets.

This silica moles calculation was only performed for crystalline phases with a strong, well-defined Raman response and it presumes these phases are composed entirely of silica. Therefore, this method was not applied to quantify silica in the glass, even though Raman cartography coupled with NMF analysis can differentiate between heterogeneous regions of the glass. Nevertheless, this attribute was used to detect potential disruptions in the dissolution front. The structural contrast identified by Raman was deemed more suitable for verifying convection than the SEM/EDS chemical contrast, given the minor difference in silica content between silica-rich glass

and the original composition (see Figure 4.48).

This segmentation of the cross-section provided a semi-quantitative analysis of both silica dissolution and phase transformation. It was assumed that the polished cross-section was representative of the entire sample.

4.3 Microstructure evolution in quartz dissolution

The initial focus of this study is the dissolution of quartz, specifically analyzed through the polished cross-sections of monocrystalline quartz (PSq) test samples. These samples were observed using binocular and optical microscopes (Appendix C). Reflection mode images, gathered in Figure 4.26, highlight the remaining solid region after dissolution, utilizing a common scale bar for better comparison. Even at short dissolution times and lower magnifications, extensive cracking and grain boundary formation in the crystalline phase and a consequent loss of transparency are evident (see binocular microscopy images in Appendix's Figure C.2). Additionally, an intricate and highly fractured layer forms at the interface, thickening up to 2 hours of dissolution. This layer begins to fracture at the corners as early as 15 minutes and gradually adopts a flower-like motif up to 4 hours, with the corners appearing to consume the solid phase toward its center.

After 4 hours, the smoother region that previously comprised the center of the crystalline part is no longer visible, and the geometry of the remaining solid starts to deviate significantly from the shape of the initial tablet, as highlighted by the rectangle in Figure 4.26. Simultaneously, a gradual replacement of the intricate layer by another microstructural region with larger grains in the lateral segments is observed. Finally, after 24 hours, the remaining structure appears homogeneous but is extensively consumed.

Scanning Electron Microscope (SEM) images in Figure 4.27 closer to the interface reveal more details, providing information about chemical contrast through the use of Backscattered Electrons (BSE) mode. Within 15 minutes, glass infiltration (lighter hue) is already present in the solid throughout the fractured layer via continuous paths. This infiltration progresses to contour the grains in tests lasting longer than 2 hours. Except for the 24-hour sample, there is also a coexistence between a region composed of rounder grains, where the glass infiltration is occurring, and a more grooved segment, closer to the core of the original tablet.

In all samples, dendrites are present at the interface between the solid and the melt. Figures 4.28 and C.3 (Appendix C) present a closer magnification to the interface of the bottom and lateral parts of the remaining solid, respectively. The glass surrounding the dendrites exhibits a higher atomic mass compared to the adjacent glass. This phenomenon is likely due to the decrease of silica solubility in the glass during quenching, leading the glass close to the interface to become over-saturated in silica, resulting in the re-precipitation of pure silica as dendrites and a surrounding glass with lower silica content. Notably, except for the 24-hour test sample where the dendrites appear smaller, the extent of the affected region does not seem to change with the duration of dissolution, arguing again for a quenching effect.

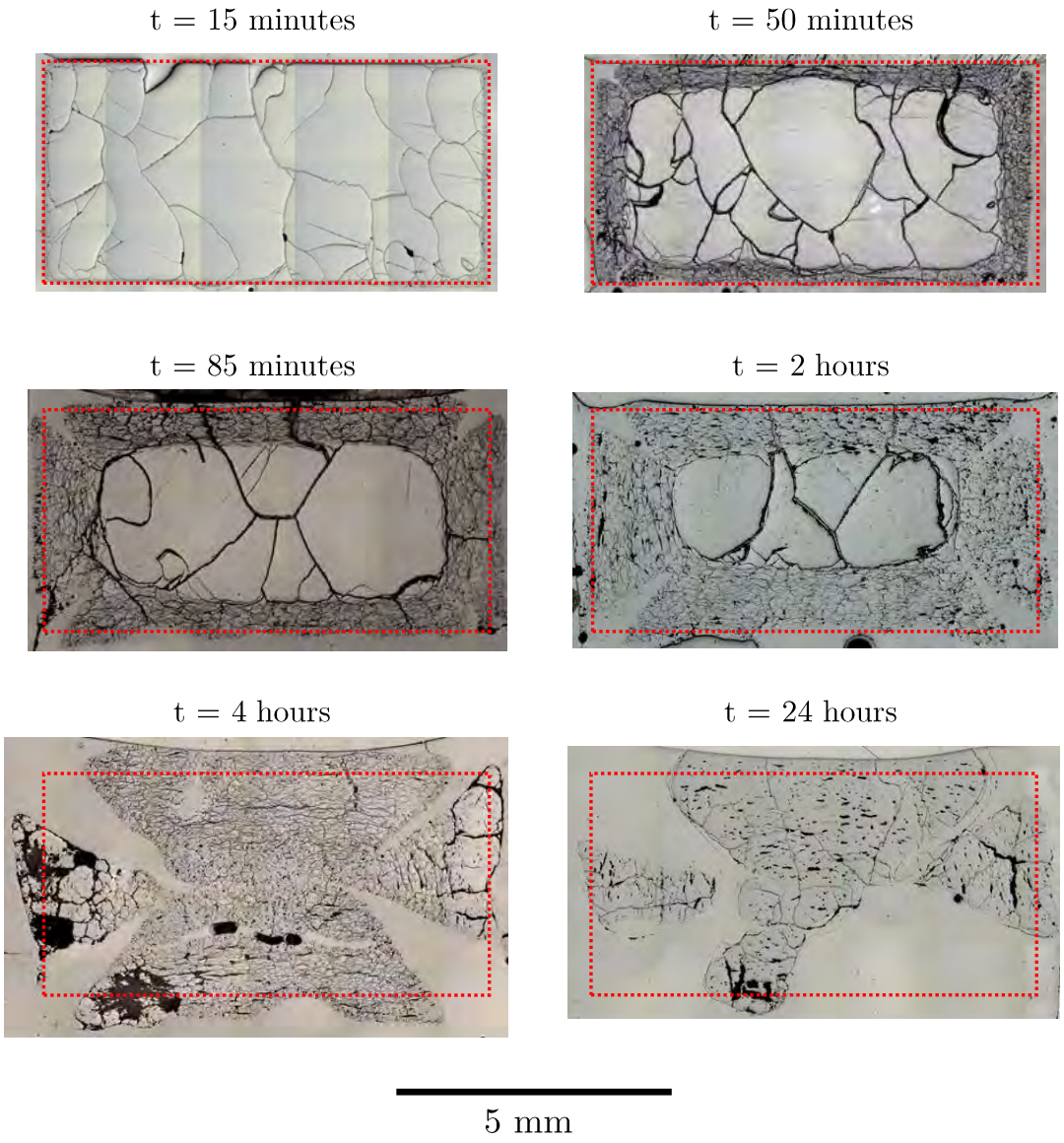

Figure 4.26 Optical microscopy photos in reflected light mode for all quartz dissolution samples. Red rectangle overlayed represents the original quartz tablet's dimension.

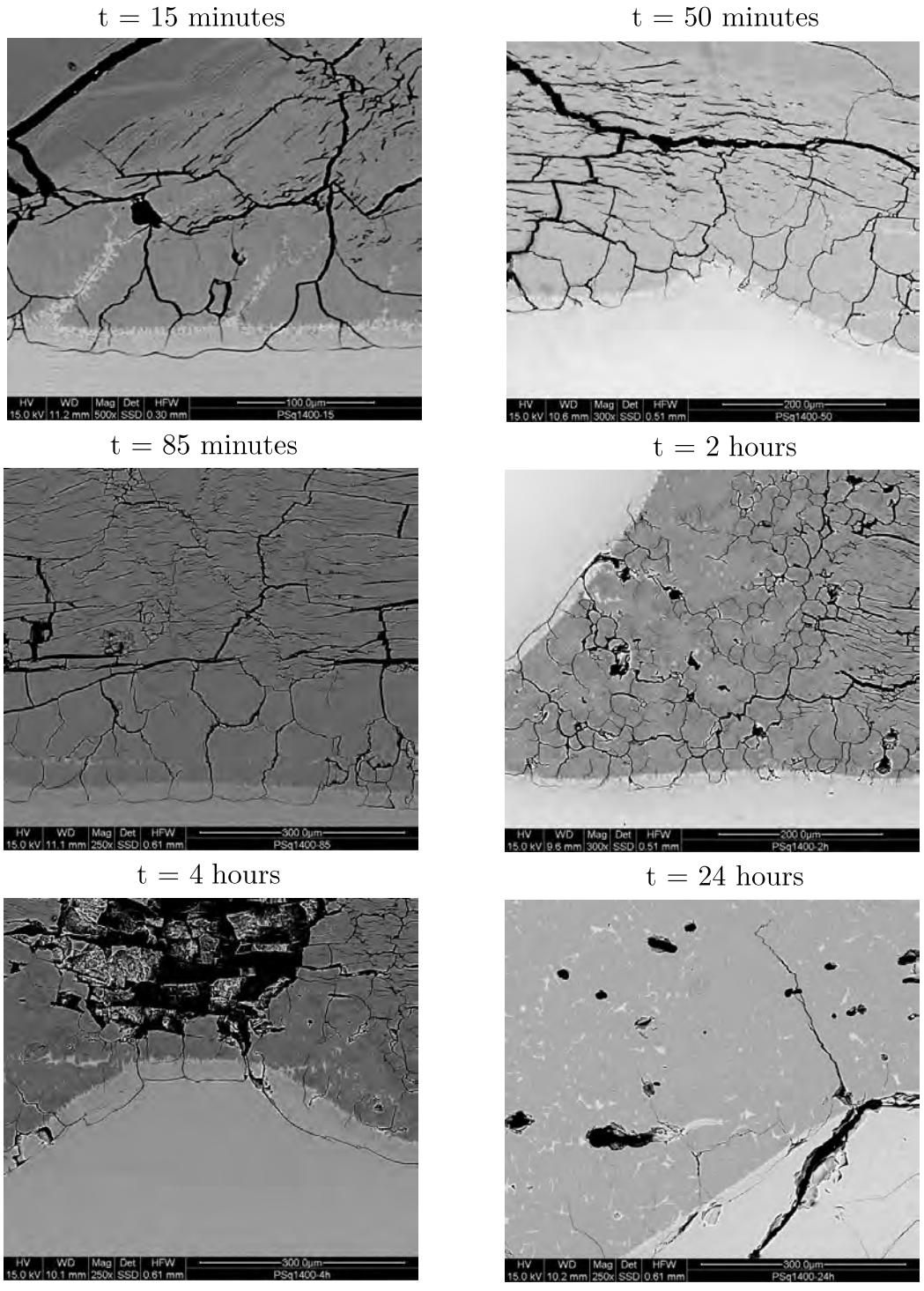

Figure 4.27 SEM images captured under Back Scattered Electron (BSE) mode. Glass infiltration can be observed closer to the interface. The images are not in the same scale.

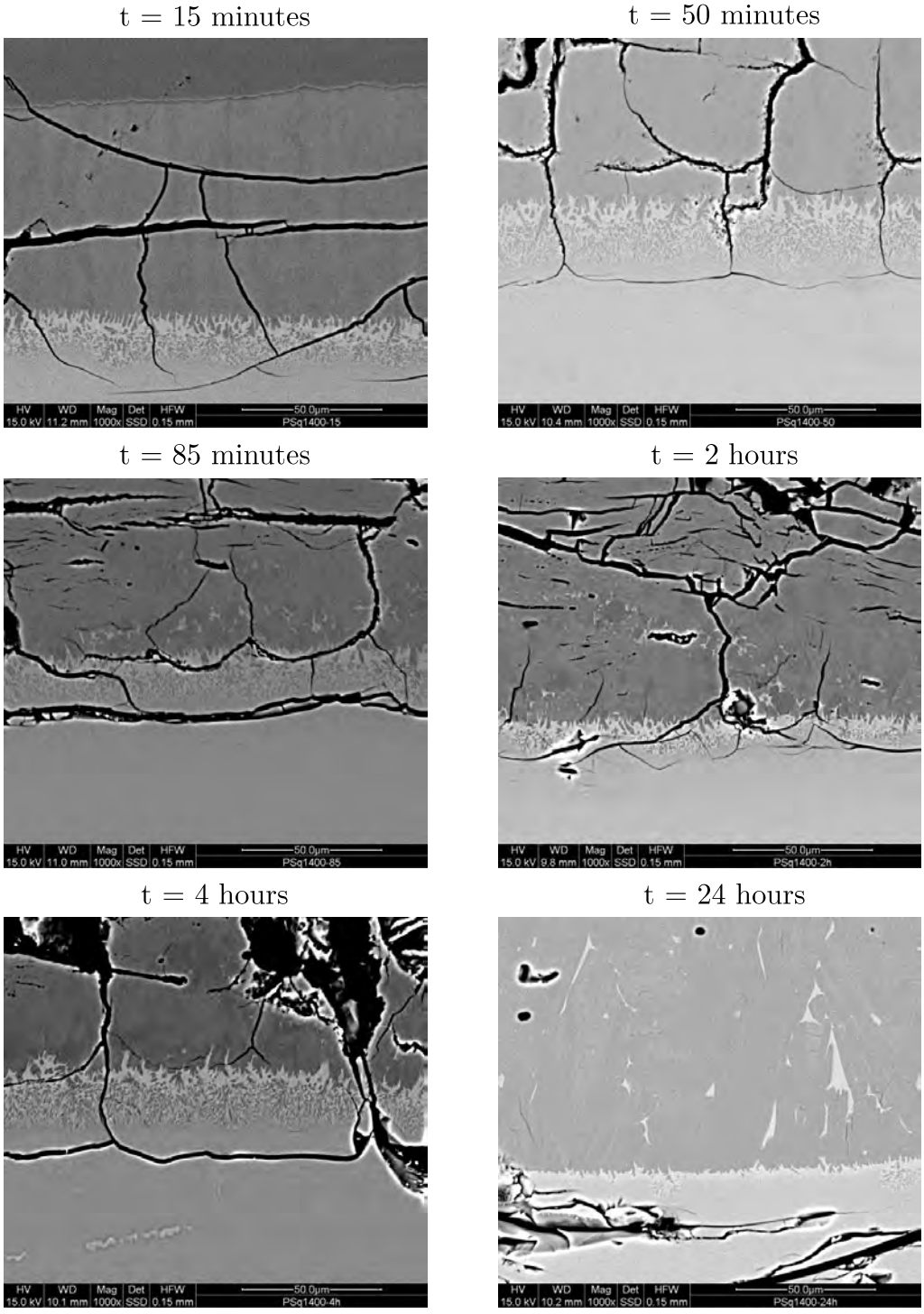

Figure 4.28 SEM images captured under Back Scattered Electron (BSE) mode, highlighting the dendrites close to the interface. All images have the same magnification and were obtained close to the lower middle part of the remaining solid.

Top-view images of the samples prior to epoxy embedding, as shown in Figure 4.29, reveal that the final shape presents radial symmetry but lacks axial symmetry. Periodic cracking disrupts the outer layer and corresponds to the lateral segments of the flower-like shape observed in cross-section images. Although the outer layer appears thick and almost continuous for up to 2 hours, the crack lengths increase with longer dissolution times, deviating further from an axial symmetry. Depending on the cross-section cut, it is possible to obtain either a flower-like with two lateral segments, only one segment, or no lateral segments, depending on whether the cut passes through a lateral crack region. These lateral crack regions are displayed as darker regions on the perimeter of the grains visualized from above. Given that all the cross section surfaces obtained (Figure 4.26) have the two lateral segments, it can be expected that the amount of solid calculated for the whole sample may be overestimated. Therefore, the assumption that a cross-section surface is representative of the three-dimensional final shape must be carefully considered, especially for longer dissolution tests.

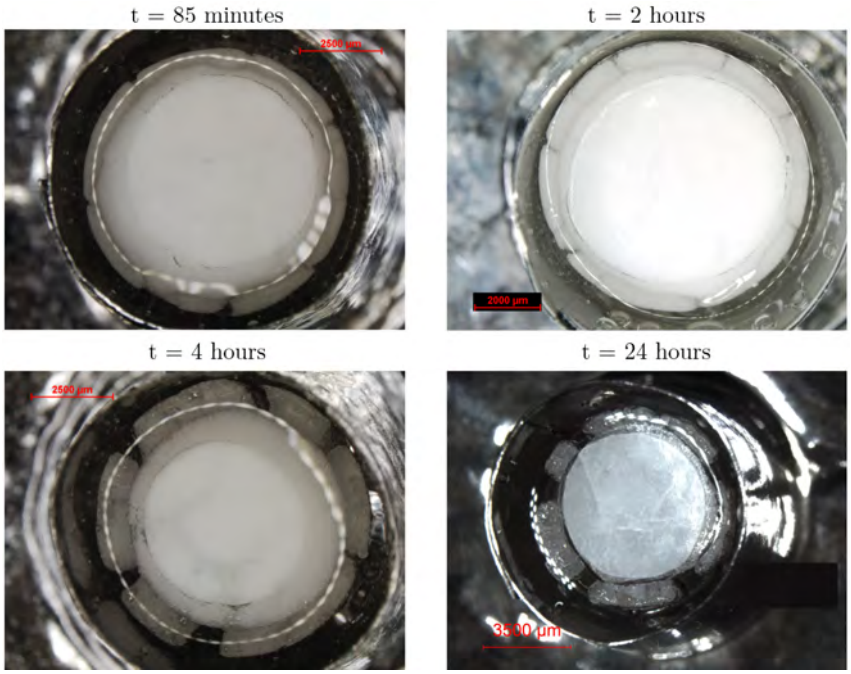

Figure 4.29 Top view images of the solid phase following dissolution tests with quartz at 1400 °C, taken before embedding in epoxy resin for polished section preparation. Over time, the progression of dissolution features and the emergence of cracks are observed, potentially affecting axial symmetry. The final shape displays approximate radial symmetry, though irregularities and fractures suggest local deviations from perfect symmetry.

4.3.1 Silica Polymorphs evolution during dissolution by Raman Spectroscopy Mapping

Coupling Raman spectroscopy with optical observations allows for the identification of different silica polymorphs and the assessment of their spatial distribution in the sample. Figures 4.30 and 4.31 illustrate the spatial distribution evolution of α-quartz and α-cristobalite over time. The obtained partial Raman spectra (PRS) for all the samples show a strong correspondence with previously reported Raman spectra in the literature, despite a minor shift in the cristobalite PRS towards lower frequencies compared to Bates' α-cristobalite spectra [87,121]. Consequently, the maps presented in Figures 4.30 and 4.31 can still be considered a suitable representation of the spatial distributions of quartz and cristobalite in the sample.

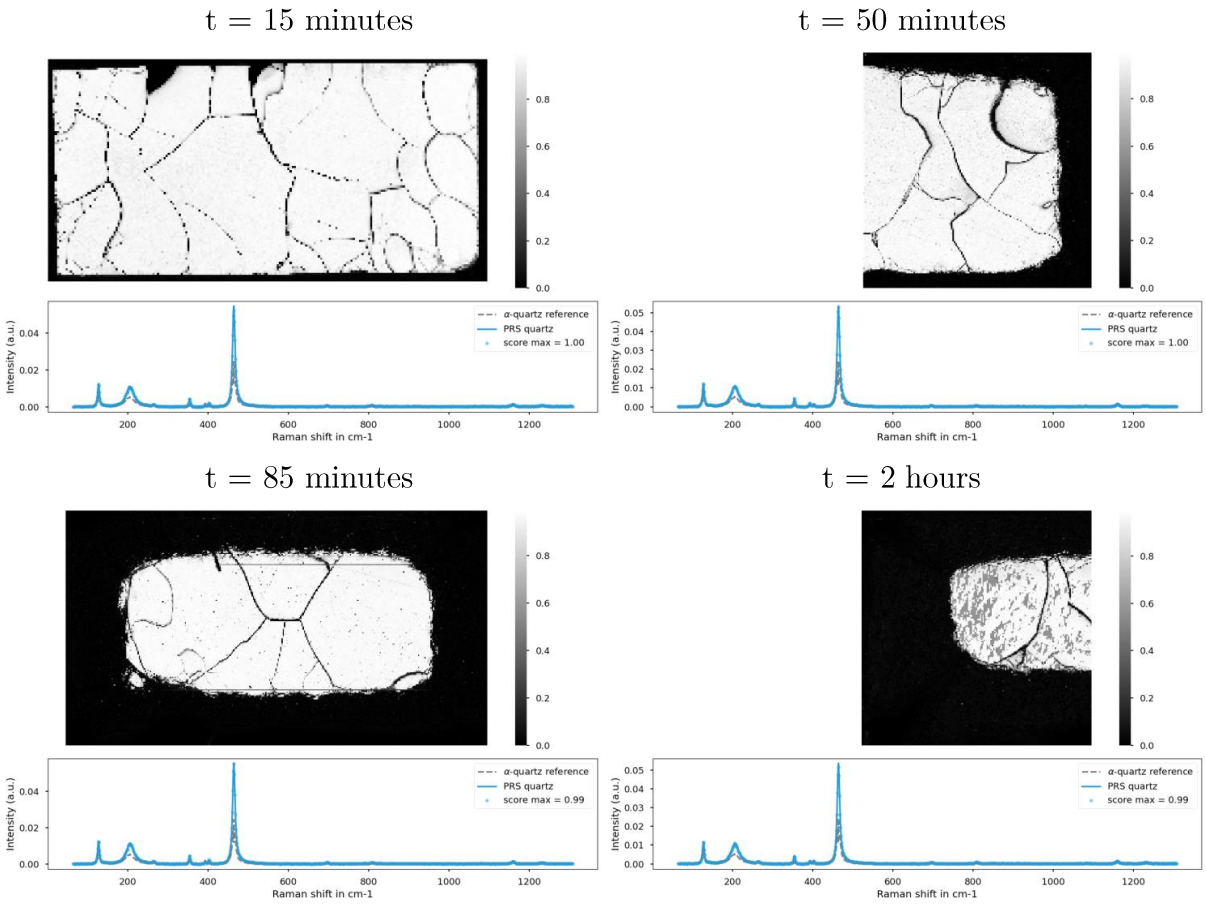

Figure 4.30 Heatmaps showing the spatial distribution of quartz, derived from NMF analysis of Raman maps. Intensities represent the score of each partial Raman spectrum (PRS) associated with a silica polymorph. Each sample's PRS is depicted by the light blue solid line, with the spectra having the highest score for this PRS indicated by translucent markers. For comparison, a reference α-quartz spectra from [87] is plotted as a dashed gray curve. Samples for dissolution tests longer than 2 hours did not displayed a quartz component.

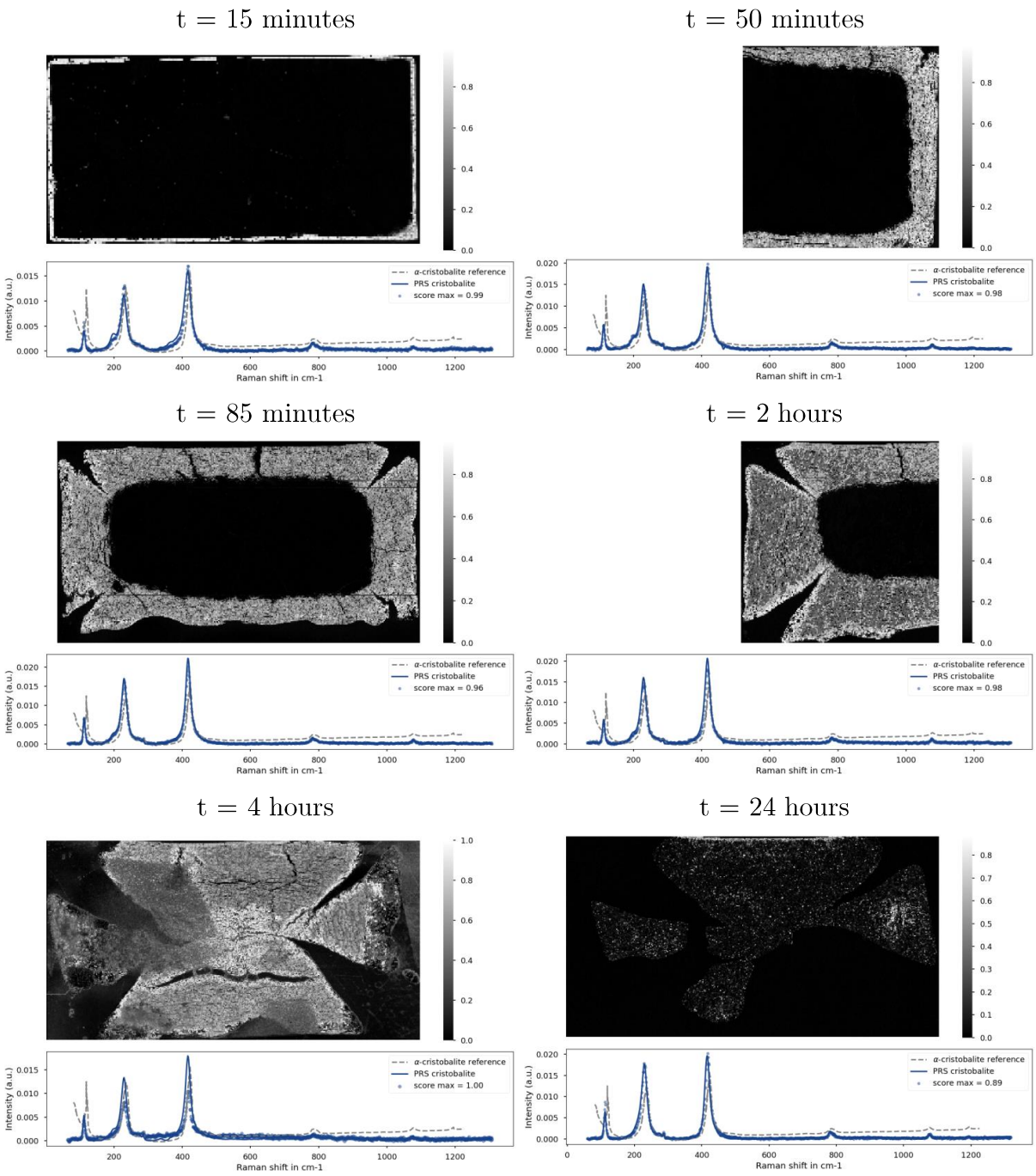

Figure 4.31 Heatmaps showing the spatial distribution of cristobalite, derived from NMF analysis of Raman maps. Intensities represent the score of each partial Raman spectrum (PRS) associated with a silica polymorph. Each sample's PRS is depicted by a colored solid line, with the spectra having the highest score for this PRS indicated by translucent markers. For comparison, a reference α-cristobalite spectra from [121] is plotted as a dashed gray curve.

One of the most remarkable observations is the absence of direct contact between quartz and glass, even after 15 minutes of dissolution. Cristobalite forms rapidly at the interface between them and can be observed as an intricate and fractured layer under optical microscopy, which continues to grow until it consumes all remaining quartz after 4 hours.

Despite optical differences between the grooved and rounder grain regions (Figure 4.27), no significant structural differences were observed. The mean Raman spectra (Figure 4.32 middle) along the distance of an area crossing both regions for the PSq-1400-50 sample did not show a shift between the two. The calculated barycenter position of the Raman shift (Figure 4.32 right) remained unchanged, except for a slight decrease as it crossed the interface with quartz. This similarity agrees with the NMF treatment results, which did not find distinct PRS for grooved and rounder cristobalite regions. The morphological differences can likely be attributed to the gradient in cracking of the solid, probably driven by significant volume expansion associated with cristobalite formation in contact with glass. These morphological changes are not insignificant. The cracking can produce channels that increase the interface between silica and glass, thereby favoring dissolution.

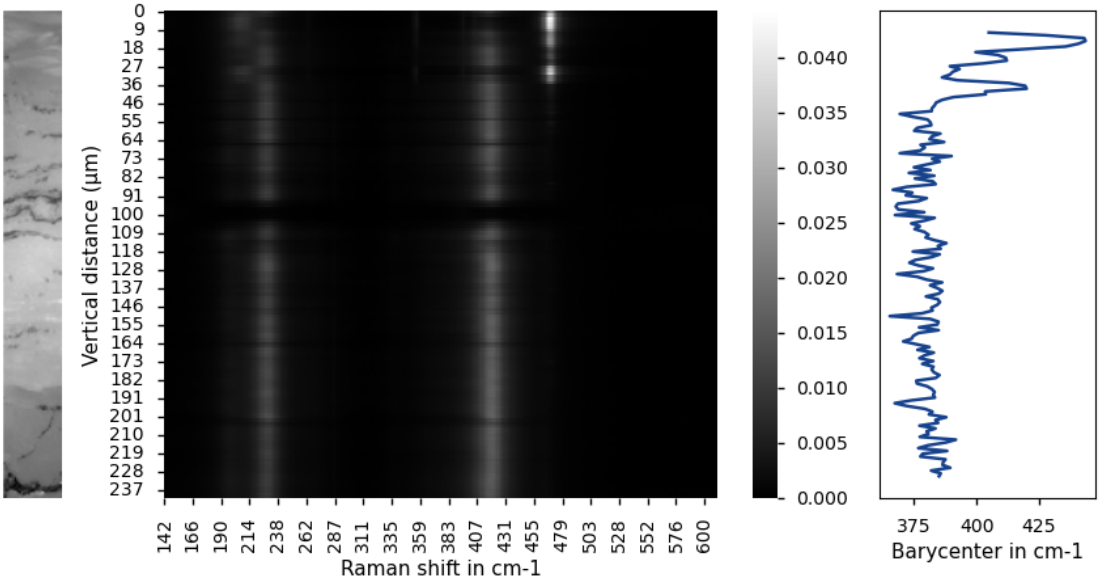

Figure 4.32 Close-up of the two different cristobalite morphologies at the PSq-1400-50 sample interface. (Left) Reflection mode photo of the analyzed region, showing a quartz portion at the top, transitioning through grooved cristobalite to rounder grains. (Middle) Spectrogram from Raman mean spectra along the vertical distance, obtained by averaging the spectra along the x axis for the same y coordinate. A spectrum was collected every 1.5 µm. The spectra were segmented at 600 cm^{-1} for better visualization, the same range used for calculating the barycenter position (Right) . In both visualizations, no clear evolution is observed.

As observed in Figure 4.26, there is a considerable change in the morphology of the remaining solid after 4 hours, which is due to the complete disappearance of quartz at the center of the flower-like shape. While a significant portion of the solid was identified as α-cristobalite, the smoother grains at the lateral parts of the remaining solid were identified as a mix of different tridymite polymorphs. Figures 4.33 and 4.34 display the spatial distribution of tridymite for tests starting at 50 minutes dissolution duration time; no tridymite was observed before that.

After 24 hours, almost all the grains correspond to a form of tridymite.

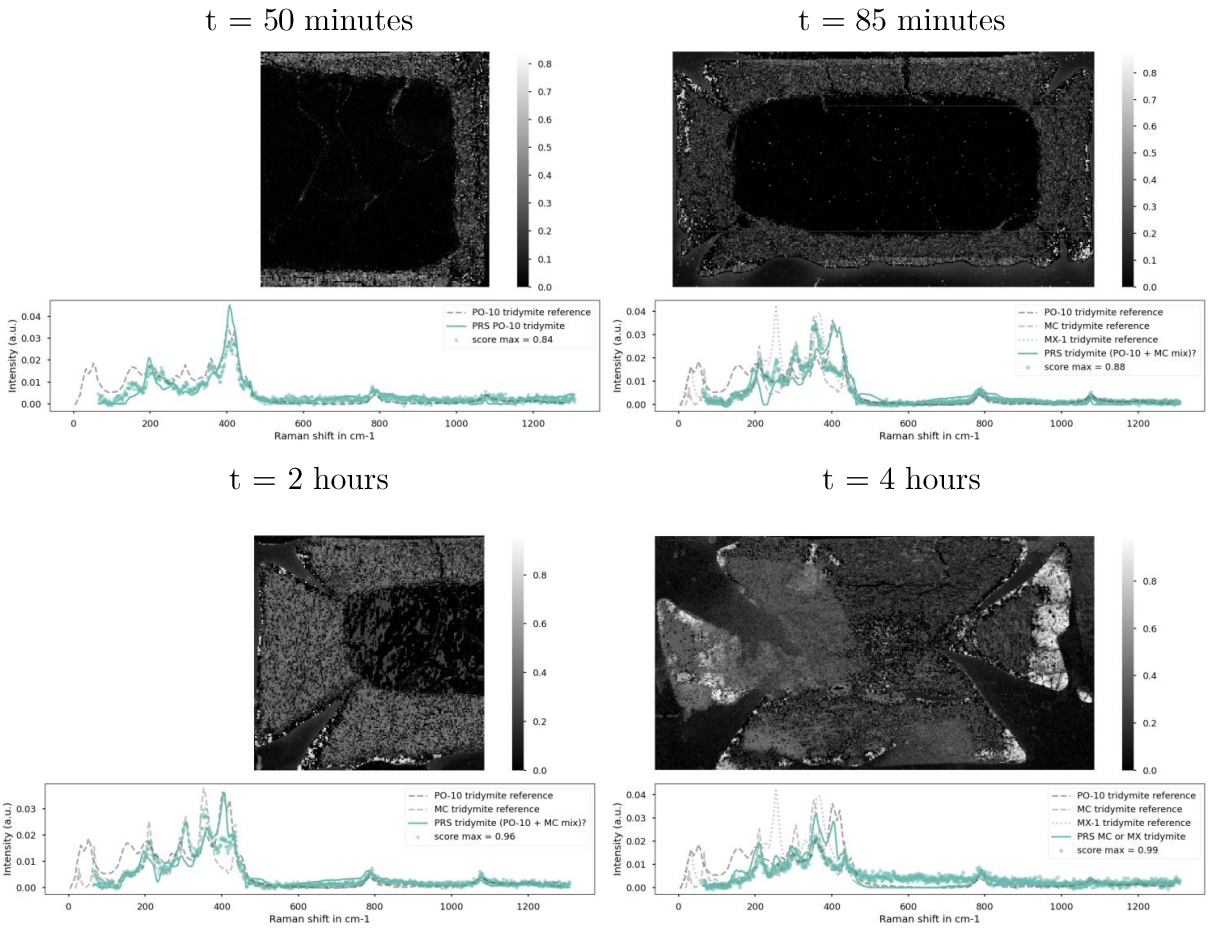

Figure 4.33 Heatmaps showing the spatial distribution of tridymite polymorphs, derived from NMF analysis of Raman maps. Intensities represent the partial Raman spectrum (PRS) score associated with tridymite. The obtained PRS is depicted by the light green solid line, with spectra having the highest score indicated by translucent markers. Unlike α-quartz and α-cristobalite, tridymite exhibits a range of low-temperature forms, suggesting that the obtained PRS is an averaged spectrum of these different tridymite forms. For comparison, reference spectra of MC, MX-1, and PO-10 [106] are plotted in gray. No tridymite forms were detected in samples from dissolution tests shorter than 50 minutes.

Contrary to α-cristobalite and α-quartz, the identification of tridymite phases was more difficult, given the multiplicity of its polymorphs [107]. At ambient conditions, two monoclinic (MC and MX-1) and one pseudo-orthorhombic (PO-10) form are known [106]. Contrary to the single displacive transformation from beta to alpha cristobalite during cooling, tridymite can assume at least five other conformations during its cooling from the hexagonal high-temperature form [122]. Besides that, they are sensitive to structural defects, i.e. faults in the stacking sequence and the presence of impurities as interstitial cations in the framework. Even grinding can also introduce stacking faults : MX-1 is often reported following deformation of MC tridymite [123].

For dissolution tests between 85 minutes to 4 hours, the spatial separation of each tridymite

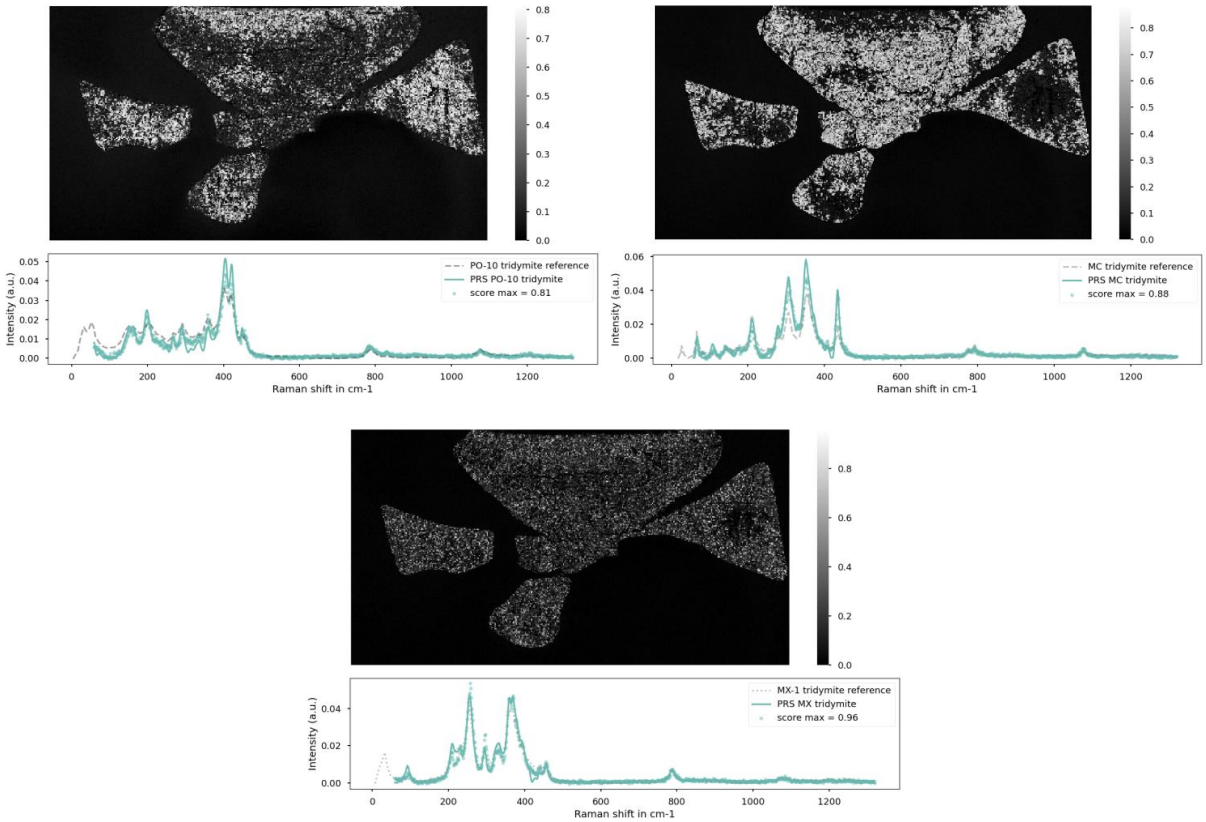

Figure 4.34 Heatmaps showing the spatial distribution of tridymite polymorphs, derived from NMF analysis of Raman maps for quartz dissolution after 24 hours. Intensities represent the partial Raman spectrum (PRS) score associated with each tridymite polymorph. The obtained PRS is depicted by the light green solid line, with the highest-scoring spectra indicated by translucent markers. For the 24-hour test, a clearer association between PRS and tridymite polymorphs was achieved. Reference spectra for low-temperature tridymite polymorphs are from [106].

polymorph was challenging, and the PRS obtained was mainly a mix of PO-10, MC, and MX-1. If one compares the PRS (solid green line in Figure 4.33) and the corresponding maximum score spectra (scattered translucent circles in Figure 4.33), it is often that they can be identified with distinct polymorphs : usually, the maximum score is an MC tridymite, while the PRS that averages all tridymite regions approaches PO-10 spectra. Since increasing the number of PRS components did not help separate each tridymite polymorph, it is possible that using a 25 µm step may not be small enough to detect the segmentation of each tridymite polymorph. This is supported by the better differentiation of each tridymite for the PSq-1400-1440 sample (Figure 4.34), where each polymorph cluster is larger.

Just like cristobalite, tridymite was mainly formed starting from the interface with the glass, following cristobalite formation. No tridymite was detected in direct contact with quartz. While it is difficult to robustly separate each tridymite form for most tests, for PSq-1400-1440 (Figure 4.34), it is possible to see that the MC form is preferentially observed at the glass interface, and PO-10 in regions away from the melt contact (top of the former tablet and core of each flower-like segment). MX-1 is homogeneously distributed but can possibly result from the grinding of other tridymite forms during the polishing of the cross-section sample surface.

Both monoclinic low-temperature forms of tridymite are often reported as a result of quenching and deformation from high-temperature tridymite and are only observed synthetically or from meteorite samples [100,106]. According to Pryde and Dove's [123] work using the rigid unit mode model, MC and MX-1 displacive transformation are most probably from HP tridymite directly (high-temperature form). Other works also pointed to a hysteresis effect on the formation of monoclinic tridymite when cooling down from the hexagonal form [107, 124, 125]. Thus, the tridymite polymorph formed after cooling seems highly dependent on its thermal history.

Despite the difficulties in distinguishing each tridymite polymorph, the quantification of silica moles is not significantly impacted. The cell volume differences between PO-10, MC, and MX-1 structures are of the order of 1% [123]. Due to the uncertainties about the segmentation of tridymites below 24 hours, their sum will be considered for the subsequent quantifications instead of each form individually.

From the Raman mappings of the different silica polymorphs after dissolution, it was possible to calculate the surface area of the remaining solid accounting for the presence of pores and cracks in post-dissolution samples, as detailed in Section 4.2.4. When the principal partial Raman spectra at a specific point corresponded to a polymorph, the pixel area was considered part of the remaining solid. This process was applied across the measured cartography to calculate the remaining solid area after dissolution. The relative surface change over time is shown in Figure 4.35.

Although the surface area of the remaining solid decreased compared to its initial value, no significant changes were observed until approximately 4 hours into the dissolution process. Figure 4.26 demonstrates that while the layer forming at the glass interface extends beyond the initial perimeter, greater erosion occurs at the corners.

Despite relying on the diameter as the characteristic length, the equivalent cylinder volume calculated by Equation 4.4 using surface data from Raman mappings offer a more accurate representation than measuring only the height and diameter after the test, as further demonstrated in Figure B.5 in the Appendix. It should be noted that after 240 minutes, the cross-section of the remaining solid deviates by almost 40% from a perfect rectangular form.

Using a single geometric proxy to describe quartz dissolution poses inherent challenges, as it may oversimplify the complex microstructural evolution. Furthermore, the interaction between

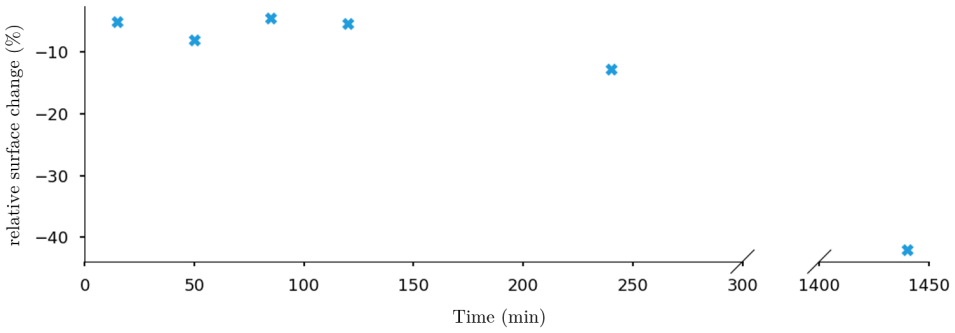

Figure 4.35 Relative surface change of the remaining solid after dissolution tests, $(A - A_0)/A_0$, where A_0 is the initial cross section area of the silica tablet.

dissolution and phase transformation complicates the interpretation of dissolution kinetics.

To quantify the dissolution of silica more precisely, the next section will focus on the number of moles of silica normalized by the available interface surface, following the method described in Section 4.2.4. Nevertheless, it is important to note that the calculated surface area likely underestimates the actual available interface, as the additional surfaces created by cracks and the corners of the flower-like shape are not quantified.

4.3.2 Dissolved silica quantification by Raman Spectroscopy Mapping

Figure 4.36 illustrates both the number of moles dissolved and the amount transformed into high-temperature polymorphs, normalized by the available interface area.

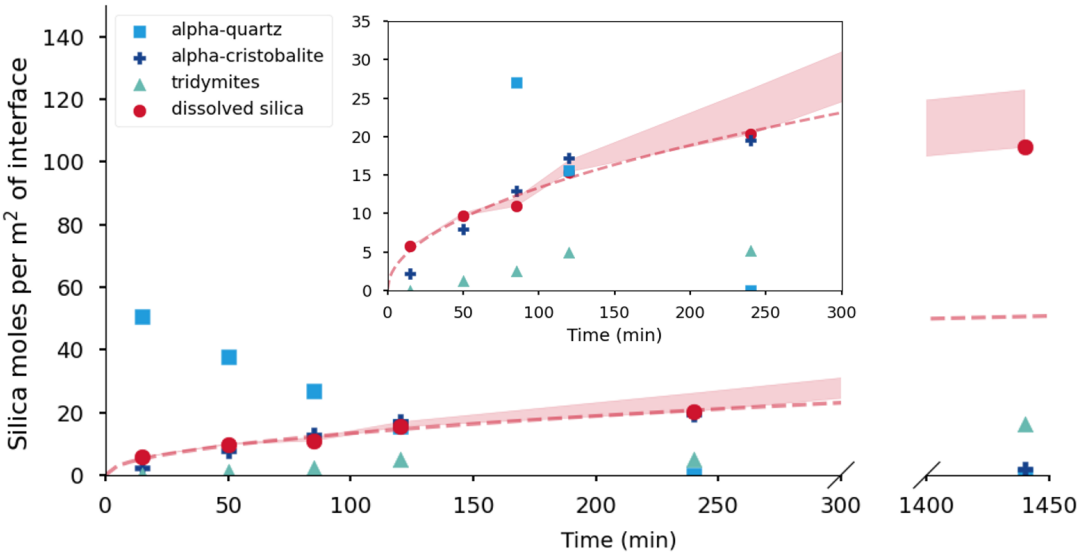

Figure 4.36 Number of silica moles that have dissolved (red circles), kept as quartz or transformed into other silica polymorphs, normalized by the available interface area. The insert is a zoom-in section until 300 minutes for better visualization. The red dashed line is a quadratic fit for dissolution data up to 2 hours, assuming the curve starts at the origin and follows the semi-infinite diffusion dissolution model. Fit results are detailed in Table 4.9.

It is important to note that the number of moles of cristobalite and tridymite present after the dissolution test reflects the balance between the amount of transformed phase and the dissolved fraction. This relationship is given by $N_{c,PSq} = N_{q\to c} - N_{diss,c}$, where $N_{q\to c}$ represents the quantity of silica moles transformed from quartz to cristobalite, and $N_{diss,c}$ is the amount of cristobalite dissolved. [(2)] Consequently, the number of silica moles dissolved incorporates contributions from all available silica polymorphs : $N_{diss,PSq} = N_{diss,q} + N_{diss,t} + N_{diss,c}$.

The data reveals that the amount of transformed polymorphs and dissolved material are comparable, with a noticeable decoupling occurring in the 24-hour test. Based on the diffusion matrix calculations under semi-infinite conditions (Figure 2.2), the analysis is divided into two distinct periods : before and after the reservoir ceases to be semi-infinite, i.e., before and after the 2-hour mark. This division also coincides with the transition from the presence of quartz to its complete replacement by cristobalite and tridymite in longer tests. Additionally, geometric uncertainties, particularly deviations from the cylindrical slab assumption, become more significant for longer dissolution periods.

Assuming diffusion-controlled dissolution, a quadratic fit is expected for $t \leq 2$ hours, consistent with the diffusion matrix calculations detailed in Section 4.1.4. Given that no silica dissolved during the furnace stabilization phase, the number of dissolved silica moles is described by the quadratic relationship $N_{diss,PSq} = 1.33\sqrt{t}$, where t is in minutes, plotted as the red dashed line in Figure 4.36.

However, as explained in the theoretical background, differences in molar volume between the dissolving solid and the partial molar volume of silica incorporated into the melt can lead to variations in the dissolution rate. The evolving molar volume due to the partitioning of silica polymorphs in the remaining solid blocks a direct coupling between this coefficient and a model based on a solid with constant molar volume (and thus constant ε), as depicted in Figure 4.15.

The onset of dissolution does not appear to be constrained by phase transformation, as no induction period was detected. Similarly, quartz transformation into cristobalite does not seem to be hindered by dissolution, as a residual cristobalite layer was consistently observed in post-dissolution samples.

Cristobalite data aligns closely with a linear trend for $t \leq 2$ hours, as detailed in Table 4.9. This trend is likely the result of competition between cristobalite formation and its subsequent dissolution. The constant net rate supports the hypothesis that these processes reach a steady state, with quartz transforming into cristobalite at a faster rate than cristobalite is dissolved, explaining the increasing presence of cristobalite in the remaining solid.

In contrast, tridymite exhibits an induction period before its formation. This observation is consistent with prior studies [114,115,118], which reported the appearance of tridymite only after cristobalite, particularly in melts containing alkali. Based on tridymite's spatial distribution at the interface between cristobalite and the melt, it appears to form from cristobalite rather than directly from quartz. Tridymite ultimately replaces both polymorphs as the dominant phase after 24 hours.

Between 2 and 4 hours, the remaining solid is entirely converted into either cristobalite or tridymite, effectively eliminating the contribution of phase transformation to the net rate of

[(2)] To evaluate the effect of quenching in the observed cristobalite, the PSq-1400-00 test conducted for only two minutes (approximately the furnace stabilization duration), a thin 3 ± 1 µm thick cristobalite layer was observed at the interface with the glass, as shown by the Raman map cartography in Figure D.1 (Appendix D) using a 1 µm step size. Therefore, the estimated normalized number of cristobalite moles that can be explained by the stabilization of the furnace temperature is 0.116 ± 0.04. This value was subtracted from $N_{c,PSq}$.

Table 4.9 Compilation of fit parameters used for dissolved silica and cristobalite molar fractions, based on experimental data from dissolution tests shorter than 2 hours, plotted in Figure 4.36

Phenomena	Equation type	plot	A	B	R^2
Dissolution	$A\sqrt{t}+B$	red dashed line	1.265 1.334	0.597 0	0.942 0.938
Cristobalite evolution	$At+B$	blue dotted line in Fig. 4.43	0.143 0.148	0.431 0	0.995 0.993

these polymorphs. From this point onward, their evolution is governed by the transformation of cristobalite to tridymite and their dissolution. As a result, no additional volume expansion is induced by further quartz replacement, explaining the sharper decline in relative surface area after 4 hours, as observed in Figure 4.35.

Although dissolution was expected to slow down once the melt reservoir ceased to be an infinite source, this slowdown was not observed during longer test durations. The number of moles dissolved after 24 hours exceeded the predicted quadratic fit based on semi-infinite conditions. Deviations from a rectangular cross-section after extended dissolution periods contribute to uncertainties in this observation. Some of these discrepancies will be analyzed later in Section 4.4 using EPMA chemical profiles of the glass near the interface.

From these observations, it can be concluded that both dissolution and cristobalite formation initiate at the onset of testing, with no observable induction period for either phenomenon. Additionally, the positive net rate of cristobalite formation indicates that its transformation from quartz outpaces its dissolution. Given that both phases are preferentially located at the glass interface, it is reasonable to conclude that most of the dissolved silica originates from the high-temperature polymorphs.

Experiments starting with pre-formed cristobalite (PSc tests) offer valuable insight into cristobalite's role in silica dissolution. These tests allow for a clearer understanding of the dissolution process without the confounding effects of quartz transformation, particularly during shorter dissolution tests. The results of these experiments will be discussed in the following section.

4.3.3 Cristobalite dissolution evolution

The presence of a cristobalite layer consistently observed at the glass interface during quartz dissolution experiments raises questions about the source of dissolved silica and the potential competition between cristobalite formation from quartz and silica dissolution. To address these questions, dissolution tests were conducted starting with cristobalite slabs prepared from fused-cast silica refractory (as detailed in Section 4.2.2), assuming their similarity to the cristobalite formed from quartz during dissolution (this hypothesis is evaluated by a Raman spectroscopy comparison between the two cristobalites in Appendix E). These samples, identified with the prefix PSc in Table 4.8, underwent the same dissolution tests as the quartz tablets.

The binocular and optical microscopy images for the PSc samples after dissolution are provided in the Appendix (Figure C.4), and the microstructure of the final grain for all samples is displayed in Figure 4.37. Contrary to the quartz dissolution tests, the grain seems to retain its overall texture derived from a polycrystalline material. The rectangular cross-section progressively rounds at the edges but without exhibiting the flower-like shape.

Crack formation was observed after 50 minutes, 2 hours, and 4 hours. Some porosity was also noticed, likely originating from the initial material.

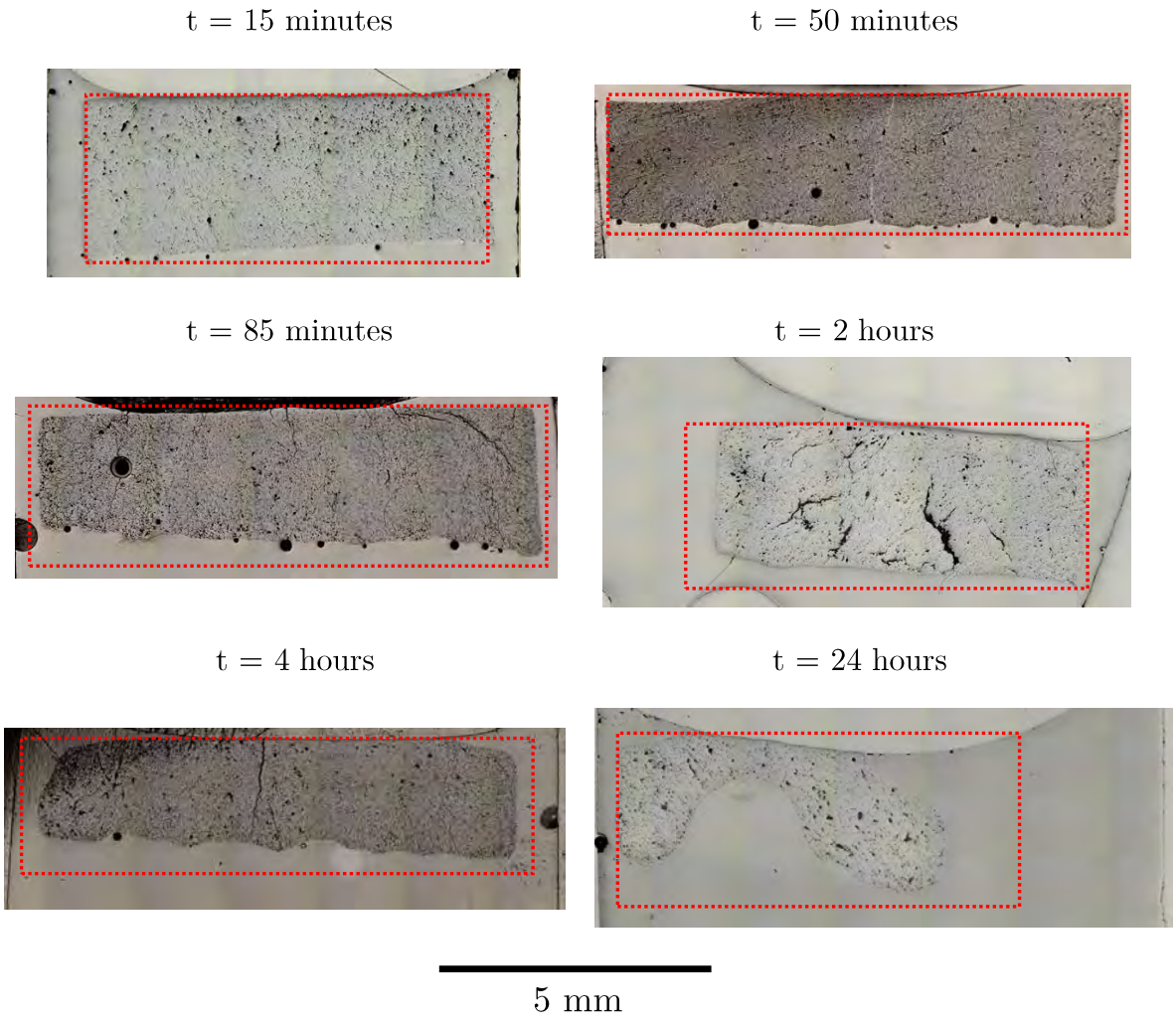

Figure 4.37 Optical microscopy photos in reflected light mode for all cristobalite dissolution samples. Red rectangle overlayed represents the original cristobalite tablet's dimension.

The lower region of the cylinder often did not remain parallel to the opposite face, either showing a slight inclination or displaying a wavy pattern. After 24 hours, the former tablet showed a concave geometry. These undulations in contact with the glass were also observed in PSq tests (Figures 4.26 and C.2). Furthermore, the cristobalite tablets after 2 hours and 24 hours were no longer centered in the setup. The lateral photos taken prior to epoxy embedding (Figure C.5 in Appendix C) indicate that the assumption of a representative cross-section is probably no longer valid after extended dissolution tests : in PSc-1400-1440, the concave geometry may represent one of the possible cross-sections.

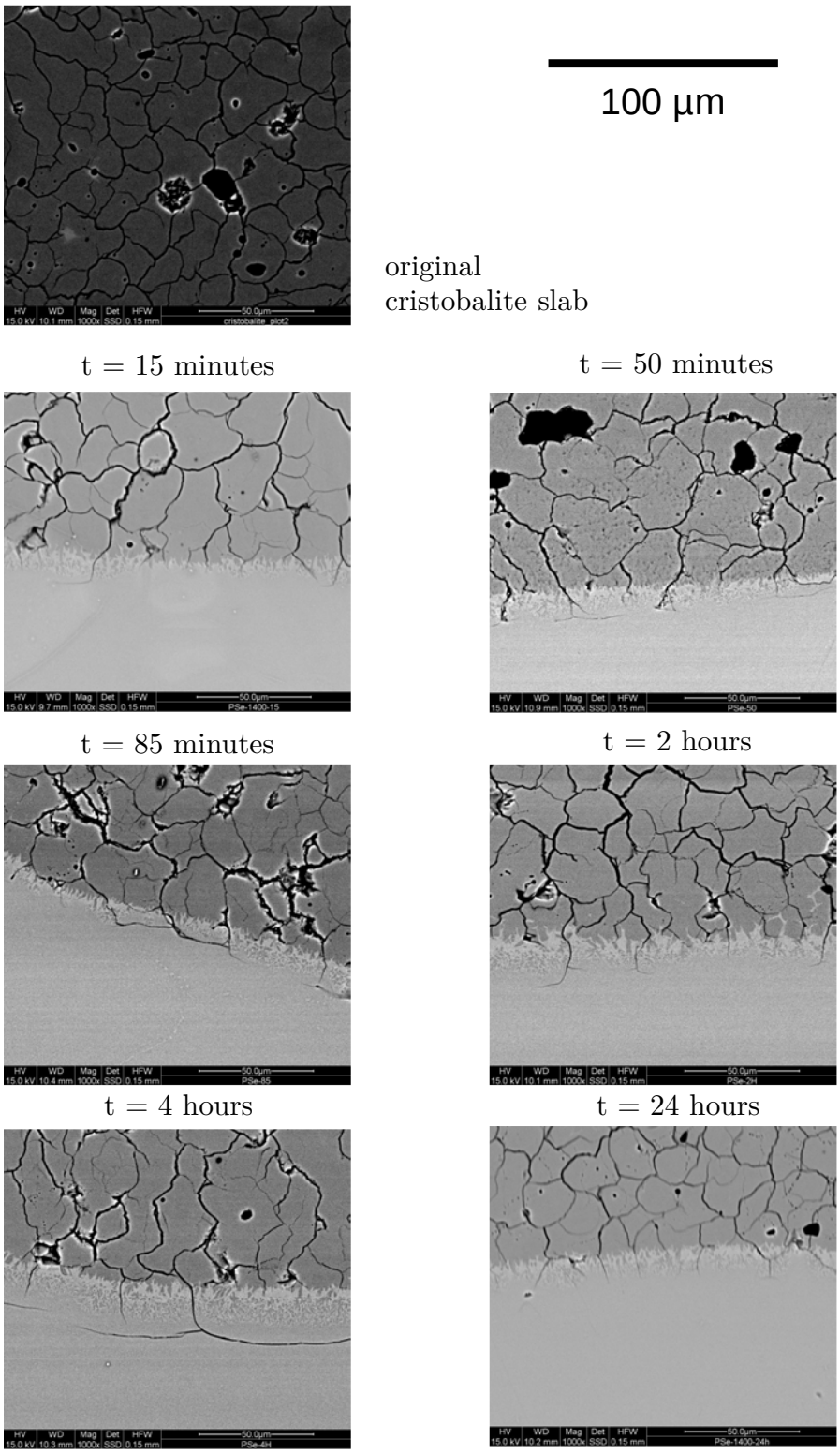

Figure 4.38 Scaning electron microscope (SEM) images obtained under the same magnification of 1000 × for all dissolution samples starting with cristobalite slab (PSc). Backscattered Electrons (BSE) mode was used to emphasize the chemical contrast close to the dissolution interfaces.

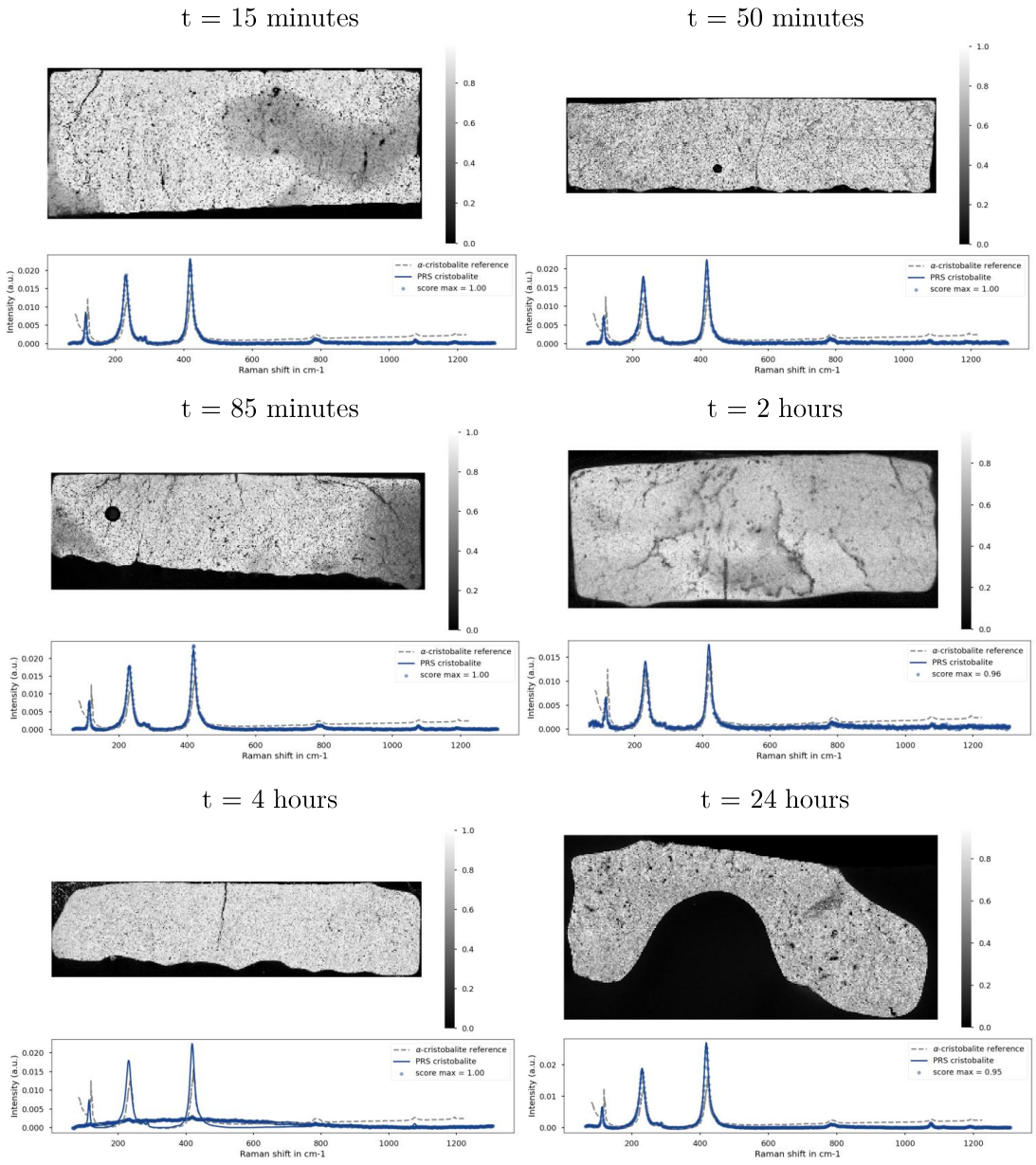

Figure 4.39 Heatmaps showing the spatial distribution of cristobalite in PSc samples, derived from NMF analysis of Raman maps. Intensities represent the score of each partial Raman spectrum (PRS) associated with a silica polymorph. Each sample's PRS is depicted by a colored solid line, with the spectra having the highest score for this PRS indicated by translucent markers. For comparison, a reference α-cristobalite spectra from [121] is plotted as a dashed gray curve. For all PSc samples, cristobalite is kept as the main phase of the remaining solid.

SEM images in Figure 4.38 show more details of the dissolution interface. The original morphology of rounder cristobalite grains was preserved in the remaining solid after dissolution, with no visible sintering even after 24 hours. As observed for quartz dissolution, the interface in PSc tests

consisted of dendrites surrounded by glass with a composition different from the nearby glass, as indicated by the lighter hue observed in BSE mode SEM images. The dendrite extension did not significantly evolve with time and was likely due to the reduced solubility limit of the glass with respect to silica during quenching. Notably, the extent of dendrites in PSq samples (shown in Figure 4.28 under the same magnification) was slightly larger than in PSc tests, especially at times up to 85 minutes.

Consistent with the homogeneous and unchanged texture observed in the remaining solid, Raman spectroscopy mappings conducted for PSc tests (Figure 4.39) revealed the presence of only α-cristobalite as the silica phase throughout the entire time range. A minor fraction of PO-10 tridymite was detected near the triple point between the glass-cristobalite-air surface after 24 hours (Figure 4.40), possibly resulting from increased alkali volatilization at the surface during extended heat treatment and subsequent silica precipitation during quenching.

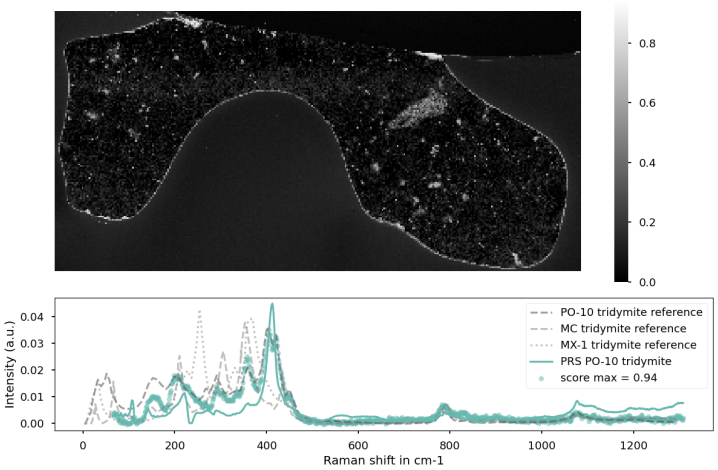

Figure 4.40 Heatmaps showing the spatial distribution of tridymite polymorphs, derived from NMF analysis of Raman maps for cristobalite dissolution after 24 hours. Intensities represent the score of the partial Raman spectrum (PRS) associated with each tridymite polymorph. The obtained PRS is depicted by the light green solid line, with the highest-scoring spectra indicated by translucent markers. A closer correspondance with the PO-10 tridymite is observed. Reference spectra for low-temperature tridymite polymorphs are from [106].

The persistence of cristobalite during dissolution for the complete time range studied facilitates direct correlation between surface change and the moles of dissolved silica. However, it is important to note that quantification using Raman mapping tends to slightly underestimate the remaining solid surface area. This underestimation occurs because the Non-negative Matrix Factorization (NMF) score associated with the polymorph does not always equal 1. Consequently, the calculation of dissolved silica, obtained from the complement of the solid after removing the contribution of epoxy resin, may lead to a slight overestimation of the dissolved amount.

Despite these limitations, the systematic nature of the quantification process across all samples allows for meaningful comparisons. Therefore, to maintain consistency with the quartz dissolution tests and facilitate direct comparison, the surface area and the amount of dissolved silica for PSc tests were also calculated using the same Raman map approach (further details on Section 4.2.4). Figures 4.41 and 4.42 illustrate the surface change and the evolution of dissolved silica over time, respectively, with quartz data (represented in light blue) included for comparison.

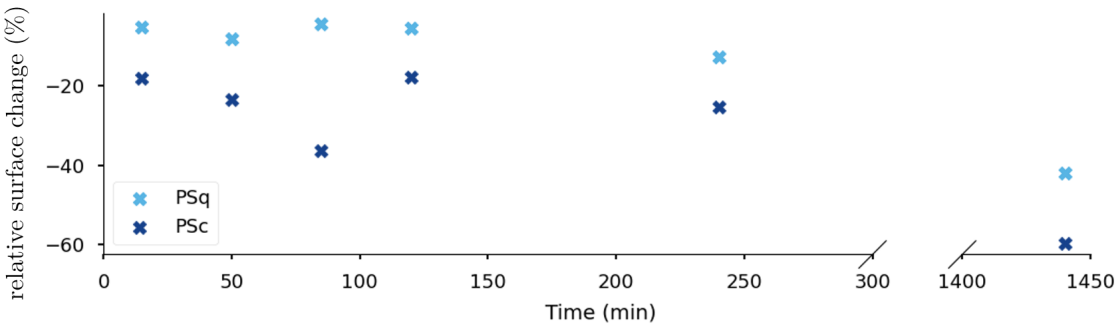

Figure 4.41 Relative surface change of the remaining solid after dissolution tests, $(A - A_0)/A_0$, where A_0 is the initial cross section area of the silica tablet.

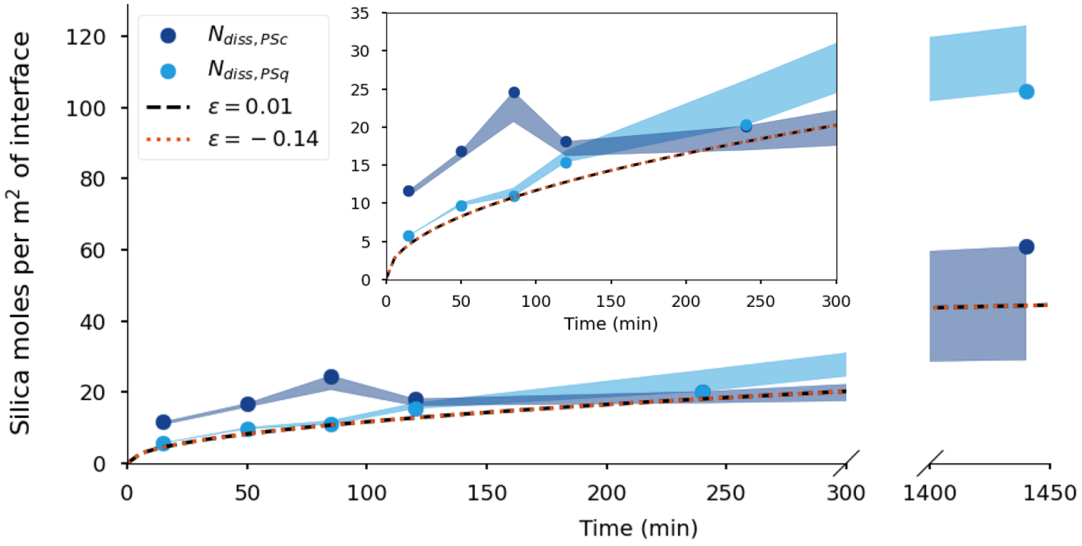

Figure 4.42 Number of moles dissolved during cristobalite dissolution tests ($N_{diss,PSc}$ in dark blue) and during quartz dissolution tests ($N_{diss,PSq}$ in light blue), normalized by the available interface area. The insert is a zoom-in section until 300 minutes. The circles depict the quantification normalized by the interface surface after dissolution. Black and orange dashed lines were calculated converting the theoretical curve for the flat slab's approximation model for cristobalite and quartz dissolved length (Figure 4.15), respectively.

Compared to quartz dissolution, the number of dissolved moles from cristobalite slabs is higher than that of PSq samples up to 2 hours. Due to an inflection point in the data at approximately 85 minutes, no clear quadratic fit can be applied to describe the dissolution of cristobalite. The origin of this inflection remains unclear, although one possible explanation is the rotation of the cristobalite slab during the dissolution test after 2 hours (Figure C.4 in the Appendix), which may have perturbed the dissolution behavior.

In a semi-infinite dissolution scenario, theoretical calculations predicted a higher dissolution rate for cristobalite due to a lower silica accumulation near the interface. To verify this, the previously calculated curves for both values of the radial flow parameter ε (Figure 4.15) were converted to an equivalent number of moles, normalized by the bottom interface surface, assuming negligible

variation in diameter [(3)]. As shown in Figure 4.42, the orange and black curves are nearly superposed, indicating that no significant difference between quartz and cristobalite dissolution is observable at this scale.

While the theoretical model aligns well with short-term quartz dissolution results, cristobalite dissolution exceeds the predicted values for purely diffusive processes. Given the absence of substantial changes in the remaining solid microstructure, this over-dissolution cannot be explained in the same way as for quartz. It is likely that free convection plays a role, a topic that will be discussed further in Section 4.4.

After departing from semi-infinite conditions, the dissolution rate slows, with cristobalite dissolution becoming nearly constant between 2 and 4 hours. The dissolution amounts were nearly identical between cristobalite and quartz tests, except after 24 hours, when PSq samples exhibited significantly higher dissolved silica moles, likely due to uncertainties in the geometric assumptions. Interestingly, over longer periods, the dissolved quantities in the cristobalite tests approach theoretical predictions.

4.3.4 Estimation of cristobalite contribution to dissolution in PSq tests

As explained in Section 4.3.2, the cristobalite fraction observed from PSq samples ($N_{c,PSq}$) does not correspond to the total amount of quartz transformed into cristobalite ($N_{q\to c}$), but rather represents the remaining cristobalite that was not dissolved. This can be expressed as the following relationships :

$$\begin{aligned} N_{c,PSq} &= N_{q\to c} - N_{diss,c} \\ \Rightarrow N_{c,PSq} &= N_{q\to c}(1-\phi_{diss,c}) \\ \Rightarrow N_{q\to c} &= N_{c,PSq}/(1-\phi_{diss,c}) \end{aligned}$$

where $\phi_{diss,c}$ is the fraction of dissolved cristobalite. Since cristobalite is the only solid phase that dissolves during PSc tests, $\phi_{diss,c}$ can be calculated as :

$$\phi_{diss,c} = N_{diss,PSc}/(N_{diss,PSc} + N_{c,PSc}) \tag{4.5}$$

where $N_{diss,PSc}$ and $N_{c,PSc}$ are the number of moles dissolved and kept as cristobalite, respectively, both normalized by the available interface surface.

To obtain corrected quantities of cristobalite formed from quartz, the fraction $\phi_{diss,c}$, derived from PSc test data, was applied to the observed cristobalite in quartz dissolution results. This analysis was limited to dissolution data for up to 2 hours to avoid potential complications related to slow-down effects from quartz disappearance and confined dissolution. Figure 4.43 illustrates the corrected cristobalite amount formed from quartz, taking into account the dissolved quantity, shown as rectangular bars above the observed remaining cristobalite in PSq tests. The corrected values for $N_{q\to c}$ exhibit a linear trend, with the corresponding linear fit represented by the solid dark blue line in Figure 4.43.

[(3)] Using Equation 1.23, it was assumed that only h was the length consumed during dissolution by the bottom surface of the cylinder (πr^2) to calculate the equivalent volume in function of dissolution time. Assuming a negligible variation in r, the interface surface was assumed constant. For a fixed value of ε, the number of dissolved moles normalized by πr^2 is given by $(F_a/V_m)\sqrt{4Dt/\pi}$, where F_a where the same as reported in Table 4.6

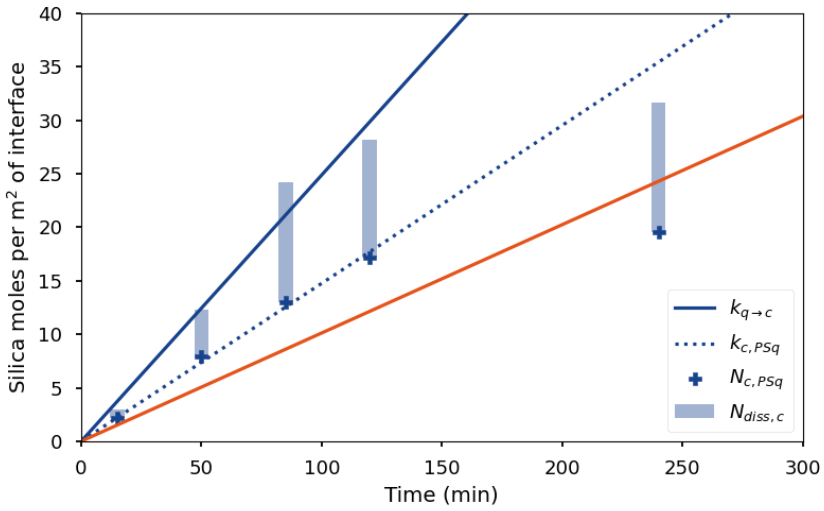

Figure 4.43 Correction on the quantification of cristobalite observed after PSq tests (for $t \leq 2$ hours : The observed cristobalite in PSq samples ($N_{c,PSq}$) results from the difference between the rate of phase transformation (dark blue line) and the dissolution rate of the newly formed cristobalite layer (orange line). The underestimation of cristobalite is the amount of cristobalite dissolved ($N_{diss,c}$)

As previously discussed, the observed cristobalite in PSq samples results from the difference between the rate of phase transformation and the dissolution rate of the newly formed cristobalite layer. From the linear fits of $N_{c,PSq}$ and $N_{q\to c}$, the following relationship is derived :

$$\begin{aligned} N_{c,PSq} &= N_{q\to c} - N_{diss,c} \\ \Rightarrow k_{c,PSq}t &= k_{q\to c}t - N_{diss,c} \\ \Rightarrow N_{diss,c} &= (k_{q\to c} - k_{c,PSq})t \end{aligned}$$

This equation accounts for the cristobalite dissolution observed during quartz dissolution, represented by the solid orange line in Figure 4.43. The linear fit results are summarized in Table 4.10. The fit, along with the values estimated for cristobalite underestimation ($N_{diss,c} = N_{q\to c} - N_{c,PSq}$), was compared to the amount of silica dissolved during PSq tests (up to 2 hours), as shown in the left graph of Figure 4.44. Not all of the dissolved silica from quartz dissolution can be attributed to this estimate of cristobalite contribution.

Table 4.10 Compilation of fit parameters used for normalized number of moles of cristobalite transformed from quartz and dissolved, based on experimental data from quartz dissolution tests shorter than 2 hours. Results for these fits are plotted in Figure 4.43

	Plot	**Equation**	k **(min $^{-1}$)**	R^2
Cristobalite transformed from quartz	Dark blue solid line in Figure 4.43	$N_{q\to c} = k_{q\to c}t$	0.251	0.968
Cristobalite dissolved in quartz tests	Orange line in Figure 4.43	$N_{diss,c} = k_{diss,c}t$	0.103	0.887

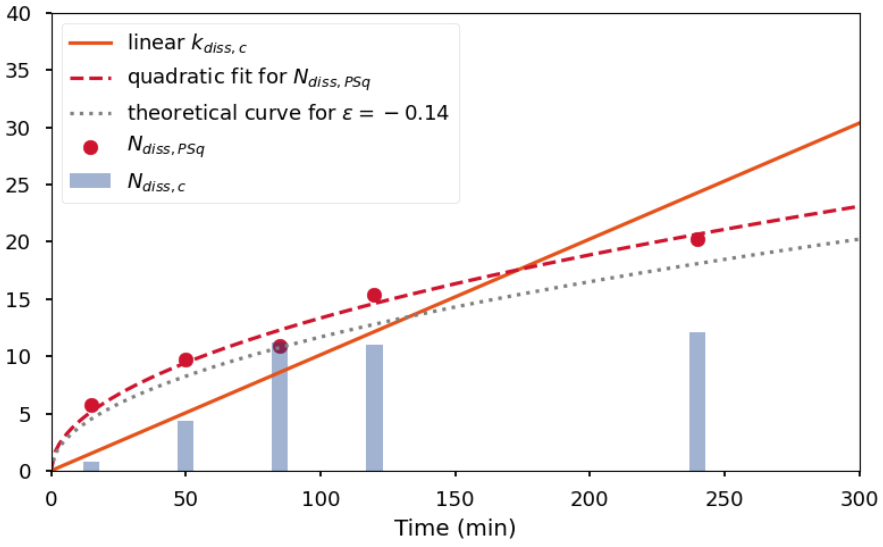

Figure 4.44 Evaluation of cristobalite contribution to dissolution during PSq tests until 2 hours : The normalized number of cristobalite moles dissolved ($N_{diss,c}$) is inferior to the number of dissolved silica during quartz dissolution ($N_{diss,PSq}$). The quadratic fit for the latter is depicted by the red dashed curve as well as the theoretical flat slab prediction for $\varepsilon = -0.14$ (solid constituted mainly of quartz). The orange curve was obtained from the net rate of observed cristobalite, as depicted in Figure 4.43

The relationship for cristobalite dissolution is linear with respect to time, contrasting with the expected quadratic relationship for diffusion-controlled processes. Therefore, the dissolution rate should be interpreted in terms of time dependence. If the dissolved silica cannot be fully explained by cristobalite dissolution alone, the following expression is obtained :

$$\begin{aligned} N_{diss,PSq} &= N_{diss,q} + N_{diss,c} + N_{diss,t} \\ \Rightarrow N_{diss,PSq} &= (k_{q\to c} - k_{c,PSq})t + (N_{diss,q} + N_{diss,t}) \\ \Rightarrow k_{diss,PSq}\sqrt{t} &= (k_{q\to c} - k_{c,PSq})t + (N_{diss,q} + N_{diss,t}) \end{aligned}$$

The total silica dissolved during PSq tests (up to 2 hours) follows the expected quadratic behavior for diffusion-controlled processes, with the dissolution rate expressed as $dN_{diss,PSq}/dt = k_{diss,PSq}/(2\sqrt{t})$. The time at which the cristobalite dissolution rate equals the silica dissolution rate is 42 minutes, marked by the orange "X" in Figure 4.45. Prior to this point, silica dissolution in PSq samples progresses more rapidly than cristobalite dissolution. Afterward, cristobalite dissolution no longer limits the overall silica dissolution rate.

This behavior persists until 2 hours, during which cristobalite continues to form from the remaining quartz. It is also important to note that tridymite is progressively formed, contributing to silica dissolution. However, isolating the effects of tridymite was beyond the scope of this study, given uncertainties surrounding its formation and the variety of possible polymorphs. Thermodynamic calculations in Section 4.1.2 indicate that the driving forces for cristobalite and tridymite dissolution in glass are very similar.

A critical assumption in this analysis is that $\phi_{diss,c}$ corresponds to the amount of cristobalite dissolved in PSc tests. Observations of the remaining solid geometries, particularly after extended

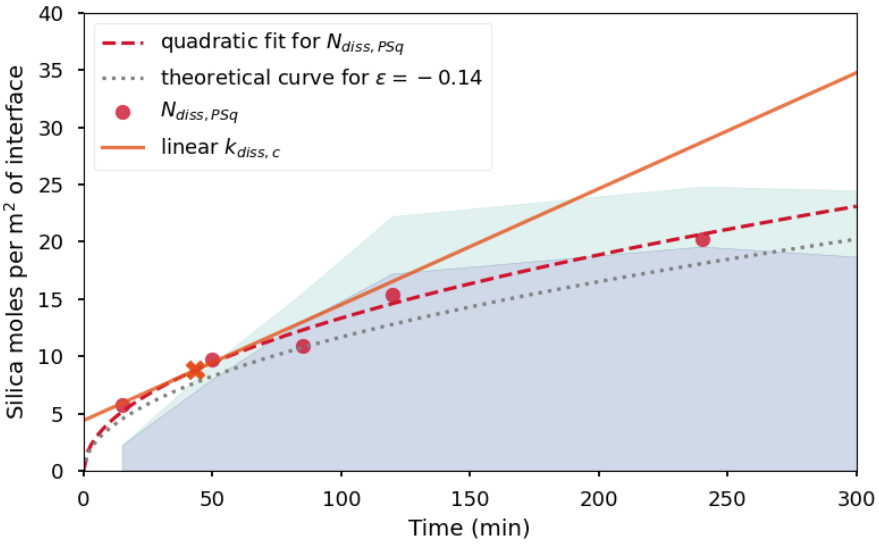

Figure 4.45 Equivalence between dissolution rates for quartz dissolution tests shorter than 2 hours : The rate of cristobalite dissolution (orange line) is equal to the quadratic fit for the dissolved silica in PSq tests (red dashed line) at 42 minutes, as highlighted by the orange "X" marker. The partitioning of cristobalite and tridymite in the remaining solid is shown in light blue and green, respectively.

dissolution times, suggest that the interface with the glass increases due to the flower-like shape in PSq samples, which tends to be underestimated by the cylindrical approximation of the interface surface. This deviation is less pronounced when starting with pre-formed cristobalite, as detailed in Appendix B.3.

Despite uncertainties in quantifying dissolution rates, this analysis of polymorph evolution demonstrates that microstructures evolve differently when phase transformations occur. Additionally, it underscores the challenges of accurately measuring length variations in quartz over time, as expansion counteracts quartz consumption due to dissolution.

Following this examination of microstructural evolution, the next section will explore the chemical composition profiles from these samples. Understanding how silica is incorporated into the melt is crucial to assess the undersaturation in multi-component glass and verifying the assumption of diffusion-controlled dissolution.

4.4 Mass transport of silica in the glass

Previous experimental investigations of silica dissolution predominantly indicate a mass-transport-controlled mechanism (see Section 1.3). This suggests that thermodynamic equilibrium is rapidly established at the solid-liquid interface, while the rate-limiting step for dissolution is the transport of silica away from the interface into the bulk melt. Although previous sections demonstrated that quartz dissolution is influenced by significant microstructural changes, in addition to the conventional kinetic mechanisms outlined in Section 1.2, it is essential to evaluate the role of silica transport and how much of the dissolution process can be attributed to diffusion.

An approach similar to that used for alumina dissolution was employed to explore this. Electron Probe Microanalysis (EPMA) measurements were conducted near the glass interface, following

the protocol outlined in Section 2.5.3. Line scans were positioned along the remaining solid's bottom interface, avoiding the sample's lateral edges. The resulting concentration profiles for silica, sodium, and calcium oxides for both quartz (in light blue) and cristobalite (dark blue) samples are presented in Figure 4.46, grouped by dissolution duration time.

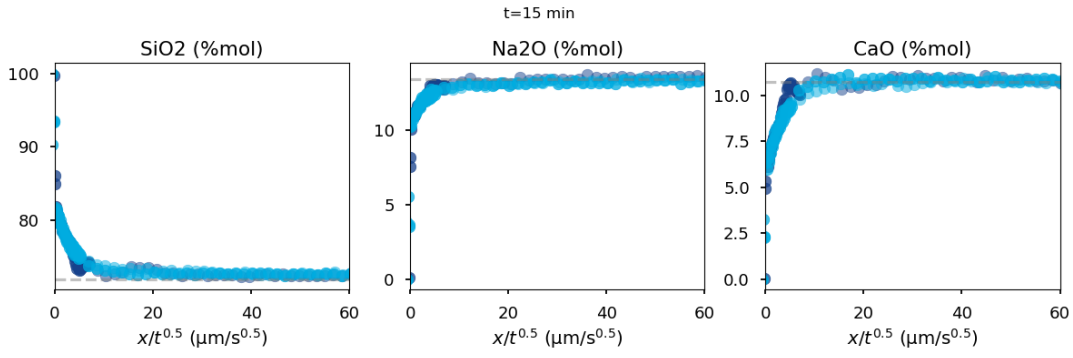

a t=15 minutes

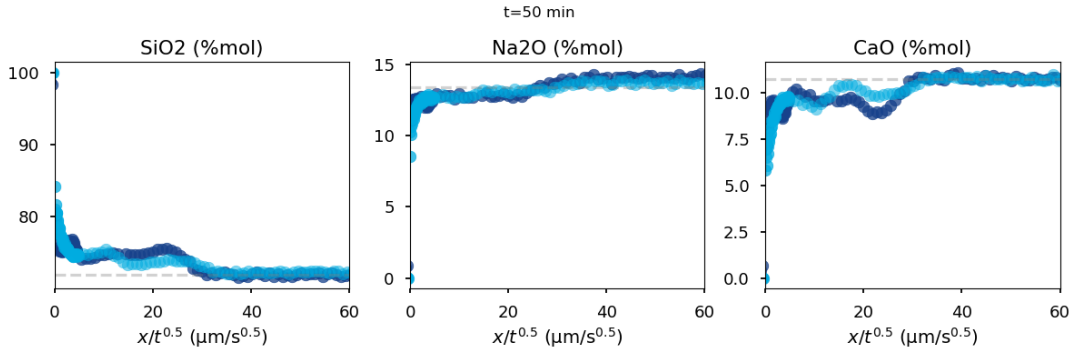

b t=50 minutes

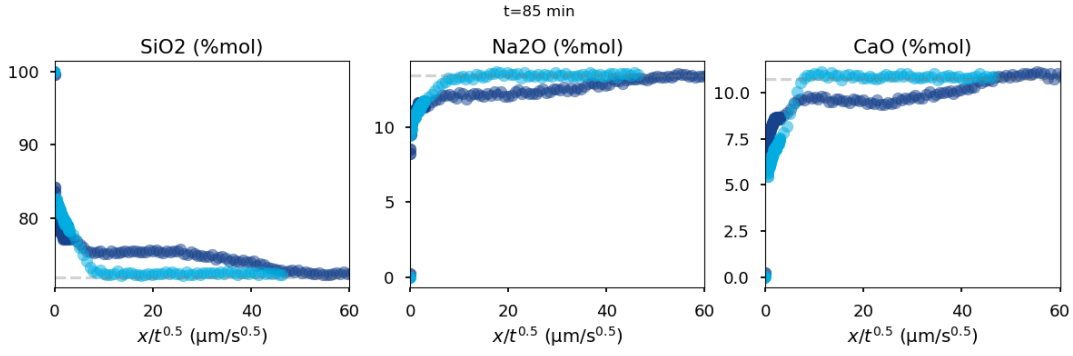

c t=85 minutes

Figure 4.46 Chemical composition profiles (in %mol) in the glass after dissolution tests using both quartz (light blue) and cristobalite (dark blue) as starting silica sources. The original glass composition is plotted as the light gray dashed line. The distance from the interface is normalized by the square root of time.

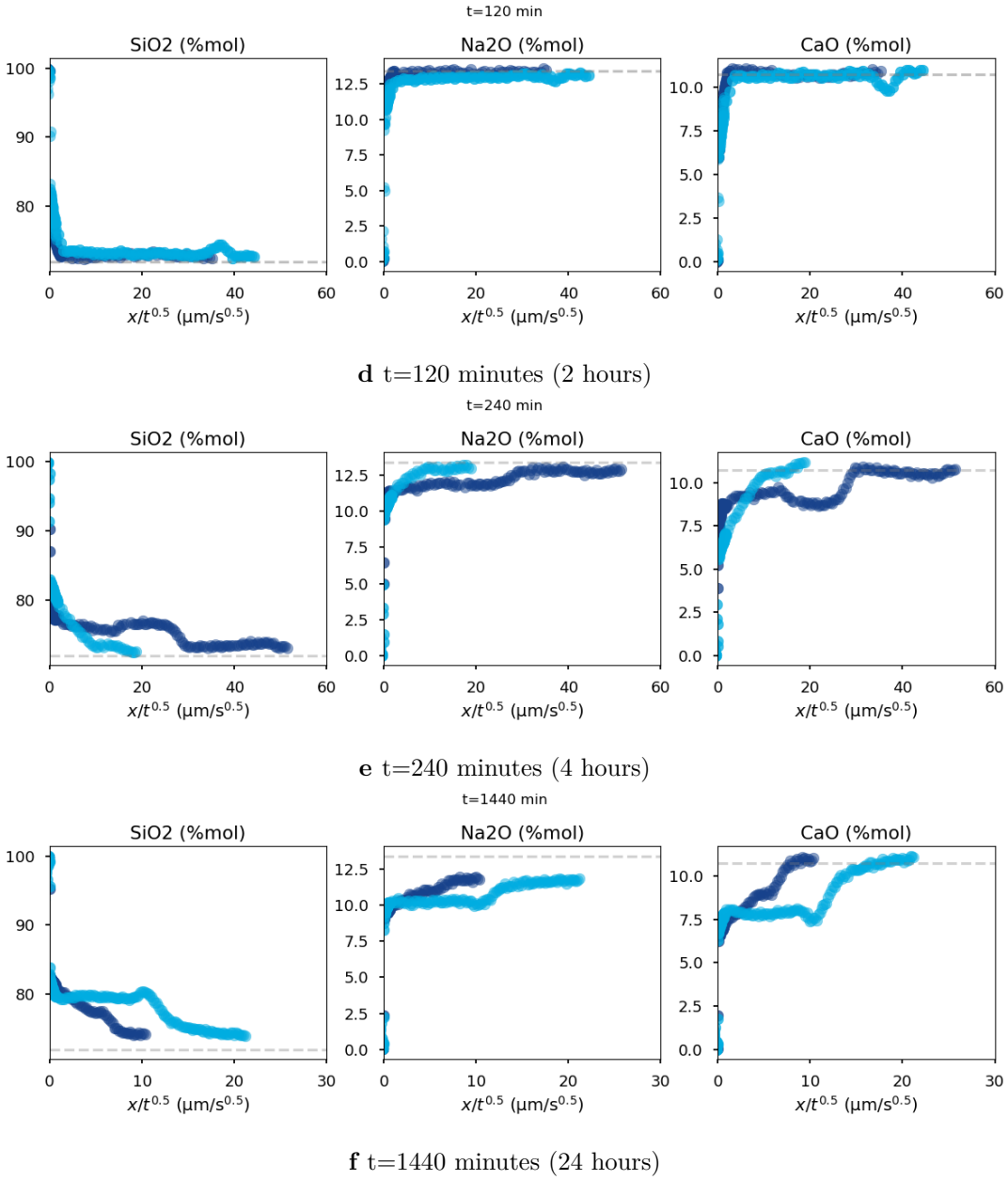

d t=120 minutes (2 hours)

e t=240 minutes (4 hours)

f t=1440 minutes (24 hours)

Figure 4.46 Chemical composition profiles (in %mol) in the glass after dissolution tests using both quartz (light blue) and cristobalite (dark blue) as starting silica sources. The original glass composition is plotted as the light gray dashed line. The scale is the same for all periods, except for 24 hours test ($x/\sqrt{t} \leq 30$ µm/s$^{0.5}$)

These profiles, normalized against the same scale except for 24 hours-test, were compared for various durations of heat-treatment. In a purely diffusive dissolution process, profiles for the same oxide would be expected to overlap when plotted against $x/\sqrt{t}$ (where x is the distance from the interface and t is time). However, such superposition is not observed for either the quartz or cristobalite samples, indicating deviations from purely diffusive behavior. Notably, plateau-like concentration curves are evident, especially in the cristobalite samples. Perturbations in the concentration profiles are seen after 50 minutes for both silica sources, with more pronounced effects at the far-field regions in PSq-120 and PSc-240 tests. After 24 hours, both materials

exhibit a plateau followed by a distinct inflection point in the profiles.

These results deviate from the theoretical profiles calculated in Section 4.1.3, where the assumption of semi-infinite diffusion held for durations under 2 hours. In contrast, sodium oxide concentrations exceed the original glass composition after 50 minutes, calcium oxide after 85 minutes, and silica after 2 hours. The distance affected by diffusion is significantly shorter than predicted by diffusion matrix calculations, with the shortest diffusion length occurring around 2 hours into the dissolution process. To further illustrate the spatial extent of diffusion, Figure 4.47 presents the profiles up to 750 µm from the interface, grouped for both PSq and PSc tests.

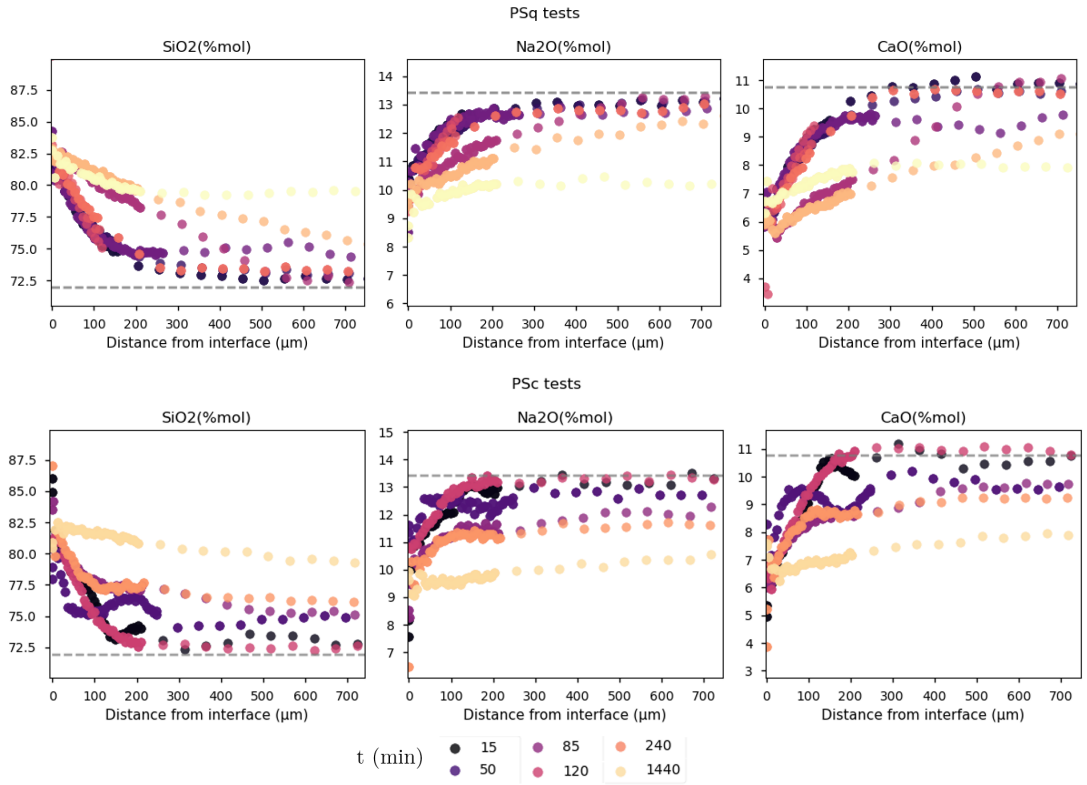

Figure 4.47 Chemical profiles for quartz (top) and cristobalite (bottom) dissolution tests, for different durations. The distance is no longer normalized, to reflect the length of the profiles. The scale is limited to 750 µm for better visualization.

In both quartz and cristobalite samples, the diffusion layer contracts between 85 and 120 minutes. Following this contraction, the layer expands again and becomes nearly horizontal after 24 hours, though this phenomenon appears earlier in the quartz samples. The cause of this layer thinning is not immediately apparent, though one plausible explanation involves the onset of natural convection, a phenomenon that may complicate the diffusion-dominated process. Even at 15 minutes, the diffusion distance is shorter than predicted by diffusion matrices (see Figure 4.12), further supporting the hypothesis that convection may contribute to this behavior.

To investigate this phenomenon further, Raman spectroscopy mapping of silica-rich regions was conducted for both PSq-15 and PSc-15 samples, as shown in Figure 4.48. The partial Raman spectra for these regions show a shift in the 560 cm^{-1} band, with an increasing tail toward lower frequencies than the original glass spectra. This band shift is often attributed to the presence of four-membered rings of silica tetrahedra, while the tail is associated with the stretching of

oxygen atoms in larger rings (five-membered or higher) [126]. These features align with the silica polymorphs' ring-based morphology description, as discussed in Section 4.1.1. No significant differences were observed between 870 cm^{-1} and 1200 cm^{-1} in the spectrum, suggesting that the dissolution process primarily affects the lower-frequency bands.

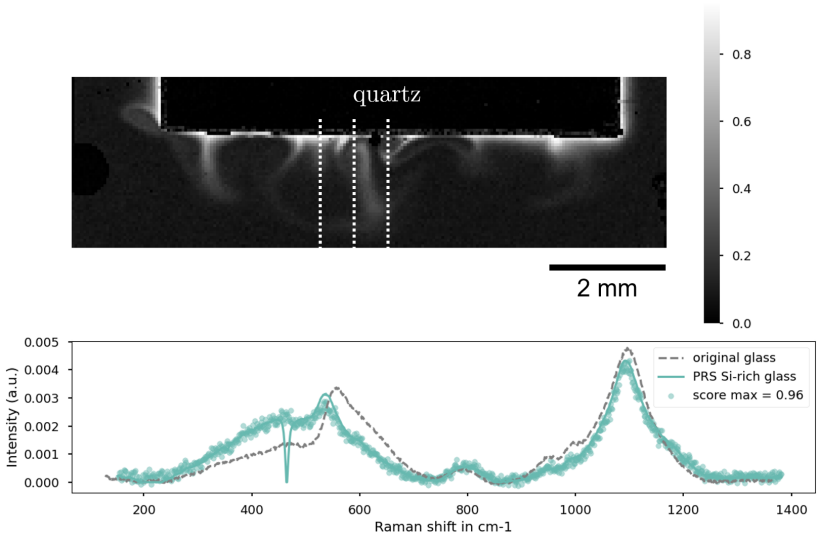

a Quartz dissolution (t=15 minutes)

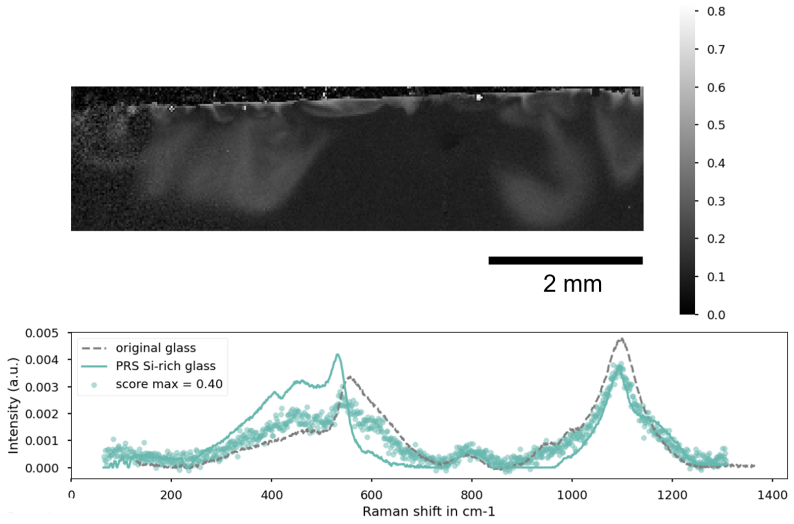

b Cristobalite dissolution (t=15 minutes)

Figure 4.48 Heatmaps showing the spatial distribution of silica enriched glass, derived from NMF analysis of Raman maps, for quartz and cristobalite dissolution after 15 minutes. Intensities represent the score of the altered glass's partial Raman spectra (PRS). Each sample's PRS is depicted by the light green solid line, with the spectra having the highest score for this PRS indicated by translucent markers. The original glass spectra are plotted as a dashed gray curve for comparison.

The lighter regions in the Raman cartographies correspond to silica-enriched glass near the dissolution interface, where significant perturbations in the dissolution front are evident. These observations suggest that the tests were no longer static and that the system was influenced by

dynamic processes. Notably, the onset of free convection, driven by Rayleigh instabilities due to coupled diffusion, was not anticipated before 17.5 hours in this setup (check Section 2.2.3). The early onset of these perturbations will be further explored in Section 4.4.2, where potential mechanisms are discussed.

The emergence of free convection implies that the dissolution process can no longer be considered strictly one-dimensional. This complexity undermines the validity of EPMA line scans for fully characterizing the dissolution front, as illustrated in Figure 4.48a. The profiles obtained depend on the line scan's position, resulting in potential discrepancies. Nevertheless, EPMA measurements remain highly valuable for assessing the composition near the interface, particularly in the narrower diffusive boundary layer unaffected by the bulk flow. These measurements allow for determining the glass composition in contact with the solid, provide insights into undersaturation conditions, and help evaluate whether thermodynamic equilibrium has been reached. The following section will delve deeper into these considerations.

4.4.1 Thermodynamic equilibrium at the interface

Assessing thermodynamic equilibrium during silica dissolution is essential for two primary reasons : first, the chemical potential gradient between the liquid and solid phases serves as the primary driving force for silica dissolution, dictating the movement of silica from the solid phase into the glass matrix (Equation 1.6) ; second, determining whether equilibrium is achieved at the interface within the timescale of interest is crucial for understanding the dissolution mechanism.

In multi-component systems, such as soda-lime-silica glass, the solubility limit of silica is not defined by a single value for a given temperature and pressure, as it would be in binary systems. Instead, equilibrium is represented by a range of compositions : in ternary systems, for instance, the equilibrium composition of the glass in contact with the solid silica phase is governed by a *liquidus* curve, as discussed in Section 1.4.1.

In Section 4.1.2, the soda-lime-silica glass + silica system was simplified using a pseudo-ternary diagram under the assumption that the alkaline-earth oxide ratio remained constant and equal to the original glass composition. Figure 4.49 validates this assumption, as the measured dissolution profiles conform to the predicted behavior, confirming that the pseudo-ternary diagram presented in Figure 4.5 can be reliably applied in this context.

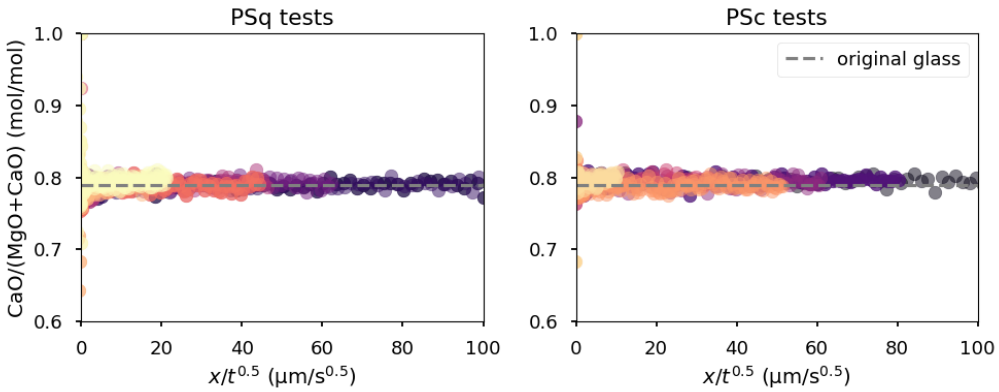

Figure 4.49 Ratio between the alkaline-earth oxides for the measured EPMA profiles shown in Figure 4.46 with the normalized distance. The value is kept constant for both PSq and PSc tests along the entire time range and has a similar value to the original glass composition ratio.

The EPMA concentration profiles from Figure 4.46 were then plotted in this compositional space, as shown in Figure 4.50, after normalization to the $Na_2O-CaO-MgO-SiO_2$ system. These profiles are overlaid with the *liquidus* curve at 1300 and 1400°C. Figure 4.50 demonstrates that the dissolution paths follow a nearly straight line extending from the original glass composition toward the SiO_2 apex, with a slight deviation toward the alkali-rich side. The curves fall between the *liquidus* boundaries at 1300°C and 1400°C, which is consistent with the quenching process and the spatial resolution of the EPMA measurements.

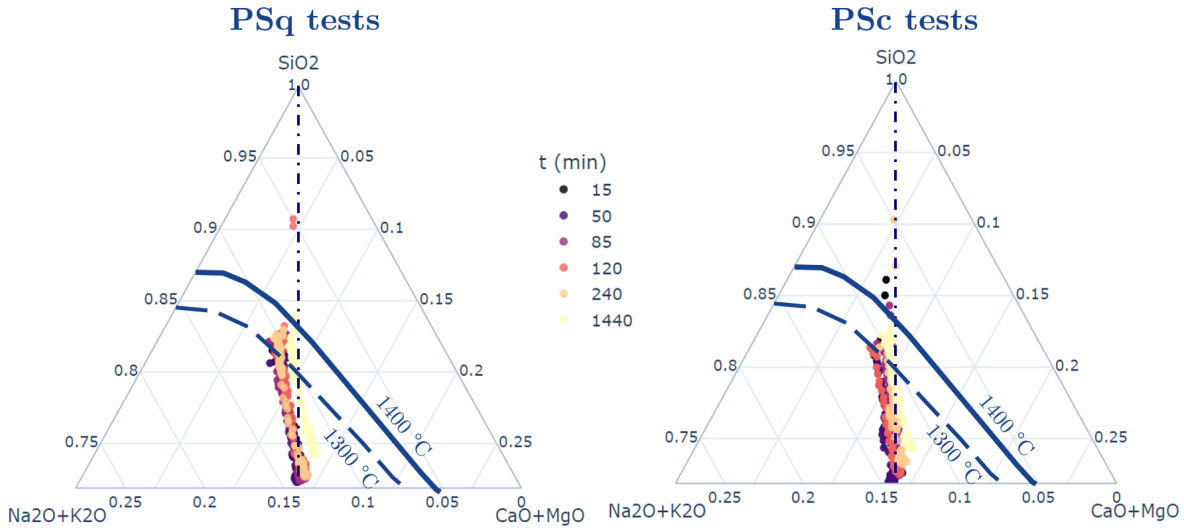

Figure 4.50 EPMA glass composition evolution plotted in the compositional space and overlaid with the isothermal *liquidus* curves for a pseudo-ternary phase diagram, assuming CaO/(CaO+MgO) = 0.78. The dot-dashed line displays the straight tie-line between the original glass and the SiO_2 apex.

Both quartz and cristobalite dissolution samples exhibit similar behavior, with only minor deviations in the far-field composition due to confined dissolution. This effect is most pronounced in the PSc samples, where continuous shifts in the initial position are observed at longer dissolution times.

Additionally, despite these shifts, the interface compositions for both cristobalite and quartz tests remain closely aligned, suggesting that equilibrium was established with the same solid phase—most likely cristobalite. Although thermodynamic predictions indicate that tridymite should form as the equilibrium phase, the proximity of the *liquidus* curves for cristobalite and tridymite explains the close agreement in the results, even in cases where tridymite was not observed, such as in all PSc samples and shorter dissolution tests for PSq samples.

The equilibrium glass composition at 1400°C was calculated using the method described in Section 2.5.4, which determines the nearest *liquidus* composition. Figure 4.51 illustrates the difference between the first experimental point and this theoretical equilibrium value. The comparison reveals that the deviation from the theoretical value does not vary significantly over time. Aside from a larger margin of error in the PSc samples, no clear differences are observed between quartz and cristobalite samples.

Since the first experimental point frequently deviates from the precise interface position (i.e., $x = 0$), it is reasonable to assume that the interface composition has reached equilibrium across all dissolution test durations. These results confirm findings from previous studies, which establish

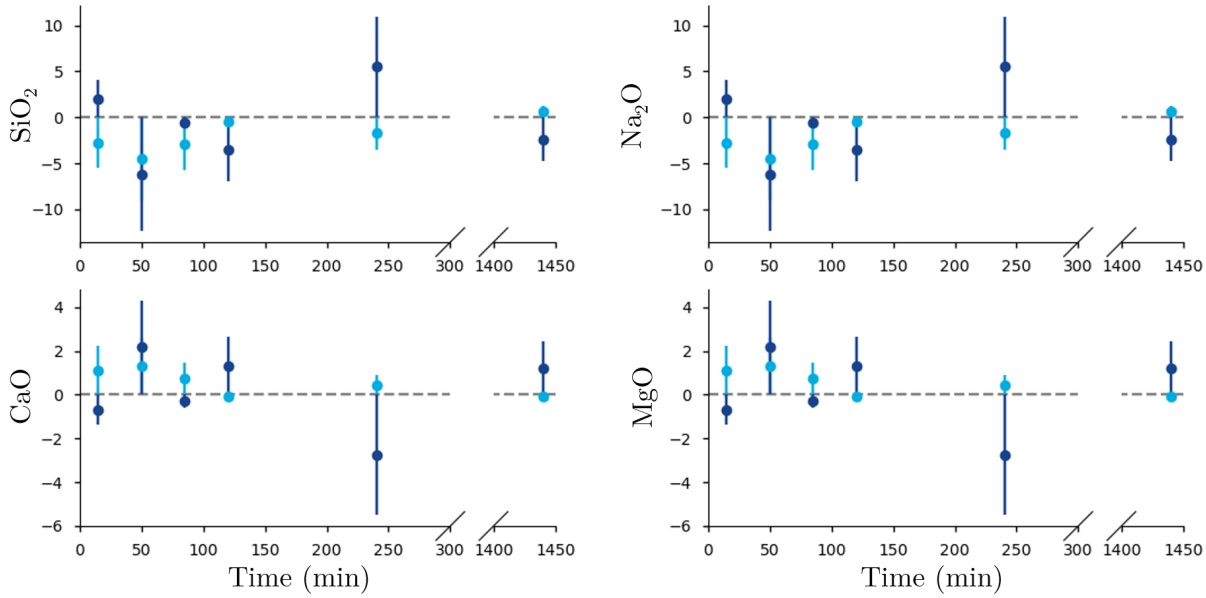

Figure 4.51 Difference between the experimental EPMA measurement closest to the dissolution interface and the theoretical *liquidus* composition at 1400 °C for quartz (light blue) and cristobalite (dark blue) dissolution samples.

that silica dissolution is predominantly governed by mass transport. However, as the chemical profiles show, achieving a purely diffusive dissolution regime is challenging, even over short periods. The onset of free convection complicates the ability to maintain a purely diffusive regime. The following section will explore the potential causes for the onset of free convection and its implications for the dissolution process.

4.4.2 Origins of convection onset

As illustrated in Figure 4.48, perturbations in the dissolution front were observed in both quartz and cristobalite samples as early as 15 minutes into the tests. This challenges the hypothesis that convection could be solely attributed to the volume expansion caused by the quartz-to-cristobalite transformation, as cristobalite had already formed in the PSc-15 sample. Additionally, as discussed in Section 2.2.3, free convection cannot be attributed to density gradients arising from double-diffusive instabilities in dissolution tests of less than 325 minutes (Figure 2.4).

Given the significant density differences between quartz and cristobalite (Table 4.1), the transformation of quartz into less dense polymorphs could contribute to the observed perturbations. In PSq samples, the initial density ratio between quartz and glass will evolve over time. Initially, quartz is denser than glass, but as it transforms into cristobalite or tridymite, it becomes less dense, potentially driving convection.

To further investigate the influence of quartz emplacement on convection onset, three different setups were employed to evaluate quartz dissolution at 1400°C for 15 minutes, as described in Section 4.2.1. In addition to the standard setup, with quartz placed on top of the melt, two alternative configurations were tested : placing quartz at the bottom and arranging it in a horizontal stack. Raman spectrometry maps were obtained in the interface region for these setups. Following NMF treatment, the spatial distributions of silica polymorphs, the original glass, and

the silica-enriched glass were identified. The results for α-cristobalite and silica-enriched glass across the three geometries are presented in Figure 4.53. Given the similarity in partial Raman spectra for silica-rich glass across the setups, a valid comparison of spatial distributions can be made. The vertical sandwich maps were rotated by 90° and aligned with the red arrow in the setup illustration.

Perturbations in the dissolution front were consistently observed across all three geometries, suggesting that these disturbances are intrinsic to the dissolution process, independent of the setup configuration. These plumes or vortexes emerged perpendicularly to the interface, even in the vertical wall configuration of the PSqs-15 sample. The fact that these perturbations appeared irrespective of the orientation relative to gravity rules out density inversions as the cause of onset. Moreover, the setup geometry influenced the cristobalite layer morphology, particularly in the silica-on-bottom setup, where the layer was less uniform and more fractured.

Since all setups exhibited convection, the silica-on-top configuration was selected for further experiments due to easier sample preparation. A plausible alternative explanation for convection onset, independent of gravitational effects, is the displacive transformation between α and β phases. As described in Section 4.1.1, silica polymorphs undergo rapid displacive transitions between high-temperature (β) and low-temperature (α) forms. These transitions occur almost instantaneously, and the volume changes involved, though smaller than those from reconstructive phase transformations, can cause abrupt interface movements. Figure 4.52 illustrates the potential transformations and their corresponding molar volume ratios.

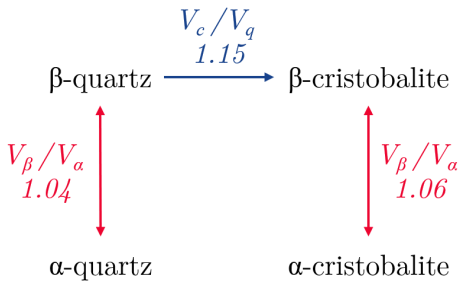

Figure 4.52 Displacive (in red) and reconstructive (in blue) phase transformations between quartz and cristobalite. Displacive transformations are reversible and instantaneous. The values indicate the ratio between the molar volumes involved in each transformation and were extracted from Table 4.1.

The sudden nature of these transformations can generate a shock at the interface between the silica-rich layer and the bulk glass. If the interface contains local asperities, these may be amplified by the shock's refraction, leading to a Richtmyer-Meshkov instability, as illustrated in Figure 4.54. This type of instability, typically triggered by a shock wave passing through an interface between two fluids of different densities, causes the interface to ripple and eventually develop turbulence [127]. Wavy patterns observed in the cristobalite layer at the interface in several PSq and PSc tests provide further evidence of this mechanism.

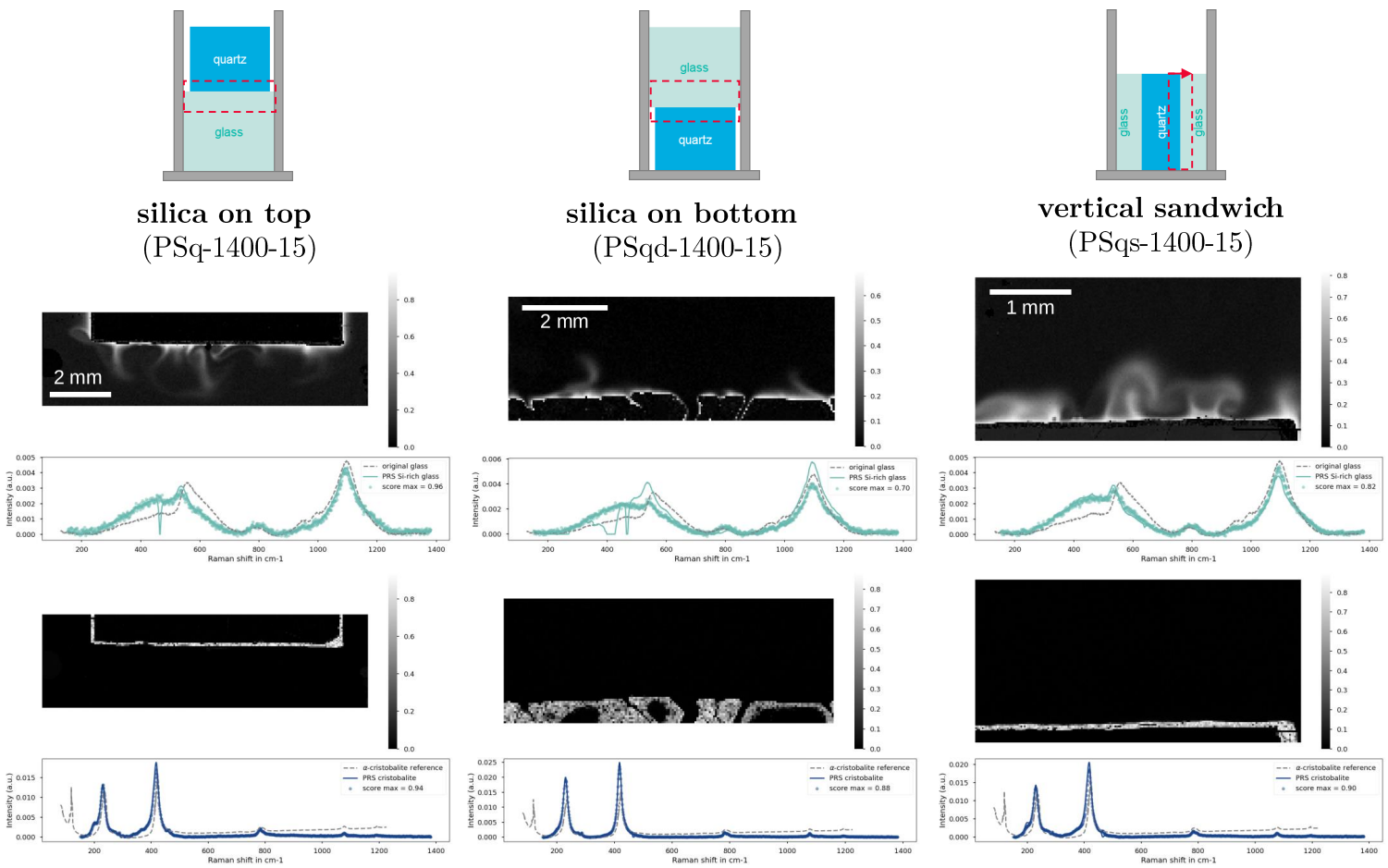

Figure 4.53 Comparison of the relative positioning of quartz in the experimental setup for the same dissolution treatment of 15 minutes at 1400 °C. The Raman mappings illustrate the spatial distribution of Si-rich glass, resulting from silica dissolution, and cristobalite. The red rectangle in the setup illustrations marks the region analyzed by Raman spectroscopy. The images from left to right correspond to different quartz orientations : silica on top, silica on bottom, and vertical sandwich, respectively. The comparison aims to elucidate the effects of quartz placement on gravitational stability of the setup as detailed in Section 4.2.1.

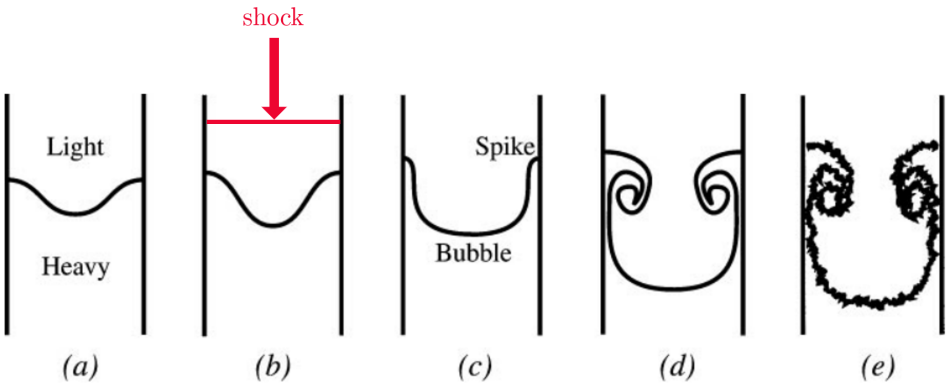

Figure 4.54 Evolution of a single-mode Richtmyer-Meshkov perturbation, induced by a sudden shock wave at the top. (a) initial configuration of the corrugated interface between two different fluids, (b) application of the shock wave at the top, (c) start of nonlinear evolution—asymmetric spike and bubble development, (d) roll-up of the spike. (e) emergence of small scales and turbulent mixing. From [127]

If the crystalline silica grain is not preheated before contact with the melt, all dissolution tests would likely exhibit convection, as the low-pressure polymorphs of silica are prone to displacive transformations. It is unclear whether starting with amorphous silica would prevent convection, although cristobalite formation is still reported at the interface in such cases [28] (Figure 4.14).

As outlined in Section 1.2.3, convection can significantly accelerate dissolution by removing solute accumulated near the interface. Based on EPMA diffusion profiles and comparisons between geometries, both PSq and PSc samples were likely influenced by free convection. This could explain the contraction of the diffusion layer compared to predictions from diffusion matrix calculations and the faster departure from the semi-infinite condition observed in these experiments.

These findings highlight the challenges in accurately evaluating silica dissolution under reproducible conditions and the potential confusion between a mass transport coefficient and diffusivity, given the difficulties in maintaining static conditions. The following section will synthesize the experimental observations and propose a potential dissolution mechanism for quartz.

4.5 Towards a quartz dissolution mechanism

Quartz dissolution is inherently linked to the progressive evolution of its solid polymorphs, significantly influencing the dissolution process. As discussed in the theoretical background (Section 4.1.4), the disparity between the solid phase molar volume and the solute's partial molar volume in the glass can induce radial flow near the interface. This expansion stretches the diffusion profiles and reduces the concentration gradient close to the interface. The ε parameter can be used to quantify the effect for binary systems, as described in Section 1.2.2.

Cristobalite, tridymite, and amorphous silica have ε values close to that of the interface glass, indicating minimal expansion. In contrast, quartz has a significantly more negative ε value with its lower molar volume, causing greater melt expansion and influencing the dissolution process. As a result, a solid phase predominantly composed of quartz is expected to dissolve more slowly than one composed mainly of cristobalite.

Figure 1.7 demonstrates that more negative epsilon values correspond to slower dissolution for a fixed undersaturation. As quartz becomes progressively depleted in the PSq tests (Figure 4.36), assuming the same solubility and purely diffusive dissolution behavior, the dissolution process is expected to shift from an $\varepsilon = -0.14$ to a curve corresponding to ε values between 0.01 and 0.02 (values from Table 4.6), as illustrated by the orange curve in Figure 4.55.

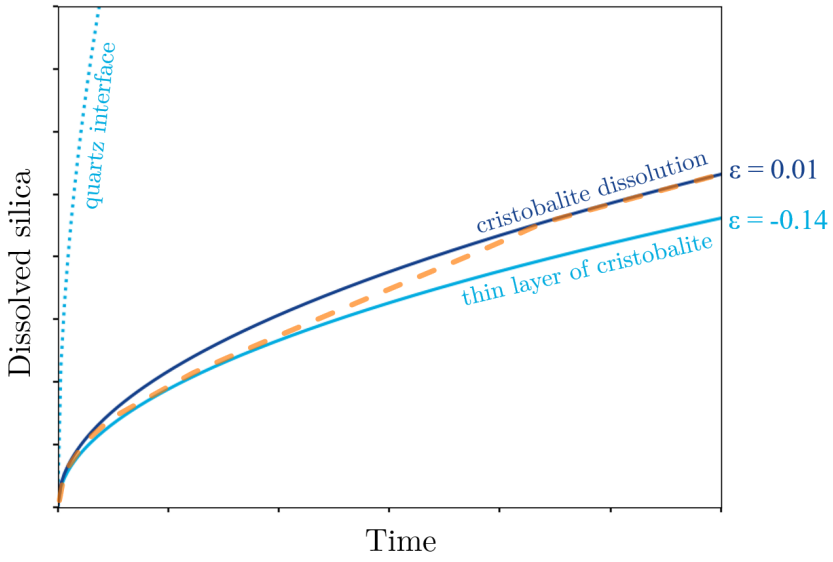

Figure 4.55 Illustration of a diffusion-controlled case dissolution for cristobalite (dark blue solid line), quartz at the interface (light blue dashed curve), and quartz enveloped by a thin layer of cristobalite at the interface (light blue solid curve). With the evolution of the cristobalite layer surrounding the quartz, quartz dissolution would shift from $\varepsilon = -0.14$ to the $\varepsilon = 0.01$ curve, like the orange curve.

For the PSc tests, the dark blue curve represents dissolution at $\varepsilon = 0.01$, while the light blue curve suggests a scenario where a thin layer of cristobalite or tridymite forms at the interface. Despite the solid phase being predominantly quartz ($\varepsilon = -0.14$), the presence of this thin layer aligns the interface composition with that of cristobalite dissolution.

Without this thin layer, the solubility limit of the glass in contact with metastable quartz would be higher (Table 4.4), leading to an accelerated dissolution rate, as represented by the dashed

light blue curve. Although this scenario is plausible in the early stages of quartz dissolution, measured interface compositions for dissolution tests ranging from 15 minutes to 24 hours are consistent with predicted equilibrium glass compositions in contact with tridymite.

Direct comparison of these experimental data with theoretical predictions is challenging for several reasons. First, the assumption of semi-infinite dissolution becomes invalid after 2 hours due to the limited glass height. As saturation increases, the dissolution rate slows, flattening the concentration gradients as shown in Figure 4.12.

Second, convection-induced perturbations were observed in all samples, likely accelerating the dissolution process. The exact cause of this convection remains unclear, as does its relative impact on the dissolution rates of quartz and cristobalite. If convection is indeed triggered by the alpha-to-beta phase transformation, then convection in crystalline silica dissolution experiments may be unavoidable.

Third, the interface in contact with the glass evolves over time, with quartz and cristobalite samples exhibiting different behaviors. For cristobalite, the remaining solid tends to form smoother edges, reducing the available interface area for dissolution as the grain becomes rounder. In contrast, PSq samples showed a flower-like structure, increasing the available interface area. However, as discussed for the lateral gap saturation (Appendix's Figure B.3), not all additional surfaces necessarily enhance dissolution.

Additionally, the phase transformation-induced expansion of quartz complicates efforts to measure the amount of dissolved silica accurately. To overcome this, an alternative approach using Raman spectroscopy mappings coupled with the molar volumes of each polymorph was adopted, allowing for a more accurate estimation of dissolution in terms of the number of silica moles. This method provided a valuable complement to geometric measurements by accounting for the effects of phase expansion.

This study has revealed the complexities associated with dissolving metastable phases, including their influence on the amount of dissolved material, the challenges of measuring dissolution, and the impact of microstructural evolution. Although the experimental setup differs from industrial glass-melting processes, the findings contribute to understanding how sand grains dissolve in glass melts. Given that the first-formed liquids are highly alkaline (Section 1.1), the transformation of quartz to cristobalite (or tridymite) is almost inevitable. The violent expansion observed in quartz slabs in this study suggests that similar transformations in micrometric sand grains could cause their collapse, breaking larger grains into smaller fragments that dissolve more readily. Further research, including a statistical failure analysis of smaller quartz grains, would be necessary to investigate this effect fully.

Overall, this study provides valuable insights into the dissolution of quartz, emphasizing the importance of phase evolution, microstructural changes, and convection-induced perturbations.

Conclusion and perspectives

Understanding the dissolution kinetics of alpha-alumina and quartz in multi-component soda-lime-silica glass melts is essential for improving the efficiency of industrial glass melting processes. As this process is highly energy-intensive, representing over 75% of the energy consumption in glass manufacturing [1], there is an increasing demand to optimize the process. This research addresses a critical gap by providing physicochemical data and insights into the dissolution mechanisms of two key refractory oxides, alpha-alumina and quartz, which are often responsible for defects in glass products. By offering a deeper understanding of the complex interactions between these oxides and multi-component glass melts, this work contributes to the efforts to produce glass with fewer defects more efficiently, thus paving the way for more sustainable and energy-efficient glass manufacturing.

A static experimental setup was designed to measure dissolution chemical profiles and microstructure evolution at the interface during alumina and quartz dissolution. The main focus was on understanding solubility and diffusivity, as these are key properties that quantify the dissolution kinetics. Electron Probe Microanalysis (EPMA) measurements and Raman spectroscopy provided a detailed understanding of the chemical and structural changes occurring during dissolution, giving new insights into the behavior of these oxides in soda-lime silica glass.

The results revealed that dissolution behavior is strongly influenced by the specific properties of both the solid and the melt. Alumina dissolution, in particular, exhibited a strong coupling between melt components, which significantly influenced how alumina was incorporated into the glass. On the other hand, quartz dissolution highlighted the critical role of solid phase transformations, especially how the presence of silica polymorphs affects the dissolution kinetics and experimental measurements. These findings underscore the need to consider both melt dynamics and solid-phase evolution when predicting dissolution in industrial glass systems.

Alumina dissolution : an illustration of the effect of coupling diffusion in the melt
The experimental results on alumina dissolution confirmed that the process is diffusion-controlled under static conditions. Both solubility limits and diffusivity were successfully described for alumina in soda-lime-silica glass across a temperature range of 1300 to 1450 °C. However, contrary to conventional approaches that approximate multi-component systems as pseudo-binary, the findings showed that neither solubility nor diffusivity could be accurately represented using this assumption. The dissolution path of alumina in the melt could not be described by a straight tie-line connecting the initial glass composition and the alumina apex. Instead, it was necessary to consider the varying mobilities of different components in the glass and their interactions to describe both the solubility of alumina and the diffusion path of the alumina-enriched melt.

This study highlighted that using a diffusion matrix is necessary for capturing the complex behavior of alumina dissolution in multi-component systems. The results demonstrated that alumina dissolution is highly dependent on the dynamics of the melt, where the interaction

between different melt components plays a key role in defining both the interface composition and the diffusion profile.

The diffusion behavior in systems with more than one network former component, such as the alumina-enriched glass and borosilicate, is more likely to show pronounced coupling effects.

Quartz dissolution : an illustration of the effect of transformations in the solid phase Quartz dissolution - in contrast to α-alumina, which is already the stable phase at high temperatures - demonstrated how solid phase transformations can drastically affect dissolution behavior. Silica, which exists in multiple polymorphic forms, undergoes phase changes that significantly complicate the measurement of dissolution rates. This is particularly challenging when relying on geometric properties to quantify dissolution. The results revealed that the microstructural evolution of quartz plays a significant role in how much material is dissolved and how dissolution kinetics are defined. The presence of different silica polymorphs and their phase transformations must be accounted for in experimental measurements, as they can lead to overestimation of dissolution due to free convection and other dynamic effects.

However, despite these solid-phase transformations, the composition at the quartz-glass interface and the diffusion path during dissolution were not strongly affected by the type of silica polymorph. This finding aligns with previous observations by previous works [28, 31], who reported similar diffusivities for both quartz and amorphous silica dissolution tests.

Although corundum is already the high-temperature stable phase of Al_2O_3, the microstructure effect of starting with a sintered alumina or a sapphire monocrystal was briefly assessed, and no differences were observed between their diffusion profiles.

Nevertheless, the work also underlines the limitations of studying dissolution in single-oxide systems, as real-world contaminations often involve more complex alumino-silicate systems where the solid phase contains multiple components that can interact with the glass melt.

Limitations and perspectives for future research This research has provided valuable insights into the dissolution of alpha-alumina and quartz in multi-component soda-lime-silica glass melts, yet it also exposed several complexities that require further investigation. Both solubility and diffusivity are context-dependent properties that cannot be easily defined as single, invariant values across different compositions and temperature ranges. The study demonstrated the usefulness of diffusion matrices for describing multi-component diffusion. Still, these matrices can be difficult to measure accurately and time-consuming, and their domain of validity remains unclear.

A major challenge is that diffusivity depends on various factors such as temperature, pressure, and composition, as dictated by thermodynamic relationships. This context dependence complicates the measurement and application of diffusion data in industrial settings. Two promising approaches have emerged for addressing these challenges. The first is to couple tracer diffusivities and thermodynamic databases, such as CALPHAD, to predict multi-component diffusion behavior. Studies like those by Kwon *et al.* [128] have shown that this strategy can provide adequate predictions of diffusion matrices for complex systems. The second approach involves using phase-field models [129, 130], which can incorporate both diffusivity and thermodynamic data to predict solid-liquid interfaces, including multi-component solubility. These models have shown promise for predicting the dissolution behavior of more complex systems and extrapolating diffusion data across broader compositional and temperature ranges.

Although these theoretical approaches show promise, their integration into industrial models, such as post-processing tools for glass melting, remains challenging. A balance must be struck between physical understanding and practical applicability. For instance, while alumina dissolution exhibited complex diffusion coupling between elements, its overall diffusion profile could still be approximated using an effective binary diffusion coefficient (EBDC). Moreover, the good agreement between this value and the viscosity at the interface suggests that viscosity could serve as a proxy for diffusion in some cases. Similarly, in quartz dissolution, dynamic dissolution tests under controlled flow conditions could help decouple the effects of convection from diffusion, given that a static setup was not feasible, providing more accurate data for use in industrial applications.

Assessing dissolution in multi-component glass melts In conclusion, this research has contributed to the understanding of the dissolution kinetics of α-alumina and quartz in soda-lime silica glass melts. By providing critical experimental data and insights into the underlying mechanisms of dissolution, this work has advanced both the theoretical understanding of multi-component diffusion and the practical application of these findings in industrial glass manufacturing. The findings underscore the importance of considering both solid-phase transformations and melt dynamics when evaluating dissolution, as well as the need for accurate diffusion matrices in multi-component systems.

Future research should focus on expanding the findings of this study to a wider range of glass compositions, incorporating other network formers such as boron, and extending the use of thermodynamic models to predict diffusion behavior. Additionally, dynamic dissolution experiments under controlled flow conditions could help isolate the effects of convection when static dissolution is impossible. By building on the methods and insights presented in this work, future research has the potential to further refine our understanding of dissolution processes, leading to more efficient and sustainable glass production.

Conclusions et perspectives

Comprendre les cinétiques de dissolution de l'alpha-alumine et du quartz dans les verres sodocalciques multicomposants est essentiel pour améliorer l'efficacité des procédés de fusion du verre industriel. Comme ce processus est extrêmement énergivore, représentant plus de 75% de la consommation d'énergie dans la fabrication du verre [1], il y a une demande croissante d'optimisation de ce procédé. Cette recherche comble une lacune critique en fournissant des données physico-chimiques et des perspectives sur les mécanismes de dissolution de deux oxydes réfractaires clés, l'alpha-alumine et le quartz, souvent responsables de défauts dans les produits verriers. En offrant une compréhension plus approfondie des interactions complexes entre ces oxydes et les verres multicomposants, ce travail contribue aux efforts visant à produire des verres de meilleure qualité avec moins de défauts, ouvrant ainsi la voie à une production de verre plus durable et écoénergétique.

Un dispositif expérimental a été conçu pour mesurer les profils chimiques de dissolution et l'évolution microstructurale à l'interface lors de la dissolution de l'alumine et du quartz dans le cas statique. L'accent principal a été mis sur la compréhension de la solubilité et de la diffusivité, ces propriétés étant essentielles pour quantifier les cinétiques de dissolution. Les mesures par microsonde électronique et la spectroscopie Raman ont permis d'obtenir une compréhension détaillée des changements chimiques et structuraux se produisant lors de la dissolution, apportant de nouvelles perspectives sur le comportement de ces oxydes dans le verre sodocalcique.

Les résultats ont révélé que le comportement de dissolution est fortement influencé par les propriétés spécifiques du solide et du verre fondu. La dissolution de l'alumine, en particulier, a montré un couplage marqué entre les composants du verre fondu, influençant significativement l'incorporation de l'alumine dans le verre. En revanche, la dissolution du quartz a mis en évidence le rôle crucial des transformations de phase du solide, notamment comment la présence de polymorphes de la silice affecte les cinétiques de dissolution et les mesures expérimentales. Ces résultats soulignent la nécessité de prendre en compte à la fois la dynamique du verre fondu et l'évolution de la phase solide lors de la prédiction de la dissolution dans les systèmes verriers industriels.

Dissolution de l'alumine : une illustration de l'effet du couplage entre les éléments du verre fondu Les résultats expérimentaux sur la dissolution de l'alumine ont confirmé que le processus est contrôlé par la diffusion dans des conditions statiques. Les limites de solubilité et la diffusivité ont été décrites avec succès pour l'alumine dans le verre sodocalcique dans une gamme de températures allant de 1300 à 1450 °C. Cependant, contrairement aux approches conventionnelles qui approximant les systèmes multicomposants comme pseudo-binaires, les résultats ont montré que ni la solubilité ni la diffusivité ne pouvaient être représentées avec précision à l'aide de cette hypothèse. Le chemin de dissolution de l'alumine dans le verre fondu ne pouvait pas être décrit par une simple ligne de connexion entre la composition initiale du verre et l'apex de l'alumine. Il était nécessaire de prendre en compte les mobilités variables des

différents composants du verre et leurs interactions pour décrire à la fois la solubilité de l'alumine et le chemin de diffusion du verre enrichi en alumine.

Cette étude a mis en évidence que l'utilisation d'une matrice de diffusion est nécessaire pour capturer le comportement complexe de la dissolution de l'alumine dans les systèmes multicomposants. Les résultats ont démontré que la dissolution de l'alumine dépend fortement de la dynamique du verre fondu, où l'interaction entre les différents composants du verre joue un rôle clé dans la définition à la fois de la composition de l'interface et du profil de diffusion.

Dissolution du quartz : une illustration de l'effet des transformations du solide En contraste avec l'alpha-alumine, déjà stable à haute température, la dissolution du quartz a montré comment les transformations de phase du solide peuvent affecter de manière drastique le comportement de dissolution. La silice, qui existe sous plusieurs polymorphes, subit des changements de phase qui compliquent considérablement la mesure des taux de dissolution. Les résultats ont révélé que l'évolution microstructurale du quartz joue un rôle significatif dans la quantité de matière dissoute et dans la définition des cinétiques de dissolution. La présence de différents polymorphes de la silice et leurs transformations de phase doivent être prises en compte dans les mesures expérimentales, car elles peuvent entraîner une surestimation de la dissolution en raison de la convection libre et d'autres effets dynamiques.

Cependant, malgré ces transformations de phase solide, la composition à l'interface quartz-verre et le chemin de diffusion pendant la dissolution n'ont pas été fortement affectés par le type de polymorphe de la silice. Ce résultat est en accord avec les observations antérieures de certains travaux [28,31], qui ont rapporté des diffusivités similaires pour les tests de dissolution du quartz et de la silice amorphe.

Bien que le corindon soit déjà la phase stable à haute température de l'Al_2O_3, l'effet microstructural de l'utilisation d'une alumine frittée ou d'un monocristal de saphir a été brièvement évalué, et aucune différence n'a été observée entre leurs profils de diffusion.

Néanmoins, ce travail a également souligné les limites de l'étude de la dissolution dans des systèmes à oxyde unique, car les contaminations réelles impliquent souvent des systèmes aluminosilicatés plus complexes où la phase solide contient plusieurs composants qui peuvent interagir avec le verre fondu.

Limitations et perspectives pour les recherches futures Cette recherche a fourni des informations précieuses sur la dissolution de l'alpha-alumine et du quartz dans les verres sodocalciques, tout en mettant en évidence plusieurs complexités qui nécessitent des investigations supplémentaires. La solubilité et la diffusivité sont toutes les deux des propriétés contextuelles qui ne peuvent pas être facilement définies comme des valeurs uniques et invariantes à travers différentes compositions et gammes de températures. L'étude a démontré l'utilité des matrices de diffusion pour décrire la diffusion multicomposante. Cependant, ces matrices peuvent être difficiles à mesurer avec précision et nécessitent beaucoup de temps, et leur domaine de validité reste incertain.

Un défi majeur est que la diffusivité dépend de divers facteurs tels que la température, la pression et la composition, comme le dictent les relations thermodynamiques. Cette dépendance contextuelle complique la mesure et l'application des données de diffusion dans les environnements industriels. Deux approches prometteuses ont émergé pour relever ces défis. La première consiste à coupler les diffusivités de traceur et les bases de données thermodynamiques, telles que CALPHAD, afin de prédire le comportement de diffusion multicomposant. Des études comme

celles de Kwon *et al.* [128] ont montré que cette stratégie peut fournir des prédictions satisfaisantes des matrices de diffusion pour des systèmes complexes. La deuxième approche implique l'utilisation de modèles de champ de phase [129,130], qui peuvent incorporer à la fois les données de diffusivité et thermodynamiques pour prédire les interfaces solide-liquide, y compris la solubilité multicomposante. Ces modèles se sont montrés prometteurs pour prédire le comportement de dissolution dans des systèmes plus complexes et extrapoler les données de diffusion sur des gammes plus larges de compositions et de températures.

Bien que ces approches théoriques soient prometteuses, leur intégration dans des modèles industriels, tels que les outils de post-traitement pour la fusion du verre, reste difficile. Il est nécessaire de trouver un équilibre entre la compréhension physique et l'applicabilité pratique. Par exemple, bien que la dissolution de l'alumine ait montré un couplage de diffusion complexe entre les éléments, son profil de diffusion global peut être approximé en utilisant un coefficient de diffusion binaire effectif (EBDC). De plus, la bonne correspondance entre cette valeur et la viscosité du verre fondu à l'interface suggère que la viscosité pourrait, dans certains cas, servir de proxy pour la diffusion. De la même manière, pour la dissolution du quartz, des tests de dissolution dynamique sous des conditions de flux contrôlé pourraient aider à découpler les effets de la convection de ceux de la diffusion, étant donné qu'un montage statique n'est pas réalisable, fournissant ainsi des données plus précises pour une application industrielle.

Évaluation de la dissolution dans des verres multicomposants En conclusion, cette recherche a contribué à la compréhension des cinétiques de dissolution de l'alpha-alumine et du quartz dans les verres silico-sodo-calciques. En fournissant des données expérimentales et des perspectives sur les mécanismes sous-jacents de la dissolution, ce travail a fait progresser à la fois la compréhension théorique de la diffusion multicomposante et l'application pratique de ces découvertes dans la fabrication industrielle du verre. Les résultats soulignent l'importance de considérer à la fois les transformations de phase solide et la dynamique du verre fondu lors de l'évaluation de la dissolution, ainsi que la nécessité d'avoir des matrices de diffusion précises dans les systèmes multicomposants.

Les recherches futures pourraient se concentrer sur l'élargissement des résultats de cette étude à une gamme plus étendue de compositions de verre, en incorporant d'autres formateurs de réseau tels que le bore, et sur l'extension de l'utilisation des modèles thermodynamiques pour prédire le comportement de diffusion. De plus, des expériences de dissolution dynamique sous des conditions de flux contrôlé pourraient aider à isoler les effets de la convection lorsque la dissolution statique est impossible. En s'appuyant sur les méthodes et les perspectives présentées dans ce travail, les recherches futures pourraient affiner encore davantage notre compréhension des processus de dissolution, conduisant à une production de verre plus efficace et durable.

Appendices

Appendix A

X-Ray Diffraction (XRD) characterization of starting materials

X-ray diffraction (XRD) is a non-destructive analytical technique used to determine the atomic and molecular structure of a crystal. The technique involves directing X-rays at a sample and measuring the intensity and angles of the diffracted beams. The fundamental principle behind XRD is Bragg's Law, which relates the wavelength of the incident X-rays and the diffraction angle to the lattice spacing in the crystal [131, 132].

In this study, XRD was employed to evaluate the crystalline phases of the starting materials used as silica and alumina sources. The measured diffraction patterns were compared with the RRUFF database and ICDD references to verify the presence of the desired crystalline phases. In addition to Raman spectroscopy, this characterization was crucial for ensuring the crystallographic integrity of the starting materials, presented in Sections 2.3 and 4.2.2.

To quantify the phases, the Rietveld refinement technique was utilized. This method involves fitting a calculated diffraction pattern to the observed data using a least squares approach. The refinement process adjusts various parameters, including lattice constants, atomic positions, and thermal factors, to minimize the difference between the observed and calculated patterns. Rietveld analysis was performed using the fundamental parameters method as described by Cheary et al. [133], along with the user manual of the TOPAS software (Bruker). The instrumental contribution was accounted for by measuring the NIST SRM 660c standard composed of LaB_6 powder. This quantification was applied to the XRD of the trial heat treatment of quartz to obtain cristobalite.

For the alumina bulk characterization, the sintered plates were broken into millimetric pieces and then ground in a tungsten carbide roller mill. To achieve a grain size under 50 µm, the material was further micronized for 10 minutes using a McCrone XRD-mill with agate grinding elements and ethanol. The final slurry was evaporated at room temperature under a laboratory fume hood for 24 hours and then dried in an oven at 50 °C for 3 hours to obtain the final powder.

Other samples were evaluated based on their surface response. While prefabricated quartz slabs featured a surface roughness of $Ra < 1$ nm, the cristobalite samples were polished beforehand to achieve a smooth surface, critical for minimizing surface irregularities that could affect the diffraction results. The polished samples were securely mounted on sample holders to prevent any movement during the measurements.

The XRD measurements were conducted using the Rigaku Smartlab II diffractometer, coupled with a monochromatic X-ray beam generated from a Cu Kα radiation source (with a wavelength

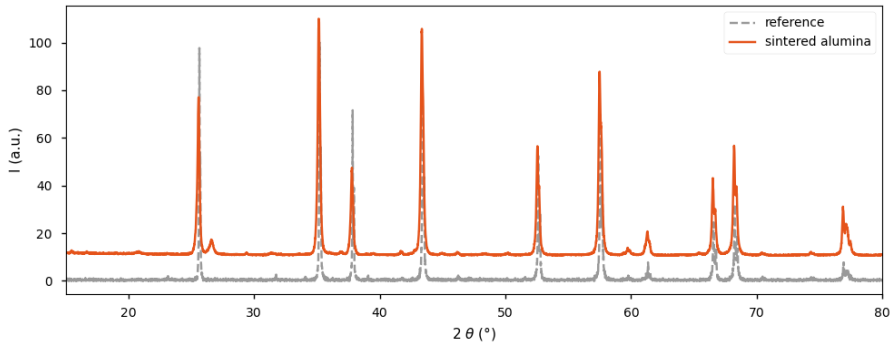

Figure A.1 XRD spectra obtained from the sintered alumina plate grounded into powder. The gray dashed line is the reference spectra for α-Al_2O_3 , reported as the sample R040096 in RRUFF database.

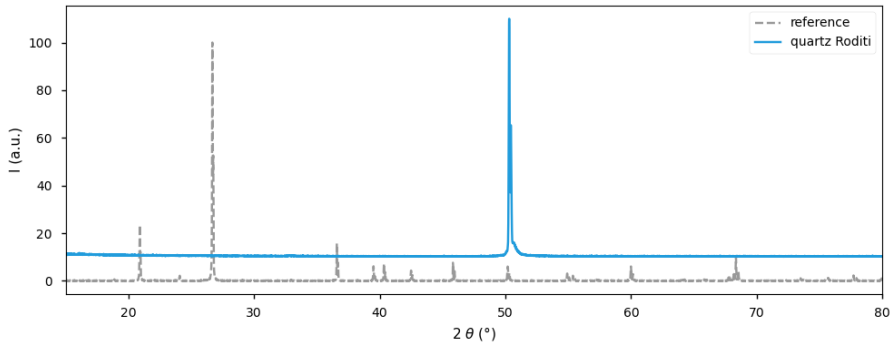

Figure A.2 XRD spectra obtained from the surface of the prefabricated quartz slab, z-oriented. The gray dashed line is the reference spectra for α-quartz powder, reported as the sample R040031 in RRUFF database.

of 1.54 angstroms). The samples were scanned over a 2θ range of 10° to 90° to capture the full diffraction profile. The step size was set to 0.02° 2θ with a counting time of 1 second per step to ensure high-resolution data. A high-resolution detector was employed to measure the intensity of the diffracted X-rays accurately.

The diffractograms for the sintered alumina, quartz, and cristobalite from both fused-cast silica refractory and heat-treated quartz are presented below. The baselines for the measured spectra were shifted to better visualization.

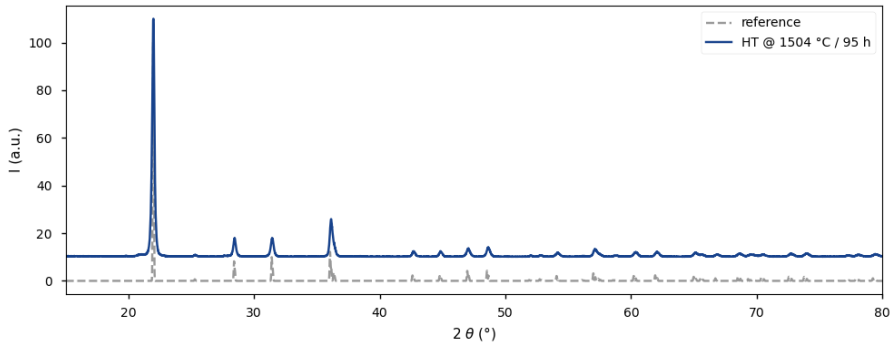

Figure A.3 XRD spectra obtained from the surface of amorphous silica tablet heat treated at 1504 °C for 95 hours. The gray dashed line is the reference spectra for α-cristobalite, reported as the sample R061107 in RRUFF database.

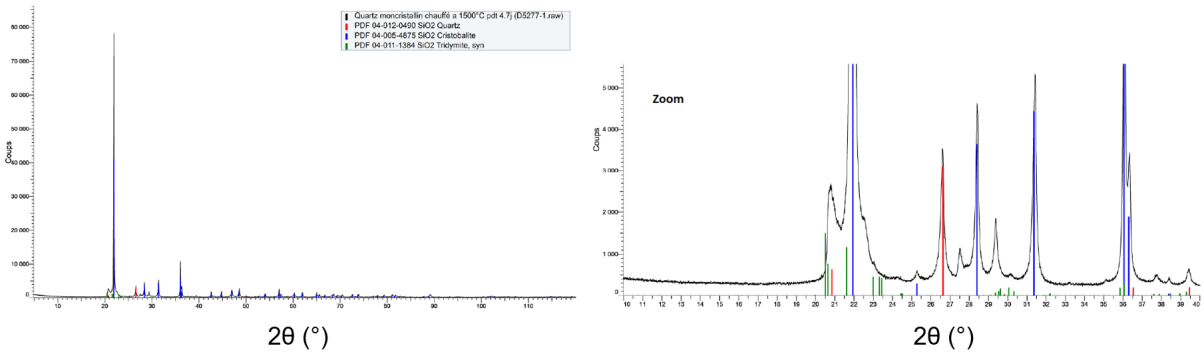

Figure A.4 XRD diffractogram of the powder obtained from quartz heat treated for 4 days and 17 hours at 1500 °C, shown in Figure 4.22 left. By Rietvelt refinement analysis, it was calculated that 85% of the spectra corresponds to cristobalite (blue pics in the diffractogram), while 8% corresponds to quartz (in red). Some pics could not be explained by available silica polymorphs.

Appendix B

Considerations on geometric assumptions for silica quantification

B.1 Comparison between methods to calculate the initial number of moles

Although a reliable comparison from the silica dissolution samples is not available to validate the cylinder approximation, the number of moles in the initial tablets can also be measured using their initial mass multiplied by the silica molar mass. The number of silica moles calculated using the cross section area approximation applied to the starting slabs, compared to the number of moles using the silica molar mass, provides a reasonable correspondence, as displayed in Figure B.1.

The cylinder equivalent volume approximation consistently overestimates the number of moles compared to the molar mass for cristobalite slabs. This discrepancy arises because cristobalite slabs are manufactured from fused-cast silica refractory and may contain internal pores, whereas quartz slabs are monolithic samples. Since the initial measurements of the slab are taken without accessing its interior, measuring its external dimensions can lead to an overestimation of the silica content in the original cristobalite tablets.

Based on Raman mapping of the manufactured cristobalite's cross section (Figure 4.21), the porosity was estimated to be 8% by volume. Correcting the cylinder equivalent volume calcula-

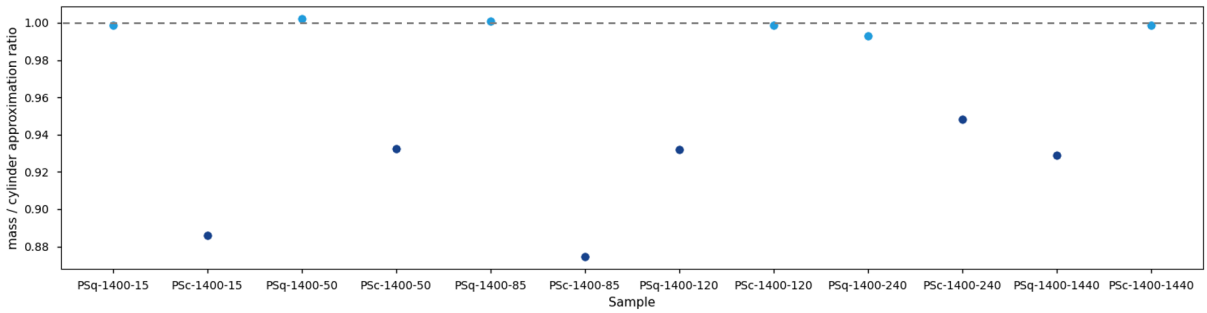

Figure B.1 Comparison between the number of SiO_2 moles in the initial tablet using the molar mass and the equivalent cylinder volume. Quartz tablets are shown in light blue (PSq- samples) and cristobalite are displayed in dark blue (PSc- samples).

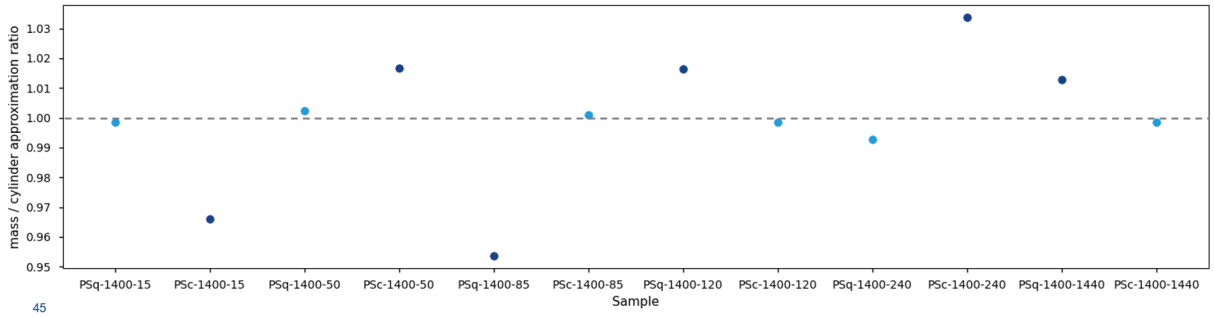

Figure B.2 Comparison between the number of SiO_2 moles in the initial tablet using the molar mass and the equivalent cylinder volume, taking into account the initial porosity of the manufactured cristobalite slabs.

tion for the initial cristobalite slabs by a 92% factor brings the comparison closer to unity, as displayed in Figure B.2.

B.2 Available interface area for dissolution and lateral gap

The procedure described in Section 4.2.4 is based on the normalization of the number of silica moles by the available interface surface. This is necessary for at least two reasons : first, the slab diameter changes during dissolution, and second, the initial diameters of quartz and cristobalite slabs were different (as shown in Table 4.8). Without this normalization, comparing the dissolution amounts of quartz and cristobalite would be problematic, as their differing diameters would lead to inconsistent dissolution measurements across the available surface.

As illustrated in Figure 4.24, the dissolution interface comprises both the bottom face of the slab (πr^2) and its lateral surface ($2\pi rh$). To accommodate the expansion, the glass slab's diameter was larger than that of the quartz slab (Figure 4.16). An additional complication arises from the fact that the lateral gap (δ) was not specifically designed to prevent confined dissolution, unlike the slab thickness. For longer dissolution tests, these lateral gaps could become saturated with silica and cease to function as active dissolution interfaces. Using eigenvalues from Trial and Spera [62], corrected for 1400 °C (Table 4.5), the characteristic length of each exchange reaction can be calculated as $\delta_i = \sqrt{t/\lambda_i}$, defining the size at which the reaction reaches steady state over time t (see Section 1.4.2for further explanations). A comparison of the initial and final lateral gaps is presented in Figure B.3, along with the values for δ_i of the two eigenvalues.

The first exchange reaction, as proposed by Trial and Spera's Na_2O-CaO-SiO_2 matrix [62], primarily involves alkali and alkaline-earth oxides. Except for the 15-minute test, all other tests appear saturated in this lateral region with respect to these more mobile components, suggesting that diffusion of alkalis in the melt is established and could proceed into the solid, provided solid solubility is possible.

However, the second exchange, between silica and calcium oxide, more accurately describes silica saturation in the lateral gap. When the $\delta < \delta_i$, the lateral dissolution interface could become "deactivated" due to saturation, leaving only the bottom interface (πr^2 instead of $\pi r^2 + 2\pi rh$) available for dissolution. Figure B.4 presents the calculated interface areas for both cases, considering the initial and final dimensions of diameter and height. Estimations for the 24-hour tests are excluded due to the significant deviation from cylindrical geometry in the remaining solid.

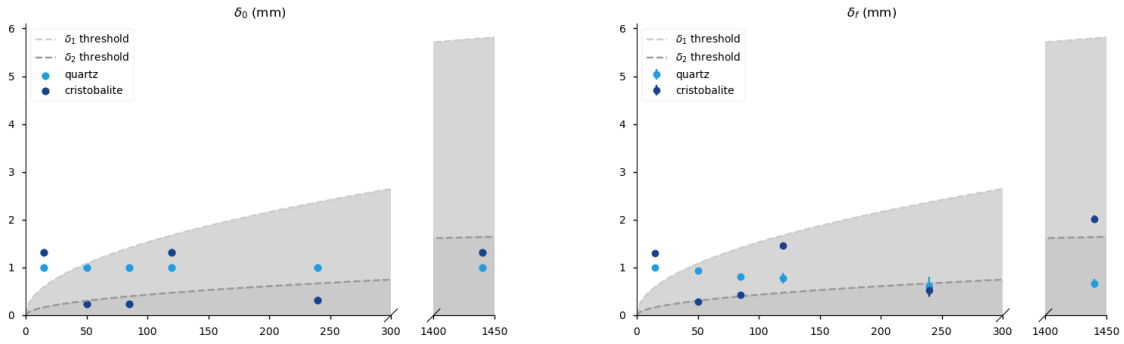

a Lateral gap before test

b Lateral gap after dissolution test

Figure B.3 Lateral gap distance in the initial setup (left) and after test (right). The characteristic lengths for the exchange reactions described by Trial and Spera's diffusion matrix [62] are also plotted for comparison. Due to the limited thickness in the lateral part of the slab, gray areas show the conditions where the steady state for each exchange reaction is achieved.

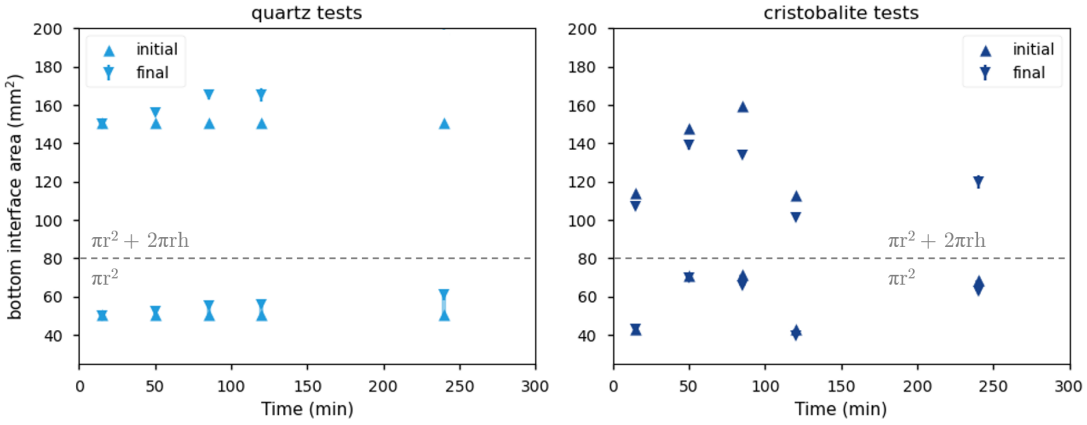

Figure B.4 Estimations of the possible contact area with the glass. Two cases are shown : (top) area underneath the cylinder and its side walls are available as dissolution interfaces (bottom) and only the bottom area acts as a source for dissolution. Markers pointing up display the calculation based on the initial dimensions of the cylinder, and the triangles pointing downwards were calculated based on the measured dimensions after dissolution.

Although larger solid slabs provide a greater bottom surface area, they are also more susceptible to lateral gap saturation. As shown in Figure B.3, determining whether PSc-50, -85, and -240 exceed the saturation threshold is challenging due to the progressive decrease in cristobalite's diameter. Therefore, only the PSq-1440 test's dissolution interface was limited to the slab's bottom face.

B.3 Deviations from a rectangular cross section

Over time, the geometry of the samples increasingly deviates from a simple cylindrical shape with a rectangular cross-section. Despite careful preparation of polished interfaces, the presence of cracks and fractures in the quartz interface, the flower-like pattern in PSq tests, as well as the wavy pattern of the cristobalite layer in contact with the glass, could not be completely avoided. These irregularities may have contributed to variations in the contact area between silica and the glass.

Figures B.5 and B.6 compare the evolution of PSq and PSc tests' surface area, respectively, using two methods : measurements of height and diameter of the remaining solid are contrasted with surface areas derived from Raman mappings. This comparison reveals that assuming a rectangular cross-section, as represented by the simplified $2rh$ equation, does not account for material loss at the corners of the flower-like shape, overestimating the final surface.

This comparison reveals that assuming a rectangular cross-section, as represented by the simplified $2rh$ equation, does not account for material loss irregularities, such as PSq tests' preferential dissolution at the corners of the flower-like shape and PSc wavy interfaces, overestimating the final surface. It should be noted that after 240 minutes quartz dissolution, the cross-section of the remaining solid deviates by almost 40% from a perfect rectangular form. On the other hand, the deviation is more pronounced for the PSc-1440 test for cristobalite dissolution samples, where the remaining cristobalite assumed a concave shape after 24 hours of dissolution.

These results highlight that using a single geometric proxy to describe quartz dissolution poses inherent challenges, as it may oversimplify the complex microstructural evolution. Furthermore, the interaction between dissolution and phase transformation complicates the interpretation of dissolution kinetics.

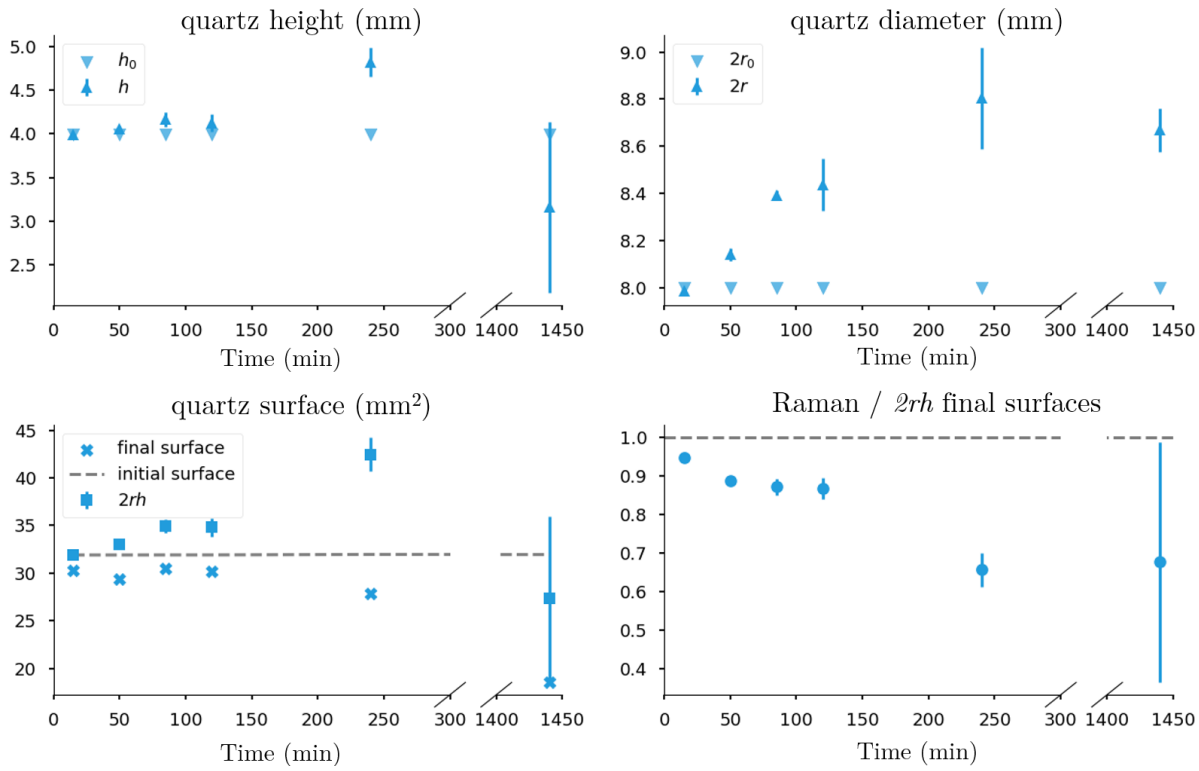

Figure B.5 Evolution of quartz height and diameter, along with the deviation from a rectangular cross-section during dissolution. (Top) : The measured height and diameter of the remaining quartz slab after dissolution (upward-pointing triangles) compared to the initial dimensions (downward-pointing triangles). (Bottom left) : Surface areas measured from Raman maps (crosses) compared with the areas calculated using only height and diameter (squares), based on the rectangular cross-section approximation ($2rh$). (Bottom right) : The ratio between the surface area estimates derived from Raman maps and those based on the rectangular cross-section approximation.

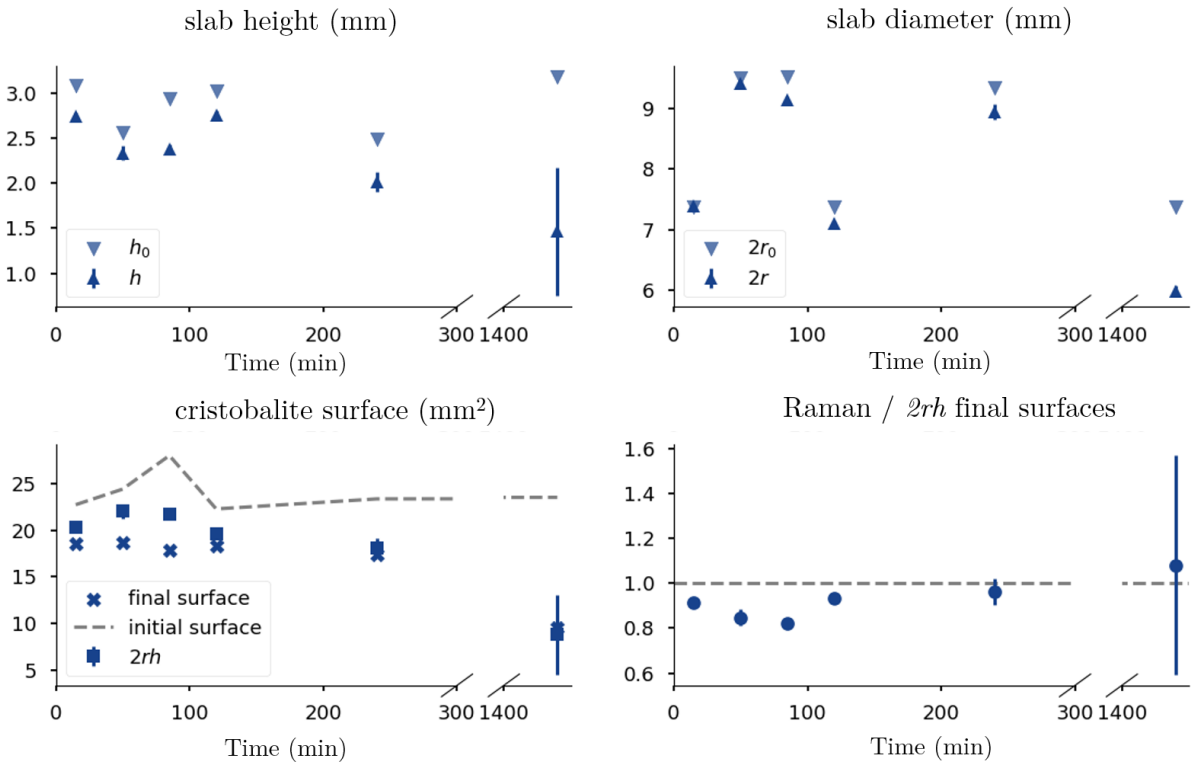

Figure B.6 Evolution of cristobalite slab height and diameter, along with the deviation from a rectangular cross-section during dissolution. (Top) : The measured height and diameter of the remaining cristobalite slab after dissolution (upward-pointing triangles) compared to the initial dimensions (downward-pointing triangles). (Bottom left) : Surface areas measured from Raman maps (crosses) compared with the areas calculated using only height and diameter (squares), based on the rectangular cross-section approximation ($2rh$). (Bottom right) : The ratio between the surface area estimates derived from Raman maps and those based on the rectangular cross-section approximation.

Appendix C

Optical and scanning electron microscope images of silica dissolution samples

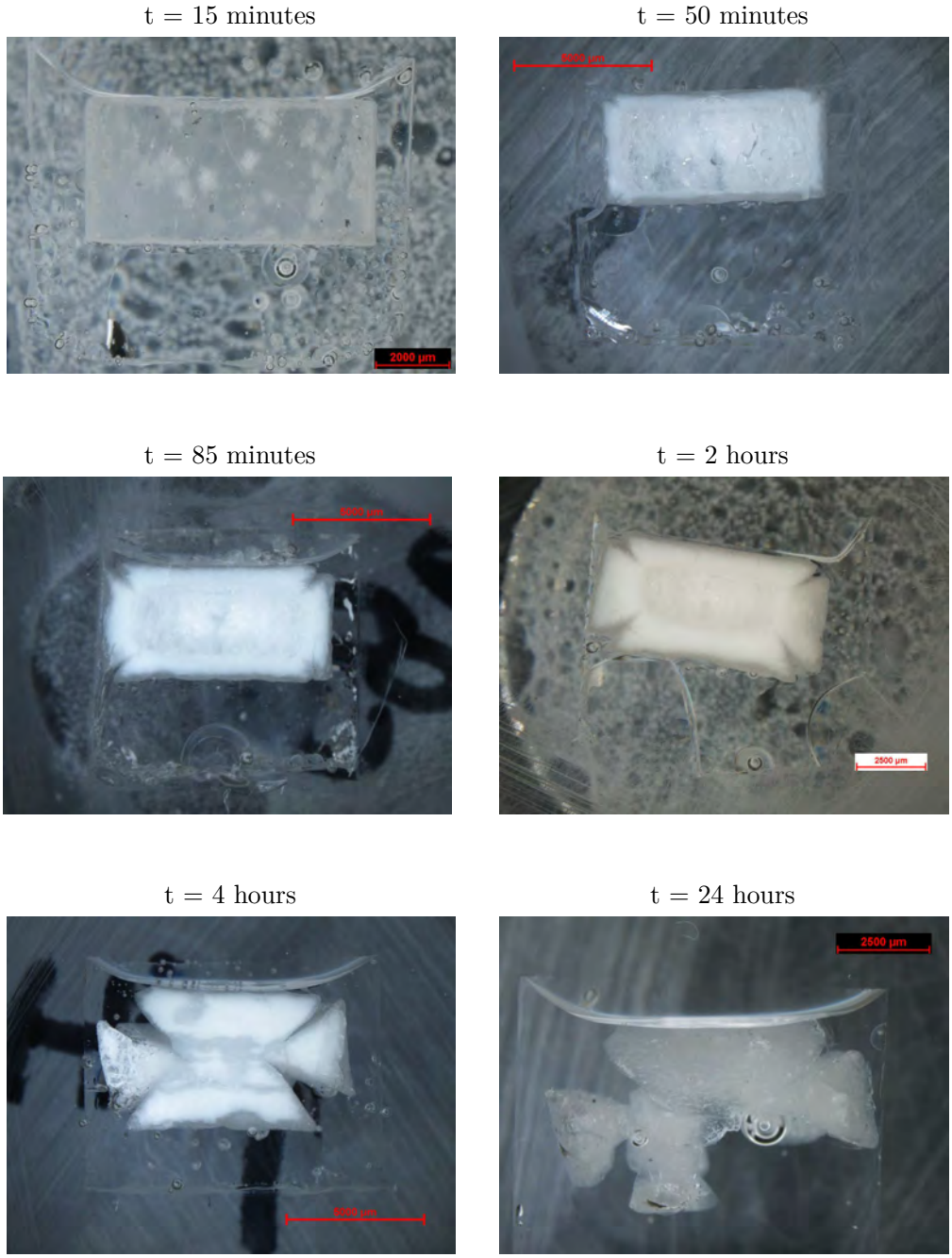

Figure C.1 Binocular microscopy photos of all quartz dissolution samples, using the standard geometry setup.

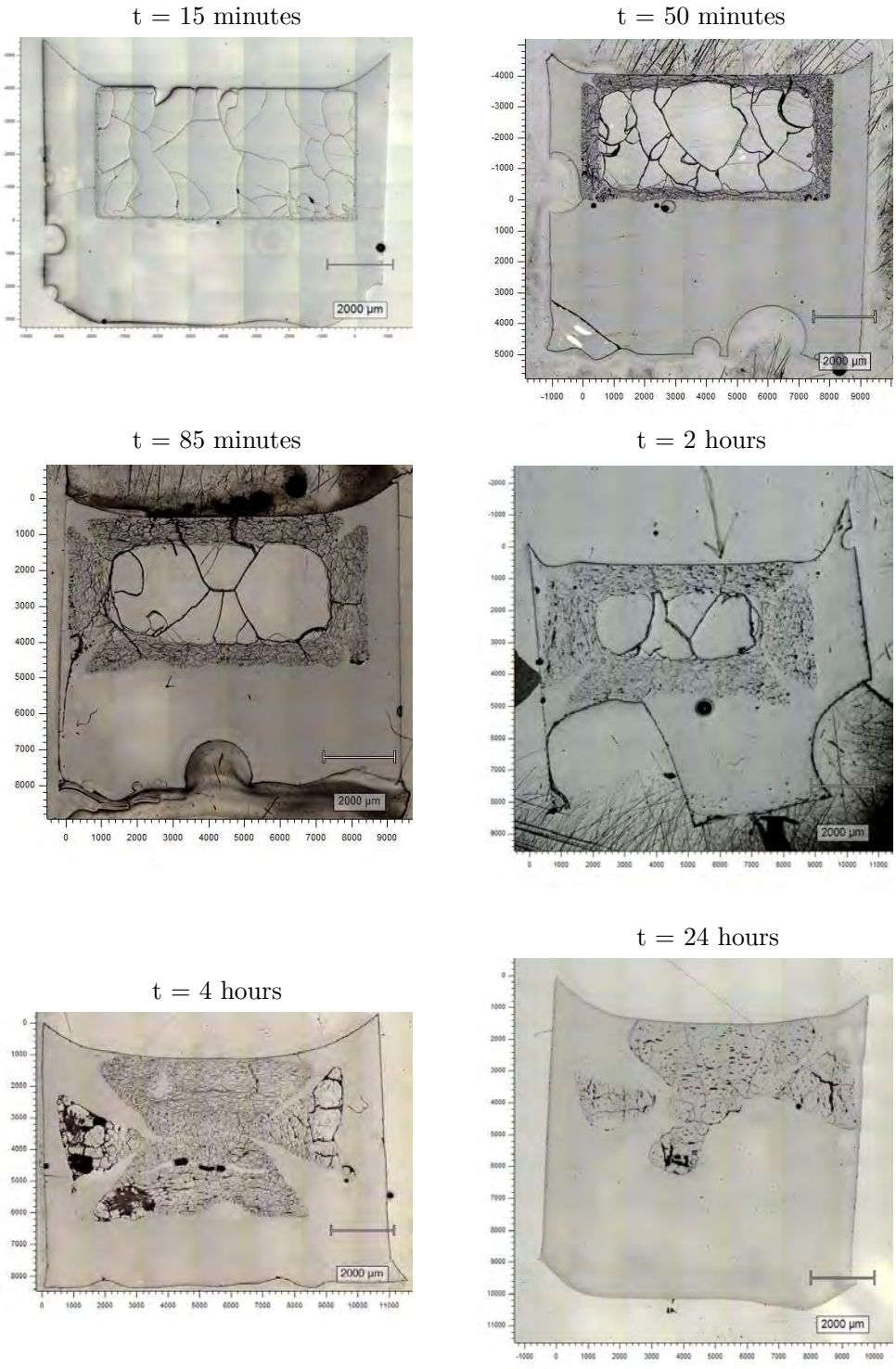

Figure C.2 Optical microscopy photos under reflection mode of all quartz dissolution samples, using the standard geometry setup.

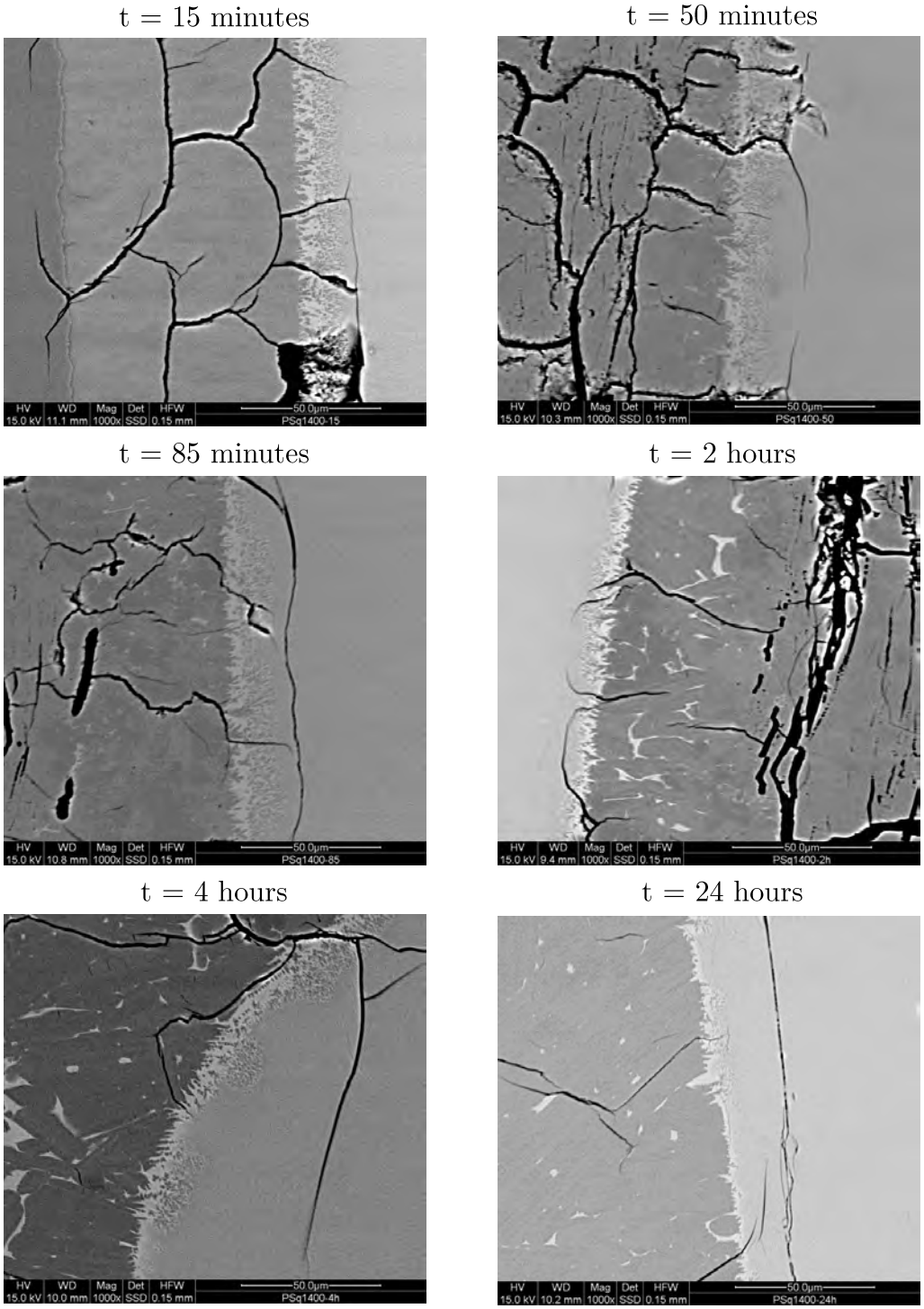

Figure C.3 SEM images captured under Back Scattered Electron (BSE) mode, highlighting the dendrites close to the interface. All images have the same magnification and were obtained close in the sides of the remaining solid, where the glass layer was thinner.



Figure C.4 Binocular microscopy photos of all cristobalite dissolution samples, using the standard geometry setup.

t = 15 minutes

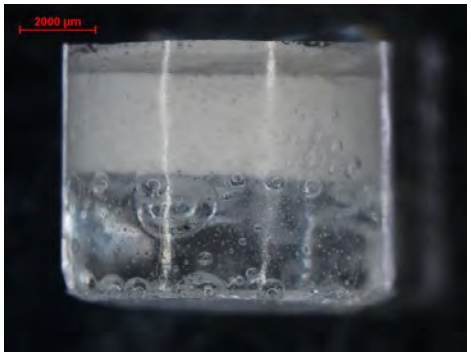

t = 50 minutes

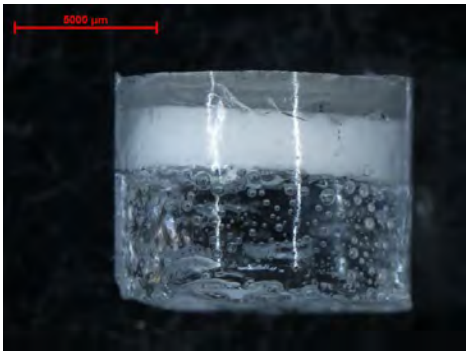

t = 85 minutes

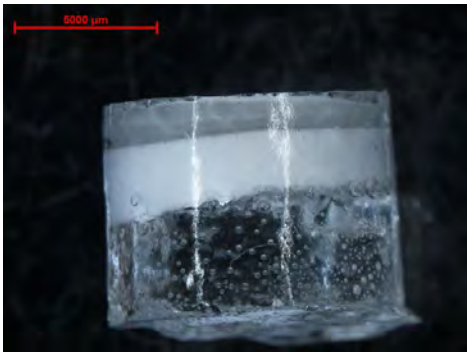

t = 2 hours

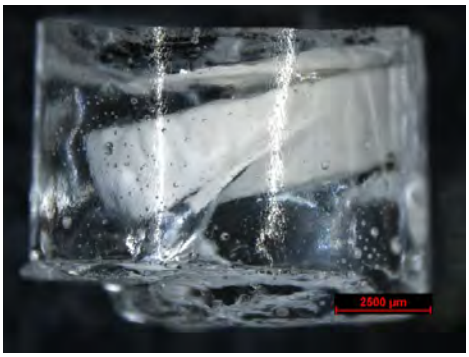

t = 4 hours

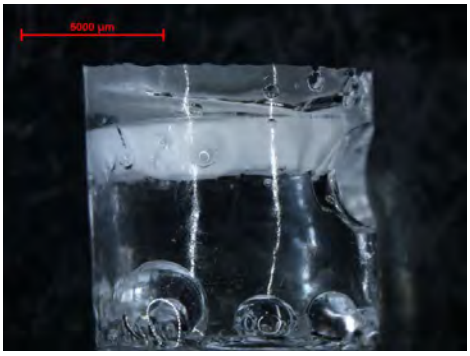

t = 24 hours

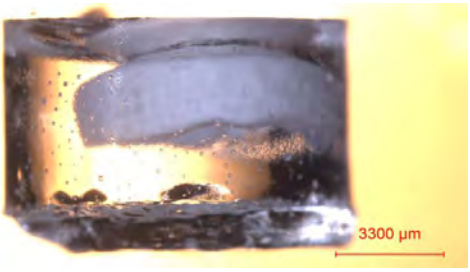

Figure C.5 Binocular microscopy photos of all cristobalite dissolution samples, viewed at the side of the setup, prior to epoxy embedding.

Appendix D

Raman mapping for quartz dissolution sample after stabilization of the furnace temperature

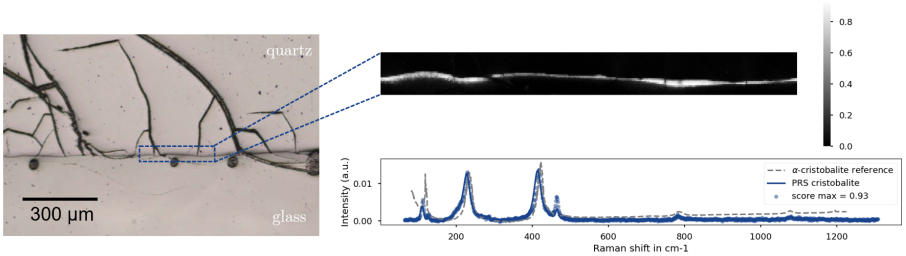

Figure D.1 Cristobalite layer formed after just two minutes of dissolution (PSq-1400-0 test). (Left) Reflection mode image near the middle of the quartz tablet's interface with the glass. (Right) Raman mapping shows cristobalite contribution in the area enclosed by the blue rectangle. The formed layer is thin yet continuous along the interface with the glass. The measurement step was 1 µm. Reference α-cristobalite spectra is from [121]

Appendix E

Cristobalite structural differences

The PSc tests were conducted under the hypothesis that the preformed cristobalite slabs were comparable to the cristobalite layer formed at the interface of quartz dissolution samples. Therefore, the primary objective of this investigation is to evaluate the validity of this hypothesis and to characterize any potential differences between these two forms of cristobalite.

To investigate the differences between the cristobalite layer formed during quartz dissolution and the cristobalite slab produced from the refractory, a comparative Raman spectra analysis was conducted. Fifty spectra from the cristobalite portion of each PSq sample were superimposed and compared with the average spectra of the cristobalite slab. The spectra were pretreated by removing the baseline and normalizing the intensities by the total area, following the methodology described in Section 4.2.

Analysis of the spectra indicated that the cristobalite layer formed from quartz dissolution more closely resembles literature-reported values for α-cristobalite compared to the cristobalite slab. This observation is particularly noteworthy given that the preparation method for the cristobalite slab (vitreous silica heat-treated at 1540 °C for 17 hours without fluxes) is similar to that employed by Bates [121].

Furthermore, the spectra of the cristobalite layer from PSq tests revealed the coexistence of multiple phases. A quartz peak at 465 cm^{-1} was observed, along with scattering between the two main cristobalite peaks. This scattering may be attributable to the increasing presence of tridymite in proximity to cristobalite during extended dissolution tests.

To quantify these differences, the barycentre and full width at half maximum (FWHM) were calculated from 200 spectra of each PSq sample and the cristobalite slab. The positions reported by Bates for the two main cristobalite peaks were used as reference points in the barycentre plot and plotted as black dashed lines in Figures E.2 and E.3. Barycentre and FWHM were both calculated around the main peaks at 230 and 416 cm^{-1}, considering a range of $\pm$ 50 cm^{-1}.

The results corroborated the initial observations, showing that cristobalite formed from PSq tests more closely approximates the reported data for synthetic cristobalite frequencies. A slight evolution in both peaks' barycentres was noted for this cristobalite layer, although it remained within the standard deviation range. Notably, the 416 cm^{-1} peak of PSq's cristobalite consistently exhibited a lower shift and broader peak compared to the cristobalite slab, potentially indicating a lower degree of crystallinity.

Both peaks of α-cristobalite at 230 and 416 cm^{-1} are assigned to an A_1 vibrational mode, primarily describing the stretching coordinate of Si-O bonds and O-Si-O bending coordinates [121,134].

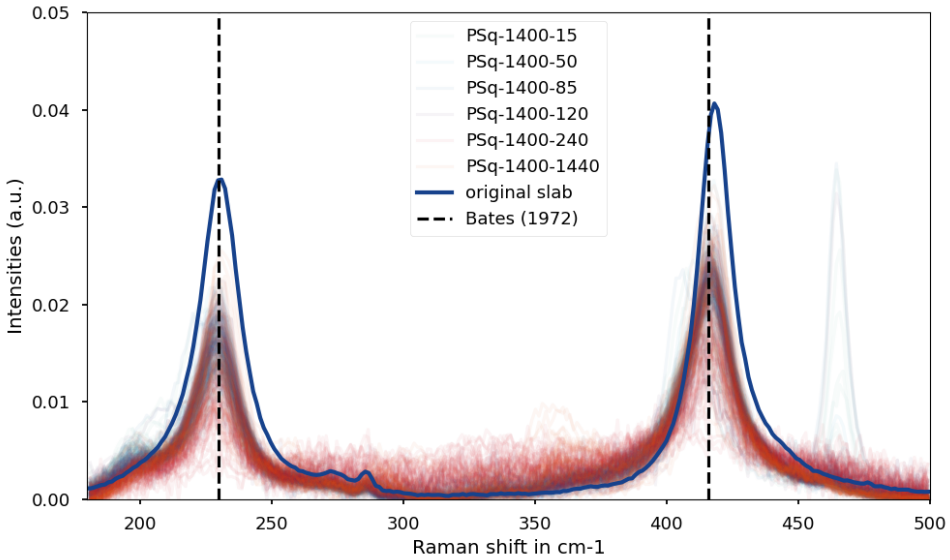

Figure E.1 Comparison between the average cristobalite slab spectra (solid blue line) and spectra from the cristobalite layer formed during PSq tests (transluscent curves). Reference values for the main peaks of α-cristobalite Raman peaks are presented as black vertical lines [121].

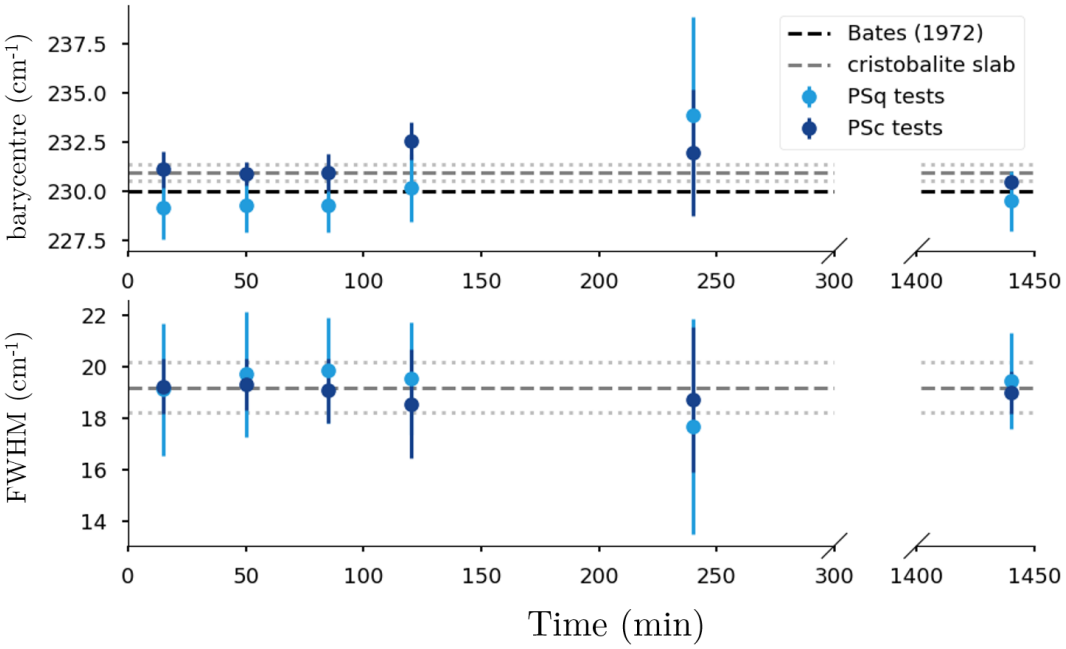

Figure E.2 Evolution of barycentre and full width at half maximum (FWHM) cristobalite Raman spectra from PSq (light blue markers) and PSc tests (dark blue markers) with dissolution time. The values were calculated in the range between 230 ± 50 cm^{-1}. The gray dashed lines represent the values for the manufactured cristobalite slab, and the dotted lines the range defined by its standard deviation.

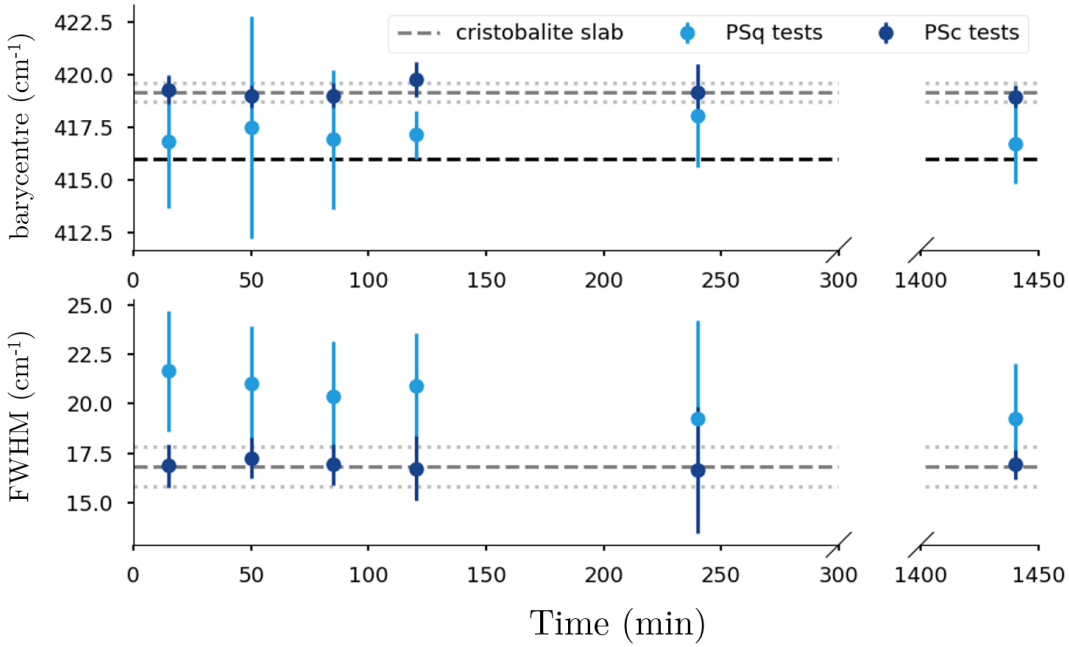

Figure E.3 Evolution of barycentre and full width at half maximum (FWHM) cristobalite Raman spectra from PSq (light blue markers) and PSc tests (dark blue markers) with dissolution time. The values were calculated in the range between 416 ± 50 cm^{-1}. The gray dashed lines represent the values for the manufactured cristobalite slab, and the dotted lines the range defined by its standard deviation.

The observed shift towards lower frequencies suggests that these vibrations are associated with a longer characteristic length in the structure compared to the manufactured cristobalite.

A comparative analysis was also performed on the cristobalite remaining after PSc dissolution tests, plotted in Figures E.2 and E.3 by the dark blue markers. The results revealed minimal changes in both barycenter and FWHM for PSc samples with respect to dissolution time and the original slab. This observation suggests that the structure of the cristobalite formed prior to the test remains stable when in contact with the glass.

These minimal variations between pre-formed cristobalite slabs and the cristobalite layer formed at the interface of PSq samples reinforces the validity of the initial hypothesis.

Bibliography

[1] S. Roudier, L. D. Sancho, B. Scalet, M. G. Muñoz, *et al.*, "Best available techniques (bat) reference document for the manufacture of glass : Industrial emissions directive 2010/75/eu :(integrated pollution prevention and control)," tech. rep., Joint Research Centre (Seville site), 2013. iii, vii, 147, 151

[2] S. Di Pierro, "Raw materials for glassmaking : Properties and constraints," *Encyclopedia of Glass Science, Technology, History, and Culture*, vol. 1, pp. 39–51, 2021. iii, vii, 3

[3] R. Beerkens, "Modeling of the melting process in industrial glass furnaces," in *Mathematical simulation in glass technology*, pp. 17–73, Springer, 2002. iv, 2, 3, 4, 5, 6, 80

[4] R. Conradt, "Fusion of glass," *Encyclopedia of Glass Science, Technology, History, and Culture*, vol. 1, pp. 53–66, 2021. 2, 3, 4

[5] L. Němec, M. Jebavá, and P. Dyrčíková, "Glass melting phenomena, their ordering and melting space utilisation," *Ceramics–Silikáty*, vol. 57, no. 4, pp. 275–284, 2013. 4

[6] M. K. Choudhary, R. Venuturumilli, and M. R. Hyre, "Mathematical Modeling of Flow and Heat Transfer Phenomena in Glass Melting, Delivery, and Forming Processes," *International Journal of Applied Glass Science*, vol. 1, no. 2, 2010. 4, 5

[7] O. Levenspiel, *Chemical reaction engineering*. John wiley & sons, 1974. 6, 7, 44

[8] C. Xuan and W. Mu, "A mechanism theory of dissolution profile of oxide particles in oxide melt," *Journal of the American Ceramic Society*, vol. 104, no. 1, pp. 57–75, 2021. 6, 7, 18, 24, 29, 31, 38

[9] K. C. Liddell, "Shrinking core models in hydrometallurgy : What students are not being told about the pseudo-steady approximation," *Hydrometallurgy*, vol. 79, no. 1-2, pp. 62–68, 2005. 7

[10] L. Gou, H. Liu, Y. Ren, and L. Zhang, "Concept of inclusion capacity of slag and its application on the dissolution of al2o3, zro2 and sio2 inclusions in cao–al2o3–sio2 slag," *Metallurgical and Materials Transactions B*, vol. 54, no. 3, pp. 1314–1325, 2023. 7, 38

[11] C. Ren, C. Huang, L. Zhang, and Y. Ren, "In situ observation of the dissolution kinetics of al2o3 particles in cao-al2o3-sio2 slags using laser confocal scanning microscopy," *International Journal of Minerals, Metallurgy and Materials*, vol. 30, no. 2, pp. 345–353, 2023. 7, 23, 25, 26, 27, 28, 38, 39, 40

[12] S. Feichtinger, S. K. Michelic, Y.-B. Kang, and C. Bernhard, "In situ observation of the dissolution of sio 2 particles in cao–al 2 o 3–sio 2 slags and mathematical analysis of its dissolution pattern," *Journal of the American Ceramic Society*, vol. 97, no. 1, pp. 316–325, 2014. 7, 17, 23, 25, 27, 28, 29, 30, 38, 39, 40, 80, 98

[13] H. Harmuth *et al.*, "Evaluation of clsm measurements for dissolution studies–a case study investigating alumina dissolution in a silicate slag," *Ceramics International*, vol. 48, no. 19, pp. 28174–28180, 2022. 7, 23, 25, 28, 29, 39, 40

[14] D. Readey and A. Copper Jr, "Molecular diffusion with a moving boundary and spherical symmetry," *Chemical Engineering Science*, vol. 21, no. 10, pp. 917–922, 1966. 9, 12, 13, 14

[15] L. Brown, "Diffusion-controlled dissolution of planar, cylindrical, and spherical precipitates," *Journal of applied Physics*, vol. 47, no. 2, pp. 449–458, 1976. 9

[16] P. Taylor, M. De Matos, and G. Martins, "Modeling of noncatalytic fluid-solid reactions : The quasi-steady state assumption," *Metallurgical Transactions B*, vol. 14, pp. 49–53, 1983. 9, 10

[17] J. R. Frade and M. Cable, "Reexamination of the basic theoretical model for the kinetics of solid–state reactions," *Journal of the American Ceramic Society*, vol. 75, no. 7, pp. 1949–1957, 1992. 9

[18] J. R. Frade and M. Cable, "Combined effects of diffusion and reaction on the growth or dissolution of spherical particles," *Journal of materials science*, vol. 30, pp. 989–994, 1995. 9, 10, 11

[19] R. Rice and D. Do, "Dissolution of a solid sphere in an unbounded, stagnant liquid," *Chemical engineering science*, vol. 61, no. 2, pp. 775–778, 2006. 9

[20] Y. Zhang, D. Walker, and C. E. Lesher, "Diffusive crystal dissolution," *Contributions to Mineralogy and Petrology*, vol. 102, pp. 492–513, 1989. 9

[21] M. Cable and J. Frade, "The diffusion-controlled dissolution of spheres," *Journal of materials science*, vol. 22, pp. 1894–1900, 1987. 12, 13, 14, 17, 18

[22] J. Crank, *The mathematics of diffusion*. Oxford university press, 1979. 16

[23] R. Clift, J. R. Grace, and M. E. Weber, *Bubbles, drops, and particles*. Courier Corporation, 2013. 20, 21

[24] F. Gallaire and P.-T. Brun, "Fluid dynamic instabilities : theory and application to pattern forming in complex media," *Philosophical Transactions of the Royal Society A : Mathematical, Physical and Engineering Sciences*, vol. 375, no. 2093, p. 20160155, 2017. 21, 48

[25] M. Choudhary, "The effect of free convection on the dissolution of a spherical particle in a viscous melt," *Glass technology*, vol. 29, no. 3, pp. 100–102, 1988. 21

[26] R. G. Beerkens, H. P. Muijsenberg, and T. van der Heijden, "Modelling of sand grain dissolution in industrial glass melting tanks," *Glass science and technology*, 1994. 22, 23, 44

[27] M. Cable and D. Martlew, "Effective binary diffusivities for the dissolution of silica in melts of the sodium carbonate-silica system," *Glass technology*, vol. 26, no. 5, pp. 212–217, 1985. 23, 25, 27, 28, 80, 98

[28] H. J. Barklage-Hilgefort and G. H. Frischat, "Reactions between sio_2 and $na_2o \cdot 3\ sio_2$ glass melts," *Glass technology*, vol. 21, no. 6, pp. 212–215, 1980. 23, 24, 25, 27, 28, 80, 97, 98, 144, 148, 152

[29] K. Schwerdtfeger, "Dissolution of solid oxides in oxide melts. the rate of dissolution of solid silica in na2o-sio2 and k2o-sio2 melts," *The Journal of Physical Chemistry*, vol. 70, no. 7, pp. 2131–2137, 1966. 23, 25, 27, 28, 80, 98

[30] K. Kreider and A. Cooper, "Dissolution kinetics of quartz spheres in a sodium silicate melt," *Glass technology*, vol. 8, no. 3, pp. 71–73, 1967. 23, 24, 25, 28, 80, 97

[31] J. Hlavac and H. Nademlynska, "Dissolution of spherical silica particles in molten sodium disilicate," *Glass technology*, vol. 10, no. 2, pp. 54–58, 1969. 23, 24, 25, 28, 29, 30, 80, 97, 99, 148, 152

[32] P. Hrma, J. Marcial, K. J. Swearingen, S. H. Henager, M. J. Schweiger, and N. E. TeGrotenhuis, "Conversion of batch to molten glass, ii : Dissolution of quartz particles," *Journal of Non-Crystalline Solids*, vol. 357, no. 3, pp. 820–828, 2011. 23

[33] T. Tian, Y. Zhang, H. Zhang, K. Zhang, J. Li, and H. Wang, "Dissolution behavior of sio2 in the molten blast furnace slags," *International Journal of Applied Ceramic Technology*, vol. 16, no. 3, pp. 1078–1087, 2019. 23, 25, 27, 28, 39, 40, 80, 98

[34] C. S. Shaw, "Effects of melt viscosity and silica activity on the rate and mechanism of quartz dissolution in melts of the cmas and cas systems," *Contributions to Mineralogy and Petrology*, vol. 151, no. 6, pp. 665–680, 2006. 23, 25, 27, 32, 41, 97

[35] C. S. Shaw, "The effect of experiment geometry on the mechanism and rate of dissolution of quartz in basanite at 0.5 gpa and 1350 c," *Contributions to Mineralogy and Petrology*, vol. 139, no. 5, pp. 509–525, 2000. 23, 24, 45

[36] Y. Liang, "Diffusive dissolution in ternary systems : analysis with applications to quartz and quartzite dissolution in molten silicates," *Geochimica et Cosmochimica Acta*, vol. 63, no. 23-24, pp. 3983–3995, 1999. 23, 24, 25, 27, 28, 32, 35, 41, 45, 97

[37] Burhanuddin, H. Harmuth, and S. Vollmann, "Quantification of magnesia dissolution in silicate melts and diffusivity determination using rotating finger test," *Applied Sciences*, vol. 12, no. 24, p. 12791, 2022. 23, 25, 26, 27, 28, 39, 40, 45

[38] J. Liu, F. Verhaeghe, M. Guo, B. Blanpain, and P. Wollants, "In Situ Observation of the Dissolution of Spherical Alumina Particles in CaO–Al2O3–SiO2 Melts," *Journal of the American Ceramic Society*, vol. 90, no. 12, 2007. 23, 24, 25, 27, 28, 39, 40

[39] K. H. Sandhage and G. J. Yurek, "Direct and indirect dissolution of sapphire in calcia–magnesia–alumina–silica melts : dissolution kinetics," *Journal of the American Ceramic Society*, vol. 73, no. 12, pp. 3633–3642, 1990. 23, 24, 25

[40] A. Cooper Jr and W. Kingery, "Dissolution in ceramic systems : I, molecular diffusion, natural convection, and forced convection studies of sapphire dissolution in calcium aluminum silicate," *Journal of the American Ceramic Society*, vol. 47, no. 1, pp. 37–43, 1964. 23, 25, 26, 27, 28

[41] B. Samaddar, W. Kingery, and A. Cooper Jr, "Dissolution in ceramic systems : 11, dissolution of aluminu, mullite, anorthite, and silica in a calcium-aluminum-silicate slag," *Journal of the American Ceramic Society*, vol. 47, no. 5, pp. 249–254, 1964. 23, 25, 27, 28, 39, 40, 80, 98

[42] X. Yu, R. Pomfret, and K. Coley, "Dissolution of alumina in mold fluxes," *Metallurgical and Materials Transactions B*, vol. 28, pp. 275–279, 1997. 23, 25, 27, 28, 39, 40

[43] M. Cable and D. Martlew, "Dissolution of silica in melts of the sodium carbonate - sodium metasilicate system," *Glass technology*, vol. 25, no. 3, pp. 139–144, 1984. 23, 44

[44] P. Hrma, J. Bartoň, and T. Tolt, "Interaction between solid, liquid and gas during glass batch melting," *Journal of Non-Crystalline Solids*, vol. 84, no. 1-3, pp. 370–380, 1986. 23, 44

[45] Q. Shu, Y. Wang, J. Li, Y. Liu, P. Li, and K. Chou, "Effect of na2o on dissolution rate of alumina in cao–al2o3–mgo–sio2 slag," *ISIJ International*, vol. 55, no. 11, pp. 2297–2303, 2015. 23, 24

[46] Y. Yu, Y. Zhang, and Y. Yang, "Kinetics of quartz dissolution in natural silicate melts and dependence of sio2 diffusivity on melt composition," *ACS Earth and Space Chemistry*, vol. 3, pp. 599–616, 2019. 23, 45

[47] M. Valdez, K. Prapakorn, A. Cramb, and S. Sridhar, "Dissolution of alumina particles in cao-al2o3-sio2-mgo slags," *Ironmaking & steelmaking*, vol. 29, no. 1, pp. 47–52, 2002. 24

[48] K. H. Sandhage and G. J. Yurek, "Indirect Dissolution of Sapphire into Silicate Melts," *Journal of the American Ceramic Society*, vol. 71, no. 6, 1988. 24

[49] C. S. J. Shaw, K. B. Klausen, and H. Mao, "Kinetics of dissolution of sapphire in melts in the CaO–Al2O3–SiO2 system," *Geochimica et Cosmochimica Acta*, 2018. 25, 27, 28, 32, 41, 45

[50] M. Cable and D. Martlew, "The effective binary diffusivity of silica in sodium silicate melts : a review and recommendation," *Glass technology*, vol. 25, no. 6, pp. 270–276, 1984. 29

[51] B. J. Monaghan, L. Chen, and J. Sorbe, "Comparative study of oxide inclusion dissolution in cao–sio2–al2o3 slag," *Ironmaking & steelmaking*, vol. 32, no. 3, pp. 258–264, 2005. 29

[52] J. W. Gibbs, "On the equilibrium of heterogeneous substances," *American Journal of Science and Arts*, vol. s3-16, pp. 441 – 458, 1878. 31

[53] Y. Oishi, A. Cooper Jr, and W. Kingery, "Dissolution in ceramic systems : Iii, boundary layer concentration gradients," *Journal of the American Ceramic Society*, vol. 48, no. 2, pp. 88–95, 1965. 32

[54] K. H. Sandhage and G. J. Yurek, "Indirect dissolution of sapphire into calcia-magnesia-alumina-silica melts : Electron microprobe analysis of the dissolution process," *Journal of the American Ceramic Society*, vol. 73, no. 12, pp. 3643–3649, 1990. 32, 41

[55] H. Ni, H. Hui, and G. Steinle-Neumann, "Transport properties of silicate melts," *Reviews of Geophysics*, vol. 53, no. 3, pp. 715–744, 2015. 32, 33, 37

[56] Y. Liang, "Multicomponent diffusion in molten silicates : theory, experiments, and geological applications," *Reviews in Mineralogy and Geochemistry*, vol. 72, no. 1, pp. 409–446, 2010. 33, 34, 35

[57] Y. Zhang, H. Ni, and Y. Chen, "Diffusion data in silicate melts," *Reviews in Mineralogy and Geochemistry*, vol. 72, no. 1, pp. 311–408, 2010. 33

[58] C. E. Lesher, "Self-diffusion in silicate melts : theory, observations and applications to magmatic systems," *Reviews in Mineralogy and Geochemistry*, vol. 72, no. 1, pp. 269–309, 2010. 33

[59] Y. Zhang, H. Ni, and Y. Chen, "Diffusion data in silicate melts," *Reviews in Mineralogy and Geochemistry*, vol. 72, no. 1, pp. 311–408, 2010. 33

[60] Y. Zhang and T. Gan, "Diffusion in melts and magmas," *Reviews in Mineralogy and Geochemistry*, vol. 87, no. 1, pp. 283–337, 2022. 33

[61] L. Onsager, "Theories and problems of liquid diffusion," *Annals of the New York Academy of Sciences*, vol. 46, no. 5, pp. 241–265, 1945. 33

[62] A. F. Trial and F. J. Spera, "Measuring the multi~omponentelusion matrix : Ex~riment~ design and data analysis for silicate melts," *Geochimica et Cosmochimica Acta*, 1994. 35, 36, 94, 97, 98, 162, 163

[63] C. Claireaux, "Influence of temperature on multicomponent diffusion in calcium and sodium aluminosilicate melts," *Journal of Non-Crystalline Solids*, 2019. 35, 37, 38, 46, 94

[64] M. Jacquemin, *Mobilité couplée à haute température et modifications structurales dans les verres Na2O-CaO-Al2O3-SiO2*. Phd thesis, Université d'Orléans, January 2022. Available at https://theses.hal.science/tel-04097368. 35, 36, 37, 46, 94, 97

[65] Y. Liang, F. Richter, A. Davis, and E. Brucewatson, "Diffusion in silicate melts : I. Self diffusion in CaO-AI203-SiO2 at 1500°C and 1 GPa," *Geochimica et Cosmochimica Acta*, 1996. 35, 36, 49

[66] H. Pablo, S. Schuller, M. Toplis, E. Gouillart, S. Mostefaoui, T. Charpentier, and M. Roskosz, "Multicomponent diffusion in sodium borosilicate glasses," *Journal of Non-Crystalline Solids*, vol. 478, pp. 29–40, 2017. 36

[67] S. Chakraborty, D. B. Dingwell, and D. C. Rubie, "Multicomponent diffusion in ternary silicate melts in the system k2o-al2o3-sio2 : I. experimental measurements," *Geochimica et Cosmochimica Acta*, vol. 59, no. 2, pp. 255–264, 1995. 35, 36

[68] J. E. Mungall, C. Romano, and D. B. Dingwell, "Multicomponent diffusion in the molten system k 2 o-na 2 o-al 2 o 3-sio 2-h 2 o," *American Mineralogist*, vol. 83, no. 7-8, pp. 685–699, 1998. 36

[69] F. M. Richter, Y. Liang, and W. G. Minarik, "Multicomponent diffusion and convection in molten mgo-al2o3-sio2," *Geochimica et cosmochimica acta*, vol. 62, no. 11, pp. 1985–1991, 1998. 36

[70] C. Claireaux, M.-H. Chopinet, E. Burov, E. Gouillart, M. Roskosz, and M. J. Toplis, "Atomic mobility in calcium and sodium aluminosilicate melts at 1200 c," *Geochimica et Cosmochimica Acta*, vol. 192, pp. 235–247, 2016. 36, 37

[71] M. Ficheux, "Influence of zirconium on cation mobilities in Na2O-CaO-Al2O3-SiO2 melts : A multicomponent diffusion and XANES study," *Geochimica et Cosmochimica Acta*, 2020. 36

[72] D. R. Baker, "Estimation of diffusion coefficients during interdiffusion of geologic melts : application of transition state theory," *Chemical Geology*, vol. 98, no. 1-2, pp. 11–21, 1992. 38

[73] D. R. Cassar, "Glassnet : a multitask deep neural network for predicting many glass properties," *Ceramics International*, 2023. 38, 49

[74] W. M. Murphy, E. H. Oelkers, and P. C. Lichtner, "Surface reaction versus diffusion control of mineral dissolution and growth rates in geochemical processes," *Chemical Geology*, vol. 78, pp. 357–380, 1989. 44

[75] S. Bordère and S. Glockner, "Numerical modeling of diffusion-controlled phase transformation using the darken method : application to the dissolution/precipitation processes in materials," *Computational Materials Science*, vol. 186, p. 109944, 2021. 44

[76] P. Kechagia, I. N. Tsimpanogiannis, Y. Yortsos, and P. C. Lichtner, "On the upscaling of reaction-transport processes in porous media with fast or finite kinetics," *Chemical Engineering Science*, vol. 57, pp. 2565–2577, 2002. 44

[77] A. Acosta-Vigil, D. London, T. A. Dewers, and G. B. Morgan, "Dissolution of corundum and andalusite in h2o-saturated haplogranitic melts at 800° c and 200 mpa : constraints on diffusivities and the generation of peraluminous melts," *Journal of Petrology*, vol. 43, no. 10, pp. 1885–1908, 2002. 45

[78] Y. Chen and Y. Zhang, "Olivine dissolution in basaltic melt," *Geochimica et Cosmochimica Acta*, 2008. 45

[79] P. Dauby and G. Lebon, "Bénard–marangoni instability in rigid rectangular containers," *Journal of Fluid Mechanics*, vol. 329, pp. 25–64, 1996. 48

[80] L. M. Rabin, "Instability threshold in the bénard-marangoni problem," *Physical Review E*, vol. 53, pp. R2057–R2059, 1996. 48

[81] A. F. V. Zee and C. I. Babcock, "A method for the measurement of thermal diffusivity of molten glass," *Journal of the American Ceramic Society*, vol. 34, pp. 244–250, 1951. 48

[82] L. Shartsis and S. Spinner, "Surface tension of molten alkali silicates," *Journal of Research of the National Bureau of Standards*, vol. 46, p. 385, 1951. 48

[83] J. Turner, "Double-diffusive phenomena," *Annual review of fluid mechanics*, vol. 6, no. 1, pp. 37–54, 1974. 49

[84] Y. Liang, "Axisymmetric double-diffusive convection in a cylindrical container : Linear stability analysis with applications to molten cao-al 2 o 3-sio 2," *Geophysical Monograph Series*, vol. 94, pp. 115–124, 1995. 49, 50

[85] B. Trouette, E. Chénier, F. Doumenc, C. Delcarte, and B. Guerrier, "Transient rayleigh-bénard-marangoni solutal convection," *Physics of Fluids*, vol. 24, 2012. 51

[86] J.-A. Xu, E. Huang, and L. Y. Xu, "Raman study at high pressure and the thermodynamic properties of corundum : application of kieffer's model," *American Mineralogist*, vol. 80, no. 11-12, pp. 1157–1165, 1995. 52, 53

[87] V. Ranieri, D. Bourgogne, S. Darracq, M. Cambon, J. Haines, O. Cambon, R. Leparc, C. Levelut, A. Largeteau, and G. Demazeau, "Raman scattering study of α-quartz and si 1- x ge x o 2 solid solutions," *Physical Review B*, vol. 79, no. 22, p. 224304, 2009. 53, 117

[88] M. Deluca, H. Hu, M. N. Popov, J. Spitaler, and T. Dieing, "Advantages and developments of raman spectroscopy for electroceramics," *Communications Materials*, vol. 4, no. 1, p. 78, 2023. 56

[89] A. Orlando, F. Franceschini, C. Muscas, S. Pidkova, M. Bartoli, M. Rovere, and A. Tagliaferro, "A comprehensive review on raman spectroscopy applications," *Chemosensors*, vol. 9, no. 9, p. 262, 2021. 56

[90] P. F. McMillan and B. Piriou, "Raman spectroscopic studies of silicate and related glass structure : a review," *Bulletin De Minéralogie*, vol. 106, pp. 57–75, 1983. 57

[91] A. Yadav and P. Singh, "A review of the structures of oxide glasses by raman spectroscopy," *RSC Advances*, vol. 5, pp. 67583–67609, 2015. 57

[92] J. Wahl, E. Klint, M. Hallbeck, J. Hillman, K. Wårdell, and K. Ramser, "Impact of preprocessing methods on the raman spectra of brain tissue," *Biomedical Optics Express*, vol. 13, p. 6763, 2022. 57

[93] R. Gautam, S. Vanga, F. Ariese, and S. Umapathy, "Review of multidimensional data processing approaches for raman and infrared spectroscopy," *EPJ Techniques and Instrumentation*, vol. 2, 2015. 58

[94] J. Röhm, "Non-negative matrix factorization for raman data spectral analysis," *Technische Universitat Berlin Institute of Mathematics*, 2017. 58

[95] W. Woelffel, C. Claireaux, M. J. Toplis, E. Burov, E. Barthel, A. Shukla, J. Biscaras, M.-H. Chopinet, and E. Gouillart, "Analysis of soda-lime glasses using non-negative matrix factor deconvolution of raman spectra," *Journal of Non-Crystalline Solids*, vol. 428, pp. 121–131, 2015. 58

[96] X. Llovet, A. Moy, P. Pinard, and J. Fournelle, "Electron probe microanalysis : a review of recent developments and applications in materials science and engineering," *Progress in Materials Science*, vol. 116, p. 100673, 2021. 59

[97] X. Llovet, "Electron probe microanalysis," *Reference Module in Chemistry, Molecular Sciences and Chemical Engineering*, 2018. 59

[98] C. Merlet, "An accurate computer correction program for quantitative electron probe microanalysis," *Microchimica acta*, vol. 114, pp. 363–376, 1994. 60

[99] C. W. Bale, P. Chartrand, S. Degterov, G. Eriksson, K. Hack, R. B. Mahfoud, J. Melançon, A. Pelton, and S. Petersen, "Factsage thermochemical software and databases," *Calphad*, vol. 26, no. 2, pp. 189–228, 2002. 60

[100] P. J. Heaney, "Structure and chemistry of the low-pressure silica polymorphs," *Reviews in mineralogy*, vol. 29, pp. 1–1, 1994. 80, 81, 82, 84, 87, 122

[101] W. D. Kingery, H. K. Bowen, and D. R. Uhlmann, *Introduction to ceramics*, vol. 17. John wiley & sons, 1976. 81, 104

[102] C. S. Marians and L. W. Hobbs, "Network properties of crystalline polymorphs of silica," *Journal of non-crystalline solids*, vol. 124, no. 2-3, pp. 242–253, 1990. 80, 82

[103] X. Yuan and A. Cormack, "Efficient algorithm for primitive ring statistics in topological networks," *Computational materials science*, vol. 24, no. 3, pp. 343–360, 2002. 80, 82

[104] M. Shiga, A. Hirata, Y. Onodera, and H. Masai, "Ring-originated anisotropy of local structural ordering in amorphous and crystalline silicon dioxide," *Communications Materials*, vol. 4, no. 1, p. 91, 2023. 80, 81

[105] L. Marini, "Chapter 5—the product solid phases," *Developments in Geo-Chemistry ; Elsevier : Amsterdam, The Netherlands*, vol. 11, pp. 79–167, 2007. 82, 83

[106] M. Kanzaki, "Raman spectra of tridymite modifications : Mc, mx–1, and po–10," *Journal of Mineralogical and Petrological Sciences*, vol. 114, no. 4, pp. 214–218, 2019. 82, 120, 121, 122, 129

[107] A. Takada, K. J. Glaser, R. G. Bell, and C. R. A. Catlow, "Molecular dynamics study of tridymite," *IUCrJ*, vol. 5, no. 3, pp. 325–334, 2018. 82, 120, 122

[108] Y.-T. Shih, S. Sundararaman, and L. Huang, "Structural origin of the anomalous density maximum in silica and alkali silicate glasses," *Journal of the American Ceramic Society*, vol. 103, no. 7, pp. 3942–3953, 2020. 82

[109] S. Stevens, R. Hand, and J. Sharp, "Polymorphism of silica," *Journal of Materials Science*, vol. 32, pp. 2929–2935, 1997. 82, 83, 84

[110] A. Chaklader and A. L. Roberts, "Transformation of quartz to cristobalite," *Journal of the American Ceramic Society*, vol. 44, no. 1, pp. 35–41, 1961. 83

[111] F. Kuellmer and T. Poe, "The quartz-cristobalite transformation," *Journal of the American Ceramic Society*, vol. 47, no. 6, pp. 311–312, 1964. 83

[112] G. I. Madden and L. H. V. Vlack, "Transformation of quartz to tridymite in the presence of binary silicate liquids," *Journal of the American Ceramic Society*, vol. 50, pp. 414–418, 1967. 83

[113] M. Dapiaggi, L. Pagliari, A. Pavese, L. Sciascia, M. Merli, and F. Francescon, "The formation of silica high temperature polymorphs from quartz : Influence of grain size and mineralising agents," *Journal of the European Ceramic Society*, vol. 35, no. 16, pp. 4547–4555, 2015. 83

[114] A. Venezia, V. La Parola, A. Longo, and A. Martorana, "Effect of alkali ions on the amorphous to crystalline phase transition of silica," *Journal of solid state chemistry*, vol. 161, no. 2, pp. 373–378, 2001. 83, 124

[115] D. C. Palmer, "Stuffed derivatives of the silica polymorphs," *Reviews in Mineralogy*, vol. 29, pp. 83–83, 1994. 83, 124

[116] I. Bajenova, A. Khvan, A. Dinsdale, and A. Kondratiev, "Implementation of the extended einstein and two-state liquid models for thermodynamic description of pure sio2 at 1 atm," *Calphad*, vol. 68, p. 101716, 2020. 83, 84

[117] S. Schnurre, J. Gröbner, and R. Schmid-Fetzer, "Thermodynamics and phase stability in the si–o system," *Journal of Non-Crystalline Solids*, vol. 336, no. 1, pp. 1–25, 2004. 83, 84

[118] S. Holmquist, "Conversion of quartz to tridymite," *Journal of the American Ceramic Society*, vol. 44, no. 2, pp. 82–86, 1961. 83, 87, 124

[119] M. J. Toplis, *Encyclopedia of Glass Science, Technology, History, and Culture*, ch. Density of Amorphous Oxides, pp. 301–311. Wiley Online Library, 2021. 98, 99

[120] C. N. Fenner, "The stability relations of the silica minerals," *American Journal of Science*, vol. 36, pp. 331–384, 1913. 104

[121] J. Bates, "Raman spectra of α and β cristobalite," *The Journal of Chemical Physics*, vol. 57, pp. 4042–4047, 1972. 105, 117, 118, 128, 173, 175, 176

[122] D. Cellai, M. Carpenter, R. Kirkpatrick, E. Salje, and M. Zhang, "Thermally induced phase transitions in tridymite : an infrared spectroscopy study," *Physics and Chemistry of Minerals*, vol. 22, pp. 50–60, 1995. 120

[123] A. Pryde and M. Dove, "On the sequence of phase transitions in tridymite," *Physics and Chemistry of Minerals*, vol. 26, pp. 171–179, 1998. 120, 122

[124] M. Kanzaki, "Phase transitions of tridymite mc : A low frequency raman spectroscopic study," *Journal of Mineralogical and Petrological Sciences*, vol. 115, no. 3, pp. 296–301, 2020. 122

[125] T. Hirose, K. Kihara, M. Okuno, S. Fujinami, and K. Shinoda, "X-ray, dta and raman studies of monoclinic tridymite and its higher temperature orthorhombic modification with varying temperature," *Journal of Mineralogical and Petrological Sciences*, vol. 100, no. 2, pp. 55–69, 2005. 122

[126] C. Le Losq, D. R. Neuville, P. Florian, G. S. Henderson, and D. Massiot, "The role of al3+ on rheology and structural changes in sodium silicate and aluminosilicate glasses and melts," *Geochimica et Cosmochimica Acta*, vol. 126, pp. 495–517, 2014. 138

[127] M. Brouillette, "The richtmyer-meshkov instability," *Annual Review of Fluid Mechanics*, vol. 34, no. 1, pp. 445–468, 2002. 142, 144

[128] S. Y. Kwon, R. J. Hill, and I.-H. Jung, "Multi-ion diffusion model and application to solid dissolution in cao–al2o3–sio2 melts," *Journal of the American Ceramic Society*, vol. 107, no. 3, pp. 1835–1847, 2024. 148, 153

[129] J. Heulens, B. Blanpain, and N. Moelans, "A phase field model for isothermal crystallization of oxide melts," *Acta materialia*, vol. 59, no. 5, pp. 2156–2165, 2011. 148, 153

[130] J. Liu, J. Zou, M. Guo, and N. Moelans, "Phase field simulation study of the dissolution behavior of al2o3 into cao–al2o3–sio2 slags," *Computational Materials Science*, vol. 119, pp. 9–18, 2016. 148, 153

[131] A. Ali, Y. W. Chiang, and R. M. Santos, "X-ray diffraction techniques for mineral characterization : a review for engineers of the fundamentals, applications, and research directions," *Minerals*, vol. 12, p. 205, 2022. 157

[132] Y. Waseda, E. Matsubara, and K. Shinoda, *X-ray diffraction crystallography : introduction, examples and solved problems*. Springer Science & Business Media, 2011. 157

[133] R. Cheary, A. A. Coelho, and J. P. Cline, "Fundamental parameters line profile fitting in laboratory diffractometers," *Journal of Research of the National Institute of Standards and Technology*, vol. 109, p. 1, 2004. 157

[134] J. Etchepare, M. Merían, and P. Kaplan, "Vibrational normal modes of sio2. ii. cristobalite and tridymite," *The Journal of Chemical Physics*, vol. 68, no. 4, pp. 1531–1537, 1978. 175

Titre : Mécanismes de dissolution de minéraux dans des liquides silicatés d'intérêt industriel

Mots clés : dissolution, diffusion multi-composante, alumine, quartz, verre silico-sodo-calcique

Résumé : Cette thèse étudie la cinétique de dissolution de l'alumine-alpha et du quartz dans un verre silico-sodo-calcique multi-composant. Un montage expérimental a été utilisé pour examiner la solubilité et la diffusivité à l'interface lors de la dissolution dans le cas statique, en utilisant la microsonde électronique et la spectroscopie Raman pour mesurer les changements chimiques et structurels. L'étude révèle le rôle important des transformations de phase et de la dynamique du bain de fusion dans la dissolution. Cet étude souligne les limites des modèles binaires conventionnels pour capturer la complexité des systèmes multicomposants et met en avant l'importance des matrices de diffusion pour des prédictions précises. Malgré ces complexités, l'étude montre que la viscosité peut parfois servir de proxy à la diffusion.

Title: Dissolution mechanisms of minerals in silicate liquids of industrial interest

Key words: dissolution, multi-component diffusion, alumina, quartz, soda-lime-silica glass

Abstract: This PhD work investigates the dissolution kinetics of alpha-alumina and quartz in multi-component soda-lime-silica glass melts. A static experimental setup was employed to examine solubility and diffusivity at the interface during dissolution, using Electron Probe Micro-Analysis (EPMA) and Raman spectroscopy to measure chemical and structural changes. The study reveals the significant role of solid-phase transformations and melt dynamics in defining dissolution behavior. The research also highlights the limitations of conventional binary models in capturing the complexity of multi-component systems, emphasizing the importance of diffusion matrices for accurate predictions. Despite these complexities, the study demonstrates that viscosity may serve as a proxy for diffusion under certain conditions.